Characterisation and Mechanical Properties of Bulk Nanostructured Al-based Composites for High Temperature Applications

Stella Pedrazzini

Trinity College

A thesis submitted for the degree of Doctor of Philosophy in the Department of Materials,

University of Oxford

Hilary Term 2014

Abstract

Rapidly solidified nanoquasicrystalline $Al_{93}Fe_3Cr_2Ti_2$ at% alloy has previously shown outstanding mechanical performance and microstructural stability up to elevated temperatures. Despite this, no in-depth study had previously been performed assessing the active strengthening mechanisms, the long term microstructural stability and the effect of plastic deformation at elevated temperature to simulate the production methods utilised for engineering applications.

The current project analysed eight bars consisting of a nanoquasicrystalline $Al_{93}Fe_3Cr_2Ti_2$ at% alloy matrix with varying amounts of pure Al fibres, produced through gas atomisation and warm extrusion.

Microstructural characterisation and thermal analysis of the as-atomized powder was carried out to assess whether microstructural changed were likely to occur at the extrusion temperature. A microstructure made primarily of nanometre-sized icosahedral particles in an FCC-Al matrix was observed through a combination of SEM, TEM (and CBDP), EDX, XRD. Thermal analysis of the powders performed by DSC showed that no change was expected to occur at the extrusion temperature.

Five bars were extruded during the course of this project: one bar of pure Al-Fe-Cr-Ti alloy, two composite bars with 10 vol% added pure Al and two bars with 20 vol% added Al. Three more bars were received from a previous project and analysed. Warm extrusion caused the powder particles to become well bonded and elongated in the extrusion direction introducing a preferred orientation in the FCC-Al grains. A bimodal distribution of grain size was observed after extrusion. Several low angle (5-15 °) grain boundaries were also identified by EBSD along the extrusion direction. No obvious change in size or shape was observed by TEM in the icosahedral phase (a bimodal distribution of hard, incoherent precipitates was observed after extrusion), or any change in the amount of solutes in solid solution in the Al matrix.

Mechanical properties at room temperature were tested by Vickers microhardness, quasi-static tensile tests, dynamic tensile tests and dynamic compression tests. A theoretical model correlating the microstructures observed with the various active strengthening mechanisms was applied in order to predict an estimate of the yield strength of the material produced. It was found that the strength of the $Al_{93}Fe_3Cr_2Ti_2$ alloy came

primarily from a combination of the effect of the hard, incoherent nanoparticles, the small grain size and work hardening. The fibre addition to this alloy caused a linear decrease in mechanical strength with increasing vol% pure Al. This work represents the first quantitative estimate of which strengthening mechanisms are active and how much they influence the mechanical strength of $Al_{93}Fe_3Cr_2Ti_2$ alloy and composites. An understanding of the yield strength is essential as engineering components would only be safe to use within the elastic region.

To investigate the thermal stability of the alloy and composites, thermal analyses involving DSC and long heat treatments (up to a maximum of 1000 hours) were performed at various temperatures along with microstructural characterisation by XRD, SEM and TEM and microhardness tests. No microstructural change was detected, however a 2-5% decrease in microhardness was observed.

Compression tests were performed across a range of temperatures and strain rates to simulate the behaviour of these composites under typical conditions necessary to process them into useful engineering components. Phase changes occurring during plastic deformation at high temperature were investigated by XRD. The measured yield strength at 350 °C was over 3x that of high strength 7075 T6 Al alloy showing outstanding thermal stability and mechanical performance. However, the microstructure was shown by XRD to undergo a phase transformation which resulted in the decomposition of the icosahedral phase at 500 °C into more stable intermetallic phases. Serrated flow was also observed in some of the tests. The high temperature compressive data was then used for the first time in a semi-quantitative analysis to determine which species in solid solution (Fe, Cr or Ti) was likely to cause the serrations. A dynamic strain ageing model, which calculates the diffusion coefficients at the minimum in ductility and strain rate sensitivity, suggested that the Ti in solid solution in the matrix could be the most likely candidate.

Acknowledgements

I must thank my supervisors Dr Marina Galano and Prof Fernando Audebert.

I would like to thank Dr Mike Jenkins and my college advisors Prof Jan Czernuszka and Prof Michael Moody for all their help and guidance throughout this project. I would also like to thank Prof George Smith whose kindness means he has been providing guidance despite being retired and helping with presentations, papers and posters. And I would also like to thank Josie Smith for providing support (and amazing cakes) during the more difficult times.

I would like to thank the MoD, EPSRC (Bulknano Project Number EP/E040608/1) and the Department of Materials (DTA) for their financial support throughout this project. I would like to thank Santander for a £1000 award that allowed me to go to Argentina to perform experiments, Trinity College for a £450 award and the Materials Department for a £750 award, which allowed me to attend conferences.

I would like to thank the people who helped me with the experimental aspects of my project, including industrial collaborator Alpoco and particularly Steve McArthur for the atomisation and ICP-OES analysis of the powders, Asuncion Garcia-Escorial and Marcela Lieblich for extruding at CENIM (Madrid), David Collins for his help with EBSD setup and Ben Britton and Susie Speller for their guidance with the interpretation of EBSD results. I would like to thank Karen Kruska for showing me how to do FIB liftouts, John Titchmarsh and Neil Young for their help with the TEM, Robert Gerlach, Petros Siegkas and Vito Tagarielli for their help with the dynamic mechanical tests. I would also like to thank industrial collaborator Tenaris (Buenos Aires, Argentina), and particularly Martin Hubig and Ramiro Mazzina for allowing use of their equipment for the high temperature compression tests.

I would like to thank Dan Haley for the recovery of my DSC data after a hard drive failure.

And finally, I would like to thank all my amazing friends and family who have supported me all the way though my PhD. In particular Paris Kontis who showed me how to improve the layout of my figures, posters and presentations, Karen Kruska and Ceri Williams who were always available for a coffee, my housemates Nikola Vlahov, Jonathan Downing and Ben Cartlidge who were always supportive and happy to have a film night, dinner party or play a badminton game, my friend Mahmoud Mostafavi for increasing my productivity

with coffee, Tom Martin who very kindly proofread my thesis and Nick Rounthwaite for keeping our office “clean and tidy”.

Thank you!

Glossary

BEI	Backscattered Electron Image
CBDP	Convergent Beam Diffraction Pattern
CI	Confidence Index
CRSS	Critical Resolved Shear Stress
DD	Dislocation Dynamics
DSA	Dynamic Strain Ageing
DSC	Differential Scanning Calorimetry
EBSD	Electron Backscatter Diffraction
EDX	Energy Dispersive X-ray spectrometry
FCC	Face Centred Cubic
FEA	Finite Element Analysis
FWHM	Full Width Half Maximum
GP	Guinier-Preston
HT	High Temperature
ICP-OES	Inductively Coupled Plasma - Optical Emission Spectrometry
IM	Ingot Metallurgy
PIPS	Precision Ion Polishing System
PLC	Portevin – Le Chatelier effect
P/M	Powder Metallurgy
QC	QuasiCrystal
RT	Room Temperature
SEI	Secondary Electron Image
SEM	Scanning Electron Microscopy

SRS	Strain Rate Sensitivity
STDEV	Standard Deviation
TEM	Transmission Electron Microscopy
TM	Transition Metal
UTS	Ultimate Tensile Strength
VHN	Vickers Hardness
XRD	X-Ray Diffraction

Symbols

r_s	Mean radius of interaction with planar surface
r_V	3D grain/particle radius
N_s	Number of grains/particles per unit area
f	volume fraction
2Rs	mean planar centre-to-centre particle separation
σ	Stress
ε	Strain
σ_y	Yield Stress
σ_O	Hall-Petch stress factor
k	Hall-Petch slope
d	Grain Diameter (also commonly referred to as D)
l	Distance between the head of a dislocation pile up and the nearest dislocation source
σ_f	Peierls Stress
σ_l	Stress required to activate a source in a neighbouring grain
ρ	Dislocation density
α, α_1, α_2, α_3, β	Constants
G	Shear modulus
b	magnitude of Burgers vector
υ	Poissons ratio
γ	Shear strain
τ^*	Critical stress for slip propagation
m	Total length of dislocations emitted per unit area of boundary

L	Inter-particle distance
Ω_M	Atomic volume
δ	Lattice misfit
C	Structure parameter
m	Strain rate sensitivity parameter
$\dot{\varepsilon}$	Strain rate
A	Constant
n	Stress exponent
R	Gas constant
Q	Activation energy
T	Temperature
θ	Angle
σ_{max}	Maximum stress during extrusion
μVHN	Microhardness
σ_{fib}	Yield stress of the fibres
σ_{mat}	Yield Stress of the matrix
V_{fib}	Volume fraction of the fibres
V_{mat}	Volume fraction of the matrix
σ_{Or}	Yield stress predicted through Orowan's equation
σ_{HP}	Yield stress predicted through the Hall-Petch equation
D	Diffusion coefficient
k_B	Boltzmann's constant
W	Absolute value of the interaction energy between a dislocation and a diffusing species

b	Magnitude of the Burgers vector
c_1	Concentration of solute atoms at the dislocation line
c_0	Total concentration of solute atoms
τ	Relaxation time
ρ_f	Density of forest obstacles
ρ_m	Density of mobile dislocations
W_{min}	Energy minimum occurring when an impurity atom reaches a dislocation
T_{min}	Temperature at which ductility reaches a minimum during dynamic strain ageing
T_m	Melting temperature
f_{HW}	Amplitude of the Huygens wave
λ	Wavelength
θ	Scattering angle
s	Huygens wave (scattered spherical wave)
$F(s)$	Atomic scattering factor
V_t	Total number of votes
V_1, V_2, V_n	Number of votes for solutions 1, 2, n respectively

Table of Contents

Chapter 1: Introduction **1**

References: 4

Chapter 2: Literature Review **6**

2.1 Introduction 6

2.2 Strength and Limitations of Conventional Al Alloys 7

2.2.1 Mechanical Properties under Quasi-Static Loading Conditions 8

2.2.2 Mechanical Properties under Dynamic Loading Conditions 9

2.2.3 Strengthening Mechanisms 10

2.2.4 High Temperature Mechanical Strength of Conventional Al Alloys 22

2.3. Rapidly Solidified Al Alloys 26

2.4. Production Routes 26

2.4.1 Melt Spinning 27

2.4.2 Atomisation 27

2.4.3 Consolidation 28

2.4.4 Properties of Bulk Rapidly Solidified Al Alloy Systems 28

2.5. Quasicrystalline Al Alloys 29

2.6 Quasicrystalline Al Alloys for High Strength at Elevated Temperature Applications 31

2.6.1 Choice of Composition 31

2.6.2 Microstructures 33

2.6.3 Mechanical Properties and Strengthening Mechanisms of Quasicrystalline Al Alloys 35

2.6.4 Thermal Stability and High Temperature Mechanical Properties 40

2.7 Nanoquasicrystalline Al Alloy Matrix Composites Containing Pure Al 41

2.7.1 Microstructure, Mechanical Properties and Strengthening Mechanisms 41

2.7.2 High Temperature Testing 44

2.8 Conclusions and Summary 46

References 49

Chapter 3: Experimental Procedure **57**

3.1 Production and Consolidation of Powders 57

3.1.1 Powder Atomisation 57

3.1.2 Sieving 58

3.1.3 Mixing 59

3.1.4 Extrusion 60
3.2 Characterisation of Powders and Bulk Specimens 61
3.2.1 Inductively Coupled Plasma - Optical Emission Spectrometry (ICP-OES) 61
3.2.2 X-Ray Diffraction (XRD) 61
3.2.3 Scanning Electron Microscopy (SEM) and Energy Dispersive X-Ray Analysis (EDX) 62
3.2.4 Transmission Electron Microscopy (TEM) and EDX 63
3.2.5 Electron Backscatter Diffraction (EBSD) 64
3.3 Room Temperature Mechanical Tests 66
3.3.1 Microhardness 66
3.3.2 Tensile Tests 66
3.3.3 High Strain Rate Tensile and Compressive Tests 67
3.4 Thermal Stability 68
3.4.1 Differential Scanning Calorimetry (DSC) 68
3.4.2 Heat Treatments, Microstructural Characterisation and Microhardness 69
3.5 High Temperature Mechanical Tests 70
3.5.1 Microhardness 70
3.5.2 High Strain Rate Compressive Tests 70
References 70
Chapter 4: Production and Characterisation of Al-Fe-Cr-Ti Alloy Bars 72
4.1 Powder Characterisation 72
4.1.1 Inductively Coupled Plasma – Optical Emission Spectrometry (ICP-OES) 72
4.1.2 SEM Analysis of the Morphology and Topography of the Powders 74
4.1.3 SEM Analysis of the Microstructure of the Powders 76
4.1.4 XRD 79
4.1.5 TEM Analysis of the Microstructure of the Powders 82
4.2 Powder Consolidation into Bulk Specimens 86
4.3 Microstructural Characterisation of the Extruded Bars 91
4.3.1 Microstructural Characterisation of the 0-1a Bar 92
4.3.2 Microstructural Characterisation of the 0-1b Bar 101
4.4 Summary 108
4.5 Conclusions 111
References 112
Chapter 5: Production and Characterisation of Al-Fe-Cr-Ti Composite Bars 115

5.1 Pure Al Powder Characterisation 115
5.1.1 ICP-OES 116
5.1.2 XRD 117
5.1.3 SEM Analysis of the Topography of the Powders 117
5.2 Powder Consolidation into Bulk Composite Specimens 118
5.3 Characterisation of the Extruded Composite Bars 122
5.3.1 Microstructural Characterisation of the Composites Containing 10 vol% Pure Al Fibres 122
5.3.2 Microstructural Characterisation of the Composites Containing 20 vol% Pure Al Fibres 134
5.4 Summary 145
5.5 Conclusions 148
References 148
Chapter 6: Thermal Stability and Phase Transformations 150
6.1 Thermal Analysis of the Atomised $Al_{93}Fe_3Cr_2Ti_2$ Alloy Powders 150
6.2 Thermal Analysis of the Atomised Pure Al Powder 151
6.3 Thermal Analysis of the Extruded $Al_{93}Fe_3Cr_2Ti_2$ Alloy Bar 152
6.3.1 DSC 152
6.3.2 Thermal Evolution: 1 Hour at 250 °C, 280 °C and 550 °C 153
6.3.3 Thermal Stability: 1000 Hours at 250 °C 160
6.4 Thermal Analysis of the Extruded Composite Bars 166
6.4.1 DSC 166
6.4.2 Thermal Evolution: 1 Hour at 250°C, 280°C and 550°C 167
6.4.3 Thermal Stability: 1000 Hours at 250°C 171
6.5 Discussion 176
6.6 Conclusions 179
References 180
Chapter 7: Room Temperature Mechanical Testing 182
7.1 Mechanical Testing 182
7.1.1 Microhardness 182
7.1.2 Quasi-Static Tensile Strength 183
7.1.3 Dynamic Tensile Strength 185
7.1.4 Dynamic Compressive Strength 186

7.2 Discussion 187
7.2.1 Microhardness 187
7.2.2 Quasi-Static Tensile Strength 188
7.2.3 Dynamic Tensile Strength 189
7.2.4 Dynamic Compressive Strength 190
7.3 Conclusions 190
References 191
Chapter 8: Mechanical Properties at Elevated Temperature 193
8.1 Compressive Testing the Pure Alloy Bar 193
8.2 Compressive Tests of the Composite Bars 198
8.3 Discussion 204
8.3.1 Strain Rate Effect 204
8.3.2 Temperature Effect 206
8.3.3 Fibre Effect 208
8.3 Conclusions 209
References 210
Chapter 9: General Discussion 212
9.1 Microstructural Comparison 212
9.1.1 Phase Analysis 212
9.1.2 Texture Analysis 213
9.1.3 Matrix Compositions 215
9.2 Extrudability 216
9.3 Mechanical Strength at Room Temperature 218
9.6 Thermal Evolution 227
9.7 High Temperature Serrated Flow in Compression 229
References 233
Chapter 10: Conclusions 238
10.1 Aims and Achievements 238
10.2 Powder Production and Characterisation 238
10.3 Extrusion and Characterisation of the $Al_{93}Fe_3Cr_2Ti_2$ Alloy and Composites 239
10.4 Mechanical Testing at Room Temperature 239
10.5 Thermal Analysis 241

10.6 High Temperature Mechanical Testing 241
10.7 Future Developments 243
References 244
Appendix 1: EBSD Resolution 246
References: 250

Chapter 1: Introduction

The stimulus for the development of structural materials with better specific strength and toughness (and therefore lower density) comes from the constantly evolving needs of the aerospace and automotive industries [Pol-06]. The need to improve strength-to-weight ratio at elevated temperatures has led research towards Ti-based alloys because the strength of commercially available Al-based alloys falls rapidly with increasing temperature [Ino-00].

Aluminium is much more widely available and easier to extract, therefore its market price is significantly cheaper leaving room for more expensive processing techniques while still keeping it a financially attractive alternative. Its density is also 2.7 g/cm^3, which is lower than Ti at 4.5 g/cm^3 [Smi-92] which means its use would lead to savings in terms of energy and natural resources.

Al alloys are not currently used for elevated temperature applications due to their lack of microstructural stability. This is partly a result of the high diffusion coefficients of the most commonly used alloying elements which cause the microstructure to coarsen as temperature increases [Ino-98]. Currently, for any application above ~200 °C Ti alloys are used despite the fact that they are heavier, overdesigned and more expensive for use in applications below ~300-350 °C.

Recent developments in novel high performance aluminum based alloy systems strengthened with nano-scale dispersoid phases have made them very attractive lightweight materials to be used in engineering components. Rapidly solidified nanoquasicrystalline $Al_{93}Fe_3Cr_2Ti_2$ based alloys made of sub-micron sized icosahedral quasicrystalline phases in an α-Al matrix have been studied because of their improved strength at elevated temperatures compared to current commercially available Al alloys [Ino-00], [Gal-09b]. The applications of these alloys have however previously been limited by their temperature sensitivity and their response to bulk processing routes. Galano *et al.* proved that the addition of Ti, V, Nb or Ta alloying elements improves thermal stability of the Al-Fe-Cr alloys in melt-spun ribbons [Gal-09a].

Rapid solidification can be achieved through a number of methods, however gas atomization is one of the very few which is industrially viable. Studies scaling up the production of rapidly solidified $Al_{93}Fe_3Cr_2Ti_2$ and $Al_{93}Fe_3Cr_2Nb_2$ alloys by performing atomization runs on an industrial scale have been performed [Rou-12], [Aud-13]. The influence of processing parameters during consolidation and their effect on the mechanical properties of the extruded material have been tested by Todd *et al.* on nanoquasicrystalline $Al_{93}Fe_3Cr_2Ti_2$ at% alloy [Tod-04].

A comparative study of the mechanical properties of a series of nanostructured Al-based melt-spun ribbons was carried out by Audebert *et al.* at room temperature and Galano *et al.* at high temperatures with the evident conclusion that the outstanding mechanical properties of the alloy are the result of a combination of solid solution strengthening, particle dispersion and grain refinement strengthening [Aud-02], [Gal-09b]. No attempt to quantify the various contributions of each strengthening mechanism was made.

An estimation of the various contributions of different strengthening mechanisms to the overall strength of an $Al_{92.4}Fe_{1.2}Cr_{3.3}Ti_{2.4}Si_{0.7}$ at% alloy produced by powder metallurgy was carried out by Vojtech *et al.*, who concluded that Hall-Petch strengthening was the dominant mechanism, followed by Orowan strengthening; the solid solution mechanisms can be neglected due to the hot processing methods which reduce the solute content in solid solution retained after the rapid solidification process [Voj-07]. One of the aims of the present work is to determine the correlation between the microstructure and yield strength of bulk processed nanoquasicrystalline $Al_{93}Fe_3Cr_2Ti_2$ at% alloy and to estimate the contributions of various strengthening mechanisms to the overall strength at room temperature. The main focus of this study is the elastic range because it would be unsafe to subject engineering components to stresses which would induce plastic deformation during use.

A partial analysis of the high strain rate behaviour of quasicrystalline Al-based alloys been started during a previous project. Mechanical tests were performed on extruded $Al_{93}Fe_3Cr_2Ti_2$ at% alloy and composite bars at strain rates around 2200 s^{-1} in tension and 3000 s^{-1} in compression at room temperature. The mechanical strength of this alloy was observed to increase with strain rate

[Ped-10], but due to time constraints no further tests were performed. No evidence of tests at higher strain rates has been found in the open scientific literature. The current project aims to test the high strain rate behaviour of this alloy and composites in tension and compression to assess their response to dynamic loading conditions.

Nanoquasicrystalline Al-Fe-Cr-Ti based alloys have been shown to have a small plastic regime during mechanical testing and therefore reduced energy absorption ability in quasi-static tests at room temperature compared to commercial 7xxx and 2xxx series Al alloys [Aud-02], [Ino-98], [Ino-00], [Bol-93]. In an effort to improve the ductility Nagy *et al.* showed that creating composites using nanoquasicrystalline Al-Cu-Fe and Al-V-Fe alloy matrices with pure Al fibres gave improved strain-to-failure in room temperature tensile tests [Nag-05]. In the present work, 10% and 20% volume fractions of pure Al fibres have been added to a nanoquasicrystalline $Al_{93}Fe_3Cr_2Ti_2$ at% alloy matrix in an effort to improve ductility in mechanical tests at varying strain rates. Both pure Al and $Al_{93}Fe_3Cr_2Ti_2$ at% alloy powders were produced through gas atomisation, then mixed and consolidated into bars through warm extrusion.

Some studies have been found in the literature on the thermal stability of this alloy [Gal-04], [Tod-04] and a few on high temperature mechanical testing [Ino-00], [Gal-09b] however no studies were found that analyse the alterations to the strength and microstructure brought by the industrially used processing methods which involve plastic deformation at temperature, the knowledge of which is essential towards safe use in engineering applications. This project aims to investigate that through a series of compression tests at varying strain rates and temperatures to investigate processing conditions for commonly used industrial practices such as forging and hot rolling.

In the current project outline, Chapter Two will summarise the background in the form of a literature review and Chapter Three will explain the experimental methodology employed.

Chapters Four and Five of this project will examine the use of a novel rapidly solidified nanoquasicrystalline alloy to make composites by adding fibres and correlate the production of the alloy and composites with their resulting microstructures. Chapter Six will study the thermal evolution of the alloy and composites at the temperatures likely to be used during processing. Chapter Seven tests the quasi-static and dynamic strength of the alloy and composites at room temperature. Finally Chapter Eight analyses the alterations to the strength and microstructure brought by the industrially used processing methods which involve plastic deformation at temperature. Chapter Nine will have a general discussion of the results, linking and drawing conclusions from the content of the previous chapters. It will include an application of some analytical models for the prediction of the yield strength at room temperature and discussing high temperature mechanical behaviour based on the microstructural analysis and thermal evolution. Chapter Ten will finally contain a summary, overall conclusion and future developments of this work.

A study like this has never been performed on this alloy and composites before. This project is a step forwards towards the safe use of this alloy in engineering applications in an attempt to overcome the shortcomings of currently available commercial Al-based alloys.

References:

[Aud-13] F. Audebert, M. Galano, C. Triveño Rios, H. Kasama, M. Peres, C. Kiminami, W.J. Botta, C. Bolfarini, J. All. Comp., (2013) 577, 650–657.

[Aud-02] F. Audebert, F. Prima, M. Galano, M. Tomut, P. J. Warren, I. C. Stone, B. Cantor, Mat. Trans., (2002) A 43, 8, 2017.

[Bol-93] W. Bolton, *Engineering Materials Technology*, Newnes (1993).

[Gal-09a] M. Galano, F. Audebert, I.C. Stone, B. Cantor, Acta Mat., (2009), 57 5107–5119.

[Gal-09b] M. Galano, F. Audebert, I.C. Stone, B. Cantor, Acta Mat. (2009), 57, 5120–5130.

[Gal-04] M. Galano, F. Audebert, B. Cantor, I. Stone, Mat. Sci. Eng., (2004) 375-377, 1206-1211.

[Ino-00] Inoue A., Kimura H., Mat. Sci. Eng., (2000), A286, 1-10.

[Ino-98] A. Inoue, Prog. Mat. Sci., (1998), 43, 365-520.

[Nag-05] Nagy, J., Balog, M., Ibdinskc, K., Simandek, F., Švec, P., Janidkovid, D., Int. J. Mat. Prod. Tech., (2005), 23, 1-2, 79-90.

[Ped-10] S. Pedrazzini, Masters Thesis, University of Oxford, (2010).

[Pol-06] I.J. Polmear, *Light Alloys, Metallurgy of the Light Metals*, Arnold, 4th Ed., (2006).

[Rou-12] N. J. Rounthwaite, PhD thesis, University of Oxford, (2012).

[Smi-92] Edited by E. A. Brandes, G. B. Brook, *Smithells Metals Reference Book*, 7th Ed, Butterworth-Heinemann, (1992).

[Tod-04] I. Todd a, Z. Chlup b, J.G. O'Dwyer, M. Lieblich a, A. Garcia-Escorial, Mat. Sci. Eng., (2004), A 375–377, 1235–1238.

[Voj-07] D. Vojtěch, J. Verner, J. Šerák, F. Simancik, M. Balog, J. Nagy, Mat. Sci. Eng., (2007), A 458, 1-2, 15, 371.

Chapter 2: Literature Review

2.1 Introduction

The constantly evolving needs of the aerospace and automotive industries fuel the development of new materials with better strength-to-weight ratios up to elevated temperatures. Aluminium alloys are traditionally used as lightweight structural materials for components used up to ~200 °C as their strength falls rapidly at higher temperatures [Ino-00]. The desire for lightweight materials for high temperature applications has led research in the direction of titanium alloys due to their excellent specific properties and microstructural stability [Pol-06].

The use of aluminium alloys for high temperature applications would have two great advantages:

- the market price is significantly cheaper (Ti6Al4V ~18,000 US$/tonne [Met-14], while 7075 T6 Al ~1,700 US$/tonne [Lme-14][1]), which leaves a margin for more expensive processing techniques while still keeping it a significantly cheaper alternative
- the density of Al is lower at only 2.7 kg/m^3 instead of 4.5 kg/m^3 for Ti [Sis-14], and therefore its use would lead to significant savings in terms of energy and fuel consumption.

Aerospace grade Al alloys, like 2000 and 7000 series alloys, are not currently used for components operating at temperatures above ~200°C because the high diffusivity of alloying elements causes the microstructure to over-age. The coarsening of particles as temperature increases causes a sharp drop in mechanical strength [Ino-98]. Currently, for any component operating above ~200 °C Ti alloys are used, but they are heavier, more expensive and overdesigned for applications below ~350 °C [Ino-00].

This literature review gives a comprehensive background to a project which tests nanostructured aluminium-based alloys and composites that show high strength at elevated temperature in order to

[1] Prices correct in January 2014.

overcome the limitations of conventional Al alloys building up on work that was performed during the authors Masters Degree project [Ped-10].

2.2 Strength and Limitations of Conventional Al Alloys

Pure Al in its annealed condition is very soft and ductile, with a yield strength of 7-10 MPa [Bol-06]. In order to increase its strength for engineering applications Al is commonly alloyed with silicon, magnesium or transition metals. These generally have very low solid solubility in Al, but even small additions can lead to great improvements in the mechanical properties. Magnesium is the most effective strengthener on a comparative weight basis, with a relatively high solid solubility. Annealed plates containing ~6% of magnesium have yield strengths up to 175 MPa at room temperature [Pol-06]. The main microstructural features and strengthening mechanisms of Al-(Mg, TM) alloys (where TM-Transition Metal) are:

- Submicron particles which generally contain transition metals such as chromium, manganese or zirconium. The alloying elements in liquid solution precipitate as dispersoids even at relatively fast cooling rates. These alloy systems exhibit slow grain coarsening and recrystallisation during heat treatments [Pol-06].
- Fine precipitates that form during age hardening or precipitation hardening for alloys which respond to this kind of treatment, like the Al-Cu-Mg, Al-Mg-Si or Al-Zn-Mg-Cu alloy systems [Pol-06].
- Refinement of grain size and shape, generally through work hardening and annealing or dynamic recovery during hot working which produces a network of sub-grains. This is usually used for commercial purity Al and alloys based on the Al-Mg and Al-Mn systems [Pol-06].
- Dislocation substructure, mainly due to treatments like cold working [Die-88].

- Crystallographic textures that form as a result of subsequent cold working and annealing and influence formability. They can lead to anisotropic mechanical properties [Gil-81], [Die-88].
- Physical addition of reinforcements, such as fibres to make a composite [Pol-06].

2.2.1 Mechanical Properties under Quasi-Static Loading Conditions

Commercial aluminium alloys used for high strength applications can be broadly divided into two main sub groups: alloys that respond to precipitation hardening and ageing treatments and alloys which do not. The strength of the alloys in this second group is determined by the dislocation sub-structure produced by cold working. For alloys that respond to ageing treatments, it is the finely dispersed precipitates that have the dominant effect in inhibiting dislocation motion and thereby raising tensile and yield strength [Pol-06]. Coarse intermetallic compounds have little effect on yield and tensile strength, but they can cause a marked loss of ductility. Also, wrought Al alloys tend to have anisotropic mechanical properties due to the alignment of grain structures and the introduction of texture during processing [Pol-06].

A summary of the quasi-static tensile properties of commonly used wrought Al alloys of the 2000 and 7000 series can be seen in Table 2.1. The “high strength” Al based alloys used in the aerospace industry have a Ultimate Tensile Strength (UTS) which is usually between 300-500 MPa. The strongest alloy is 7075-T6, which shows a UTS of 570 MPa and is the bench mark for the development of high strength Al alloys at room temperature. 2000 series Al alloys are used in the aerospace industry mostly because despite their UTS being lower at room temperature, they retain good microstructural stability and strength up to higher temperatures [Ino-00].

Alloy	*Temper*	*UTS (MPa)*	*% Elongation*	*VHN*
2011	*T3*	*380*	*15*	*95*
	T8	*405*	*15*	*100*
2014	*-*	*185*	*18*	*45*
	T4	*425*	*20*	*105*
	T6	*485*	*13*	*135*
2024	*-*	*185*	*20*	*47*
	T3	*485*	*18*	*120*
	T4	*470*	*20*	*120*
2168		*440*	*10*	*-*
7075	*-*	*230*	*17*	*60*
	T6	*570*	*11*	*150*

Table 2.1: UTS, elongation and hardness of commonly used Al alloys, tensile tested following ASTM standards at room temperature [Bol-06].

2.2.2 Mechanical Properties under Dynamic Loading Conditions

Commercial Al alloys have been studied extensively in high strain rate tests performed with split Hopkinson bars both in tension and in compression. As seen in Tables 2.2 and 2.3, conventional high strength Al alloys like 7000-series alloys have a UTS at high strain rate (~3000 s^{-1}) in tension is between 385-650 MPa.

Source	*Alloy*	*Strain rate*	*UTS/MPa*	*Strain-to-failure*
[Bør-10]	*7075 T651*	*1128*	*550*	*1.50%*
[Che-09]	*7003 T6*	*1000*	*450*	
[Che-09]	*7108 T6*	*1000*	*500*	
[Rey-06]	*7003 T79*	*1300*	*500*	*0.5*
[Rey-06]	*7108 T6*	*1300*	*385*	*0.8*
[ElM-06]	*7075*	*3500*	*650*	*22*

Table 2.2: dynamic tensile properties of commercial Al alloys, showing very low strain rate sensitivity (SRS) compared to quasi-static tests, according to the paper they were found in.

Source	*Alloy*	*Strain rate*	*UTS/ MPa*	*Strain-to-failure*
[Dja-00]	*7108 T79*	*3000*	*~450*	
[ElM-06]	*7075*	*2500*	*650*	*3.5*
[ElM-06]	*7075*	*3500*	*670*	*4.5*
[ElM-06]	*7075*	*5000*	*700*	*7.5*

Table 2.3: dynamic compressive properties of commercial Al alloys.

2.2.3 Strengthening Mechanisms

The use of any alloy in engineering applications requires a deeper knowledge and understanding of its mechanical strength and the mechanisms that lead to it. There is a need to study the elastic regime because any engineer when designing components would want to avoid stressing a part anywhere near the yield stress. However, learning about the plastic regime will also be useful because the shaping and forming of components before use will be performed in the plastic range [Hon-77]. The following section will cover relevant models that describe strengthening mechanisms currently available in the published literature.

Dislocation motion is responsible for the onset and extent of plastic deformation in crystalline metals, therefore mechanical behaviour can be controlled by affecting dislocation dynamics [Hon-77]. The main methods of interfering with dislocation motion are [Pol-06]:

- Grain refinement.
- Precipitation strengthening.
- Solid solution strengthening.
- Dislocation structures (eg. formed by cold working).
- Addition of reinforcements (such as fibres).

2.2.3.1 Grain Refinement

One method of improving the mechanical strength of Al-based alloys is the refinement of grain size and shape, generally through work hardening and annealing or dynamic recovery during hot working which produces a network of sub-grains [Pol-06]. A fine-grained structure can also be achieved through rapid solidification and other procedures such as cryomilling [Jos-06].

Crystalline materials exhibit an inherently anisotropic behaviour in their mechanical and physical properties depending on the alignment and direction of the crystal structure. Most of the variations of these properties would have little effect if the material was polycrystalline and constituted of randomly arrayed grains. In this case the properties would be an average value constant in all directions [Hon-77]. In practice, metals are rarely completely random polycrystalline structures, but instead possess textures (or preferred orientations) caused by the processing methods, which then introduce anisotropy in the mechanical behaviour [Die-88].

However, before discussing the mathematical models for calculating the strength of a material based on grain refinement which are currently available in the literature we need to discuss the methods for measuring grain sizes accurately and describing their 3D structure.

Most grain size measurements tend to be two-dimensional, coming from surface techniques. One of the simplest ways of turning a 2D measurement obtained through a surface technique such as Electron Backscatter Diffraction (EBSD) into an estimate of the size of the underlying 3D grain size relies on the assumption that all particles are spherical and uses a mean and standard deviation value on a statistically significant number of measurements. The following method was originally developed by Ashby [Ash-64] to describe the structure factors of particles in a matrix. There are many points of similarity in the geometrical properties of particles and grains as both represent volume elements with well-defined surface boundaries, and similar methods are used to geometrically derive their mean diameters, size distributions and volume fractions. Therefore the analysis of the geometric properties of particles and grains can be mathematically approached the same way [Und-70]. Ashby's method approaches these calculations, where r_s is the mean radius of interaction with a planar surface (the experimentally measured value), r_v is the 3D grain radius, N_s is the number of grains intersecting unit area (planar) and f is their volume fraction. The relationships between these values, calculated using simple geometry are:

$$r_s = \sqrt{\frac{2}{3}} r_v \text{ [Ash-64]} \tag{2.1}$$

and

$$f = N_s(\frac{2}{3})\pi r_v \text{ [Ash-64]} \tag{2.2}$$

In order to calculate the mean, planar centre-to-centre spacing the assumption that their 3D arrangement cannot be random is necessary. A commonly used assumption is that the centre-to-centre spacing between grains are arranged like points in an FCC lattice [Ash-64]. Using $2R_s$ as the symbol for mean planar centre-to-centre particle separation (which has also been described as λ in literature [Ash-64]), geometrically is then follows that:

$$2R_S = \sqrt{\frac{4}{f}} r_s \text{ [Ash-64]} \tag{2.3}$$

therefore

$$2R_s = \sqrt{\frac{4}{f} * \frac{2}{3}} r_v \text{ [Ash-64]} \quad (2.4)$$

This is the simplest method available that allows 3D values to be extrapolated from 2D surface measurements, however it relies on the assumption of spherical, equiaxed, equally spaced and randomly oriented grains only, which is usually an oversimplification. However it can still be used for rough calculations and estimations, taking into account the sources of error and relative margins.

Once the grain size can be measured, there are several ways of correlating its size to the overall strength of the alloy. While grain size can influence the whole stress-strain curve, the effect on the elastic limit (yield point) is particularly marked [Hon-77]. The yield point of each metal is defined by a Critical Resolved Shear Stress (CRSS) required to start moving dislocations, which depends on the bond strength and the orientation of the crystal with respect to the loading axis [Hon-77].

Schmid's law uses the fact that the stress needed to initiate plastic deformation is constant for each specific metallic single crystal to determine the grain orientation with respect to the loading axis [Hon-77]. This works well for single crystals where the yield point is a defined point however in polycrystalline materials we must consider the macroscopic elastic limit to be a range. This means that the most favourably oriented grains will have undergone plastic deformation prior to this point in the stress-strain curve [Hon-77].

The dependence of the flow stress on grain size can be calculated using the Hall-Petch equation:

$$\sigma_y = \sigma_O + kd^{-1/2} \text{ [Hal-51]} \quad (2.5)$$

This equation is derived using the following assumptions [Cah-83]:

- Dislocations are static and immobile until the applied stress reaches the upper yield point.
- At this point plastic deformation starts in a single grain.
- A dislocation source becomes unpinned and starts sending out dislocation loops.
- The dislocation loops move to the grain boundary and stop.
- The dislocation pile-up at the boundary causes a stress concentration in adjacent grains.

- When the stress is high enough the neighbouring grains will be activated.

Assuming "l" is the distance between the head of the pile-up and the nearest dislocation source, (which is assumed to be l<d/2, where d is the grain diameter), the stress applied by a pile-up will be $\sim\sigma(d/4l)^{1/2}$.

Adding the effect of frictional stress from impurities (also known as Peierls stress), then it will be $\sim\sigma+(\sigma-\sigma_f)(d/4l)^{1/2}$ where σ_f=frictional stress. If σ_1 is the stress required to activate a source in a neighbouring grain, then:

$$\sigma_1=\sigma_f+(\sigma-\sigma_f)(d/4l)^{1/2} \text{ [Cah-83]} \quad (2.6)$$

Re-arranging this equation to give σ as a function of l:

$$\sigma=\sigma_f+(\sigma_1-\sigma_f)(4l/d)^{1/2} \text{ [Cah-83]} \quad (2.7)$$

Which is in perfect agreement with the empirically derived equation:

$$\sigma=\sigma_O+kd^{-1/2} \text{ [Hal-51]} \quad (2.8)$$

Often, for simplicity the assumption that $\sigma_O\sim0$ is made, and in this case the equation simplifies to:

$$\sigma=kd^{-1/2} \text{ [Cah-83]} \quad (2.9)$$

This method describes what happens at the yield point within an individual grain and how it affects the neighbouring grains. One of the main sources of error is the difference in size between neighbouring grains, which is completely ignored by this model. Also the fact that in polycrystalline materials the elastoplastic transition will be long due to the fact favourably oriented grains will have started plastic deformation while others are still in the elastic range [Hon-77].

The original derivation of the Hall-Petch equation is based on the theoretical consideration that grain boundaries will act as barriers to dislocation motion [Hal-51], [Esh-51], [Hon-77], [Cah-83]. There is however experimental evidence also suggesting that grain boundaries could act as both sources and barriers to dislocation motion [Sut-96]. Studies have shown that during the early stages of plastic flow, grain boundaries can act primarily as sources of dislocations [Mur-79]. These

findings have led to the development of alternative theories based on the correlation between grain size and dislocation density.

A widely used model developed by Li assumes that at the onset of yielding grain boundaries act as dislocation sources, causing a sharp increase in the dislocation density near the grain boundary. Li's model calculates the strength required for a dislocation to start moving among the forest of grain boundary dislocations that have been created [Li-63]. Li proposes using the Taylor formula $\sigma \propto \sqrt{\rho}$ (where ρ is the density of dislocation) [Tay-34]. Using this method, the equation for the dislocation density as an inverse function of grain size was defined by Conrad, who postulated that the average slip distance travelled by a dislocation is proportional to the grain size [Con-63]. Since the Orowan relationship establishes that this distance is inversely related to the dislocation density [Oro-40] the dislocation density will therefore be inversely related to the grain size [Con-63]. Conrad uses the method proposed by Li [Li-63] combined with his own equations as an alternative derivation for the Hall-Petch equation $\sigma \propto \sqrt{D^{-1/2}}$, where D is the grain diameter [Con-63].

Finally, Meyers proposed and developed another model [Mey-82]. The strengthening effect here is not explained in terms of the Taylor equation $\sigma \propto \sqrt{\rho}$, instead the strengthening effect is defined as a combination of several factors combining all the previous theories. Like Hall, Petch and Cottrell [Hal-51], they see the grain boundaries as barriers to dislocation motion. Like Li, they see the grain boundaries as dislocation sources at low plastic flow [Li-63].

To that Meyers *et al.* add the idea that elastic anisotropy would cause additional stresses in the grain boundary surroundings and that multislip would be activated in the grain boundary region while the interior of the grains would be dominated by single slip (if properly oriented).

Meyers works under the consideration that the dislocations generated by grain boundaries would remain in the grain boundary area and form a work hardened layer encompassing each grain. The material would then be modelled as a composite consisting of a harder structure with a softer core [Mey-82]. The fraction of the composite that is work hardened and the softer fraction depend on the grain size, and ultimately also leads to a Hall-Petch relation $\sigma \propto D^{-1/2}$. All the models

reviewed led to a Hall-Petch relation of $\sigma \propto D^{-1/2}$ between the yield strength and grain size, however they produce different formulations of the Hall-Petch slope, based on different theoretical considerations.

The relationships of the Hall-Petch slope found are (expressions for the empirically derived constant Hall's paper called "k" [Hal-51]):

- According to Eshelby $\alpha_1\sqrt{\frac{Gb\tau^*(2-\upsilon)}{2\pi(1-\upsilon)}}$ [Esh-51].
- According to Conrad $\alpha_2 G\sqrt{b\gamma/\beta}$ [Con-63].
- According to Li $\alpha_3 Gb\sqrt{m}$ [Li-63].

Where α_1, α_2, α_3, β are constants, G is the shear modulus, b is the magnitude of the Burgers vector, υ is the Poissons ratio, γ is the shear strain, τ^* is the critical stress for slip propagation, m is the total length of dislocations emitted per unit area of grain boundary.

More recently, Dunstan and Bushby developed an alternative equation to the well-established Hall-Petch relation and fitted it to data-sets used from Conrad, Eshelby and Li as well as many other data-sets providing a fit, which was shown to be more accurate through Bayesian statistical analysis [Dun-14]. According to their theory, the relationship between the yield strength and the grain size should be an inverse linear relationship instead of an inverse square root:

$$\sigma_Y \propto kD^{-1} \text{ [Dun-14].} \qquad (2.10)$$

All these models have been produced assuming a single grain size measurement (and its corresponding error analysis). However, more recently some alloys with more complex microstructures have been developed during attempts to improve the mechanical behaviour of Al-based alloys. One method for improving mechanical strength is the production of metals with a bimodal grain size distribution. The effect of this type of distribution has been shown to improve strength (from the smaller grains) while retaining ductility (due to the larger grains) [Jos-06]. The

mechanical response of metals with a bimodal grain size distribution has been modelled extensively throughout the literature using the Mori-Tanaka mean field approach [Mor-73] as an alternative to Finite Element Analysis (FEA) using explicit analytical expressions to model the constitutive response over an extensive range of inclusion shapes and volume fractions. The original theory was developed to model the stress-strain relations of dual phase metals of the inclusion-matrix type because Mori and Tanaka found all previous theories had the fundamental flaw of dealing exclusively with internal stresses which are the result of plastic deformation occurring solely in the matrix [Mor-73]. Their approach is based on the fact that the internal stress developed by uniform plastic deformation in the matrix can be duplicated by giving uniform transformation strain to the inclusions alone. Therefore it characterises the internal stress by dealing with inclusions with uniform transformation strain.

In the modified version of this theory proposed by Weng the Mori-Tanaka approach allows the elastoplastic representation of both phases by considering the fine grain-coarse grain areas depending on their volume fraction as a matrix-inclusion topology and modelling the weakening constraint of the matrix as the macroscopic stress or strain increases [Wen-90]. This approach was then used by Joshi *et al.* to model the constitutive response of bimodal metals [Jos-06] by analysing a material which contained solely the ultra-fine grains and a simulation of the material which contained solely the coarse grains. Joshi *et al.* found the stress-strain response of the bimodal material as a linear addition of the two separate stress strain responses of each phase adjusted by the volume fraction.

Some studies have also shown that in the sub-micron range there is no guarantee that the Hall-Petch slope would remain constant. For instance the work of Yu *et al.* [Yu-05] divided the grain sizes and the predominant deformation mechanisms into 3 main groups:

(a) the “traditional” group ($d>\sim10^{-6}$) which mostly deforms by dislocation intersections [Con-03], [Che-03],

(b) the "ultra-fine grained" group ($\sim 10^{-8} < d < \sim 10^{-6}$) which would deform by dislocation emission by grain boundary sources [Con-03], [Hay-04] or grain boundary shear due to dislocation pile ups [Che-03], and

(c) the nanocrystalline group ($d < \sim 10^{-8}$) which deforms by grain boundary processes only [Con-03], [Che-03].

The transition from the traditional regime to the ultra-fine grained regime in Al was studied by Yu *et al.* [Yu-05]. It was also found to be temperature and strain rate dependent. In the traditional (micron-sized grain) regime a Hall-Petch type relationship would be used to predict the yield strength as discussed previously in this section, however the Hall-Petch slope hasn't always been found to be linear in the ultra-fine grained regime.

2.2.3.2 Precipitation Strengthening

The strength of Al-based alloys can also be improved by precipitation hardening. This can be achieved either by precipitating secondary phases directly from the melt during solidification or by selecting and optimizing the appropriate composition and heat treatment of the alloy in order to form precipitates and tailor the microstructure to achieve the required properties [Pol-06]. A precipitation strengthened microstructure with secondary particles forming directly in the melt can also be achieved through rapid solidification [Ino-98], [Gal-04], [Gal-09a].

Precipitation strengthened materials can be produced with coherent, semi-coherent and fully incoherent particles. The strengthening mechanisms which are activated in the alloys with each type of precipitate are different. A very common way to strengthen Al-based alloys is through the creation of GP-zones, which are very small, fully coherent clusters [Por-06].

All models that describe particle strengthening are based on accurate particle size measurements, therefore a review of the main methods to measure them and extrapolate the three dimensional size is a necessary starting point. Just like with the grain size, one of the most widely used ways of turning a 2D measurement obtained through a surface technique such as SEM into an estimate of

the size of the underlying 3D particle can be performed by assuming all particles are spherical and using a mean and standard deviation value on a statistically significant number of measurements.

One method was originally developed by Ashby [Ash-64] to describe the structure factors of particles in a matrix. Ashby's method was discussed previously as it applies to grain size measurements too. The equations developed by Ashby are the previously cited equations 4.1, 4.2, 4.3 and 4.4. Ashby's method is the simplest method available allowing 3D values to be extrapolated from 2D surface measurements. However, it relies on the assumption of spherical, equiaxed, equally spaced and randomly oriented particles only, which can be used for rough calculations and estimations, taking into account the sources of error and relative margins.

The first theoretical model describing the degree of strengthening due to precipitation hardening was proposed by Mott and Nabarro [Mot-48]. This model estimates the disruption to dislocation motion due to elastic strains in the matrix that come from coherent precipitates. Then Orowan published his famous equation relating the strength of an alloy containing hard, incoherent particles to the ratio of shear modulus and mean interplanar particle spacing [Oro-48]:

$$\sigma_O = 3Gb/L \tag{2.11}$$

where 3 is the Taylor factor, G is the shear modulus of the matrix, b is the Burgers vector and L is the inter-particle distance.

The Orowan equation has been refined over the years, but still stands as a landmark achievement as a basis for the theory of dispersion strengthening by non-deformable particles.

This theory of dislocation-particle interactions relies on the following assumptions [Ard-85]:

- All particles have the same strength.
- All particles are assumed spherical.
- When a dislocation encounters an obstacle it will bow out under the influence of the applied stress into an arc of constant radius R.

- Dislocation line tension is assumed constant and independent of the character of the dislocation.
- Even spacing between the particles, which act as impenetrable obstacles.

Further refinements to Orowans model have been performed by Foreman and Makin [For-67] and Kocks [Koc-67] to account for the effect of non-regular distributions of obstacles using the concept of effective obstacle spacing. Hirsch and Humphreys [Hir-69] and Bacon [Bac-73] proposed later models on elastic field screening, which impose a logarithmic dependency of dislocation line energy on the effect of precipitate finite size. Many Dislocation Dynamics (DD) simulations have been produced since which account for increasingly realistic microstructures [Moh-01], [Moh-04], [Shi-05]. Despite all these efforts quantitative prediction of particle strengthening remains difficult in some materials.

2.2.3.3 Solid Solution Strengthening

Further strengthening effects coming from solutes in solid solution and their surrounding strain field interfering with dislocation motion have also been modelled in the literature. Most solid solution strengthening models rely on a concept of frictional drag, induced on dislocations as they migrate through fields of point-like lattice-misfitting obstacles (randomly dispersed or clustered) [Mot-48], [Nab-77]. The models therefore rely on a measurement of the interaction of a dislocation with a substitutional impurity atom of different size from the solvent atoms [Fle-63], [Lab-70], [Fri-64].

Friedel developed a simple equation [Fri-64] for the prediction of the yield strength based on the lattice misfit:

$$\Delta\sigma_y = \alpha f G \Omega_M \frac{\delta}{b} \tag{2.12}$$

Where $\Delta\sigma_y$ is the yield strength increase, α is a constant which is 1 for most cases, but can be 0.5-1, f is the fraction, Ω_M is the atomic volume, G is the shear modulus of the matrix, δ is the lattice misfit and b is the burgers vector.

Quantitative measurements of atomic radii (to determine δ, the lattice misfit) are generally difficult due to the radius not being a well-defined physical entity but a probability distribution without a sharp cut-off point, which is also affected by electronegativity interactions with the surrounding atoms [Sla-64]. Fleischer found that the lattice misfit due to the difference in atomic sizes and the difference in shear modulus of the solute atom both had a significant contribution to the hardening effect, however the modulus difference supplied the main effect [Fle-63]. Nevertheless an extensive survey of solid solution hardening models concludes that most of the solid solution hardening models available do not encompasses the principal features of solid solution hardening, such as the temperature dependence of the yield stress, the stress-temperature dependence of the activation volume, etc. [But-93]. Studies that extrapolate through models the behaviour at 0K have been performed [Han-75] but largely most models are empirically descriptive and do not account for temperature factors [But-93].

2.2.3.4 Work Hardening

The work hardening contribution to the yield strength due to plastic deformation is usually modelled using dislocation dynamics simulations [Ars-07]. However, an idea of the strength which comes from work hardening as a result of interactions of dislocations with other dislocations and with other barriers to their motion within the lattice can be estimated using the basic equation relating flow stress to structure [Die-88]:

$$\Delta\sigma_y \approx \alpha G b \rho^{1/2} \text{ [Die-88]} \tag{2.13}$$

Where $\Delta\sigma_y$ is the yield strength increase, α is a constant which is 1 for most cases, but can be 0.5-1, G is the shear modulus of the matrix, b is the magnitude of the Burgers vector and ρ is the density of dislocations.

2.2.3.5 Fibre Addition

The physical addition of reinforcements such as fibres can be modelled using the simple but effective rule of mixtures technique, which is widely used in the literature [Cly-95].

2.2.4 High Temperature Mechanical Strength of Conventional Al Alloys

2.2.4.1 Hot Compression Testing

Hot compression testing at a variety of strain rates is used to simulate the conditions under which alloys would be forged, rolled, extruded or otherwise processed by means of plastic deformation into engineering components.

Several models have been reviewed in the literature to describe the hot compressive behaviour of Al alloys, using temperature, degree of deformation and strain rate as the main variables.

The traditional method considers the flow stress to have a power law dependence on the imposed strain rate [Nar-03], [Su-04], [Sri-08]:

$$\sigma = C\dot{\varepsilon}^{m} \tag{2.14}$$

where C is a parameter which depends on many factors including the structure of the material and testing temperature and m is the strain rate sensitivity parameter. Equation 4.13 is therefore only valid at constant temperature. The strain rate sensitivity parameter quantifies the effect of strain rate on the flow stress and can be derived based on Equation 4.13 by plotting ln(σ) and ln($\dot{\varepsilon}$) at steady state and constant temperature [Sas-01], [Hos-11].

The effect of working temperature on the flow stress behaviour and activation energy can be calculated using the Arrhenius-type equation [Cav-06], [Gan-04], [Sri-08]:

$$\dot{\varepsilon} = A\sigma^{n} e^{\frac{-Q}{RT}} \tag{2.15}$$

where A is a constant, n is the stress exponent (=1/m), R is the gas constant and Q the activation energy. At a given strain rate therefore the slope of ln(σ) and 1/T will give the value of the activation energy Q divided by m and the gas constant R (only valid in the steady state condition).

The calculated activation energy Q for a given compression test set is usually not comparable with individual mechanisms of diffusion [Sri-08]. However if it is found to be close to the activation energy for self-diffusion in Al (142 kJ/mol) [Gan-04], [Sri-08] this would suggest that dislocation climb plays a more significant active role in the selected material [Sri-08], however the mechanisms involved are still a matter for debate. In some cases it has been found to be higher, and it has been suggested by McQueen *et al.* that a higher activation energy could be the result of additional matrix hardening due to the constraints imposed by reinforcements such as particles [McQ-99].

2.2.4.2 Dynamic Strain Ageing (DSA)

Dynamic strain ageing has been observed previously in Al alloys in the form of serrated tensile stress-strain curves [Rob-94b]. This is the cause of the Portevin-Le Chatelier effect (PLC), named after the pioneering work of its discoverers in 1923 [Por-23]. The PLC effect has been shown to reduce the ductility of the material at higher temperature and reverse the strain rate effects on the UTS of the alloys [Rob-94b]. Serrated flow in tensile stress strain curves is extremely common in a very broad range of commercial and non-commercial Al based alloys where substitutional or interstitial solutes have been considered responsible [Rob-94a].

This phenomenon can be observed at room temperature only in alloys which have smaller mobile solute atoms like Si or Li that can “pin” dislocations by diffusing faster than the dislocations move and placing themselves just underneath the extra half plane in a very stable low energy position [Rob-94a]. A higher amount of energy is then required in order to move the dislocation, which can then be pinned again by the fast diffusion of the solute atoms. This gives rise to serrated flow in tensile stress-strain curves, following the same principle described with C atoms in steel by Cottrell

[Cot-53]. Chossat, testing two Al alloys containing 0.5 and 0.7 mass% Si, reported tensile deformation with slight steps [Cho-50a], [Cho-50b]. Much more recently, Al-Si alloys containing 0.2 mass% and 19.90 mass% Si were examined and the PLC effect was present in the 0.2 mass% Si alloy tested in the as-cast, annealed, and solution treated conditions. In the 19.9 mass% Si alloy the effect was not observed at all [Nii-86].

At high temperatures the PLC effect is observed in substitutional alloy systems and the solutes to which this effect is attributed generally include Mg, Cu and Mn [Wu-00], [Rob-94a] but high temperature deformation has suggested the probability of Fe as a solute also responsible for serrated flow [Rob-94a]. Two papers by Chossat in 1950, not directly dealing with serrated flow, show Al-Fe to exhibit steps during deformation during tensile tests [Cho-50a], [Cho-50b]. Iron has very low equilibrium solubility in Al, from 0.02% at 400°C to 0.05% at 650 °C (immediately before melting) [Mas-90]. Skinner *et al.* [Ski-89] used an Al-Si-X alloy with X being a transition element, such as Ti or Fe and proved that at room temperature DSA behaviour was caused by the migration of the Si atoms interfering with dislocation motion, but over ~167 °C the titanium atoms also started contributing to this effect and the Fe atoms started contributing too at temperatures above ~227 °C. All the alloys in this study showed ductility reductions at temperature ranges that varied depending on which solute atom was in solid solution and depending on the strain rate of the tests.

Dynamic strain ageing does not require high concentrations of solute atoms to occur. It has been shown that impurity atoms alone may result in serrated flow in commercially pure Al [Rob-94a], however the effect is also shown be more evident with increasing solute concentrations [Ski-89].

Dynamic strain ageing becomes more obvious with increasing temperature or decreasing strain rate [Kin-81], [Wag-99], [Wu-00]. There is very extensive literature suggesting that DSA starts at a critical strain, which depends on temperature, grain size and strain rate [Pin-98], [Dzi-96], [Rob-94b]. A summary of the dynamic strain ageing effect in various Al based alloys with the temperature range and strain rates is found in table 2.4.

			Temp range for DSA		Strain Rate range			
Source	*Alloy*	*Condition*	*T min*	*T max*	*ε min*	*ε max*	*Solute responsible for DSA*	*Comments*
[Rob-94a]	*Al-1, 3 and 4.5%Cu*	*Heat treated 2 h at 345, 485, 535 °C, air cooled*	*All tests at RT*		*$1x10^{-5}$*	*$1x10^{-2}$*	*Cu*	*Serrated flow and negative SRS*
[Rob-94a]	*Al-Mg*		*~-80 °C*	*~80 °C*	*$1x10^{-6}$*	*$1x10^{-2}$*	*Mg*	*Serrated flow and surface markings*
[Bou-91]	*Al-Fe-V-Si*	*Rapidly Solidified*	*127 °C*	*227 °C*	*$5x10^{-5}$*	*constant*	*Fe*	*At room temp Si responsible for DSA, at high T Fe responsible*
[Ski-89]	*Al-Fe-V-Si*		*27-52 °C*	*only minimum temperature studied in this paper*	*$5.56x10^{-4}$*	*$1.11x10^{-2}$*	*Si*	*RT Dsa due to Si, HT DSA due to transition element*
[Ski-89]	*Al-Fe-V-Si*		*227 °C*		*$5.56x10^{-5}$*	*$1.11x10^{-3}$*	*Fe*	
[Ski-89]	*Al-Si-Ti*		*167±30 °C*		*$5.56x10^{-6}$*	*$1.11x10^{-4}$*	*Ti*	*RT Dsa due to Si, HT DSA due to transition element*
[Ski-89]	*Al-Si-Fe*		*227 °C*		*$5.56x10^{-7}$*	*$1.11x10^{-5}$*	*Fe*	
[Rob-94a]	*Commercially pure Al*		*-10 °C*	*50 °C*	*doesn't say*		*Cu, Fe, Si impurities*	*Effect more evident with higher amounts of impurities*
[Fuj-77]	*2024*	*different grain sizes obtained by work hardening and anneal*	*-196 °C*	*20 °C*	*all tests at $1.7x10^{-5}$*		*Cu, Mg*	*paper on effect of work hardening and grain size on serrations*
[Rob-94a]	*3004*		*RT*	*150 °C*			*Mg with Fe and Si impurities*	
[Rob-94a]	*6061+20 vol% SiC*	*solution treated and quenched*	*All tests at RT*		*serrated flow observed*		*Mg,Si*	*attributed to solute depletion due to precipitation of Mg_2Si*
[Rob-94a]	*6061+20 vol% SiC*	*T6*	*All tests at RT*		*no serrated flow*			

Table 2.4: summary of dynamic strain ageing behaviour found in commercial or non-commercial Al alloys.

2.3. Rapidly Solidified Al Alloys

As conventional crystalline aluminium alloys do not fulfil the strength requirements at the required temperatures of operation for some aerospace and engineering applications, current research is focussing on new compositions and production methods that would improve the mechanical properties in a significant way without reducing the ductility of the alloy.

Rapid solidification can lead to superior mechanical properties due to the higher cooling rates [Pic-81], which

- reduces grain size,
- allows supersaturation of other alloying elements without harmful precipitation,
- allows elements that are essentially insoluble to be found in solution in the rapidly solidified particles,
- produces metastable phases that are not found in conventional cast alloys.

In addition, finer dispersed particles are less apt to initiate fracture than large localised particles, and they also allow the introduction of other mechanisms to slow or stop dislocation motion, such as oxide dispersion strengthening [Cah-96]. Rapid solidification has been shown to improve strength and fatigue properties of Al alloys by up to 50% [Kat-04]. Froes *et al.* suggested that rapidly solidified Al alloy could substitute Ti alloys for applications below ~300 °C [Fro-94].

A variety of different rapidly solidified Al alloys systems which retain their strength up to elevated temperatures have been produced including Al-Fe-Ce, Al-Fe-V-Si, Al-Fe-Mo(-V), Al-Fe-Mo-Si, Al-Cr-Zr, Al-Ti-Fe [Kaw-97], [Li-03]. The addition of transition metals as alloying elements in Al improve the elevated temperature strength due to their low diffusivity [Sla-87].

2.4. Production Routes

There are two main methods of producing large quantities of rapidly solidified alloys from liquid: gas atomisation and melt spinning.

2.4.1 Melt Spinning

Melt spinning is performed by ejecting a thin stream of liquid onto a rotating Cu wheel which solidifies as a ribbon. Cooling rates achievable with this technique go up to 10^6 Ks^{-1} [Cah-96], however only very thin ribbons can be produced, as thin as 10 µm, which then have to be ground into a powder or flakes before being consolidated [Das-91].

The cooling rate of the ribbons produced by melt spinning is controlled by the wheel speed. Controlling the wheel speed allows control over the microstrusctures produced. Tomut *et al.* worked on rapidly solidified $Al_{92}Fe_3V_3Ti_2$ at% alloy and found that specific desirable metastable phases useful for high temperature strength were only produced at wheel speeds of 20-40 m/s, while lower speeds produced more stable intermetallic phases [Tom-04].

2.4.2 Atomisation

Atomisation consists of liquid metal being sprayed through a nozzle and breaking up by jets of inert gas, the resulting droplets being solidified quickly producing powder particles [Cah-96]. The cooling rate achievable by atomization is only around 10^5 Ks^{-1}.

Atomisation conditions such as the heat transfer coefficient of the cooling gas and nozzle geometry can affect the powder size produced. Decreasing the powder size increases the cooling rate and can therefore alter the phases present in the final microstructure [Ram-94], [Tod-04]. In the case of Al-Fe-Cr-TM (TM: Transition Metals) alloys, this difference in cooling rate means that melt spinning produces almost exclusively the desired metastable phases associated with high temperature strength in an α-Al matrix (depending on the ribbon thickness) [Gal-09a], while atomisation (depending on the particle size) with its lower cooling rates expected to produce also other intermetallic phases, as described by Tomut *et al.* [Tom-04] and Audebert *et al.* [Aud-13]. Atomization is however often preferred in practice as a tried and tested method for producing powders on an industrial scale.

2.4.3 Consolidation

Once the powder has been produced through rapid solidification methods it needs to be consolidated in order to produce bulk samples. Todd *et al.* worked with $Al_{93}Fe_3Cr_2Ti_2$ alloy and studied the influence of extrusion conditions of atomised powder on the mechanical properties of the extruded bars. They sieved the atomised powder into 75-100 µm, 50-75 µm, 25-50 µm and <25 µm size fractions and putting the sieved powder fractions in 24mm diameter Al cans with no prior degassing. Extrusion was then performed at 375 °C with a ram speed of 0.3 mm/s [Tod-04].

Sieving sorts the powder by particle size and extrusion deforms it through shear stresses producing a bulk sample. Hot extrusion can cause the decomposition of metastable phases within the atomized powders [Voj-07], but Todd *et al.* [Tod-04] have shown that extrusion at 375 °C of $Al_{93}Fe_3Cr_2Ti_2$ atomised powder alloy does not cause phase transformations in the quasicrystalline powder. Cold compaction can also be used prior to extrusion. This produces a green compact without altering the microstructure of the powder [Kaw-93].

2.4.4 Properties of Bulk Rapidly Solidified Al Alloy Systems

As previously described, typical rapidly solidified Al alloy systems for high temperature applications have been based on the Al-Fe-Ce, Al-Fe-V-Si, Al-Fe-Mo(-V), Al-Fe-Mo-Si, Al-Cr-Zr and Al -Fe-Ti [Kaw-97], [Li-03]. These systems have been alloyed with transition metals as they have low diffusivity in Al and this enables them to retain strength up to higher temperatures. These systems typically lose strength when held above 250 °C as microstructural changes start to occur [Rag-91].

Despite the strength reduction above 250 °C, promising results have been shown in the Al-Fe-V-Si alloys for elevated temperature engineering applications [Pra-99], [Li-03]. Tests performed in tension at 300 °C on an Al-8Fe-1V-2Si (wt%) showed a 0.2% yield stress of 208 MPa [Pra-99]. These alloys are strengthened with spherical precipitates of composition $Al_{12}(Fe,V)_3Si$ which are hard, incoherent particles that interfere with dislocation motion [Mit-92], [Mit-94] and pin grain

boundaries [Ski-89]. Changing the composition has been shown to affect the vol% of precipitates. Mitra has shown that a change from Al-11.7Fe-1.2V-2.4Si to Al-6.5Fe-0.6V-1.3Si decreased the volume fraction of precipitates from 37% to 16% and the alloy with a higher volume fraction of precipitates retained improved elevated temperature strength [Dav-93].

Other alloy compositions with high Si content have also been produced through rapid solidification. An example which is already in use in engineering components are the RSA-4XX series. These alloys contain almost 20 wt% Si and can be used up to ~400 °C [Kat-04]. The improved mechanical properties of this alloy series is attributed to the refined grain structure and high content of transition metals [Kat-04]. Their elevated temperature strength means they are currently being produced by RSP Technology as pistons in racing cars [Rsp-14]. The yield strength of conventional 2618 Al alloys used for car pistons decreases from 165 MPa at 250 °C to 30 MPa at 350 °C. RSA447 alloy pistons made of Al-17.5Si-4.5(Fe, Ni)-3.5Cu-1.1Mg (wt%) have a yield strength of 230 MPa at 250 °C and retain 95 MPa of yield strength at 350 °C [Rsp-14].

2.5. Quasicrystalline Al Alloys

Inoue [Ino-98] observed that some rapidly solidified alloys show excellent microstructural stability and mechanical properties up to high temperatures better than others. Particularly alloys which contain elements with low diffusion coefficients in Al, like transition elements. The alloy they found which showed the best high temperature strength was shown to contain metastable, spherical quasicrystalline phases, which were only discovered 15 years earlier by Daniel Shechtman [She-84]. Quasicrystals are of high interest in the development of new temperature resistant rapidly solidified Al alloys.

Quasicrystals are structures with long-range non-periodic order first discovered by Shechtman *et al.* in 1984 in rapidly solidified Al-Mn alloys [She-84]. They were shown to be ordered phases which show rotational symmetry but lack translational symmetry. Experimentally, this aperiodicity was revealed by the unusual diffraction pattern symmetries (such as five-fold symmetry) that was

not previously believed to be possible. Later, many other polyhedral quasicrystals with other unusual symmetries were shown to exist, such as twelve-fold symmetry in Ni-Cr alloy systems [Ish-85] or eight-fold symmetry in V-Ni-Si and Cr-Ni-Si [Wan-87].

This review focuses on Al-based alloys with quasicrystalline phases of the icosahedral point group, which show two, three and five fold symmetries, shown in Figure 2.1 [She-84].

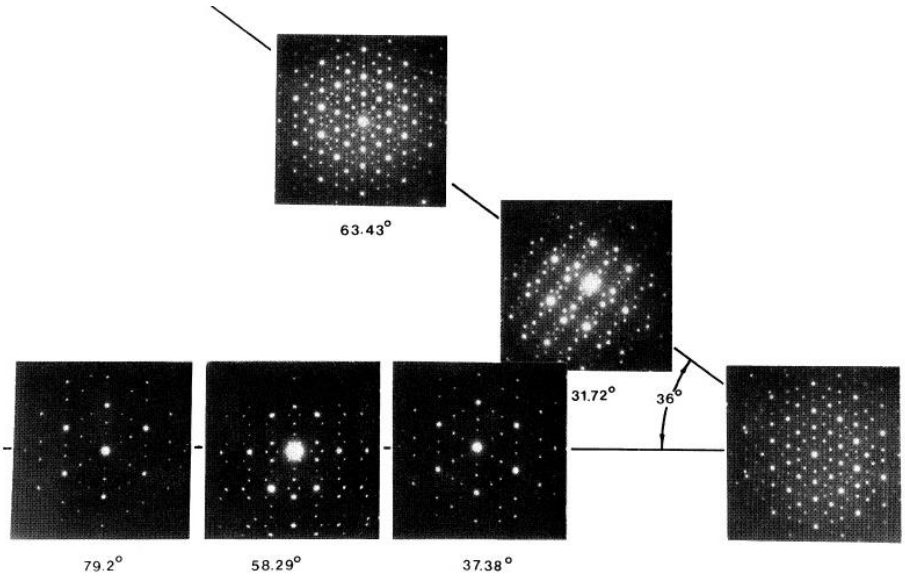

Figure 2.1: Diffraction patterns produced from icosahedral quasicrystals in an Al-Mn alloy [She-84]. (Reprinted Fig. 2 with permission from Shechtman, D., Blech, I., Gratias, D., Cahn, J. W., Phys. Rev. B, 28, 784–805. Copyright (1983) by the American Physical Society).

Icosahedral quasicrystals seem to form mainly in Al-TM systems, where TM=Transition Metal. Soon after the discovery of quasicrystals in the Al-Mn system [She-84], [Ish-85] similar ones were found in other systems, including Al-Cu [Dub-86], Al-V [Ino-86] and Al-Cr [Ino-87]. In all these systems, the icosahedral quasicrystals are distributed in the FCC α-Al matrix in a similar way to how equilibrium precipitates are distributed in a precipitation hardened Al alloy [Ino-98].

Quasicrystalline phases were later discovered in ternary and quaternary aluminium alloys, such as Al-Fe-V [Ski-88], Al-Fe-Nb [Aud-96] and Al-Fe-Cr-Ti [Ino-99]. They were also found in Al-Fe-Cr alloys by Inoue *et al.* [Ino-98].

2.6 Quasicrystalline Al Alloys for High Strength at Elevated Temperature Applications

2.6.1 Choice of Composition

In 1999 Inoue and Kimura observed that the Al-Fe-(Cr/V)-Ti alloys containing icosahedral quasicrystals exhibit high elevated temperature strength [Ino-99]. This was thought to be due to the stability of the icosahedral phase containing Fe, Cr/V and Ti, all of which have low diffusivities in Al [Mas-86]. The elevated temperature strength and low density of this alloy makes it of great industrial interest because it is much lighter than other materials with similar mechanical properties and retains its strength and microstructural stability up to higher temperatures [Ino-00], [Ino-01].

More recently, Galano *et al.* [Gal-04], [Gal-09a], [Gal-09b] have studied the effect of alloying additions (Ti, Nb, V and Ta) to the Al-Fe-Cr system on microstructural stability.

It was found that the addition of a fourth alloying element to the Al-Fe-Cr system leads to a more refined microstructure and a more stable icosahedral phase. The maximum stabilising effect was reached with the $Al_{93}Fe_3Cr_2(Nb,Ta)_2$ alloys, which retained icosahedral quasicrystals up to 550 °C [Gal-09a]. The icosahedral phase in other compositions decomposed after heat treatment at 450 °C. Figure 2.2 is an X-ray diffractogram that shows this effect in the Al-Fe-Cr-Ti alloy [Gal-09a]. It shows that from the as-spun state to 450 °C the icosahedral phase is present and FCC-Al, with small amounts of other intermetallic phases. At 550 °C however the icosahedral phase can no longer be detected by XRD and larger amounts of stable intermetallic phases can now be identified [Gal-09a].

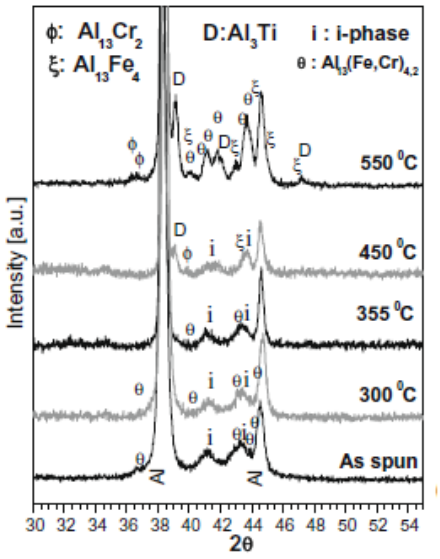

Figure 2.2: XRD scan showing the phases present in melt-spun nanoquasicrystalline $Al_{93}Fe_3Cr_2Ti_2$ after heat treatments. [Gal-09a].

For the $Al_{93}Fe_3Cr_2Ti_2$ alloy used by Galano *et al.* it was found that the as-spun microstructure showed quasicrystals of about 100nm in size, but after heat treatment at 355 °C their size increased to about 150-200 nm. Only at 450 °C the metastable quasicrystalline phases started to form intermetallics. After heat treatment at 550 °C no quasicrystalline phases were seen [Gal-04].

Inoue *et al.* first produced quasicrystalline quaternary Al-Fe-Cr-Ti alloys, initially of composition $Al_{84.3}Fe_7Cr_{6.3}Ti_{2.5}$ at% which was found to produce a single icosahedral quasicrystalline phase [Ino-00]. By altering the composition to $Al_{93}Fe_3Cr_2Ti_2$ at% they found that the microstructure consisted of nanoquasicrystals embedded in an α-Al matrix [Ino-00]. Kimura and Inoue [Kim-00] found that the composition of the nanoquasicrystalline phases was close to that of the previous alloy, with most of the alloying additions found in the quasicrystalline i-phases and the α-Al matrix being ~97.5 at% Al, ~1.1 at% Fe, ~1.1 at% Cr and ~0.5 at% Ti. The $Al_{93}Fe_3Cr_2Ti_2$ at% alloy showed does not undergo many microstructural changes during heat treatments, only a small amount of coarsening before decomposing into stable intermetallic phases [Kim-00].

There is also strong evidence in the literature to suggest that the failure modes of the Al-Fe-Cr-Ti alloys change quite significantly with composition. It was shown by Audebert *et al.* [Aud-02] that by increasing the amount of Al in the alloy from $Al_{91}Fe_5Cr_2Ti_2$ at% to $Al_{93}Fe_3Cr_2Ti_2$ at% the tensile

failure mode, in ribbon shape, went from brittle (200-250 MPa) to ductile fracture (510-575 MPa) at room temperature. It was also shown that 40-45 vol% quasicrystalline phases in α-Al give improved strength while retaining ductility. To achieve that percentage of quasicrystals the composition of the alloy has to be set between 91-93 at% Al, any lower vol% of quasicrystals and the strengthening effect will be limited, any higher and the alloy will be extremely brittle [Aud-02].

Inoue *et al.* [Ino-99] found high strength for a quasicrystalline $Al_{91.1}Fe_{3.6}Cr_{3.5}Ti_{2.5}$ at% alloy even at elevated temperatures: 510 MPa at 200 °C and 360 MPa at 300 °C as well as high room-temperature strength of 650 MPa. The strength of this alloy was also maintained after annealing for 1000 h at 300 °C. This was attributed to the fact that the icosahedral phase in this alloy was made to be finely dispersed quasicrystals in a single grain, highly ductile FCC α-Al matrix [Ino-99].

2.6.2 Microstructures

Galano *et al.* [Gal-09a] performed a microstructural characterization and study of the phase transformation of the $Al_{93}Fe_3Cr_2Ti_2$ at% alloy produced by melt spinning. They found this alloy has a microstructure composed of nano-scale icosahedral quasicrystalline phase embedded in an α-Al matrix, as shown in Figure 2.3 [Gal-09a]. Figure 2.3 also shows the microstructural stability of the icosahedral phase after heat treatments. Very low levels of coarsening are observed until the phase decomposes into stable intermetallics after being heated up to 550 °C for 30 minutes [Gal-09a].

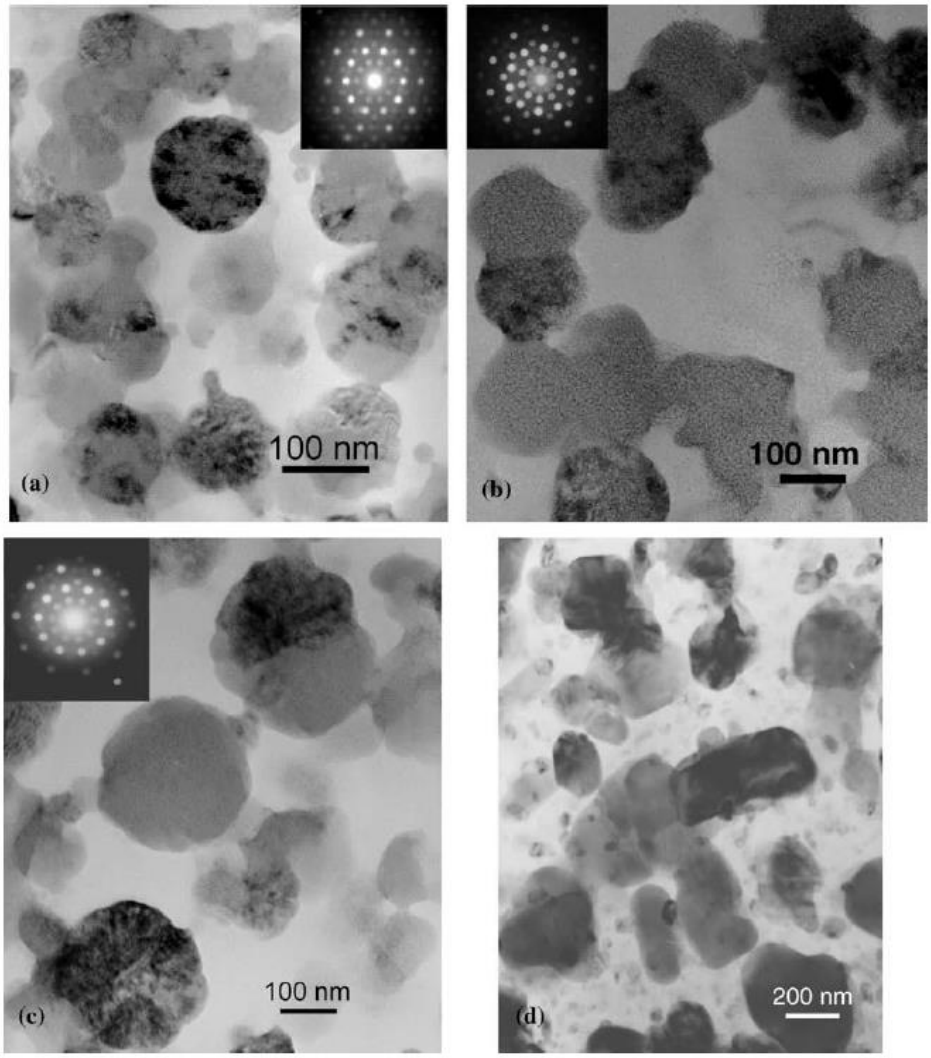

Figure 2.3: Bright field TEM images showing the Al-Fe-Cr-Ti alloy under different heat treatments: (a) as-spun state, (b) heat treated 30 minutes at 355 °C, (c) heat treated 30 minutes at 450 °C, (d) heat treated 30 minutes at 550 °C [Gal-09a]

The same alloy produced by atomisation has been shown to also have a microstructure made of nano-scale icosahedral quasicrystalline phases dispersed in an FCC α-Al matrix (Figure 2.4), however even in the smallest powder fraction (0-25 μm) the quasicrystalline phases appear larger, which is likely to be due to the slower cooling rates during atomisation [Ped-10].

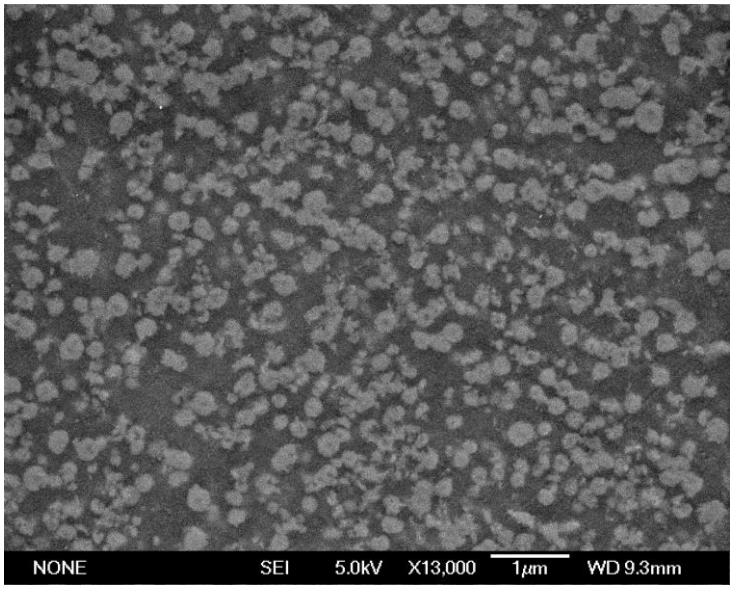

Figure 2.4: Secondary Electron Image of atomised 0-25 μm Al-Fe-Cr-Ti alloy showing what is believed to be icosahedral quasicrystalline phases in an α-Al matrix because of the combined results of SEM and XRD [Ped-10].

The phases found in the as-spun ribbons were different from those found in the atomised powder through XRD scans: the melt-spun nanoquasicrystalline $Al_{93}Fe_3Cr_2Ti_2$ ribbons analysed by Galano *et al.* [Gal-09a] contained only icosahedral quasicrystalline phase, in an α-Al matrix with small amounts of the metastable θ-$Al_{13}(Fe,Cr)_{2-4}$ intermetallic phase (Figure 2.3). After heat treatments, the θ-$Al_{13}(Fe,Cr)_{2-4}$ phase transformed into stable intermetallics of $Al_{13}Fe_4$, $Al_{13}Cr_2$, Al_3Ti [Gal-09a]. The as-atomised powders already contain those stable intermetallics, and no evidence of the θ-$Al_{13}(Fe,Cr)_{2-4}$ phase was found, perhaps due to the much slower cooling rates compared to the melt spinning process [Ped-10].

2.6.3 Mechanical Properties and Strengthening Mechanisms of Quasicrystalline Al Alloys

2.6.3.1 Hardness

Hardness tests on alloys of nominal chemical composition $Al_{93}Fe_3Cr_2Ti_2$ at% have been performed on melt-spun ribbons. Audebert *et al.* [Aud-02] used a ribbon of measured composition $Al_{92.37}Fe_{3.32}Cr_{2.14}Ti_{2.12}$ and found a Vickers microhardness of 390 μHV and Galano *et al.* [Gal-09b] analysed a $Al_{92.94}Fe_{3.02}Cr_{2.02}Ti_{2.02}$ ribbon and found the microhardness to be 350 μHV for the as-

spun sample, and of 200 μHV after heat treating at 550 °C for 30 minutes [Gal-09b]. Inoue and Kimura [Ino-00] reported similar values, and showed that the hardness was almost unchanged even after annealing 1000 hours at 300 °C.

Todd *et al.* [Tod-04] analysed the same alloy composition, but produced by gas atomisation and extrusion of bars, and the hardness values measured were found to vary with powder size fraction and extrusion temperature according to Table 2.5.

		Extrusion Temperature/°C								
		375			*400*			*450*		
Source	*Powder size/µm*	*ER*	*σ_{max}/MPa*	*µVHN*	*ER*	*σ_{max}/MPa*	*µVHN*	*ER*	*σ_{max}/MPa*	*µVHN*
[Tod-04]	*<25*				*10:01*	*1400*	*172±9*			
[Tod-04]					*07:01*	*1155*	*151±6*			
[Ped-10]	*<25*				*14:1*	*1593*	*207±2*			
[Tod-04]	*25-50*	*10:01*	*1473*	*169±10*	*10:01*	*1313*	*162±6*	*10:01*	*1041*	*143±7*
					14:01	*1473*	*159±10*			
					07:01	*980*	*118±6*			
[Tod-04]	*50-100*	*10:01*	*1164*	*131±2*	*10:01*	*1058*	*124±6*	*10:01*	*863*	*116±6*
					14:01	*1155*	*123±7*			

Table 2.5: variation of hardness with extrusion temperature and powder size [Tod-04], [Ped-10].

This shows values which are significantly lower if the alloy is produced by gas atomisation rather than melt spinning, but even these values compare well with currently available Al alloys such as 7075 T6 which has a hardness of 140-150 μHV [Gal-09b].

2.6.3.2 Quasi-Static Tensile Strength

Individual quasicrystals have been reported to have high hardness [Mas-86], high Young's modulus [Yok-93] and low friction coefficient [Rus-05]. Individual quasicrystals are also very brittle, with no appreciable plastic regime at room temperature [Mas-86]. All plastic deformation in mechanical tests occurs in the ductile alloys containing the quasicrystalline phases distributed in an α-Al matrix [Tod-04], [Gal-09b]. Generally, dislocations are found to loop around the quasicrystals rather than cutting through them (as it would destroy the quasiperiodic lattice) [Ino-00].

Outstanding mechanical properties were found by Galano *et al.* [Gal-09b] in tensile tests of melt-spun quaternary $Al_{93}Fe_3Cr_2X_2$ alloys, with X being Ti, Nb, V or Ta. The $Al_{93}Fe_3Cr_2X_2$ alloys were also considerably superior in such tests to the ternary $Al_{93}Fe_{4.2}Cr_{2.8}$ alloy. The alloys were studied both in the as-spun state and after heat treatments up to 450 °C with strain rates between 10^{-3}-$5x10^{-6}$ s^{-1}. They had a microstructure consisting of an α-Al matrix with icosahedral quasicrystals and small amounts of intermetallics. The deformation mechanisms at room temperature were found to be localized and through slip bands developed under plane-stress conditions.

The strength at room temperature measured in quasi-static tensile tests for melt spun ribbons of $Al_{92.37}Fe_{3.32}Cr_{2.14}Ti_{2.12}$ alloy was 575 MPa [Aud-02] and $Al_{92.94}Fe_{3.02}Cr_{2.02}Ti_{2.02}$ alloy was ~700 MPa [Gal-09b].

2.6.3.3 Toughness and High Strain Rate Tests

Some preliminary high strain rate tests on the $Al_{93}Fe_3Cr_2Ti_2$ alloy in the form of extruded bars made of atomised powder have been performed recently at room temperature in tensile and compression configuration using Hopkinson bars [Ped-10].

The dynamic flow stress of the Al-Fe-Cr-Ti alloy at 2200 s^{-1} was 970 MPa [Ped-10]. Conventional Al based alloys have much lower values, like 7075 at strain rate 3500 s^{-1} has a dynamic flow stress of 650 MPa [ElM-06], Ti-6Al-4V at strain rate 3000 s^{-1} has a dynamic flow stress of 1600 MPa [ElM-06]. This seems much higher, but if divided by the density, the specific strengths are 346 MPa, 356 MPa and 241 MPa respectively for the $Al_{93}Fe_3Cr_2Ti_2$, the Ti-6Al-4V and the 7075 alloys.

In terms of specific properties, the $Al_{93}Fe_3Cr_2Ti_2$ alloy shows a strength which is much higher than any commercially available Al alloy, and which is comparable to Ti6Al4V. However only one sample was tested and fractography revealed that it failed on a large defect [Ped-10] therefore further testing would be required to assess the dynamic mechanical response of the $Al_{93}Fe_3Cr_2Ti_2$ alloy in tension.

The same Al-Fe-Cr-Ti alloy tested in compression showed a significant increase in the dynamic flow stress with increasing strain rate, and still retained about 20% strain to failure. The flow stress of the Al-Fe-Cr-Ti alloy was 1100 MPa at 3000 s^{-1} strain rate, however only one sample was available for testing [Ped-10]. Commercial alloys like 7075 at strain rate 3500 s^{-1} have a dynamic compressive flow stress of 670 MPa [ElM-06], Ti-6Al-4V at strain rate 3100 s^{-1} has a dynamic flow stress of 1750 MPa [ElM-06]. If divided by the density, the specific strengths are 393 MPa, 389 MPa and 248 MPa respectively for the $Al_{93}Fe_3Cr_2Ti_2$, the Ti-6Al-4V and the 7075 alloys. The dynamic flow stress of $Al_{93}Fe_3Cr_2Ti_2$ per unit weight is actually higher than the Ti-6Al-4V in compression at room temperature [Ped-10]. Further tests would be necessary to confirm this result however statistics are not available due to the fact only one test was performed.

2.6.4 Thermal Stability and High Temperature Mechanical Properties

The strength of commercially available aerospace-grade Al alloys, such as 2000 or 7000 series, falls rapidly with increasing temperature due to microstructural instability [Ino-00]. Figure 2.5 shows the strength of some 2000 and 7000 series Al alloys produced by ingot metallurgy (IM) and compares it to the strength of rapidly solidified quasicrystalline Al alloys produced by powder metallurgy (P/M). The conventional Al alloys have high UTS values up to 150-200 °C, but then there is a sharp drop in strength. Quasicrystalline $Al_{93}Fe_3Cr_2Ti_2$ and $Al_{91}Fe_5Cr_2Ti_2$ alloys however show a gentler slope and retain their strength up to higher temperatures.

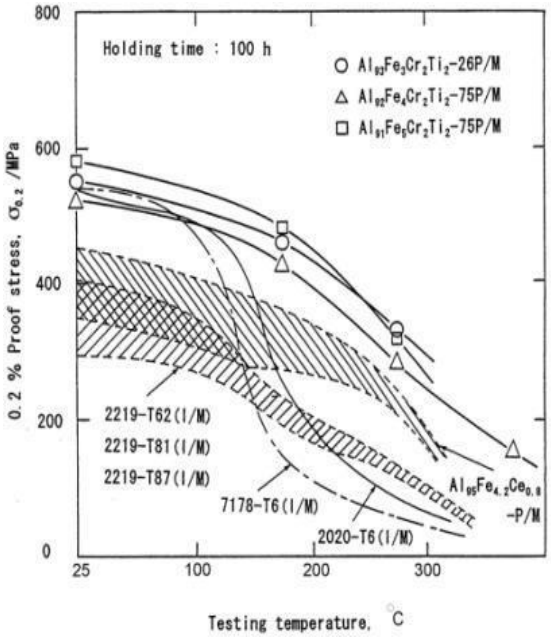

Figure 2.5: Strength of 2020-T6 and 7178-T6 alloys produced by ingot metallurgy compared with nanocrystalline Al-Fe-Ce and nanoquasicrystalline Al-Fe-Cr-Ti alloys produced by powder metallurgy [Ino-00].

Galano *et al.* [Gal-09b] have studied the mechanical properties of melt-spun ribbons of nanoquasicrystalline Al-Fe-Cr and Al-Fe-Cr-(Ti, V, Nb or Ta) alloys. They have performed tensile tests in vacuum in a range of 300 °C to 350 °C varying strain rates between 10^{-3} and $5x10^{-6}$ s^{-1}. They found for the $Al_{93}Fe_3Cr_2Ti_2$ alloy a value of UTS of 570 MPa at 300 °C, 530 MPa at 315 °C, 450 MPa at 330 °C and 420 MPa at 350 °C. Between 300-350 °C the deformation mechanisms

were found to be through dislocation movement, with ductile fracture surfaces initiated either by cavity formation around the hard quasicrystalline particles or due to dislocation pile-ups at grain boundaries. It was suggested that cavity formation could be inhibited in alloys with smaller quasicrystalline particles, or by testing at lower strain rates and higher temperatures [Gal-09b].

2.7 Nanoquasicrystalline Al Alloy Matrix Composites Containing Pure Al

2.7.1 Microstructure, Mechanical Properties and Strengthening Mechanisms

In an effort to improve ductility, Nagy *et al.* [Nag-05] investigated the possibility of creating a composite using a rapidly solidified $Al_{94}V_4Fe_2$ alloy powder that contained icosahedral quasicrystalline phases, mixed and extruded with pure Al powder. The initial size of the Al-V-Fe powder was 63-200 μm, and of the Al powder was 1μm, and the weight ratio was 1:1 and 2:1. The final extruded microstructure showed a mixture of lightly deformed Al-V-Fe grains and heavily deformed Al grains, which will from now on be referred to as fibres.

The ductility of this composite compared with the pure Al-V-Fe alloy alone allowed the extrusion temperature and pressure to be dropped from 0.6 MPa at 450 °C to 0.5 MPa at 420 °C. It was also found that the compression strength of the composite was significantly lower, but with a much higher strain-to-failure, which is expected as the pure Al powder is very ductile and allows more plastic deformation. The difference between compressive and tensile strength was also much smaller in the case of the composite, showing that the added ductility allowed for improved compaction and less residual porosity after extrusion. The final tensile strength shown was 500 MPa with a strain-to-failure of 0.6% [Nag-05], while gas-atomized Al-Fe-Cr-Ti alloy extruded at 400 °C exhibited strength of 520 MPa and a strain–to–failure of 4-7% [Ino-99].

Nanoquasicrystalline Al alloys matrix composites have also been produced with the same powder metallurgy method as Nagy *et al.* [Nag-05] but using the $Al_{93}Fe_3Cr_2Nb_2$ alloy and 35 vol% and 20 vol% pure Al powders by Wei Hao Gu at Oxford [Gu-09]. They were compacted and extruded at temperatures between 440-560 °C. These temperatures were found to be high enough to cause

transformations of the quasicrystalline phases into more stable intermetallics. In microhardness tests, composites with 35% pure Al had hardness values of ~100 μVHN_{500}, while composites with 20% pure Al the hardness was ~140 μVHN_{500}. The UTS values in compression tests were 440 MPa and 620 MPa respectively. It was also found that decreasing the diameter of the pure Al powder from 63 µm to 4 µm improved the hardness up to 115 μVHN_{500} and 170 μVHN_{500} for the 35% Al and 20% Al composites respectively.

Also within the same Oxford research group [Ped-10] composites were made using $Al_{93}Fe_3Cr_2Ti_2$ and 20 vol% and 10 vol% pure Al powders, both <25 µm in diameter, which were placed in Al cans and extruded without compaction and without prior degassing. The microstructure of the $Al_{93}Fe_3Cr_2Ti_2$ at% alloy both in the as-atomised powder and in the extruded composites showed spherical particles believed to be icosahedral phase embedded in an α-Al matrix with very small volume fractions of other intermetallic particles. Icosahedral quasicrystalline phases were found in the microstructure even after extrusion at ~390 °C. Strength was shown to increase with strain rate both in tension and in compression. Increasing the volume fractions of pure Al fibres caused a linear decrease in UTS and microhardness.

The dynamic flow stress of the Al-Fe-Cr-Ti alloy, the composite with 10 vol% pure Al and the one with 20 vol% pure Al were 970 MPa, 875 MPa and 770 MPa respectively at 3000 s^{-1} in tension, however there were issues with the strain gauges and due to a time constraint only one test was performed.

A summary of the dynamic tensile properties of the quasicrystalline $Al_{93}Fe_3Cr_3Ti_2$ alloy and the composites in comparison with the corresponding to conventional Al and Ti alloys can be seen in Table 2.6 [Ped-10]. Further testing would be required to confirm these values.

Source	*Alloy*	*Strain rate (s^{-1})*	*UTS (MPa)*	*Specific strength ($MPa/g/cm^3$)*	*Strain-to-failure*
[Ped-10]	*$Al_{93}Fe_3Cr_2Ti_2$*	*2200*	*970*	*346*	*0.34*
[Ped-10]	*$Al_{93}Fe_3Cr_2Ti_2$ +10 vol% Al*	*2200*	*875*	*313*	*0.30*
[Ped-10]	*$Al_{93}Fe_3Cr_2Ti_2$ +20 vol% Al*	*2200*	*770*	*287*	*0.45*
[Bør-10]	*7075 T651*	*1128*	*550*	*203*	*0.15*
[Che-09]	*6060 T6*	*1000*	*270*	*100*	
[Che-09]	*6082 T6*	*1000*	*360*	*133*	
[Che-09]	*7003 T6*	*1000*	*450*	*167*	
[Che-09]	*7108 T6*	*1000*	*500*	*185*	
[Rey-06]	*7003 T79*	*1300*	*500*	*185*	*0.5*
[Rey-06]	*7108 T6*	*1300*	*385*	*143*	*0.8*
[ElM-06]	*7075*	*3500*	*650*	*241*	*22*
[ElM-06]	*Ti-6Al-4V*	*3000*	*1600*	*356*	*26*
[ElM-06]	*Mg AZ80*	*2000*	*420*	*233*	*10*

Table 2.6: UTS and strain-to-failure at high strain rate test of quasicrystalline $Al_{93}Fe_3Cr_2Ti_2$ *alloy and its composites, compared to commercially available Al and Ti based alloys [Ped-10]*

A summary of the dynamic compression properties of the quasicrystalline $Al_{93}Fe_3Cr_3Ti_2$ alloy and the composites in comparison with the corresponding to conventional Al and Ti alloys can be seen in Table 2.7 [Ped-10]. Again, only one test was available per sample. The high strain rate tests performed using a split Hopkinson bar compression showed dynamic flow stresses that exceeded 1 GPa, which was never previously seen in Al alloys, and which in terms of specific strength is only 20 MPa less than Ti6Al4V.

Source	*Alloy*	*Strain rate (s^{-1})*	*Strength (MPa)*	*Specific Strength ($MPa/kg/m^3$)*	*Strain-to-failure*
[Ped-10]	*$Al_{93}Fe_3Cr_2Ti_2$*	*3000*	*1100*	*392.86*	*0.27*
[Ped-10]	*$Al_{93}Fe_3Cr_2Ti_2$ +10 vol% Al*	*3000*	*1000*	*357.14*	*0.23*
[Ped-10]	*$Al_{93}Fe_3Cr_2Ti_2$ +20 vol% Al*	*3000*	*750*	*267.86*	*0.33*
[Oos-00]	*6082 T6*	*3000*	*~370**	*137.04*	
[Oos-00]	*7108 T79*	*3000*	*~450**	*166.67*	
[ElM-06]	*7075*	*2500*	*650*	*240.74*	*3.5*
[ElM-06]		*3500*	*670*	*248.15*	*4.5*
[ElM-06]		*5000*	*700*	*259.26*	*7.5*
[ElM-06]	*Ti-6Al-4V*	*2300*	*1700*	*377.78*	*3*
[ElM-06]		*3100*	*1750*	*388.89*	*2.5*
[ElM-06]		*3900*	*1800*	*400.00*	*2.2*
[ElM-06]	*Mg AZ80*	*2000*	*400*	*222.22*	*1.5*
[ElM-06]		*3000*	*430*	*238.89*	*1.5*
[ElM-06]		*4500*	*450*	*250.00*	*1.5*

*Table 2.7: showing the strength and elongation to failure for high strain rate compressive tests of nanoquasicrystalline Al-Fe-Cr-Ti alloy and its composites compared to commercially available Al and Ti based alloys. *dynamic flow stress at 0.5% strain measured, not UTS.*

2.7.2 High Temperature Testing

It has been observed that the bulk nanoquasicrystalline $Al_{93}Fe_3Cr_3Ti_2$ alloy and its composites containing Al particles when tested at 250 °C had serrated stress-strain curves, which can be seen in Figure 2.6 [Ped-10]. In the tensile tests performed at 250 °C, both strength and ductility of the composites were seen to decrease. Serrated flow stress was observed after the yield stress.

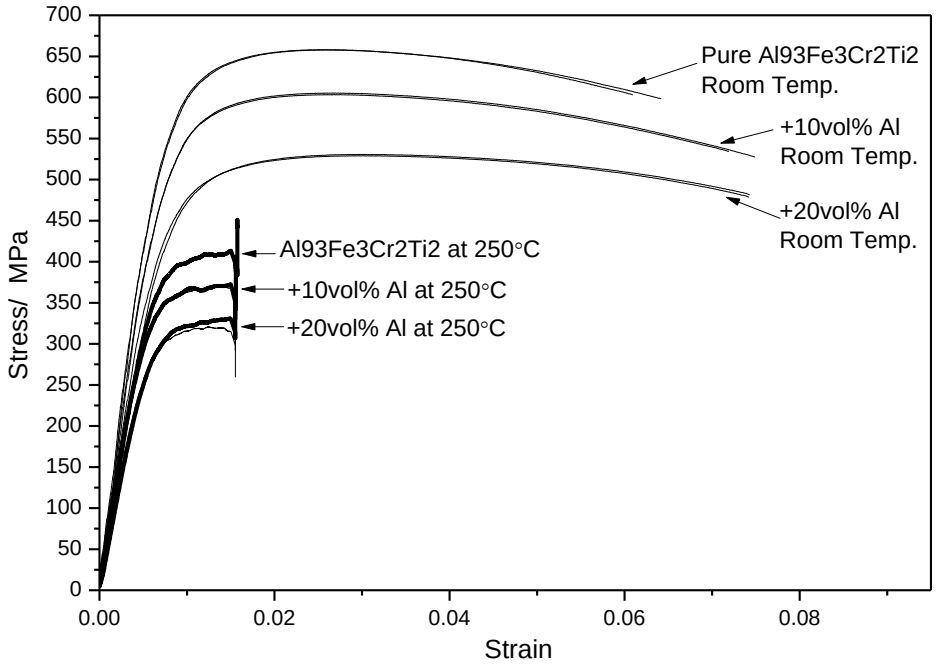

Figure 2.6: Stress-strain curves at room temperature and 250 °C showing high temperature serrations and a loss of ductility [Ped-10].

This effect has been tentatively attributed to a dynamic strain ageing (DSA) effect which needs further investigation [Ped-10]. No account confirming dynamic strain ageing on quasicrystalline Al-based alloys has been found in the open scientific literature, however it has been seen in other rapidly solidified crystalline Al-based alloys. A study by Bouchaud *et al.* on rapidly solidified AI-Fe-V-Si alloy showed both a small anomaly in the flow stress - temperature curve and a dip in the strain rate sensitivity at ~127 °C. This unusually high temperature for the appearance of DSA effects (in Al alloys) was attributed to the mobility of dissolved Fe. The reason suggested for the high temperature occurrence of the effect was that Fe is a transition element whose diffusivity in Al is much lower than conventional alloying elements. In this case no serrated flow was observed, but the alloy was proved to have a dynamic strain ageing behaviour due to a decrease in strain rate sensitivity between 127 and 227 °C [Bou-91].

A decrease in strain rate sensitivity is known to promote a loss of ductility [Koc-81]. Bouchaud *et al.* [Bou-91] published some experiments that indicate that the activation energy associated with DSA is substantially lower than that for bulk diffusion. Therefore, either diffusivity is enhanced by

vacancies created during plastic flow, or the solute atoms diffuse rapidly due to a pipe-diffusion mechanism. DSA has also been shown to be less likely to occur in single crystal systems, suggesting that grain boundaries play a significant role in making diffusion of atoms faster [Rob-94a].

2.7.3 Mechanical Behaviour of the Composites

The rule of mixtures can be used to predict the mechanical properties of the composites in tensile and compressive tests, as long as all the phases are micro-sized [Cly-95]. This concept is based on the idea that the force on the specimen is carried by the matrix and the fibres according to their respective volume fractions [Cly-95]. The mean stress on the specimen can therefore be expressed as

$$\sigma = \sigma_{fib} V_{f\,ib} + \sigma_{mat} V_{mat} \quad \text{[Cly-95]} \tag{2.16}$$

where V_{fib} and V_{mat} are the volume fractions of fibre and matrix and σ_{fib} and σ_{mat} are the stresses experienced by the fibres and matrix respectively [Cly-95]. This model is used to describe long fibre composites, but it is a very limited approximation that does not take into account the level of bonding between the fibres and the matrix and any porosity or other defects if present. This model has been used to describe the behaviour of rapidly solidified $Al_{93}Fe_3Cr_2Nb_2$ based composites by [Gu-09] and showed a reasonable prediction of their behaviour both in microhardness and in compressive tests (within experimental errors).

2.8 Conclusions and Summary

The studies described in this literature review have shown that a significant improvement in high temperature strength and hardness can be achieved by using quasicrystalline Al alloys compared to the strongest available aerospace grade Al alloys. Also toughness and ductility can be improved by adding pure Al fibres to the quasicrystalline alloys. This has been tested on ternary Al-V-Fe alloy

systems by Nagy *et al.* [Nag-05]. Previous work within our Oxford research group [Gu-09], [Ped-10] has been performed using quaternary Al-Fe-Cr-Ti and Al-Fe-Cr-Nb alloys with improved mechanical properties [Gal-09b] and thermal stability [Gal-04] as matrix for the composites, which have shown outstanding mechanical properties both at room temperature and up to ~300 °C when compared to commercially available Al alloys and Ti-6Al-4V (specific properties) [Ino-00], as summarised in Table 2.8 and 2.9. Particularly, it is observed that the specific yield stress at 250 °C of the nanoquasicrystalline alloys and the composites are very competitive with the corresponding to the Ti-6Al-4V alloy. The addition of pure Al has improved the energy absorbing ability and increased the strain to failure. However, this reduced the strength of the original alloy which would be an acceptable compromise in favour of ductility, formability and toughness in a search for the optimum range of useful properties for the required applications.

Alloy	*0.2% Yield Stress (MPa)*	*Density (g/cm^3)*	*Specific Yield Stress, σ_y (MPa/ gcm^{-3})*	*Total elongation*
$Al_{93}Fe_3Cr_2Ti_2$	*555*	*2.88*	*192.7*	*6.25%*
$Al_{93}Fe_3Cr_2Ti_2$ +10 vol% Al	*507.5*	*2.86*	*177.4*	*7.25%*
$Al_{93}Fe_3Cr_2Ti_2$ +20 vol% Al	*441.5*	*2.84*	*155.5*	*7.50%*
7075-T6	*505*	*2.7*	*187*	*11%*
2014-T6	*415*	*2.7*	*153.7*	*13%*
Ti6Al4V	*940*	*4.42*	*212.7*	

Table 2.8: Room temperature Mechanical properties of Al and Ti based alloys.

	0.2% yield Stress (MPa)	*Density (g/cm^3)*	*Specific Yield Stress, σ_y (MPa/gcm^{-3})*
$Al_{93}Fe_3Cr_2Ti_2$	*382*	*2.88*	*132.64*
$Al_{93}Fe_3Cr_2Ti_2$ +10 vol% Al	*346.5*	*2.86*	*121.15*
$Al_{93}Fe_3Cr_2Ti_2$ +20 vol% Al	*299.25*	*2.84*	*105.37*
*7075-T6**	*80*	*2.7*	*29.63*
*2014-T6**	*200*	*2.7*	*74.07*
*Ti6Al4V**	*531*	*4.42*	*120.14*

*Table 2.9: High temperature mechanical properties of Al and Ti based alloys taken at 250 °C.*taken at 200 °C, unlike the $Al_{93}Fe_3Cr_2Ti_2$, which were taken at 250 °C.*

Some aspects of the $Al_{93}Fe_3Cr_2Ti_2$ alloy and composites are however still not understood. The following chapters will focus on the production and characterisation of the nanoquasicrystalline $Al_{93}Fe_3Cr_2Ti_2$ alloy powder and its consolidation into bulk alloy and composite bars. Then the bars will be used for thermal analysis, room temperature mechanical tests and elevated temperature mechanical tests to further understand the properties and correlate them to the microstructures.

One of the aims of this project is to determine the correlation between the microstructure and yield strength of bulk processed nanoquasicrystalline $Al_{93}Fe_3Cr_2Ti_2$ at% alloy and composites and to estimate the contributions of various strengthening mechanisms to the overall strength at room temperature. This project also aims to further test the high strain rate behaviour of this alloy and composites at room temperature in tension and compression to assess their response to dynamic loading conditions. It also aims to investigate processing conditions for commonly used industrial practices such as forging and hot rolling through a series of compression tests at varying strain rates and temperatures and analyse the materials thermal evolution at selected temperatures.

References

[Ard-85] A. Ardell, J. Metall Trans, (1985), 16A, 2131.

[Ars-07] A. Arsenlis, W. Cai, M. Tang, M. Rhee, T. Oppelstrup, G. Hommes, T. G. Pierce and V. V. Bulatov, Model. Simul. Mater. Sci. Eng., (2007), 15, 553–595.

[Ash-64] M. Ashby, Z. Metallk., (1964), 55, 5-17.

[Aud-13] F. Audebert, M. Galano, C. Triveño Rios, H. Kasama, M. Peres, C. Kiminami, W. J. Botta, C. Bolfarini, J. All. Comp., (2013), 577, 650-657.

[Aud-02] F. Audebert, F. Prima, M. Galano, M. Tomut, P. J. Warren, I. C. Stone, B. Cantor, Mat. Trans. A, (2002), 43, 8, 2017.

[Aud-96] F. Audebert, H. Sirkin, A. Garcia-Escorial, Scripta Mat., (1996), Vol. 36, No. 4, 405-410.

[Bac-73] D. J. Bacon, U. F. Kocks, R. O. Scattergood, Phil. Mag. (1973), 28, 1241.

[Bol-06] W. Bolton, *Engineering Materials Pocket Book*, Newnes, 3rd Edition, (2006).

[Bør-10] T. Børvik, O. S. Hopperstad, K. O. Pedersen, Int. J. Impact Eng., (2010), 37, 537-551.

[Bou-91] E. Bouchaud, L. Kubin and H. Octor, Metall. Trans., (1991), 22A, 1021.

[But-93] M. Z. Butt and P. Feltham, J. Mat. Sci., (1993), 28, 2553-2576.

[Cah-96] R. W. Cahn, *Physical Metallurgy*, 3rd edition, Elsevier Science Publishers B. V. (1996).

[Cah-83] R. W. Cahn, P. Haasen, *Physical Metallurgy*, Part I, North-Holland, (1983).

[Cav-06] P. Cavaliere, E. Evangelista, Compos. Sci. Tech., (2006), 66, 357–362.

[Che-03] S. Cheng, J. A. Spencer, W. W. Milligan, Acta Mat., (2003), 51, 4505.

[Che-09] Y. Chen, A. H. Clausen, O. S. Hopperstad, M. Langseth, Int. J. Sol. and Struc., (2009), 46, 3825–3835.

[Cho-50a] H. Chossat, Rev. Metall., (1950), 47, 167.

[Cho-50b] H. Chossat, Rev. Metall., (1950), 47, 343.

[Cly-95] T. W. Clyne, P. J. Withers, *An introduction to metal matrix composites*, Cambridge University Press, (1995).

[Con-03] H. Conrad, Mat. Sci. Eng., (2003), A341, 216.

[Con-63] H. Conrad, Acta Metall., (1963), 11, 75.

[Cot-53] A. H. Cottrell, *Dislocations and plastic flow in crystals*, 1st edition, Oxford Clarendon Press (1952).

[Das-91] S. K. Das, R. L. Bye and P. S. Gilman, Mat. Sci. Eng., (1991), A 134, 1103, 106.

[Dav-93] J. R. Davis, *Aluminium and Aluminium Alloys*, ASM International Handbook Committee (1993).

[Die-88] G. E. Dieter, *Mechanical Metallurgy*, McGraw-Hill, 2nd Edition, (1988).

[Dja-00] L. Djapic Oosterkamp, A. Ivankovic, G. Venizelos, Mat. Sci. Eng., (2000), A278, 225–235.

[Dub-86] B. Dubois, J.M. Lang, M. Tanaka, P. Sainfort, M. Audier, Nature, (1986), 324, 48-50.

[Dun-14] D.J. Dunstan and A. J. Bushby, Int. J. Plast., (2014), 53, 56-65.

[Dzi-96] A. Dziadon, Scripta Mat., (1996), 34, 3, 375-380.

[ElM-06] E. El-Magd, M. Abouridouane, Int. J. Impact Eng., (2006), 32, 741–758.

[Esh-51] J. D. Eshelby, F. C. Frank, F. R. N. Nabarro, Phil. Mag., (1951), 42, 351.

[Fle-63] R. L. Fleischer, Acta Met., (1963), 11, 203-209.

[For-67] A. J. E. Foreman, M. J. Makin, Can. J. Phys., (1967), 45, 511.

[Fri-64] J. Friedel, *Dislocations*, p 379, Pergamon, Oxford, (1964).

[Fro-94] F. H. Froes, Mat. Sci. Eng. (1994), A184, 119.

[Fuj-77] H. Fujita, T. Tabata, Acta Met., (1977), 25, 793-800.

[Gal-09a] M. Galano, F. Audebert, I. C. Stone, B. Cantor, Acta Mat., (2009), 57, 5107–5119.

[Gal-09b] M. Galano, F. Audebert, I. C. Stone, B. Cantor, Acta Mat., (2009), 57, 5120–5130.

[Gal-04] M. Galano, F. Audebert, B. Cantor, I. C. Stone, Mat. Sci. Eng. (2004), A 375-377, 1206-1211.

[Gan-11] C. L. Gan, Y. D. Xue, M. J. Wang, Mat. Sci. Eng., (2011), A 528, 4199.

[Gan-04] G. Ganesan, K. Raghukandan, R. Kartikeyan, B.C. Pai, Mat. Sci. Eng. (2004) A 369, 230–235.

[Gil-81] J. Gil Sevillano, P. Van Houtte and E. Aernould, Prog. Mat. Sci., (1981), 25, 69–412.

[Gu-09] W. H. Gu, Masters thesis, Department of Materials, University of Oxford, (2009).

[Hal-51] E. O. Hall, Proc. Phys. Soc., London, Sect B, (1951), 64, 747.

[Han-75] K. Hanson and J. W. Morris Jr., J. Appl. Phys., (1975), 46, 3, 983-990.

[Hay-04] R. W. Hayes, D. Witkin, F. Zhou, E. J. Lavernia, Acta Mater, (2004), 52, 4259.

[Hir-69] P. B. Hirsch, F. J. Humphreys, editor A. S. Argon, *The physics of strength and plasticity*, Cambridge (MA), MIT Press, (1969).

[Hon-77] R. W. K. Honeycombe, *The Plastic Deformation of Metals*, Edward Arnold Publishers, (1977).

[Hos-11] W. F. Hosford, R. M. Caddell, *Metal Forming: Mechanics and Metallurgy*, Cambridge University Press, (2011).

[Ino-01] A. Inoue, Mat. Sci. Eng., (2001), A 304-306, 1.

[Ino-00] A. Inoue, H. Kimura; Mat. Sci. Eng., (2000), A286, 1-10.

[Ino-99] A. Inoue, H. Kimura, NanoStructured Mat., (1999), 11, 2, 221–231.

[Ino-98] A. Inoue, Prog. Mat. Sci., (1998), 43, 365-520.

[Ino-87] A. Inoue, H. Kimura, T, Masumoto, Formation Mater. Sci., (1987), 22, 1758.

[Ino-86] A. Inoue, L. Arnberg,, B. Lehtinen, M. Oguchi, T, Masumoto, Metall. Trans., (1986), 17A, 1657.

[Ish-85] T. Ishimasa, H. U. Nissen and Y. Fukano, Phys. Rev. Lett., (1985), 55-511.

[Jos-06] S. P. Joshi, K. T. Ramesh, B. Q. Han, E. J. Lavernia, Met. Trans A, (2006), 37A, 2397-2404.

[Kat-04] L. Katgerman, F. Dom, Mat. Sci. Eng., (2004), A375-377, 1-2, 1212.

[Kaw-97] Y. Kawamura, H. B. Liu, A. Inoue, T. Masumoto, Scripta Mat., (1997), 37, 2, 205.

[Kaw-93] Y. Kawamura, A. Inoue, T. Masumoto, Scripta Metall. et Mat., (1993), 29, 1, 25.

[Kim-00] H. M. Kimura , K. Sasamori, A. Inoue, Mat. Sci. Eng., (2000), 294–296, 168–172.

[Kin-81] J. E. King, C. P. You, J. F. Knott, Acta Metall., (1981), 29, 1553.

[Koc-81] F. Kocks, A. S. Argon, and M. F. Ashby: Prog. in Mat. Sci., (1975), 19, 1.

[Koc-67] U. F. Kocks, Can. J. Phys., (1967), 45, 737.

[Lab-70] R. Labusch, Phys. Status Solidi, (1970), 41, 650.

[Li-03] Y. P. Li, H. J. Yu, S. C. Chai, Y. R. Li, Scripta Mat., (2003) 49, 819.

[Li-63] J. C. M. Li, Trans. AIME, (1963), 227, 239.

[Lme-14] www.lme.co.uk

[Mas-90] T. B. Massalski, H. Okamoto, P. R. Subramian, L. Kacrzak, editors. *Binary alloy phase diagrams*, (1990), Materials Park (OH): ASM International.

[Mas-86] T. Masumoto and A. Inoue, Bull. Jpn. Inst. Metals., (1986) 25, 99.

[McQ-99] H. J. McQueen, E. V. Konopleva, M. Sauerborn, *In Synthesis of Lightweight Metals III*, TMS, Warrendale, (1999), 121.

[Met-14] www.metalprices.com

[Mey-82] M. A. Meyers, E. Ashworth, Phil. Mag. A, (1982), 46, 737.

[Mit-94] S. Mitra, J. of Mat. Sci. Lett., (1994), 13, 1296.

[Mit-92] S. Mitra, Scripta Metall. et Mat., (1992), 27, 521.

[Moh-04] V. Mohles, Mat. Sci. Eng., (2004), A 365, 1-2, 144-150.

[Moh-01] V. Mohles, V. Phil. Mag. A, (2001), 81, 4, 971-990.

[Mor-73] T. Mori, K. Tanaka, Acta. Met., (1973), 21, 571-574.

[Mot-48] N. F. Mott and F. R. N. Nabarro, Phys. Soc., (1948), 1.

[Mur-79] L. E. Murr, S. S. Hecker, Scripta Metall., (1979), 13, 3, 167-171.

[Nab-77] F. R. N. Nabarro, Phil. Mag., (1977), 35, 613.

[Nag-05] Nagy, J., Balog, M., Iždinský, K., Simančík, F., Švec, P., Janičkovič, D., Int. J. Mat. Product Tech., (2005), 23, 1-2, 79-90.

[Nar-03] S.V.S. Narayana Murty, B. Nageswara Rao, B.P. Kashyap, Compos. Sci. Tech., (2003), 63, 119–135.

[Nii-86] M. Ninomi, T. Kobayashi, K. Ikeda, J. Mater. Sci. Lett., (1986), 5, 847.

[Oos-99] L. Djapic Oosterkamp, A. Ivankovic, G. Venizelos, Mat. Sci. Eng., (2000), A278, 225–235.

[Oro-48] E. Orowan, Symposium on internal stresses. In: *Metals and alloys*. London: Institute of Metals; (1948).

[Oro-40] E. Orowan, Proc. Phys. Soc., (1940), 52, 8.

[Ped-10] S. Pedrazzini, Masters thesis, Department of Materials, University of Oxford, (2010).

[Pic-81] J. R. Pickens, J. Mat. Sci., (1981), 16, 1437-1457.

[Pin-98] E. Pink and H. Weinhandl, Scripta Mat., (1998), 39, 9, 1309-1316.

[Pol-06] I. J. Polmear; *Light Alloys, Metallurgy of the Light Metals*, Edward Arnold; London; 4th edition (2006).

[Por-06] D. A. Porter, K. E. Easterling, Phase Transformations in Metals and Alloys, CRC Press, (2006).

[Por-23] A. Portevin and F. Le Chatelier: CR Acad. Sci., (1923), 176, 507.

[Pra-99] U. Prakash, T. Raghu, A. A. Gokhale, S. V. Kamat, J. Mat. Sci., (1999), 34, 20, 5061.

[Rag-91] N. Raghunathan, E. K. Ioannidis, T. Sheppard, J. Mat. Sci., (1991), 26, 4, 985.

[Ram-94] K. N. Ramakirishnan, Mat. Charact., (1994), 33, 119.

[Rey-06] A. Reyes, O. S. Hopperstad, O. G. Lademo, M. Langseth, Comput. Mat. Sci., (2006), 37, 246–268.

[Rob-94a] J. M. Robinson, Int. Mat. Rev., (1994), 39, 6, 217.

[Rob-94b] J. M. Robinson and M. P. Shaw, Int. Mat. Rev., (1994), 39, 3, 113.

[Rsp-14] www.rsp-technology.com

[Rus-05] A. M. Russell and K. L. Lee, *Structure-Property Relations in Nonferrous Metals*, Wiley and sons, Hoboken, N. J. (2005).

[Sas-01] D. H. Sastry, Y. V. R. K. Prasad, S. C. Deevi, Mat. Sci. Eng., (2001), A 299, 157-163.

[She-84] D. Shechtman, I. Blech, D. Gratias, and J. W. Cahn, Phys. Rev. Lett., (1984), 53, 1951-1953. http://prl.aps.org

[Shi-05] C. S. Shin, M. C. Fivel, M. Verdier, C. Robertson, Mater. Sci. Eng., (2005), A400-401, 166.

[Sis-14] www.sismetric.co.uk

[Ski-88] D. J. Skinner, V. R. V. Ramanan, M. S. Zedalis, H. J. Kim, Mat. Sci. Eng., (1988), A99, 407-411.

[Ski-89] D. J. Skinner, M. S. Zedalis, P. Gilman, Mat. Sci. Eng., (1989), A119, 81-86.

[Sla-87] J. M. Slater, S. C. Jha, T. H. Sanders, Mat. Sci. Eng., (1987), 91, 201.

[Sla-64] J. C. Slater, J. Chem. Phys., (1964), 41, 3199.

[Sri-08] V. C. Srivastava, V. Jindal, V. Uhlenwinkel, K. Bauckhage, Mat. Sci. Eng., (2008), A 477, 86–95.

[Su-04] Y. H. F. Su, Y.C. Chen, C.Y.A. Tsao, Mater. Sci. Eng., (2004), A 364, 296–304.

[Sut-96] A. P. Sutton, R. W. Balluffi, *Interfaces in Crystalline Materials*. Oxford: Oxford University Press, (1996).

[Tay-34] G. I. Taylor, Proc. Roy. Soc. A, (1934), 145, 362.

[Tod-04] I. Todd a, Z. Chlup b, J.G. O'Dwyer, M. Lieblich, A. Garcia-Escorial, Mat. Sci. Eng., (2004), A 375–377, 1235–1238.

[Tom-04] M. Tomut, F. Prima, G. Huenen, G. Vaughan, A. R. Yavari, P. Svec, I. C. Stone, B. Cantor, Mat. Sci. Eng., (2004), A 375–377, 1239–1245.

[Und-70] E. E. Underwood, *Quantitative Stereology*, p 80, Addison Wesley, (1970).

[Voj-07] D. Vojtěch, J. Verner, J. Šerák, F. Simancik, M. Balog, J. Nagy, Mat. Sci. Eng., (2007), A 458, 1-2, 15, 371.

[Wag-99] Wagenhofer, Erikson-Natishan, Armstrong, Zerilli, Scripta Mat., (1999), 41, 1177-1184.

[Wan-87] N. Wang, H. Chen, and K. H. Kuo, Phys. Rev. Lett., (1987), 59, 1010–1013.

[Wen-90] G. C. Weng, J Mech. Phys. Solids, (1990), 38, 3, 419-441.

[Wu-00] Y. L. Wu, C. G. Chao, Mat. Sci. Eng., (2000), A 208, 193-202.

[Yok-93] Y. Yokoyama, A. Inoue, and T. Masumoto, Mater. Trans. JIM. (1993), 34, 135.

[Yu-05] C. Y. Yu, P. W. Kao, C. P. Chang, Acta Mat., (2005), 53, 4019–4028.

Chapter 3: Experimental Procedure

This chapter describes the experimental methodology that was undertaken in order to produce the powders, analyse them and characterise their microstructures. It outlines the extrusion procedure utilised to consolidate the powders into bulk specimens and the microstructural characterisation performed after extrusion. It also explains which mechanical testing methods and thermal analysis techniques were employed to determine the strength and investigate the thermal evolution of the samples.

3.1 Production and Consolidation of Powders

3.1.1 Powder Atomisation

Both batches of $Al_{93}Fe_3Cr_2Ti_2$ alloy powders and pure Al powders used for the duration of this project were produced by gas atomisation by industrial collaborator Alpoco. As discussed in Chapter 2: Literature Review, a previous project analysed the atomisation conditions performed by Alpoco and their effect on the $Al_{93}Fe_3Cr_2Ti_2$ alloy powders produced [Rou-12]. Alpoco have an atomiser capable of producing up to 70 kg of powder with each run. They supplied the master alloys of aluminium, Al-80Fe (wt %), Al-20Cr (wt %) and Al-10Ti (wt %). These master alloys were melted in a crucible at the base of the atomiser, then drawn upwards through a ceramic straw to reach the atomising nozzle. Atomisation had to be performed at 1200 °C to ensure that the alloy was homogeneously molten. The liquid was then ejected through the nozzle and broken up by high pressure gas jets. The gas used was Nitrogen with 3% Oxygen, the latter of which was added to create a thin layer of oxide on the surface of the powders preventing the risk of explosion. The powders then reached the collector and were sieved to remove any flakes and particles larger than 200 µm in diameter.

Initially one batch of $Al_{93}Fe_3Cr_2Ti_2$ powder was produced, which will be referred to as batch 1. Further analysis of the powder within this batch performed by Scanning Electron Microscopy and

Energy Dispersive X-ray analysis (SEM-EDX) during a previous project [Ped-10] revealed that it was contaminated with pure Al powder.

The pure Al powder came from the standard cleaning procedure for the atomiser, which was flushed with a pure Al run before any runs with different alloys. After the contamination was found, Alpoco agreed to ensure the atomiser was not contaminated by further cleaning and performing two consecutive atomisation runs of $Al_{93}Fe_3Cr_2Ti_2$ powder, which will be referred to as batches 2 and 3. Only batches 1 and 2 were used in the current project.

The nominal and measured chemical compositions of each batch found through wet chemical analysis are shown in Table 3.1. Alpoco also provided the commercially pure Al powder used to make the composites and sieved it to <63 µm diameter.

at%	*Nominal Chemical Composition*	*Batch 1*	*Batch 2*
Al	*93.00*	*93.15*	*93.00*
Fe	*3.00*	*2.88*	*2.90*
Cr	*2.00*	*1.89*	*1.93*
Ti	*2.00*	*1.92*	*1.98*

Table 3.1: nominal and measured chemical composition of the Al-Fe-Cr-Ti powder batches used during the present study analysed by Alpoco through wet chemical analysis.

3.1.2 Sieving

The powders were sieved using a stack of four Retsch 200mm diameter sieves, of gauge sizes <25 µm, 25-50 µm, 50-75 µm and 75-100 µm. The sieves were placed onto a Retsch A200 automatic shaker, as shown in Figure 3.1. Approximately a tablespoon of powder (~20 g) was placed into the sieves, which were sealed with a lid and shaken automatically for 7 minutes. Each fraction of powder was collected in a jar and the sieves were cleaned. Only the <25 µm diameter $Al_{93}Fe_3Cr_2Ti_2$ and pure Al powder was used for further experiments during this project.



Figure 3.1: Retsch sieves placed onto the Retsch A200 automatic shaker.

3.1.3 Mixing

All the composites were produced by adding the required volume fractions of pure Al powder to the $Al_{93}Fe_3Cr_2Ti_2$ powder and placing them in glass jars. The jars were left half empty to ensure movement of the powders during mixing. They were then placed in a Turbula T2F mixer for 2 hours, as shown in Figure 3.2.



Figure 3.2: Turbula T3F automatic mixer.

3.1.4 Extrusion

The mixed powders were placed into Al cans sealed with an Al lid at each end. A hole was drilled in the front lid of every can to let air out during extrusion.

All the extrusions were performed by Dr M. Lieblich at the Centro Nacional de Investigationes Metalúrgicas (CENIM) in Madrid using the custom made extruder seen in Figure 3.3 available thanks to a collaboration with Prof. A. Garcia-Escorial. Extrusions were performed between 383 °C and 420 °C with an extrusion ratio of 14:1 and ram speed of 0.3 mm/s. The filled cans were preheated in the extruder container for 15 minutes while the die was being preheated in a separate furnace, then the die was inserted in the extruder and the can in the die.

The extrusion conditions were chosen following the work performed by Todd *et al.* [Tod-04] and Rounthwaite [Rou-12], who performed extrusions at CENIM using $Al_{93}Fe_3Cr_2Ti_2$ powders of various sizes. Todd *et al.* concluded that the <25 μm powder could be fully compacted at 400 °C and an extrusion ratio 7:1 or 10:1, and that the higher the extrusion ratio, the higher the temperature required for full consolidation of the alloy powder. Attempts at extruding the pure alloy powder were performed at ratio 14:1 successfully during the present project by increasing the temperature up to 420 °C. Rounthwaite performed some extrusions with the pure alloy and also made composites with the addition of pure Al powder, and he concluded that the pure Al lowered the extrusion pressure and therefore also the temperature required [Rou-12].

Once the ram made contact with the can, the powders were consolidated against the die first and then extruded. Some of the extrusions of the pure $Al_{93}Fe_3Cr_2Ti_2$ powders failed due to the extrusion press reaching its maximum safety limit, so some of the powders were just compacted into billets. The composites could all be extruded due to the additions of pure Al, which lowered the strength required for extrusion.



Figure 3.3: Extrusion Press, CENIM, Madrid. Photo courtesy of Nicholas Rounthwaite.

3.2 Characterisation of Powders and Bulk Specimens

3.2.1 Inductively Coupled Plasma - Optical Emission Spectrometry (ICP-OES)

ICP-OES analysis of the $Al_{93}Fe_3Cr_2Ti_2$ powders from batches 1 and 2 and of the pure Al powder was performed by industrial collaborator Alpoco after atomization in order to determine the elemental composition of the powders accurately.

This analysis will count the pure Al contamination as part of the composition of the $Al_{93}Fe_3Cr_2Ti_2$ alloy powder from batch 1.

3.2.2 X-Ray Diffraction (XRD)

XRD was performed in order to identify the phases present in the alloys produced. A Philips 1810 θ-2θ diffractometer was used for most of the scans, also an X'Pert θ-2θ diffractometer was used in the Department of Physics, University of Oxford and another Philips θ-2θ diffractometer available in Begbroke Science Park. The scanning angles 2θ used were 20-100 °, voltage of 35 kV, current of 50 mA and step size 0.02 °. A combination of data sheets [JCP-99] and published papers [Gal-09a], [Aud-99] was used for indexation of the peaks.

All the powders analysed were attached to a glass slide using Dow Corning High Vacuum Grease, as it only produced one low-angle broad peak at 10-13 ° and no further peaks in the scans at higher angles.

A longitudinal section and a cross section of all the extruded bars was cut and ground using 4000 grit SiC paper. For each bar a powdered sample was produced by grinding it and the powder was put onto a glass slide using vacuum grease. This was done to provide a qualitative assessment of texture by comparing a specimen cut along the extrusion direction to one cut perpendicular to it and an un-textured powder. A specimen of powder can be seen in Figure 3.4.

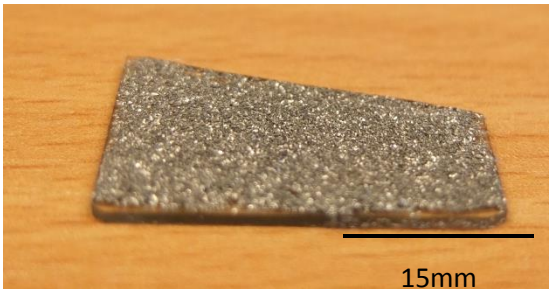

Figure 3.4: powder specimen attached to a glass slide using vacuum grease.

3.2.3 Scanning Electron Microscopy (SEM) and Energy Dispersive X-Ray Analysis (EDX)

SEM analysis of the powders and extruded bars was performed using W-filament SEMs (JEOL 6300 and JEOL 840A).

The powders were analysed first, in two different ways. The powder shape and size was assessed by putting them onto a carbon double sided sticker attached to a 12.5 mm SEM Al stub. Micrographs of the powders have been taken using Secondary Electron Imaging (SEI) mode, with a working distance of ~30 mm to get better depth of field for topographic images. The powder microstructure and the pure Al contamination were assessed by mounting powder in Bakelite using a Kemet Metapress-A mounting press, grinding it up to 4000 grit SiC paper and polishing it with 3-1 µm diamond solutions and a 0.04 µm colloidal silica solution with 10 vol% hydrogen peroxide (H_2O_2) added to prevent corrosion. Micrographs of the microstructure have been taken in

Backscattered Electron Imaging (BEI) mode for better compositional contrast, with a working distance between 8-15 mm, voltage of 30 kV and current ~$1x10^{-8}$ A.

The extruded bars were cut into cross sections and longitudinal sections using a Kemet Micracut slow saw and mounted in Bakelite, ground and polished in the same way as the powders.

EDX was also performed on the same specimens, using an Oxford instruments EDX detector attached to either the JEOL 6300 SEM or the JEOL 840A W-filament SEMs. The data was analysed using INCA software. The standard calibration of the peaks made using a Ti sample was selected for this work. The imaging conditions were the same as described previously, except the working distance had to be 15-20 mm in order to optimise the signal on the EDX detector.

3.2.4 Transmission Electron Microscopy (TEM) and EDX

TEM analysis was performed using a Philips CM20 and a JEOL 2000FX W-filament TEMs. In order to obtain accurate values from the EDX analysis a double tilt Beryllium holder was used.

Specimens from each of the extruded bars were prepared by cutting them with a Kemet Micracut slow saw and grinding them on SiC paper down to 3 mm disks. The disks were then ground down to ~100 µm thickness using SiC paper, then single-sided dimpled and polished on both sides using a Gatan Dimpler up to ¼ µm diamond paste until the specimens were approximately 20 µm thick in the centre. The specimens were finished by ion milling in a Gatan Precision Ion Polishing System (PIPS) from the top and the bottom at an angle varying between 2-4 ° using Argon ions.

Powder specimens were prepared by liftout using a Focused Ion Beam microscope (FEI FIB 200 and Zeiss NVision FIB). The powder specimens were mounted in Bakelite and polished with different grades of SiC paper, diamond polish and finally 0.04 µm colloidal silica. The FIB was used to then dig trenches and lift the specimens using a micromanipulator onto Cu half grids. The specimens were then thinned using very low currents to minimise Ga contamination. The final thickness of the specimens was measured in the FIB to be ~80 nm.

Diffraction patterns were obtained, however very often the particles present in the microstructure were too small to use the smallest selected area aperture. Therefore, convergent beam diffraction had to be performed using the smallest spot sizes, which, when converged, allowed diffraction patterns to be taken from microstructural features as small as ~40 nm. The aim was to produce micrographs of the microstructures, diffraction patterns and EDX scans in order to correctly identify the phases present and know their composition. The EDX scans were performed using an Oxford Instruments EDX detector with Inca software.

The standard calibration of the peaks made using a Ti sample was selected for this work. The beam was converged onto the particles using the smallest spot size, which would allow the counts to come exclusively from the particle and the matrix above and below it. To minimise errors, particles were only sampled using the EDX system from the thinnest areas of the sample, close to the hole and they were always tilted first to ensure no overlap of particles was visible. The part of the sample which is electron transparent needs to be ~100 nm or less in thickness, therefore errors were also minimised by selecting larger particles for EDX analysis. Small variations in the thickness of the samples are expected to influence the EDX results despite efforts to minimise them. The EDX of the lift-out samples is expected to be more accurate due to the even thickness of the samples.

3.2.5 Electron Backscatter Diffraction (EBSD)

EBSD was performed to assess grain size, shape and orientations initially in JEOL 6300 and JEOL 840A W-filament microscopes then in a JEOL 6500 FEG SEM.

Surface finish is extremely important for EBSD analysis. Plastic deformation during processing needs to be minimised and the surface produced needs to be extremely flat and parallel to the holder to maximise accuracy and resolution. Specimens were prepared by cutting longitudinal sections of the bars using a Kemet Isomet 200 slow saw and attaching them to 12.5 mm Al stubs with silver conductive paint. They were polished with various grades of SiC paper, diamond polish

and finally 0.04 μm colloidal silica. Each specimen had to be polished for at least 30 minutes on the smallest grade of diamond (1/4 μm), then 10 minutes on colloidal silica with 10 vol% H_2O_2 before a good enough surface finish was achieved. The samples were then cleaned using an ultrasonic bath for 5-10 minutes to remove any colloidal silica or diamond which might still be on the surface and dried using an air duster.

In the W-filament SEMs a working distance of 15 mm was used, which was the optimal working distance for EBSD in that set up, with a spot size $6x10^{-9}$ A and initially a voltage of 30 kV. The camera was calibrated using 4x4 binning, gain usually ~-8.20 and exposure time ~0.14. The binned pattern size, peak symmetry and rho function were calibrated in different scans to maximise confidence during indexing. Usually a binned pattern size of 120, a peak symmetry of -0.55 and a rho function of 83% were used. This lead to the discovery of several issues with pattern quality, indexability and therefore the achievable level of resolution within the specimens. In addition to that, some problems with thermal drift of the specimens, charging of the top oxide layer and contamination due to the scanning electron beam were encountered. It was also established that the grain size of the samples was approaching the limits of the resolution achievable by EBSD in a W-filament SEM.

In an effort to improve spatial and lateral resolution, scan attempts were made by reducing the voltage and spot size to 20kV and $1x10^{-10}$ A respectively, which lead to an increased exposure time. It was also established that several short scans of under 20 minutes each performed on the same specimen next to each other would minimise issues with the sinusoidal beam drift detected with the specimen as well as reduce charging of the surface and contamination, but still provide a statistically significant number of data points from which to measure grain size distributions. Most of the EBSD results were obtained this way, however due to the importance of the accuracy of the EBSD results for the modelling of the alloy, attempts were made to improve resolution by moving onto a FEG JEOL 6500 SEM. A working distance of 15 mm was used, the samples were tilted at 70 °, a medium probe size was selected and a voltage of 15 kV. The camera was used with 1x1 binning to maximise resolution, with longer exposures (up to 0.94) and this increased the

Confidence Index. It has been empirically established in Al alloys that the software is correctly indexing 95% of the patterns when the confidence index is 0.1 [Wri-92].

Due to the complications encountered while performing EBSD maps of the $Al_{93}Fe_3Cr_2Ti_2$ alloy, a more extensive literature survey on the subject was compiled. More information on how EBSD works, how patterns are formed and processed by the software, what parameters affect resolution and what the maximum achievable resolution can be are found in Appendix 1.

3.3 Room Temperature Mechanical Tests

3.3.1 Microhardness

Microhardness tests of as-extruded sections of the bars were performed using a Wilson-Wolpert Instruments microindenter and measured with MinuteMan software.

The tests were performed using a 500 g load held in place for 20 s, following the ASTM E92-82 standards which means that the average spacing between indents must be at least 2.5 x the average diagonals and specimen thickness must be greater than 1.5 x the average diagonals [AST-10]. Overall lines of at least 20 microindents were made across the samples and averages were calculated over a minimum of 20 indents. Errors were calculated using standard deviation values.

Polished SEM samples either mounted in Bakelite or attached to 12.5 mm Al stubs were used for microhardness tests.

3.3.2 Tensile Tests

The tensile tests presented in this thesis were performed at room temperature by external contractors Westmoreland during a previous project [Ped-10]. Specimens were cut and threaded using a lathe following E8 ASTM standards (specimen sub size 4) as seen in Figure 3.5 [AST-10].

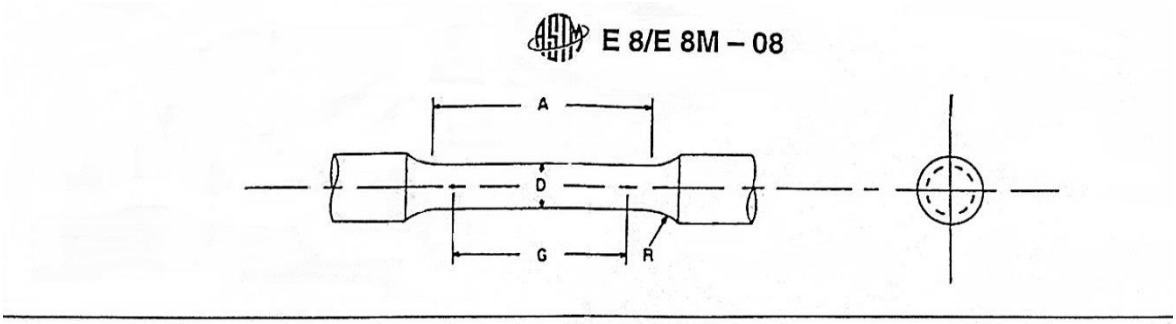

Dimensions, mm [in.]
For Test Specimens with Gage Length Four times the Diameter [E 8]

	Standard Specimen	Small-Size Specimens Proportional to Standard		
	Specimen 1	Specimen 2	Specimen 3	Specimen 4
G—Gage length	50.0 ± 0.1 [2.000 ± 0.005]	36.0 ± 0.1 [1.400 ± 0.005]	25.0 ± 0.1 [1.000 ± 0.005]	16.0 ± 0.1 [0.640 ± 0.005]
D—Diameter (Note 1)	12.5 ± 0.2 [0.500 ± 0.010]	9.0 ±0.1 [0.350 ± 0.007]	6.0 ± 0.1 [0.250 ± 0.005]	4.0 ± 0.1 [0.160 ± 0.003]
R—Radius of fillet, min	10 [0.375]	8 [0.25]	6 [0.188]	4 [0.156]
A—Length of reduced section, min (Note 2)	56 [2.25]	45 [1.75]	30 [1.25]	20 [0.75]

Figure 3.5: ASTM standard by which the tensile test specimens were made (Specimen 4) [AST-10].

3.3.3 High Strain Rate Tensile and Compressive Tests

High strain-rate tensile samples were turned and threaded on a lathe and polished using 4000 grit SiC paper to ensure a smooth surface. The tests were performed by Dr Robert Gerlach in tension and Dr Petros Siegkas in compression. They were performed using Split Hopkinson Bar equipment made available courtesy of Dr Vito Tagarielli in the Solid Mechanics Group (Department of Engineering, University of Oxford). The tensile samples were turned down to a diameter of 2 mm in the central part and threaded.

The tests were performed at strain rates of 2000-2200 s^{-1} in tension and 3000 s^{-1} in compression. These strain rates were selected to ease comparisons with commercially available Al and Ti based alloys used in engineering applications found in the literature. A high speed camera was used to get pictures of the fracture every 15 μs. The pictures were then used to confirm the strain measurements and reduce the errors introduced by the difference in compliance between the sample and the testing apparatus. Strain gauges were connected to the bars on either side of the specimen and were used to measure the incoming signal, the transmitted signal and the signals which were reflected off the end of the bar. These results were then processed using a Matlab

routine written by Dr Robert Gerlach to obtain a stress-strain measurement. The strain measurement was then confirmed by correlating the measurements taken in the images with the strain gauge measurement.

3.4 Thermal Stability

Thermal ageing of the bars and powders and the potential for microstructural evolution at the extrusion temperature or during high temperature mechanical testing was investigated.

3.4.1 Differential Scanning Calorimetry (DSC)

Atomised powders and ground powder from the extruded bars were analysed using a TA Instruments 2010 DSC calibrated by Dr Nicholas Rounthwaite and Mr Christian Bridge with the commercial high purity metals Indium, Aluminium and Tin by extrapolation.

The powders and ground bars were placed in Cu pans and, to prevent any reaction with the Cu, they were isolated using Mo sheets. About 10 mg of powder was placed in each pan before crimping to seal them. Empty pans with Mo sheets were also crimped and used as references.

Samples were heated from 50 °C to 630 °C at a heating rate of 40 °C/min. DSC runs with empty pans were also performed as references. All tests were performed in an inert Argon atmosphere. The curves obtained were then processed by subtracting a scan of an empty pan to remove the background and energy fluctuations produced by the pan during heating. The curve produced by heating the empty pan and used for subtraction can be seen in Figure 3.6.

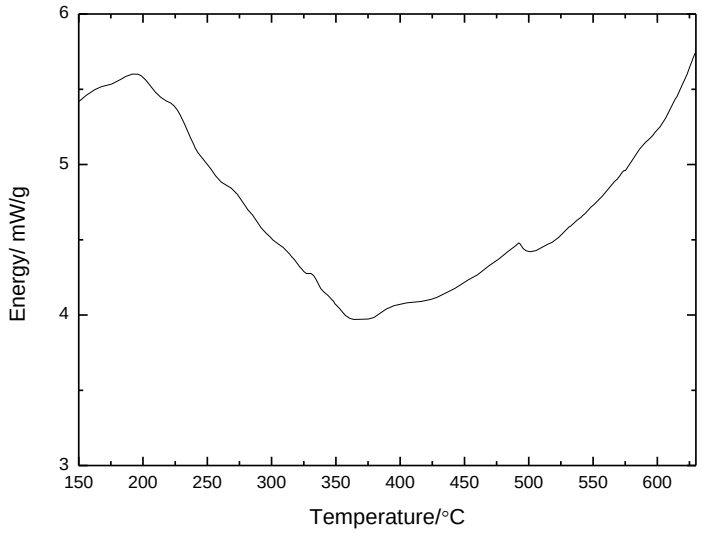

Figure 3.6: DSC scan performed at 40 °C/min of the empty container the Al samples were held in, used as reference.

3.4.2 Heat Treatments, Microstructural Characterisation and Microhardness

Isothermal heat treatments were performed in a small furnace in air and under vacuum, sealing the specimens in quartz tubes with an oxyacetylene torch. Dummy specimens made of Al 6082 with thermocouples attached were inserted in the furnace to ensure temperature accuracy at the selected testing conditions. Specimens were inserted in the furnace while it was already at the required temperature, removed after pre-established lengths of time and left to air cool. Three temperatures were chosen for the heat treatments: 250 °C, 280 °C and 550 °C. The specimens were heat treated until a difference in either the microstructure or microhardness (or both) could be identified, which would indicate a reaction taking place.

The specimens were extruded bars, cut using a Kemet Micracut slow saw into 6 x 6 mm cubes. After heat treatment they were polished to remove the oxide layer that formed before further analysis by SEM, XRD and microhardness. TEM specimens were also prepared as described in section 3.2.4.

3.5 High Temperature Mechanical Tests

3.5.1 Microhardness

Room temperature microhardness tests of heat treated sections of the bars were performed following the procedure outlined in section 3.3.1.

Samples were 6 mm x 6 mm cubes from the extruded bars. One side was ground using 4000 grit SiC paper before indentation to remove oxide layers produced during heat treatments.

3.5.2 High Strain Rate Compressive Tests

Compression tests were performed by Mr Martin Hubig using a Gleeble 3500 machine available thanks to a collaboration with Dr Ramiro Mazzina from Tenaris (TechInt Group), Buenos Aires, Argentina. The selected temperatures were 350 °C, 400 °C, 450 °C and 500 °C at strain rates 0.1, 1, 10 and 50 s^{-1}. These temperatures and strain rates were selected to analyse the feasibility of forging the alloy and composites into engineering components.

Specimens were prepared from the extruded bars on a lathe and were cylinders 15 mm in length and 10 mm in diameter. Extra care was taken in order to ensure the sides were flat and polished with 1200 grit SiC paper for even induction heating during tests. A thermocouple was welded to the centre of each specimen before it was induction heated to the selected temperature and compressed between WC discs.

References

[AST-10] Handbook of the American Society for Testing of Metals, (2010).

[Aud-99] F. Audebert, R. Colaco, R. Vilar, H. Sirkin, Scripta Mat., (1999), 40, 551.

[Gal-09a] M. Galano, F. Audebert, I.C. Stone, B. Cantor, Acta Mat., (2009), 57, 5107–5119.

[JCP-99] JCPDS-International Centre for Diffraction Data v2.02 (1999) Codes: 04-0787, 13-0146, 29-0014, 29-0042.

[Ped-10] S. Pedrazzini, Masters thesis, University of Oxford, (2010).

[Rou-12] N. J. Rounthwaite, DPhil Thesis, University of Oxford, (2012).

[Tod-04] I. Todd, Z. Chlup, J.G. O'Dwyer, M. Lieblich, A. Garcia-Escorial, Mat. Sci. Eng., (2004), A 375–377, 1235–1238.

[Wri-92] S. I. Wright and B. L. Adams, Met Trans A, (1992), 23, 3, 759-767.

Chapter 4: Production and Characterisation of Al-Fe-Cr-Ti Alloy Bars

The following chapter describes the production and microstructural characterisation of two batches of $Al_{93}Fe_3Cr_2Ti_2$ alloy powder. It also analyses the extruded bars produced from the consolidation of the powder and correlates the production with the final microstructure of the bars.

4.1 Powder Characterisation

Two batches of $Al_{93}Fe_3Cr_2Ti_2$ powders were produced by industrial collaborator Alpoco using the methods described in section 3.1.1.

Each powder batch was analysed by ICP-OES analysis to determine how close they were to the nominal chemical composition $Al_{93}Fe_3Cr_2Ti_2$, then sieved into size fractions 0-25 µm, 25-50 µm, 50-75 µm and 75-100 µm. A previous study reported that the mechanical properties showed a ~150 MPa increase in tensile strength by using the smaller size fractions (from 50-100 to 25-50 µm) [Tod-04]. Therefore, the smallest 0-25 µm fraction was selected and used to extrude bars in an attempt to improve the mechanical strength. The morphology and topography of the 0-25 µm powders were analysed by SEM. Polished cross sections of the powder were also analysed by SEM to observe their internal structure. The phases present in the powders were then analysed by XRD, TEM, EDX and Convergent Beam Diffraction.

4.1.1 Inductively Coupled Plasma – Optical Emission Spectrometry (ICP-OES)

Two batches (numbered 1 and 2) of powders with nominal chemical composition $Al_{93}Fe_3Cr_2Ti_2$ were produced for this project. Both batches were analysed to confirm their elemental composition by ICP-OES analysis by an external contractor as described in section 3.2.1. The results of this analysis are shown in Table 4.1.

At%	*Nominal*	*Al-Fe-Cr-Ti Batch 1*	*Al-Fe-Cr-Ti Batch 2*
*Al**	*93*	*93.1451*	*93.0005*
Fe	*3*	*2.8833*	*2.897*
Cr	*2*	*1.8937*	*1.9344*
Ti	*2*	*1.9175*	*1.9796*
Zn	-	*0.0057*	*0.021*
Pb	-	*0.0014*	*0.001*
Co	-	*0.0058*	*0.006*
Ni	-	*0.0103*	*0.012*
Si	-	*0.1135*	*0.114*
Mg	-	*0.0071*	*0.017*
Mn	-	*0.0094*	*0.01*
Cu	-	*0.0027*	*0.004*
Zr	-	*0.0013*	*0.001*
Ga	-	*0.0033*	*0.003*

*Table 4.1: composition profile of both powder batches measured by ICP-OES analysis. *The amount of Al was calculated by subtraction.*

ICP-OES analysis confirmed that the composition of the powders is close to the required nominal composition of $Al_{93}Fe_3Cr_2Ti_2$. Batch 2 had 0.15 at% less Al than batch 1. The most prevalent impurity atom in both batches is ~0.1 at% Si. The oxygen content was not measured, but it is expected to be another prevalent impurity due to the deliberate oxidation process during atomization.

Al evaporation and gravitational segregation can cause inaccuracy in chemical composition of powders during atomisation [Rou-12]. Neither was found to have a strong influence on the portions of the powders on which ICP-OES analysis was performed as both powder batches had a very

similar chemical composition to the nominal value. A previous project worked on the atomisation process of the powders used in the present work and explained the need to add pure Al to compensate for the predicted amount of evaporation as aluminium is the most volatile of the elements present in the alloy [Rou-12]. In this case, Alpoco added pure Al to compensate for evaporation and produced alloys which are within <0.2 at% of the nominal chemical composition.

4.1.2 SEM Analysis of the Morphology and Topography of the Powders

0-25 µm was the smallest sieve available therefore the powders collected underneath this sieve contained a variety of sizes between <1 µm and 25 µm. The powder morphology and topography of this size fraction was analysed by SEM.

The shape of the powder particles was not uniform and spheroidal, but more elongated and nodular. This can be seen in the secondary electron micrographs of the powder from batch 1 in Figure 4.1 (a) batch 2 in Figure 4.1 (b). Some of the smallest particles were welded to larger ones, these are called satellite particles and have been indicated in Figure 4.1 (c) and (d) for batch 1 and 2 respectively. Extremely small powder particles, which were more spheroidal in shape were seen in both powder batches. Spheroidal particles have a reduced surface area and therefore a smaller amount of oxide around them.

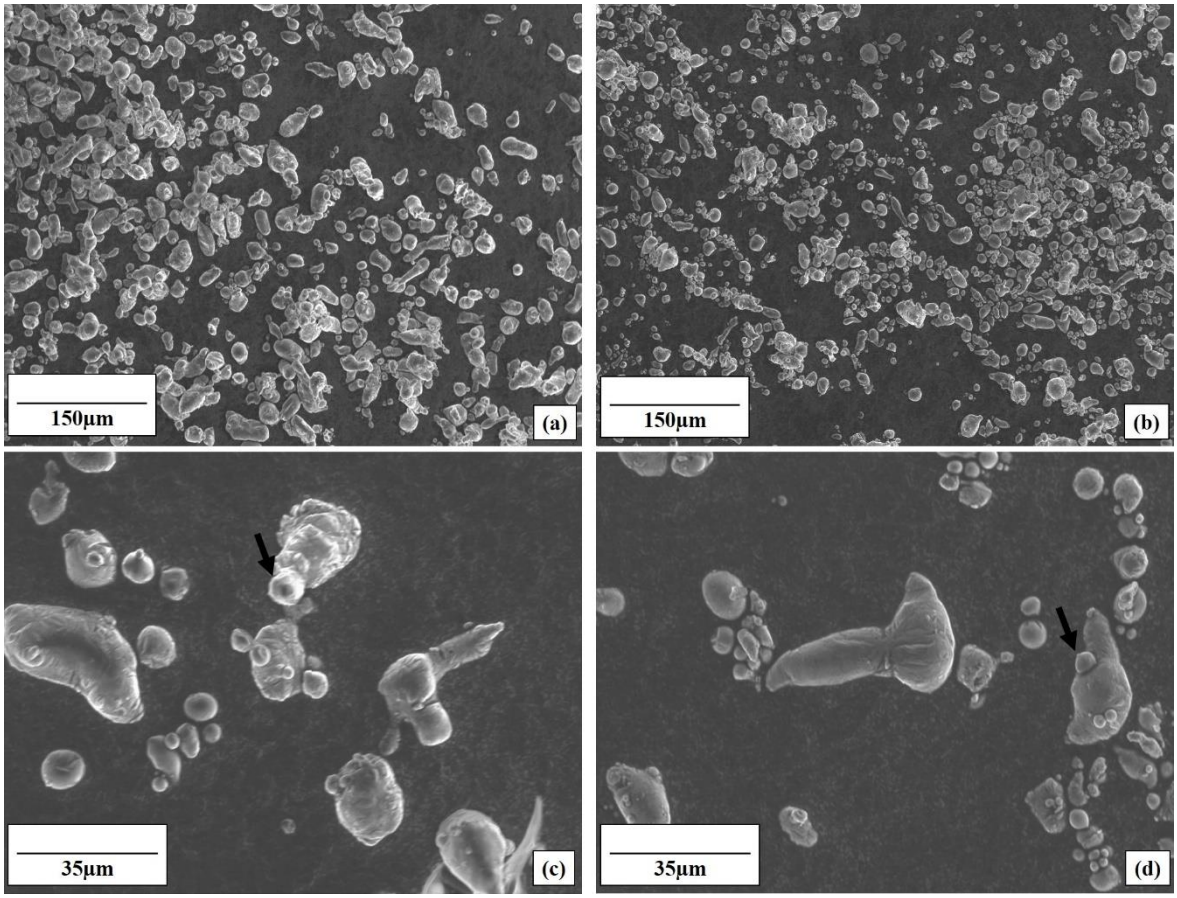

Figure 4.1: Secondary electron images (a) Batch 1 powder <25 µm in diameter, (b) Batch 2 powder <25 µm in diameter, (c) satellite particles welded to a larger particle in the powder from batch 1 and (d) satellite particles welded to a larger particle in the powder from batch 2.

Both batches of powder analysed were found to have irregular, elongated and nodular powder shapes as seen in Figure 4.1 (a) and (b) and therefore it is expected that the surface area and oxide layer would be larger and friction between the powders during extrusion would be higher than if their shape was spherical [Smi-83].

Non-spherical powder particles can be associated with premature freezing. This occurs when the temperature of the liquid droplets is not high enough, and they do not have the time for their own surface tension to make the shape spherical before solidification [Nic-68], [Zhe-09], [Zho-91]. Also the oxygen content in the Alpoco atomiser (3 vol% O_2 was added deliberately to oxidise the surface and prevent explosion) can oxidise the surface of the molten droplets stopping the surface tension from making the particles spherical [Boh-86], [Özb-00]. In some cases overheating the molten alloy has also been shown to produce irregular particle shapes [Sin-06].

The presence of satellite particles is generally associated with turbulence during atomisation [Gra-77], [Özb-99], which causes smaller particles to weld onto larger ones. The probability of this interaction was found to increase with larger amounts of finer particles but also when the shape of the coarser particles is irregular and the surface texture is rough.

A study performed by Rounthwaite [Rou-12] comparing six $Al_{93}Fe_3Cr_2Nb_2$ powder batches and one $Al_{93}Fe_3Cr_2Ti_2$ powder batch (batch 1, used in the present work) processed under different atomisation conditions and in two different atomisers, has shown that a more even, spherical powder shape could be achieved with a reduced temperature (from 1550 °C to 1350 °C) and a reduced oxygen content (from 3 vol% to 0.1 vol%).

4.1.3 SEM Analysis of the Microstructure of the Powders

The regularity and scale of the internal microstructure of the cross sectioned powders was analysed. Representative backscattered electron micrographs showing the internal microstructure of the powder particles in the <25 µm diameter size fraction are shown in Figure 4.2.

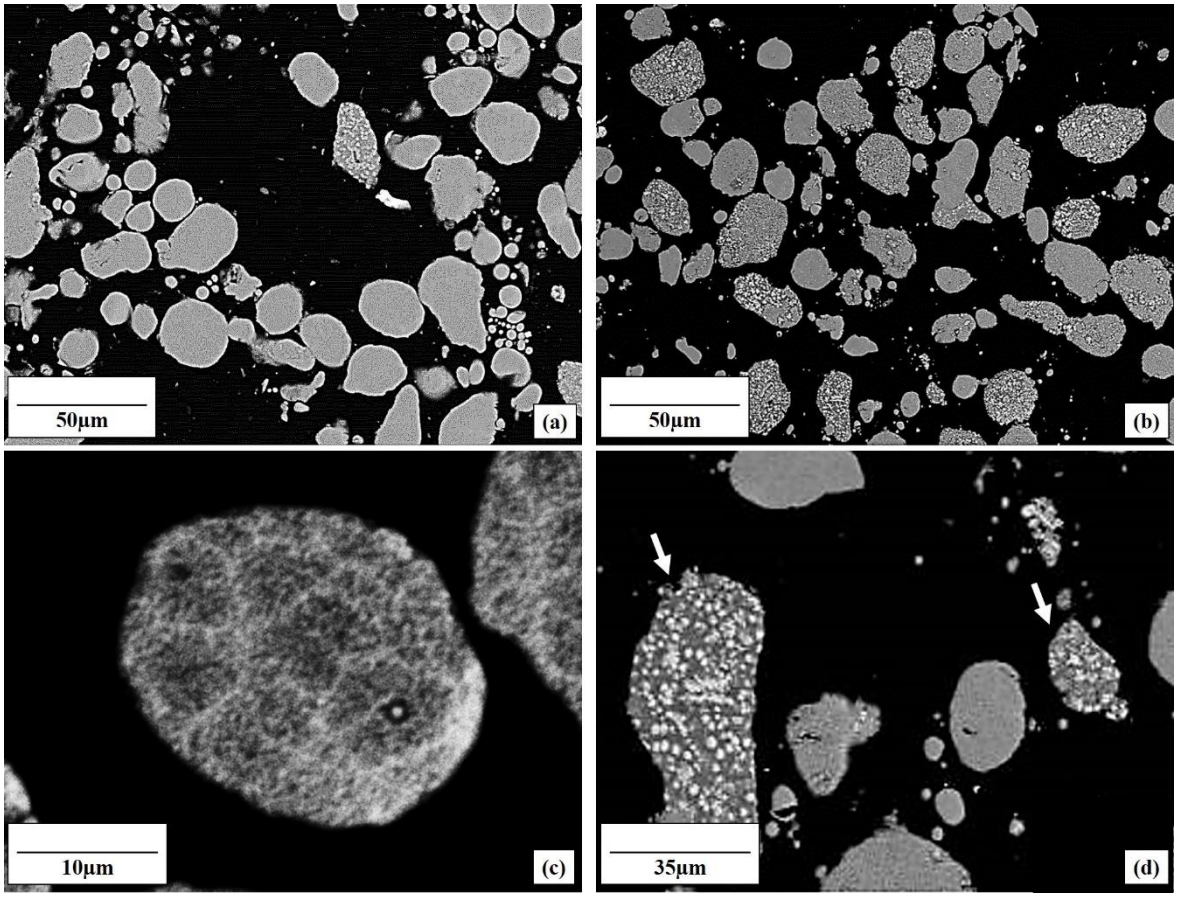

Figure 4.2: (a) overview of the microstructure of the powder from batch 1, (b) overview of the microstructure of the powder from batch 2, (c) microstructure of one ~25 µm diameter particle from batch 1, (d) close-up microstructure of a few particles including some which contain a coarser microstructure, from batch 2.

The microstructure of both powder batches shown in the micrographs in Figure 4.2 (a) and (b) consisted mostly of intermetallic phases, all of which smaller than ~500 nm in diameter, within an Al matrix. The intermetallic size and shape was found to be generally consistent within each single powder particle, this can be seen in Figure 4.2 (a) and (b), but vary depending on the particle size. A coarser internal microstructure was found in larger particle sizes, while smaller particles were found to have a very fine microstructure. This observation was consistent within both powder batches.

Some of the largest particles with more irregular shapes have been found to have a coarser internal microstructure sometimes also containing more dendritic shaped intermetallic particles, like the ones seen in the large elongated particle highlighted by an arrow in Figure 4.2 (d). A similar

observation was made by Bartova *et al.* [Bar-05] on an $AlCr_6Fe_2Ti_{(0-1.5)}Si_1$ alloy powder, by Todd *et al.* in $Al_{93}Fe_3Cr_2Ti_2$ [Tod-04] and by Rounthwaite in $Al_{93}Fe_3Cr_2Ti_2$ and $Al_{93}Fe_3Cr_2Nb_2$ alloy powders [Rou-12]. The powder particles with a coarser microstructure constitute only a small fraction of the overall powder. The majority of particles exhibit a finer, more even microstructure of spherical intermetallic phases. Bartova [Bar-05], Todd [Tod-04] and Rounthwaite [Rou-12] all reported that the 0-25 μm powder fraction contains a much smaller fraction of particles with this type of coarser internal microstructure, but as the powder size increases that fraction increases as well.

The powder particle size does not only affect the morphology of the intermetallic phases found, it will also affect their size and the spacing between them. The difference in microstructure due to different powder size is expected to be due to the higher undercooling in smaller particle sizes which encourages more nucleation to take place and does not allow intermetallics to grow to larger sizes before they are fully solidified [Por-92]. Also, the smaller powder particles will contain proportionally the same amount of alloying elements as the larger powder particles (since the nominal chemical composition is the same) but due to their smaller size the total amount of alloying elements the contain will be smaller therefore the phases produced with these elements will be smaller [Bar-05], [Rou-12].

Evidence of pure Al contamination was initially found in batch 1. Figure 4.3 (a) shows a backscattered electron micrograph of the powder with the contamination particles highlighted by arrows. The contamination is expected to be a result of the standard industrial practice to clean the atomiser by performing a pure Al run between runs of other alloys. Therefore the contamination was found in this alloy because it was produced on a small scale, one atomisation run at a time. If this alloy was to be used commercially in the future then doing multiple consecutive runs would become the standard practice minimising the risk of contamination. Once this contamination was found, industrial collaborator Alpoco agreed to produce two batches from consecutive runs and improve cleanliness of the atomiser in between. The powders from these batches, hereby called

batch 2 and 3, can be seen in Figures 4.3 (b) and (c). Evidently, better cleanliness of the atomiser was enough to ensure a significant reduction in contamination because none of it was detected in batch 2 in Figure 4.3 (b). No contamination was detected in batch 3 in Figure 4.3 (c); however batch 3 was not used in the current project.

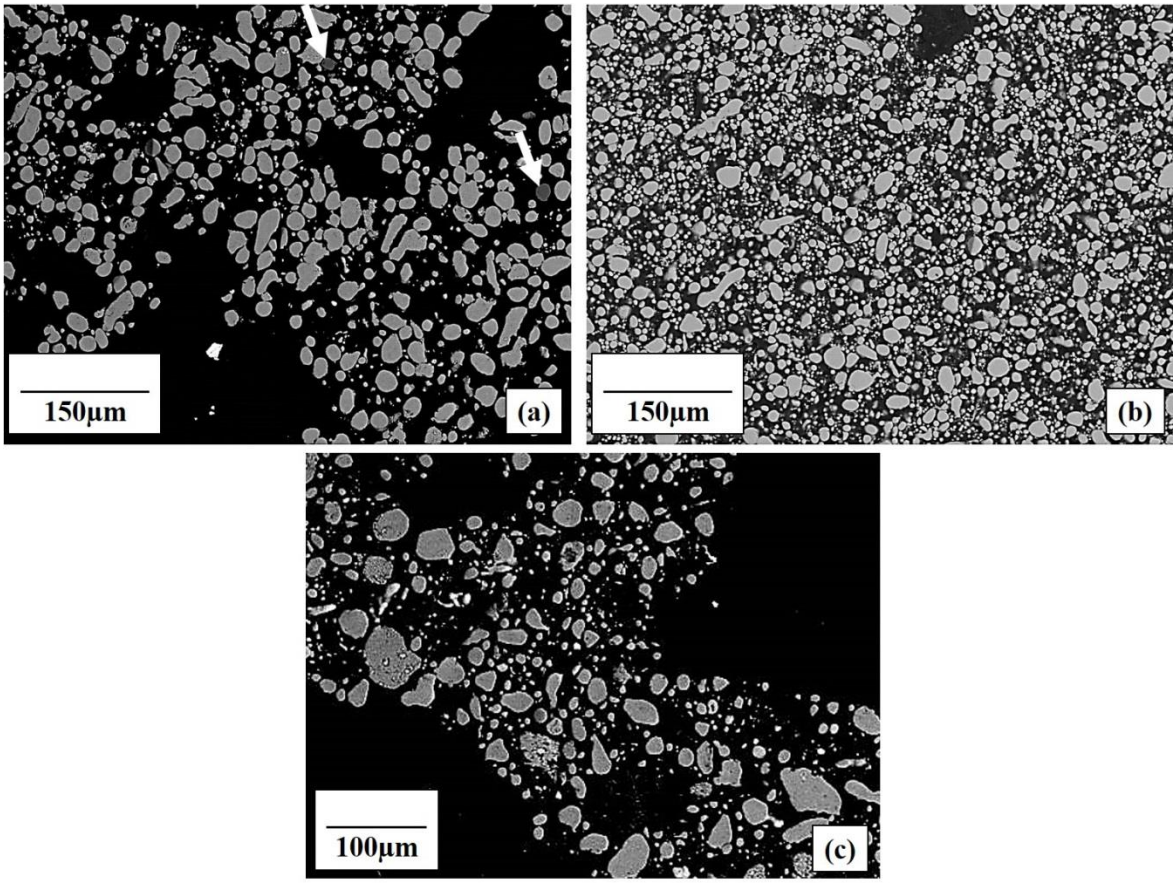

Figure 4.3: SEM BE micrographs showing polished cross sections of the powders form (a) batch 1, with the impurity is shown in a darker grey colour, as highlighted by the arrows, (b) batch 2 and (c) batch 3.

4.1.4 XRD

X-ray diffractograms were produced for both powder batches and are displayed in Figure 4.4 (a), with an enlargement of the central section of the scan in Figure 4.4 (b) to ease phase identification. All the phases present in the powders were indexed as follows. α-Al peaks were identified by indexing the reflections corresponding to the (111), (200), (220), (311), (222) and (400) planes in the 2θ = 20 °-100 ° range at 38.5 ° (100% intensity), 44.7 °, 65.2 °, 78.3 °, 82.5 ° and 99.2 ° [JCP-99]. Intermetallic phases were also identified, the most prevalent of which was the

icosahedral phase shown by peaks at 2θ ~ 22.9 °, 41.3 °, 43.5 °, 61.6 ° and 73.7 °. These were the 2θ values calculated by Galano *et al.* and Audebert *et al.* for the icosahedral phase in an alloy of the same nominal chemical composition using Cahn's indexation scheme of quasiperiodic crystals [Cah-86], [Gal-09a], [Aud-02]. Additional peaks found at 2θ ~ 36.7 °and 75.5 ° were attributed to the metastable phase labeled by other authors as distorted monoclinic θ-$Al_{13}(Cr,Fe)_{2-4}$ produced through rapid solidification. Two phases with monoclinic space group θ-$Al_{13}Fe_4$ and θ-$Al_{13}Cr_2$ were found by several authors to dissolve large amounts of Cr and Fe respectively during rapid solidification and produce by distortion twinning of the monoclinic structure a metastable phase θ-$Al_{13}(Fe,Cr)_{2-4}$ with a chemical composition which lies between the two stable compositions [Gal-09a], [Cop-02], [Aud-99], [Man-89]. The other two characteristic peaks of the θ-phase at 44.2 ° and 44.6 ° overlap with the large α-Al peak at 44.7 °. Small volume fractions of Al_3Ti intermetallic phase can also be identified through the peaks at 39.3 ° (100% intensity), 45.6 °, 66.5 ° and 80.1 ° corresponding to the (111), (200), (220) and (311) planes [JCP-99].

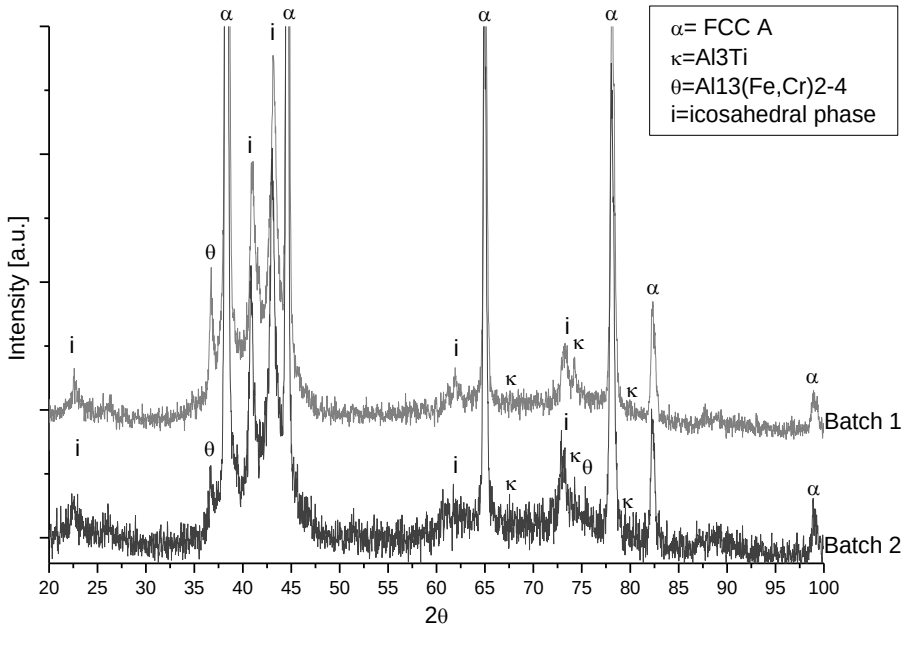

(a)

Figure 4.4: (a) XRD scan showing the phases present in the <25 µm fraction of the atomised powder batches produced.

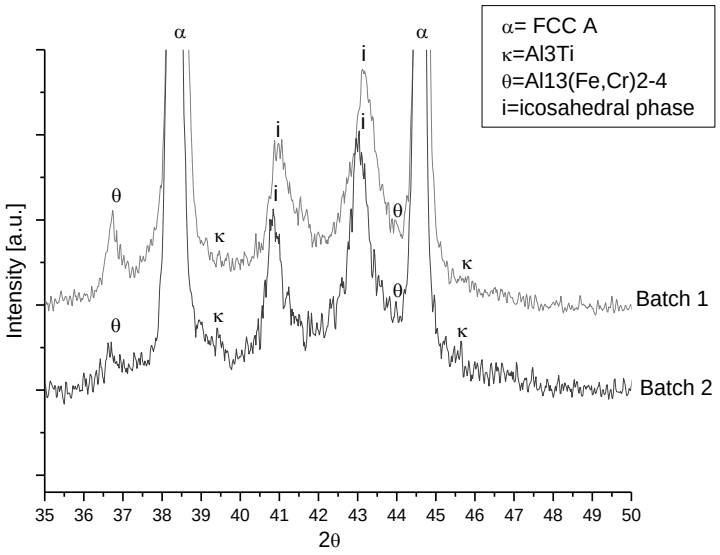

(b)

Figure 4.4 (cont): (b) enlargement of the 35-50 ° section for easier phase identification.

Previous XRD studies on gas atomised quasicrystalline Al-Fe-Cr-Ti alloy all reported a microstructure composed mainly of an FCC α-Al matrix and icosahedral phase, but varied in the amounts and types of other intermetallic phases found. Todd *et al.* reported the presence of tetragonal $Al_{23}Ti_9$ [Tod-04] which is a metastable phase also seen in the work of Inoue and Kimura [Ino-99]. Garcia Escorial *et al.* [Gar-07] and Yamasaki *et al.* [Yam-07] also showed Al-Ti intermetallics in their diffractograms, however this time it was the very similar but stable chemical composition of tetragonal Al_3Ti intermetallics, also observed in the current work.

Metastable distorted $Al_{13}(Fe\text{-}Cr)_{2\text{-}4}$ also known as θ-phase was found in $Al_{93}Fe_3Cr_2Ti_2$ alloy produced at a higher cooling rate by melt spinning by Galano *et al.* [Gal-04], as well as Al_3Ti, $Al_{13}Fe_4$ and $Al_{13}Cr_2$ intermetallics. Garcia Escorial *et al.* showed that the same alloy produced by spray forming (lower cooling rate) contained stable Al_3Ti, $Al_{13}Fe_4$ and $Al_{13}Cr_2$ intermetallic phases [Gar-10]. A study by Rounthwaite has also shown the same result with the added observation that as the powder size increases the amount of θ-phase decreases and the amount of Al_3Ti increases [Rou-12] due to the slower cooling rate of the larger powder size fractions.

4.1.5 TEM Analysis of the Microstructure of the Powders

Powder particles of ~15-20 μm in diameter were selected and FIB lift-outs were taken from areas which were considered representative of the overall powder microstructure. Bright field TEM micrographs of these liftouts and convergent beam diffraction patterns are shown in Figure 4.5. The overall powder microstructure from batches 1 and 2 is shown in Figure 4.5 (a) and (d) respectively. Figure 4.5 (b) and (e) identify the icosahedral quasicrystalline particles with their corresponding 5-fold symmetry diffraction patterns. Figure 4.5 (c) shows a cluster of icosahedral particles which was revealed to be more than a single particle by tilting and finding a 5-fold symmetry diffraction pattern. Due to the variation in intermetallic sizes depending on the initial powder particle size, no general trends can be extrapolated from this data in terms of intermetallic sizes in the overall powder. However this work identifies the type and morphology of intermetallics found in the powder before extrusion, complementing the XRD and SEM analyses.

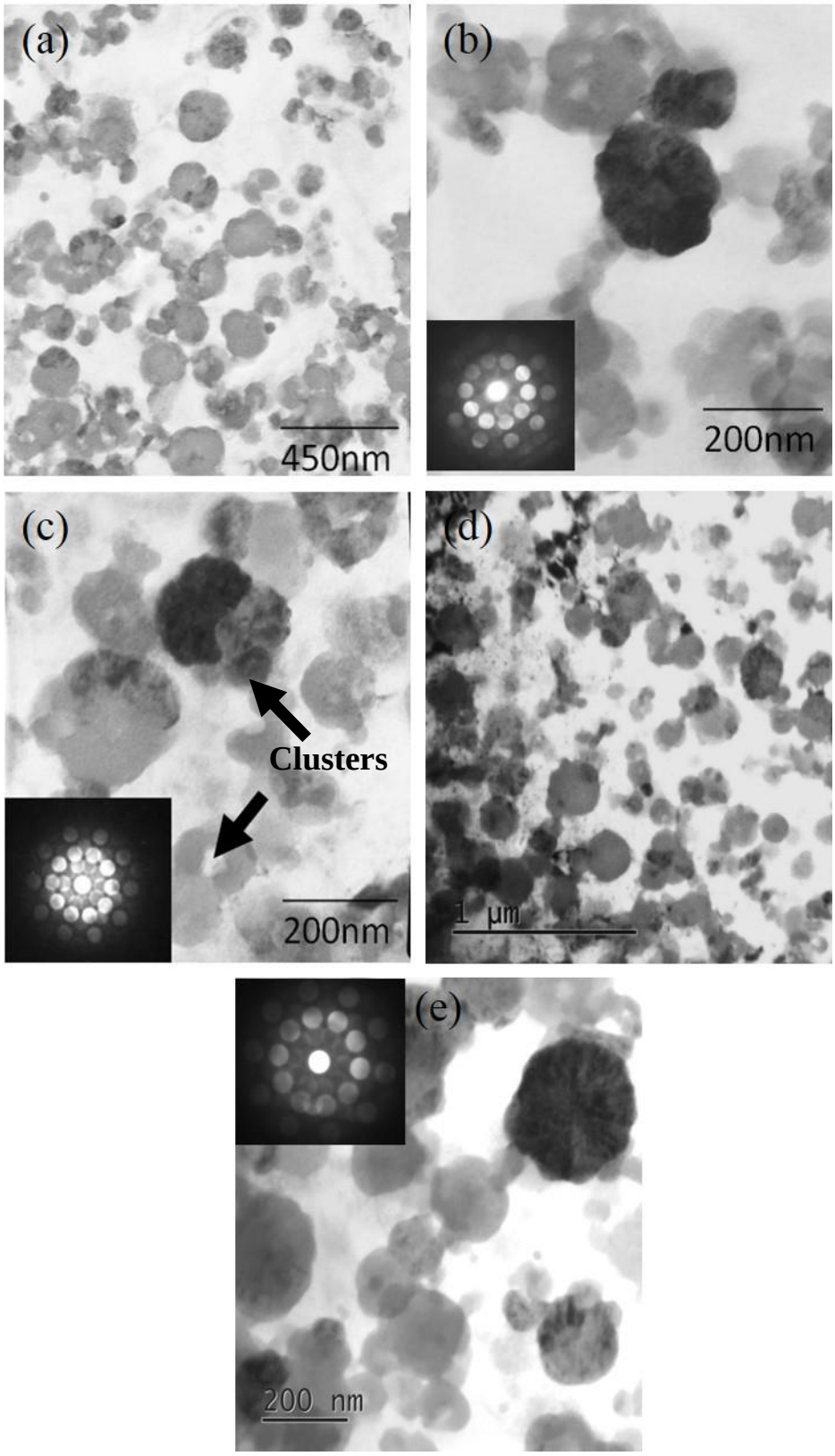

Figure 4.5: (a) Overall powder particle microstructure from batch 1, (b) 5-fold symmetry diffraction pattern characteristic of the icosahedral phase, (c) cluster of particles, proven not to be a single particle by the fact they have different orientations when tilted in batch 1, (d) overall powder particle from batch 2, (e) 5-fold symmetry diffraction pattern proving the presence of icosahedral phase in the powder from batch 2.

The TEM observations showed that the microstructure of the powder consists of spheroidal shaped particles distributed within the matrix. The TEM-EDX analysis combined with the XRD showed that the matrix was made of FCC α-Al. It was measured by EDX to contain small amounts of Fe, Cr and Ti atoms in solid solution. The chemical composition of the matrix measured by EDX can be seen in Table 4.2 (a). Errors in the TEM-EDX measurements have been minimised by tilting the samples to establish whether the areas measured by EDX consisted solely of matrix with no underlying particles.

(a)	*Average Batch 1 Matrix Composition*				*Average Batch 1 Quasicrystal Composition*			
Element	*Weight%*	*Error*	*Atomic%*	*Error*	*Weight%*	*Error*	*Atomic%*	*Error*
Al	*96.7*	*0.4*	*98.2*	*0.2*	*76.2*	*1.4*	*86.0*	*1.0*
Ti	*2.4*	*0.5*	*1.4*	*0.3*	*7.7*	*3.5*	*4.9*	*2.1*
Cr	*0.6*	*0.1*	*0.3*	*0.1*	*7.8*	*1.7*	*4.6*	*1.0*
Fe	*0.4*	*0.2*	*0.2*	*0.1*	*8.3*	*2.5*	*4.5*	*1.4*
Totals	*100.0*		*100.0*		*100.0*		*100.0*	

(b)	*Average Batch 2 Matrix Composition*				*Average Batch 2 Quasicrystal Composition*			
Element	*Weight%*	*Error*	*Atomic%*	*Error*	*Weight%*	*Error*	*Atomic%*	*Error*
Al	*96.1*	*1.3*	*97.9*	*0.7*	*76.2*	*2.5*	*86.1*	*1.7*
Ti	*1.8*	*0.3*	*1.0*	*0.2*	*5.4*	*1.1*	*3.5*	*0.7*
Cr	*0.9*	*0.4*	*0.5*	*0.2*	*8.7*	*1.2*	*5.1*	*0.7*
Fe	*1.1*	*0.5*	*0.6*	*0.3*	*9.7*	*0.4*	*5.3*	*0.2*
Totals	*100*		*100*		*100*		*100*	

Table 4.2: (a) Matrix and quasicrystal compositions in the powder particle from batch 1, (b) Matrix and quasicrystal compositions in the powder particle from batch 2, removing the C, and O impurities that come from processing and the top oxide layer, the Ga contamination from the FIB and the Cu which was measured due to the fact this specimen was welded to a Cu grid. Average and errors were calculated over 10 measurements.

The particles visible in Figure 4.5 (b), (c) and (e) were confirmed to be icosahedral phase by finding the characteristic 5-fold diffraction patterns through convergent beam diffraction. Their chemical composition was measured by EDX and the measured Al content in the icosahedral quasicrystalline phase was 86 at%, shown in Table 4.2. Very few measurements by other authors have been found on quaternary quasicrystal forming alloy compositions of the Al-Fe-Cr system, and the ones which have been found were performed solely on melt spun ribbons. In every case the quasicrystals have been found to contain all of the four elements in the alloy, but in varying proportions. Other authors have shown an Al content of 85-87 at% in the Al-Fe-Cr, Al-Fe-Cr-Nb, Al-Fe-Cr-Ta and Al-Fe-Cr-V alloy systems [Gal-09a] and 84 at% in $Al_{93}Fe_3Cr_2Ti_2$ [Kim-00] but with different amounts of transition metals. The measured amounts of ETM in the icosahedral phase measured in Table 4.2 is higher than Kimura's composition, and the matrix composition is depleted in comparison with the measurements performed on melt spun ribbons by Kimura *et al.* [Kim-00]. In the micrographs analysed, the estimated volume fraction of particles in the FCC-Al matrix was ~0.4, which is slightly lower than the 0.42 found by Audebert *et al.* [Aud-02] and the 0.45 found by Inoue *et al.* [Ino-00] on melt spun alloys of the same nominal chemical composition.

In some cases, what would have initially appeared to be a single particle was revealed by tilting to be a cluster, like the ones seen in Figure 4.5 (c). Tilting produced different diffraction patterns in different areas of the cluster confirming that it was not one single particle. This clustering effect was also observed on a melt spun alloy of the same nominal chemical composition by Galano *et al.* [Gal-09a]. Some clusters, visible in Figure 4.5 (a), (c) and (d), appeared to have a ring-shape with a different structure in the centre. Diffraction patterns could not be obtained in the centre of each cluster to verify the structure, however EDX scans of the center of the cluster shown by an arrow in Figure 4.5 (c) produced similar results to the EDX composition analysis of the matrix. The EDX composition of the centre of a cluster found in Figure 4.5 (c) can be seen in Table 4.3, while EDX composition of the matrix can be seen in Table 4.2 (a). It is therefore suggested that some of the particles form a ring shaped cluster with FCC-Al matrix in the centre.

Element	*Atomic%*
Al	*97.9*
Ti	*1.6*
Cr	*0.3*
Fe	*0.2*
Totals	*100*

Table 4.3: EDX scan in the centre of the cluster highlighted by an arrow in Figure 4.6 (c), showing a very similar elemental composition as the rest of the matrix of powder batch 1.

4.2 Powder Consolidation into Bulk Specimens

The powders from both batches 1 and 2 were consolidated into bulk specimens by extrusion as explained in section 3.1.4. Two extrusions were performed, one from batch 1 and one from batch 2. Another bar made of batch 1 powder was received from a previous project and used for comparison [Ped-10].

For ease, the bars were numbered using two numbers and a letter. The first number refers to the vol% of pure Al added (in this case zero, since these are the extruded pure alloy bars, but this numbering system will be useful once they are compared to the composite specimens described in Chapter 5), the second number is the batch of powder used. The letter has just been added to differentiate between bars of the same composition, from the same powder batch produced separately.

					Temperature							
						Sample			Stem Pressure (MPa)		Force (kN)	
#	Batch	Powder Size	Powder weight (g)	Extrusion ratio	Aim	Max	Min	At Peak	Peak	Final	Peak	Final
0-1a [Ped-10]	1	< 25 µm		14:1	375	400	357	357	1593	1252	2422	1904
0-1b			311			420	385	377	1670	1420	2539	2159
0-2	2		313			398	377/345	Failed	1777	Failed	2702	Failed

Table 4.4: Table summarising the extrusion conditions for each pure alloy bar. The 0-1a bar was produced during a previous project [Ped-10]. The 0-2 bar compacted to a billet and failed to extrude because it reached the upper pressure safety limit of the extrusion press.

Todd *et al.* analysed the processing parameters such as extrusion temperature and ratio and their effect on the microhardness and tensile strength of the bars. They found that the extrusion pressures increased with decreasing powder particle size, decreasing temperature and increasing extrusion ratio. Changing the ratio from 10:1 to 14:1 was shown to have negligible effect on the tensile strength of the bars [Tod-04].

In the present work, the smallest available powder size fraction was extruded. The microstructure of the powder from both batches consists of ~0.4 volume fraction of icosahedral phase, shown by TEM and XRD, which has been found by other authors to decompose around 500-550 °C [Tod-04], [Gal-04], [Kim-00]. It was therefore of vital importance to maintain the extrusion temperature below the observed onset of phase transformations.

The combination of low extrusion temperatures and using the smallest powder size available pushed the extrusion press to its safety limits. During the first extrusion attempts at 400 °C, both the 0-1b and 0-2 bars reached the maximum limit of 2700 kN of the extruder at CENIM, Madrid. After a second attempt at 420 °C one of the bars was extruded successfully (the 0-1b), however the extrusion pressures reached the safety limit again while processing the 0-2 and the extrusion had to be stopped. The powder was consolidated in the extrusion can to produce a compacted billet. No further attempts to extrude it were made.

Equally, the 0-1b bar was compacted to a billet during the first extrusion attempt, but was not extruded. A second attempt was made since the extrusion was stopped just under the safety limit in this case, by heating it to 420 °C. The bar was extruded on the second attempt. The surface finish was rough and the edges appeared to be peeling. This bar was used for characterisation and mechanical tests; however due to its shape extra care had to be taken while producing specimens to ensure only parts of the bar were used where the surface finish was smooth and the internal structure was fully consolidated.

The stem pressure and temperature of the billet during each extrusion were logged and Figure 4.6 shows plots of the extrusion data from the newly produced bars compared with the previously

received bar 0-1a [Ped-10]. The different stages of extrusion can be identified in the plot. Initially the powder is compacted into the can to form a billet, and this produces a shallow, steadily increasing gradient in the curve. Then the breakthrough pressure is reached and the extrusion can containing loosely compacted powder starts coming out of the die [Zho-91]. The maximum pressure is reached when the fully consolidated powder starts being extruded. After this a steady state pressure level is required in order to complete the extrusion process. The temperature was recorded with a thermocouple, which had to be removed from the die after the breakthrough pressure was reached as the bar started to emerge.

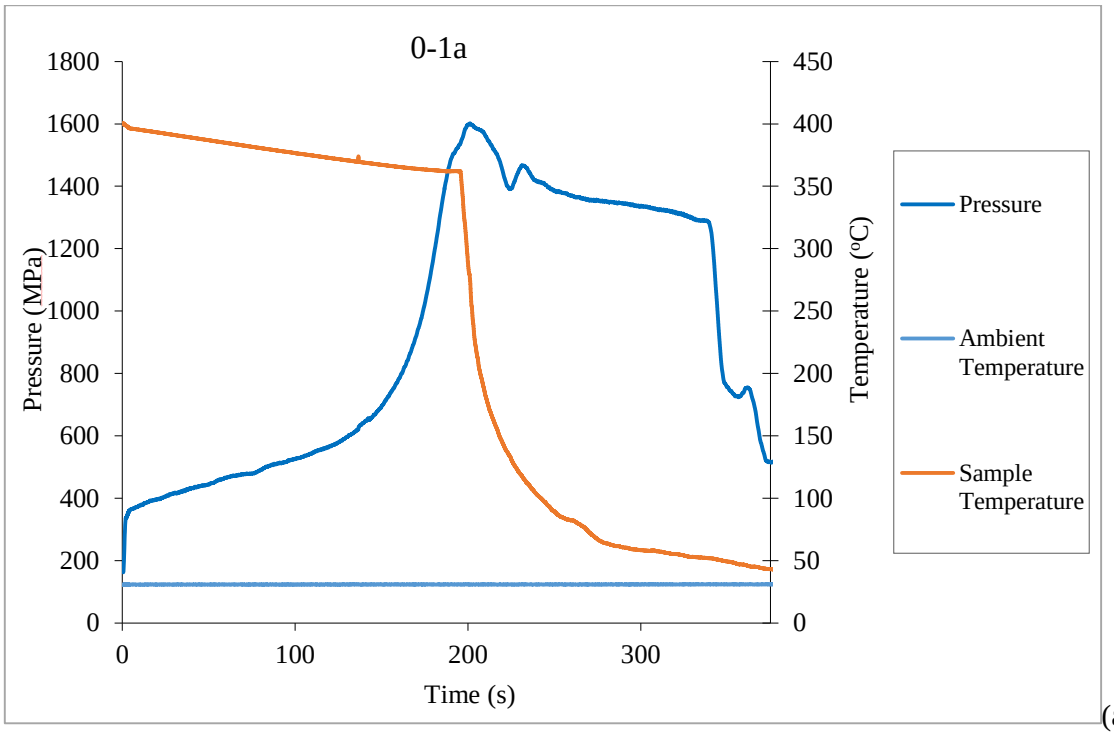

(a)

Figure 4.6: (a) Temperature and stem pressure conditions during extrusion of the bar 0-1a.

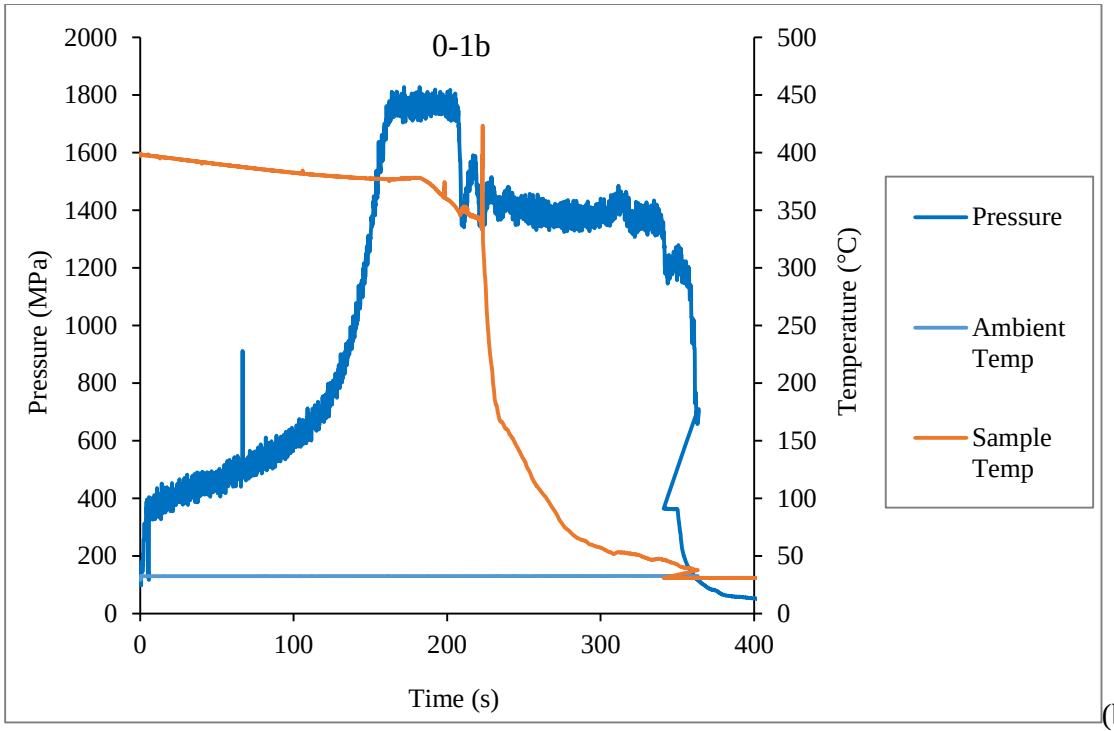

(b)

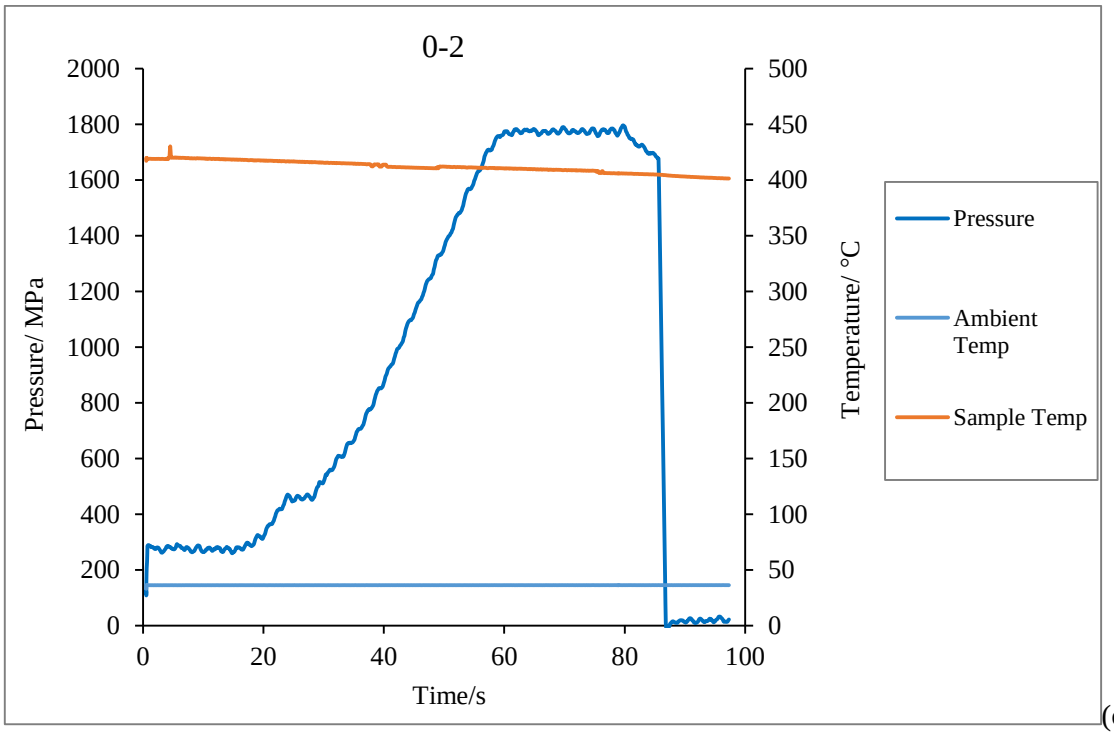

(c)

Figure 4.6: (cont.) (b) temperature and stem pressure conditions during the extrusion of bar 0-1b and (c) temperature and stem pressure conditions during the failed extrusion of the bar 0-2. The y axis on the left shows the extrusion pressure, while the one on the right shows the temperature.

The two bars produced from powder batch 1 were expected to extrude both at the same temperature and require the same pressure, however the first extrusion attempt of the 0-1b bar at 400 °C was unsuccessful and the second attempt at 420 °C required a higher pressure than the pressure required by the 0-1a bar extruded at 400 °C. This difference in temperature and breakthrough pressure can be seen in Figure 4.8 (a) and (b). An increase in extrusion temperature is well documented to cause a decrease in breakthrough pressure in bars made with the same powder batch and size fraction [Rou-12]. A further investigation of the microstructure of both bars will be required to explain this difference. However a potential reason for this increase in breakthrough pressure and temperature could be the pure Al powder contamination, which will vary randomly within each powder batch. The addition of pure Al has been shown to decrease the breakthrough pressure [Ped-10], [Rou-12].

The lack of pure Al contamination observed in the 2nd powder batch would also explain its failure to extrude during the first attempt at 400 °C. The failure of the second attempt to extrude at 420 °C (as seen in Figure 4.8 (c)) could be a result of the very small reduction in the atomic percentage of pure Al content of the atomised powder from batch 2 shown by ICP-OES analysis in Table 4.1. A reduction as subtle as 0.8 at% in the Al content of the alloy powder was shown to increase the breakthrough pressure by 300 MPa and have a negative effect on extrudability [Rou-12].

4.3 Microstructural Characterisation of the Extruded Bars

This section describes the microstructural characterisation of the $Al_{93}Fe_3Cr_2Ti_2$ bars produced and its correlation with the batch of powder and the extrusion conditions used. This analysis revealed extruded bars made of deformed well bonded powder particles with no evidence of residual porosity. Some of the pure Al contamination was visible, and the amount was estimated and correlated to the conditions required for extrusion.

4.3.1 Microstructural Characterisation of the 0-1a Bar

The 0-1a bar was received from a previous project [Ped-10] and further analysis was performed. Its extrusion temperature was 400 °C.

The microstructural characterisation in a previous project involved an XRD analysis of the cross section, the longitudinal section and the ground up filings made from the front of the bar. It showed that the microstructure consists mainly of FCC-Al and icosahedral phase. The XRD scans were checked for metastable θ-phase but it was no longer present as an identifiable peak. Small peaks were labelled as Al_3Ti, $Al_{13}Fe_4$ and $Al_{13}Cr_2$, however due to the size of the peaks being comparable to the size of the noise in the overall scan, it was concluded that further evidence would be needed to confirm the presence of these phases. Several authors reported evidence of other intermetallic phases such as $Al_{13}Fe_4$ and $Al_{13}Cr_2$ [Gal-09a], metastable θ-$Al_{13}(Fe, Cr)_{2-4}$ [Gal-09a], [Cop-02], [Aud-99], [Man-89], Al_6Fe [Gar-10], $Al_{23}Ti_9$ [Ino-00], [Tod-04], Al_3Ti [Gar-07], [Yam-07] in XRD analysis of alloy systems with the same nominal chemical composition. In the XRD results obtained by the previous project, with the exception of the θ-phase, none of these intermetallics were observed [Ped-10]. The previous projects analysis also compared peak intensities to perform a qualitative texture assessment of the front of the bar and concluded that anisotropy was likely to be found [Ped-10].

The previous projects analysis did not include X-ray diffractograms of the back of the bar, which were performed to check for consistency and homogeneity within the extruded bar. They can be seen in Figure 4.7. α-Al peaks were identified by indexing the reflections corresponding to the (111), (200), (220), (311), (222) and (400) planes in the 2θ = 20 °-100 ° range at 38.5 ° (100% intensity), 44.7 °, 65.2 °, 78.3 °, 82.5 ° and 99.2 ° [JCP-99]. Icosahedral phase was also identified by peaks at 2θ ~ 22.9 °, 41.3 °, 43.5 °, 61.6 ° and 73.7 ° [Gal-09a], [Aud-02]. The microstructure of the back of the bar was shown to consist of an α-Al matrix and icosahedral phase. θ-phase, which was detected in the powder, was no longer present in the bar after extrusion at 400 °C (or if it was present, not in a large enough quantity to be detected by XRD). No other intermetallic phases were detected by XRD.

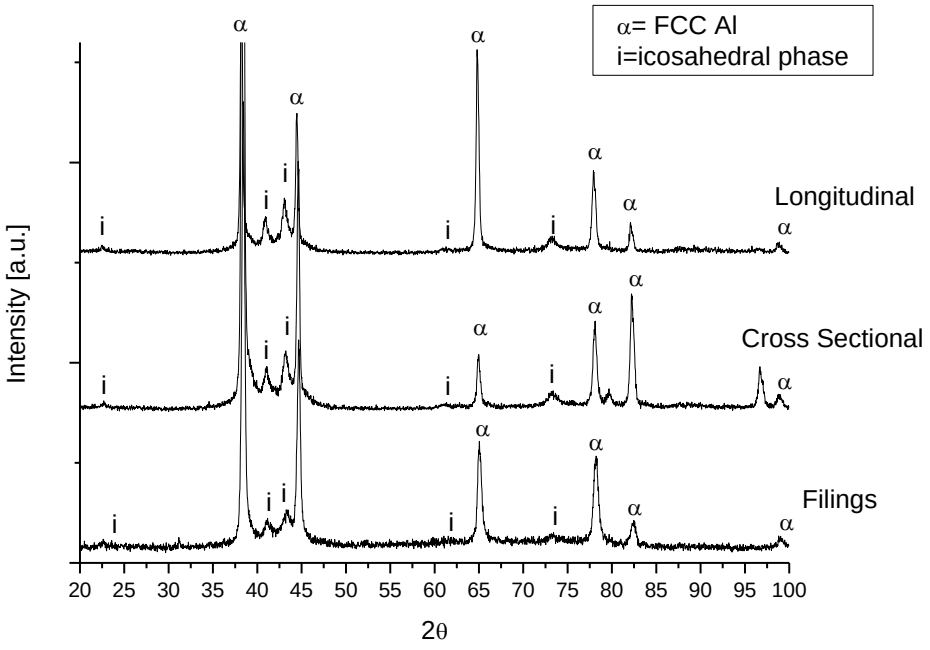

(a)

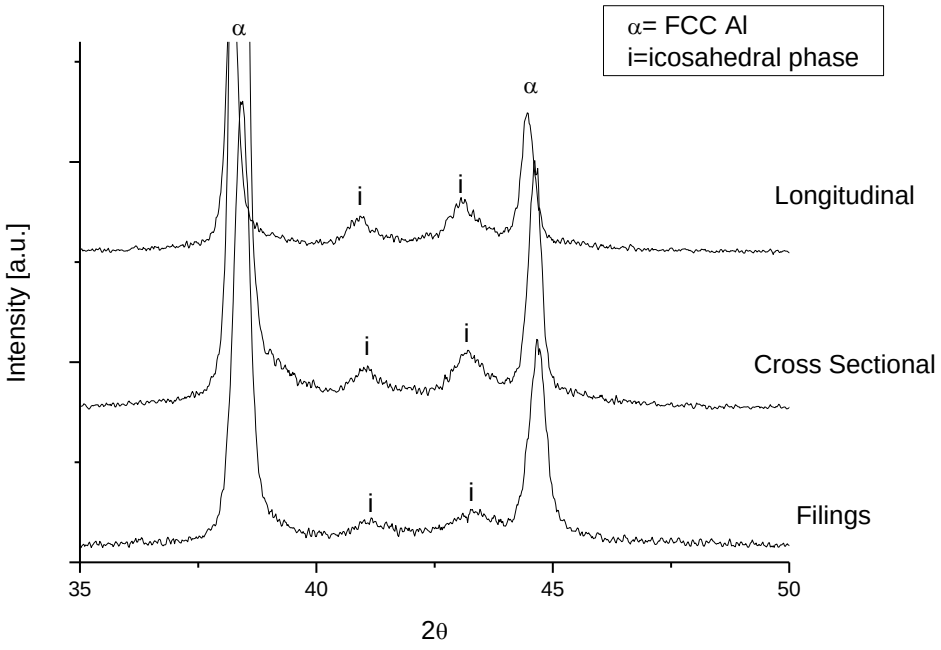

(b)

Figure 4.7: (a) XRD analysis of a longitudinal section, cross section and filings made from the back of the 0-1a bar to check for homogeneity with the front of the bar, (b) an enlargement of the central section from 35-50 ° for clearer peak identification.

The intensity of the aluminium peaks in Figure 4.7 was compared to analyse the presence of texture in a qualitative way and the differences, between the front and the back of the bar. This analysis is shown in Figure 4.8.

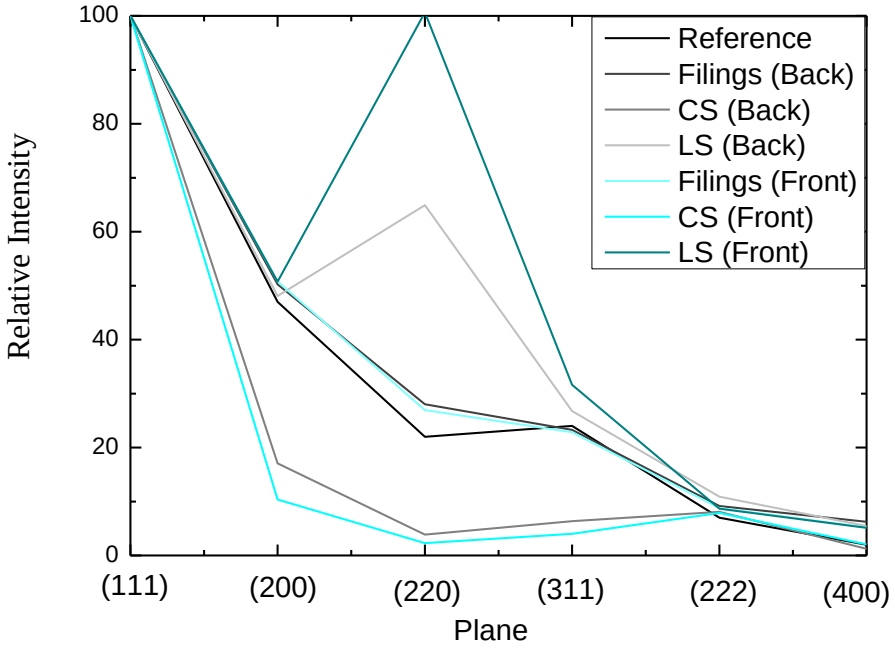

Figure 4.8: Qualitative texture analysis of the front and back of the 0-1a bar. The grey lines indicate the back of the bar while the blue ones the front. CS indicates the cross section, while LS indicates the longitudinal section.

From Figure 4.8 we can see that the filings produced by grinding both the front and back of the bar were untextured, their relative intensities matching those of the reference values. The cross section showed a reduced texture, particularly along the (200), (220) and (311) planes. In the longitudinal section, a higher relative intensity (60-100% of the maximum intensity) was detected along the (220) plane in both the front and the back of the bar, a result which was consistent with the work performed by Rounthwaite [Rou-12], Pedrazzini [Ped-10] and Gu [Gu-09].

The microstructural characterisation previously performed on the 0-1a bar included SEM microscopy of the front of the bar, revealing a structure made of deformed well bonded powder

particles. Some of the pure Al contamination was visible, and the powder particles had deformed into elongated fibres [Ped-10]. Further analysis of their micrographs estimated the amount of pure Al contamination at between 2-3 vol%.

The presence of texture and the elongation of the powder particles into “bands” showed that the powder particles underwent a significant amount of plastic deformation during extrusion. EBSD analysis was used to confirm the size and shape of the grains within the extruded bar and one of the maps can be seen in Figure 4.9 (a) along with (b) the colour coded pole figure showing the grain orientations, (c) a plot of the grain sizes and (d) the inverse pole figure showing the texture trends in grain orientations.

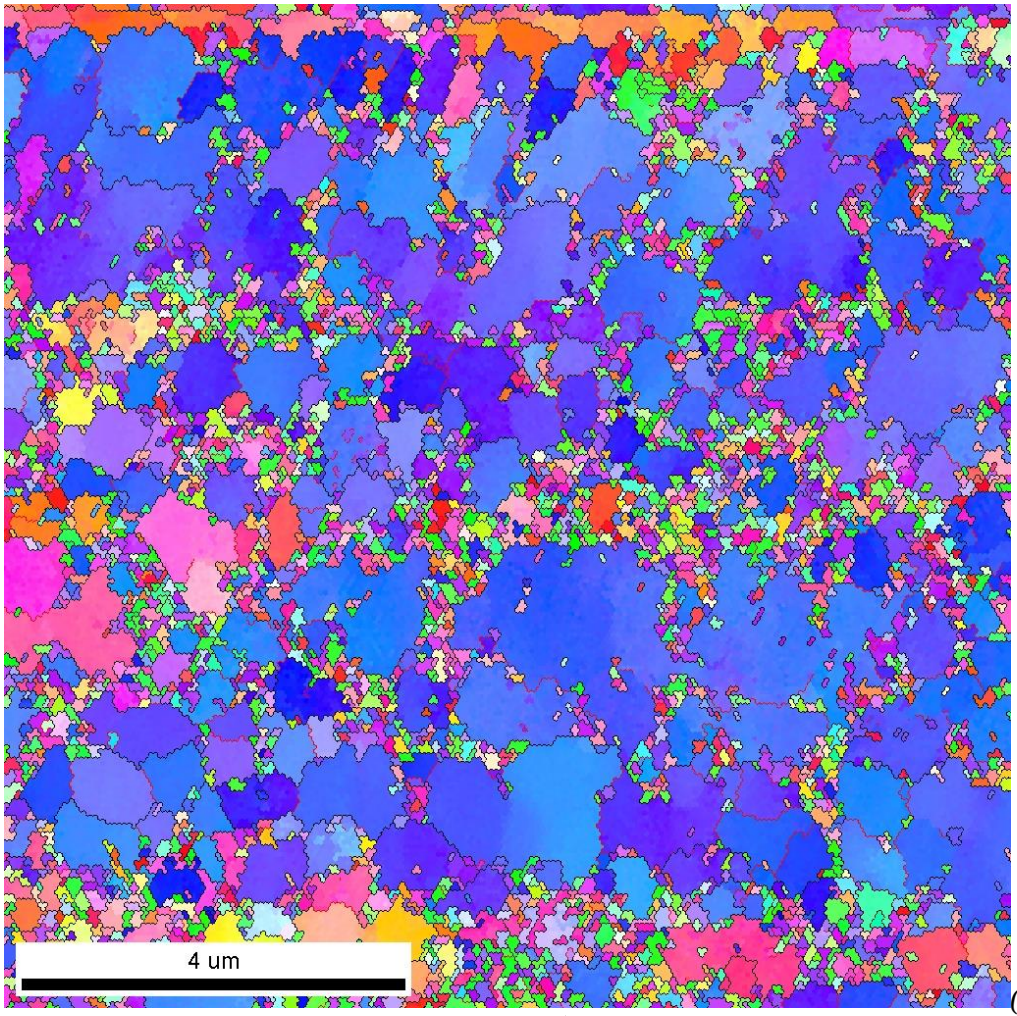

(a)

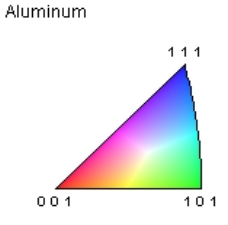

(b)

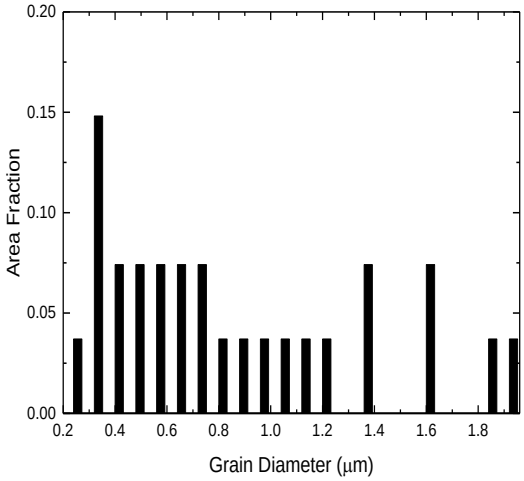

(c)

Figure 4.9: (a) EBSD map showing the elongated Al grains along the extrusion direction (horizontal, as indicated by the arrow) and (b) pole figure showing the grain orientations in the map (c) plot of the grain sizes and their relative frequency.

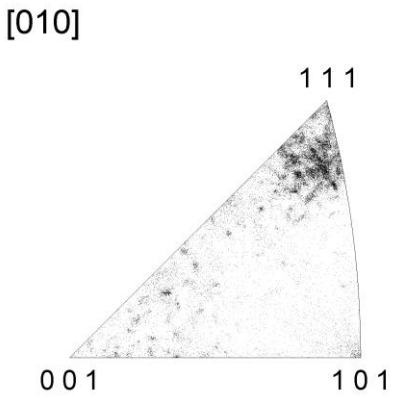

(d)

Figure 4.9 (cont): (d) inverse pole figure showing the grain orientations and texture trends.

In Figure 4.9 (a) high angle and low angle grain boundaries are highlighted in red and black. High angle grain boundaries are defined as having 15 ° or more between their plane orientations, and are shown in black. Low angle grain boundaries are highlighted in red and are defined by a grain orientation 5-15 ° from each other.

The area of each elongated grain was measured and the diameter values were obtained based on the assumption of spherical, equiaxed grains which cover the same area fraction. The measurements were taken as planar surface diameters. The geometric method used to extrapolate 3D grain size from 2D surface measurements was originally developed by Ashby [Ash-64] to describe the structure factors of particles in a matrix. However there are many points of similarity in the geometrical properties of particles and grains as both represent volume elements with well-defined surface boundaries, and similar methods are used to geometrically derive both their mean diameters, size distributions and volume fractions. Therefore the analysis of the geometric properties of particles and grains can be mathematically approached the same way [Und-70]. Grain size distributions were measured in the extruded bar samples, geometrically converted into 3D measurements using Ashby's method and plotted against their relative frequency in Figure 4.9 (c). Any grains smaller than 200 nm were discarded as EBSD noise following the reasoning detailed in Appendix 1. An improved curve fit for the experimental data collected was achieved by using a

bimodal distribution rather than a simple Gaussian with peaks at d_1=0.32±0.25 µm and d_2=1.5±0.3 µm. The majority of the area fraction of grains fit into the sub-micron peak (~70%).

Analysing Figure 4.9 (a) could suggest that the originally more spheroidal-shaped powder particles have now been deformed along the extrusion direction and formed elongated bands in which there are several grains with low misorientation angles (generally less than 15 °, the grain boundaries highlighted in red). However the exact location of the boundary between powder particles cannot be accurately detected using this method.

Further microstructural analysis to confirm the phases present in the 0-1a bar after extrusion and complement the XRD results was performed by TEM. Bright field TEM micrographs were taken with convergent beam diffraction patterns as the smallest selected area aperture proved to be too large for the ultra-fine microstructure observed in the samples. These micrographs can be seen in Figure 4.10. TEM-EDX was also performed to measure the chemical composition of each phase for a comparison with the powder composition, the results of which are summarised in Table 4.5.

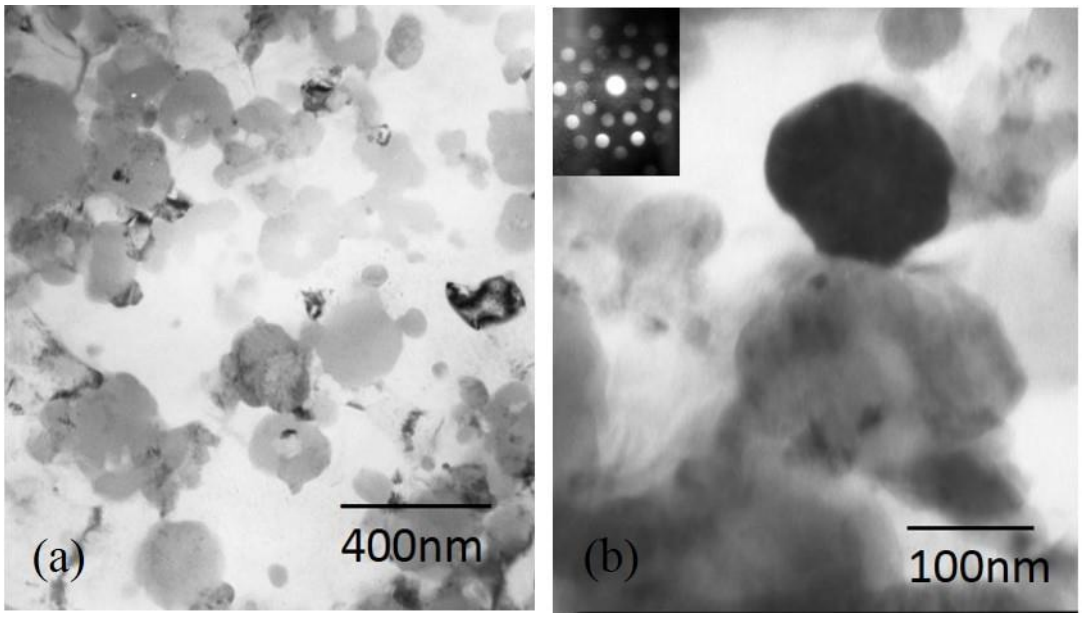

Figure 4.10: (a) Overall bar microstructure of the 0-1a bar, (b) 5-fold symmetry diffraction pattern characteristic of the icosahedral phase.

	0-1a bar matrix composition		*Batch 1 powder matrix composition*		*0-1a bar quasicrystal composition*		*Batch 1 powder quasicrystal composition*	
Element	*Atomic%*	*Error*	*Atomic%*	*Error*	*Atomic%*	*Error*	*Atomic%*	*Error*
Al	*98.2*	*0.7*	*98.2*	*0.2*	*87.8*	*1.0*	*86.0*	*1.0*
Ti	*1.3*	*0.6*	*1.4*	*0.3*	*3.4*	*1.7*	*4.9*	*2.1*
Cr	*0.4*	*0.2*	*0.3*	*0.1*	*4.2*	*0.8*	*4.6*	*1.0*
Fe	*0.2*	*0.1*	*0.2*	*0.1*	*4.6*	*1.3*	*4.5*	*1.4*
Totals	*100*		*100*		*100*		*100*	

Table 4.5: Matrix and quasicrystal composition in the 0-1a bar, compared to the batch 1 powder compositions, removing the C, and O impurities that come from processing and the top oxide layer. Average and errors were calculated over 10 measurements.

Table 4.5 shows that the measured chemical composition of the α-Al matrix by TEM-EDX before and after extrusion proved within each other's error bars and the matrix had a higher solute content than the equilibrium solid solubility of Fe, Cr and Ti in Al even after the extrusion at 400 °C [Mas-90], [Mon-43]. The equilibrium solid solubility for Cr in Al at 400 °C is ~0.18 at% [Mon-43], the solid solubility of Fe at 400°C is ~0.02 at% [Mon-43] and the maximum solid solubility of Ti in Al at 400°C is ~0.032 at% [Xu-06]. A summary of the average solute concentration that exceeds the equilibrium solid solubility after extrusion at 400 °C values and errors can be found in Table 4.6.

Element	*Equilibrium values (at%)*	*Powder (at%)*		*Bar (at%)*	
		Average	*Error*	*Average*	*Error*
Fe	*0.02*	*0.18*	*0.05*	*0.18*	*0.01*
Cr	*0.18*	*0.12*	*0.04*	*0.18*	*0.16*
Ti	*0.032*	*1.368*	*0.18*	*1.268*	*0.24*

Table 4.6: solute concentration that exceeds the equilibrium solid solubility after extrusion at 400°C measured by TEM-EDX and compared with literature values [Mon-43], [Xu-06]. Averages

were taken over 10 measurements. Errors are the maximum range (subtracting the lowest value from the highest value).

Microstructural analysis by TEM was consistent with the results observed by XRD. Figure 4.10 shows bright field TEM micrographs and their corresponding convergent beam diffraction patterns of the extruded 0-1a bar. They contain icosahedral quasicrystalline particles embedded in an α-Al matrix. No noticeable size difference compared to the powders was recorded by TEM after warm extrusion, but no attempts were made to measure accurate particle size distributions in the as-atomized powders.

Particle size distributions were measured in the extruded bars, with over 120 diameter measurements taken and plotted against the relative frequency in Figure 4.11. Stereology structure factors were calculated assuming all particles are spherical and working from measurements from planar surfaces following the method outlined by Ashby [Ash-64]. The particle radius was calculated by using $r_s=\sqrt{(2/3)}r_v$ where r_s is the mean radius of interaction with a planar surface, r_v is the particle radius. The number of particles intersecting a unit area N_s was then measured and used to calculate the volume fraction using $f=N_s(2/3)\pi r_v^2$.

The mean planar centre-to-centre particle separation λ (also referred to as $2R_s$) can then be calculated assuming particles are arranged like points in an FCC lattice $2R_s=\sqrt{(4/f)}*\sqrt{((2/3)*r_v)}$ [Ash-64]. An improved fit for the experimental data collected was achieved by using a bimodal distribution rather than a simple Gaussian with peaks at r_1=42.9±6.1 nm and r_2=128.6±6.1 nm, shown in Figure 4.11. By using the two peaks and the equations described above we can calculate the inter-particle spacing and volume fraction using the larger and smaller particle radii: using r_1 the partial volume fraction of smaller particles was f=0.15, $2R_s=1.8x10^{-7}$ m and using r_2 the partial volume fraction of coarser particles was f=0.26 and $2R_s=4.12x10^{-7}$ m. Assuming they can be added linearly the overall volume fraction of quasicrystalline and intermetallic particles was f=0.41. Which appears consistent with the literature as Audebert *et al.* found f=0.42 in melt-spun ribbons of the same nominal composition [Aud-02], and Inoue *et al.* found a value of f=0.45 [Ino-99].

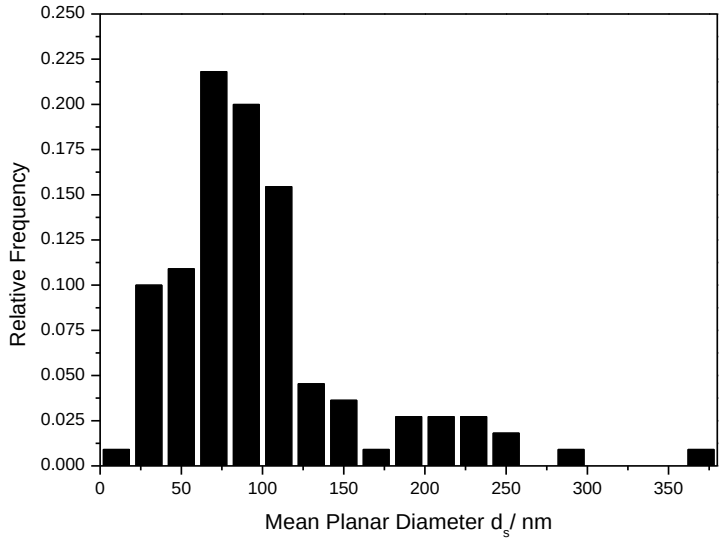

Figure 4.11: plot of the particles sizes and their relative frequency measured from TEM micrographs. 120 measurements were taken and plotted, the bimodal distribution was fitted using the Origin curve fitting plugin.

4.3.2 Microstructural Characterisation of the 0-1b Bar

The 0-1b bar was pre-heated and extruded at a maximum temperature of 420 °C during its second, successful extrusion attempt.

The phases present in the bar after extrusion were analysed by XRD in the cross section, the longitudinal section and filings produced by grinding the bar. The result of these scans is shown in Figure 4.12. α-Al peaks were identified by indexing the reflections corresponding to the (111), (200), (220), (311), (222) and (400) planes in the 2θ = 10 °-100 ° range at 38.5 ° (100% intensity), 44.7 °, 65.2 °, 78.3 °, 82.5 ° and 99.2 ° [JCP-99]. The presence of the icosahedral phase was shown by broad peaks at 2θ ~ 22.9 °, 41.3 °, 43.5 °, 61.6 ° and 73.7 ° which were the peaks calculated by Galano *et al.* on melt spun ribbons of the same nominal chemical composition using Cahn's indexation scheme [Cah-86], [Gal-09a]. Other intermetallic phases were identified including Al_3Ti, $Al_{13}Fe_4$, $Al_{13}Cr_2$ which were indexed using data sheets [JCP-99]. The presence of Al_3Ti was shown by the peaks at 2θ~39.2 ° (100% intensity), 66.5 ° and 80.1 ° corresponding to the (111), (220) and (311) reflections respectively. The $Al_{13}Fe_4$ was shown by peaks at 43.1 ° corresponding to the

100% intensity ($\bar{6}23$) reflection. The $Al_{13}Cr_2$ phase was shown by the peaks at 42.0 ° and 43.9 ° (100% intensity), corresponding to the (331) and ($\bar{8}20$) respectively.

The XRD scans were checked for metastable θ-phase but it was no longer present as an identifiable peak.

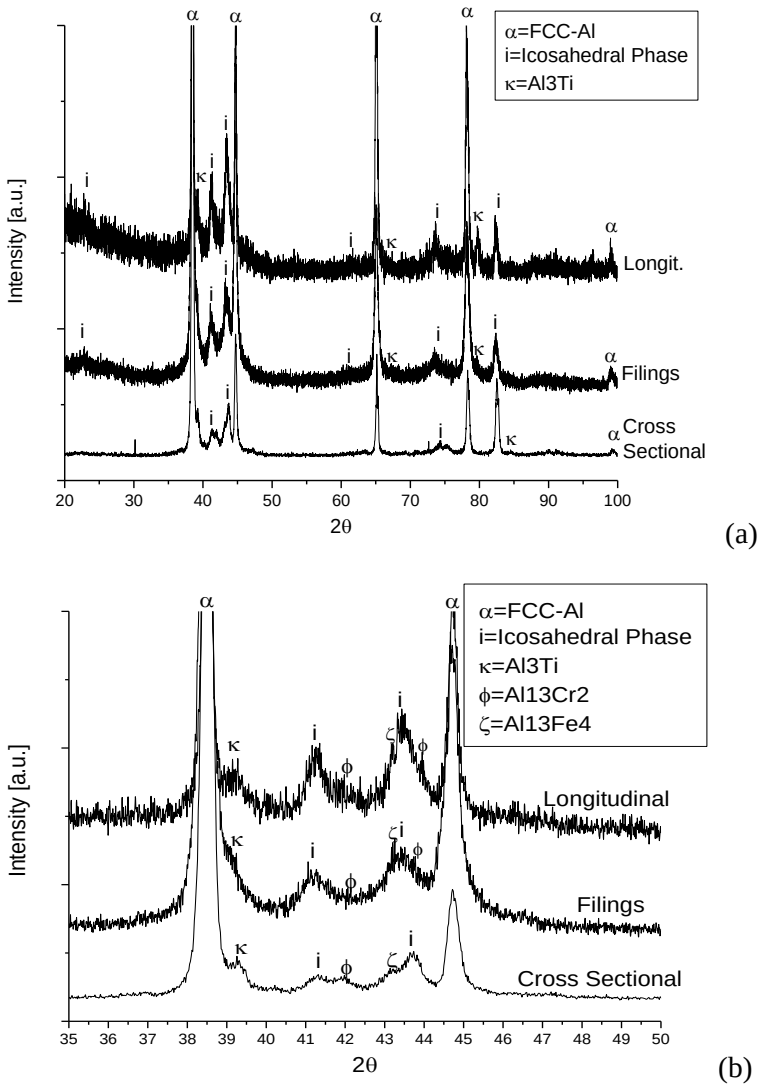

Figure 4.12: (a) x-ray diffractogram of the front of the 0-1b bar showing a cross section, a longitudinal section and powder made by grinding the bar, (b) an enlargement of the 35-50 ° section of the diffractogram to allow easier phase identification.

X-ray diffractograms of the back of the bar were also performed to check for consistency and homogeneity of the extruded bar and can be seen in Figure 4.13. The microstructure of the back of the bar was shown to consist of an α-Al matrix and icosahedral phase. Icosahedral phase was again

shown by peaks at 2θ ~ 22.9 °, 41.3 °, 43.5 °, 61.6° and 73.7 °. θ-phase which was detected in the powder was no longer present in both the front and the back of the bar after extrusion at 420 °C (below the XRD detection limit). Small amounts of Al_3Ti were detected by the peak at 2θ~39.2 ° (100% intensity) corresponding to the (111) reflection.

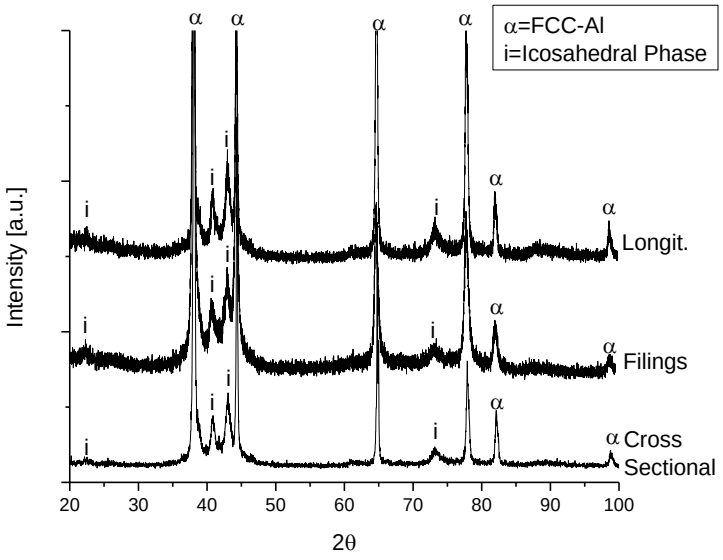

(a)

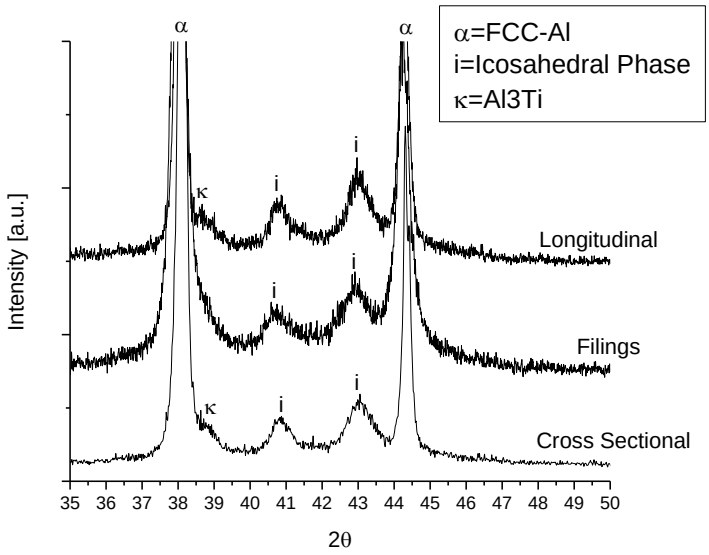

(b)

Figure 4.13: (a) x-ray diffractogram of the back of the 0-1b bar showing a cross section, a longitudinal section and powder made by grinding the bar, (b) an enlargement of the 35-50 ° section of the diffractogram to allow easier phase identification.

The relative intensity of the aluminium peaks in Figure 4.12 and 4.13 was compared to analyse qualitatively the presence of texture and the differences between the front and the back of the bar. Texture analysis is shown in Figure 4.14.

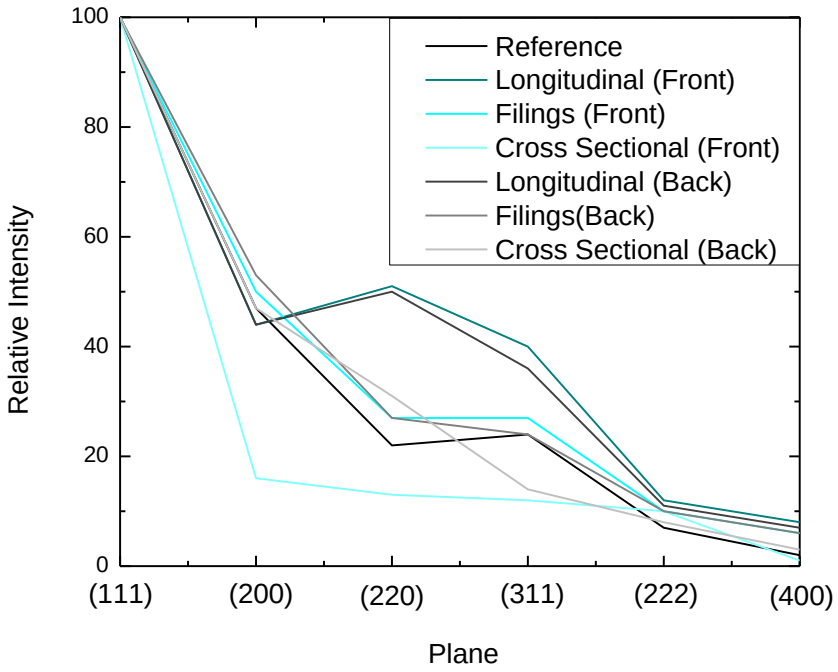

Figure 4.16: Texture analysis of the front and back of the 0-1b bar. The grey lines indicate the back of the bar while the blue ones the front.

The filings produced by grinding the bar were untextured, their relative intensities matching those of the reference values. The cross section showed a reduced texture, particularly along the (200), (220) and (311) planes. In the longitudinal section, a large relative intensity (~50% of the maximum intensity) was detected along the (220) plane in both the front and the back of the bar. However, the previously analysed 0-1a bar showed 60-100% of the maximum intensity in the (220) plane. Also, the 0-1b bar showed a 10% increase in relative intensity along the (311) plane both in the front and the back of the bar. Differences in texture can be created in several ways however in this case it was likely that the extended exposure to higher temperature and pressures due to the fact two extrusion attempts were made on this bar could have caused some changes. The

0-1b bar was initially held at 400 °C for 30 minutes and subjected to ~1750 MPa before the extrusion press was stopped, then it was held at 420 °C for 30 minutes and extruded at 1670 MPa.

SEM microscopy of the front of the bar was performed as part of the microstructural characterisation after extrusion. This analysis, shown in the backscattered electron micrographs in Figure 4.15, revealed a structure made of deformed well bonded powder particles with no evidence of residual porosity. Pure Al contamination was not observed in this bar. Some of the larger powder particles had a much coarser microstructure which was also visible in the extruded bars. EDX points were taken on these large particles and an EDX map of the matrix containing the finer particles was taken for comparison, the results of which are summarised in Table 4.7.

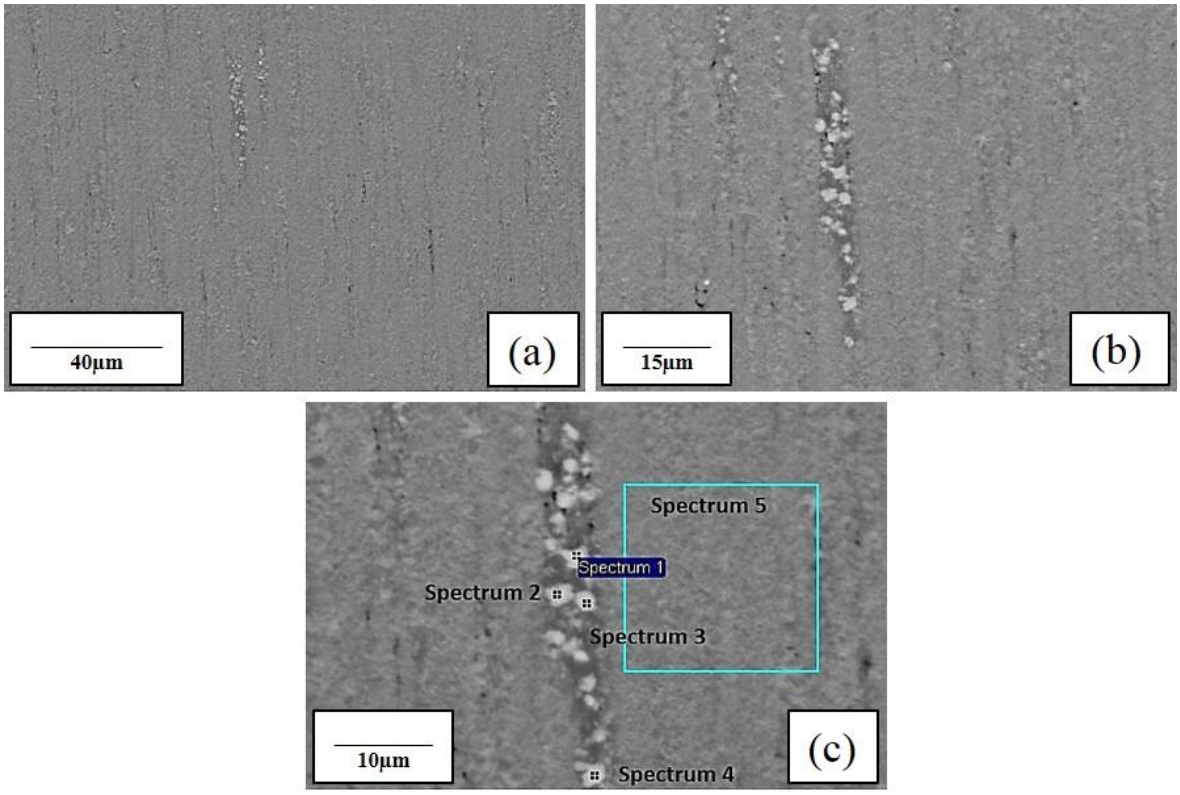

Figure 4.15: (a) SEM backscattered image showing the microstructure of the 0-1b bar, (b) a higher magnification overview of the larger intermetallic phases present and (c) EDX of the larger intermetallic particles and an EDX map of the matrix.

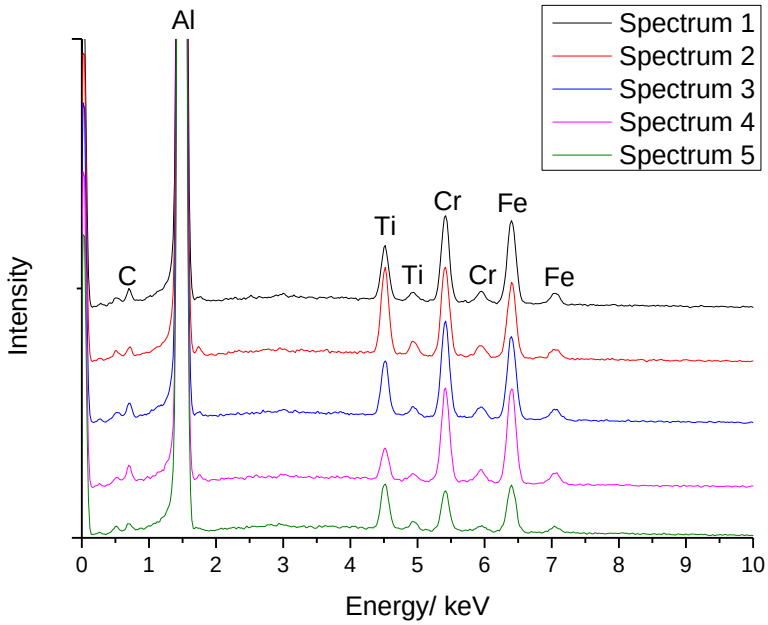

(d)

Figure 4.15: (cont.): (d) EDX spectra associated with Figure 4.17 (c).

0-1b bar Intermetallic Composition		
	Average	*Error*
Al	*85.4*	*0.5*
Ti	*2.78*	*1.3*
Cr	*5.4*	*0.2*
Fe	*6.5*	*1.0*

Table 4.7: Intermetallic composition average and errors were calculated over 10 measurements performed by SEM-EDX, some of which are Spectra 1, 2, 3 and 4 in Figure 4.15.

The measured chemical composition of the large particles seen in Figure 4.15 by SEM-EDX showed to be intermetallic phases which contain all four alloying elements present. Their composition is within the experimental error of the measured chemical composition by TEM-EDX of the icosahedral phase within the powder from batch 1.

EBSD analysis was used to confirm the size and shape of the grains within the extruded bar and one of the maps can be seen in Figure 4.16 (a) along with the pole figure (b) and a plot of the grain sizes.

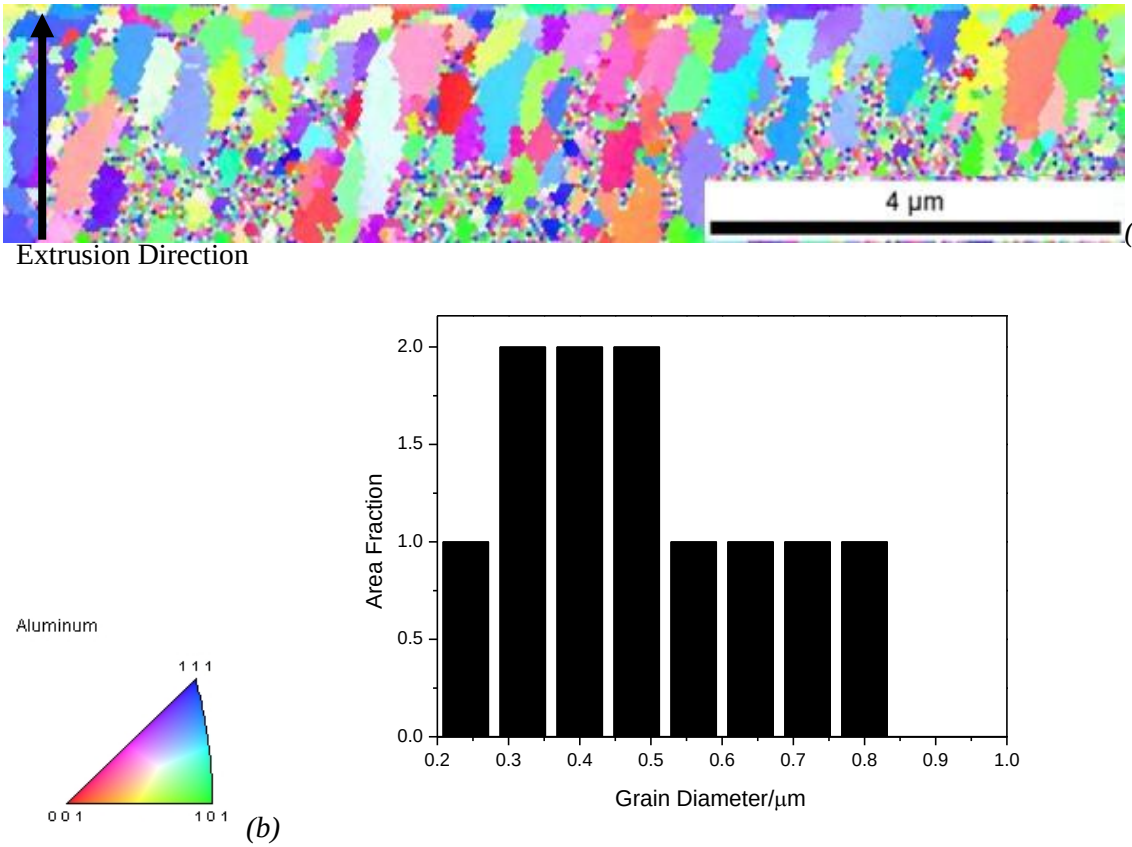

Figure 4.16: (a) EBSD map showing the elongated Al grains along the extrusion direction (vertical, as indicated by the arrow) and (b) pole figure showing the orientations in the map (c) plot of the grain size diameters and their relative frequency.

The same assumptions relating the extrapolation of a likely grain structure in 3D based on 2D surface measurements explained when discussing the grain structure of the bar 0-1a were made, as developed by Ashby [Ash-64].

Grain size distributions were measured, with the mean diameter d=0.4±0.12 µm. All of grains detected fit into the sub-micron range and are therefore approaching the limits of the resolution of the technique and the instrument used.

Further microstructural analysis to confirm the phases present and grain sizes seen in the bars after extrusion, complementing the information obtained by XRD and EBSD, was performed by TEM. Bright field TEM micrographs were taken with convergent beam diffraction patterns. These micrographs can be seen in Figure 4.17. Figure 4.17 (a) shows the overall microstructure of the bar and Figure 4.17 (b) shows an ultra-fine Al grain or sub-grain. Unlike the bar 0-1a, a large numbers of smaller grains/sub-grains were observed in the TEM specimen.

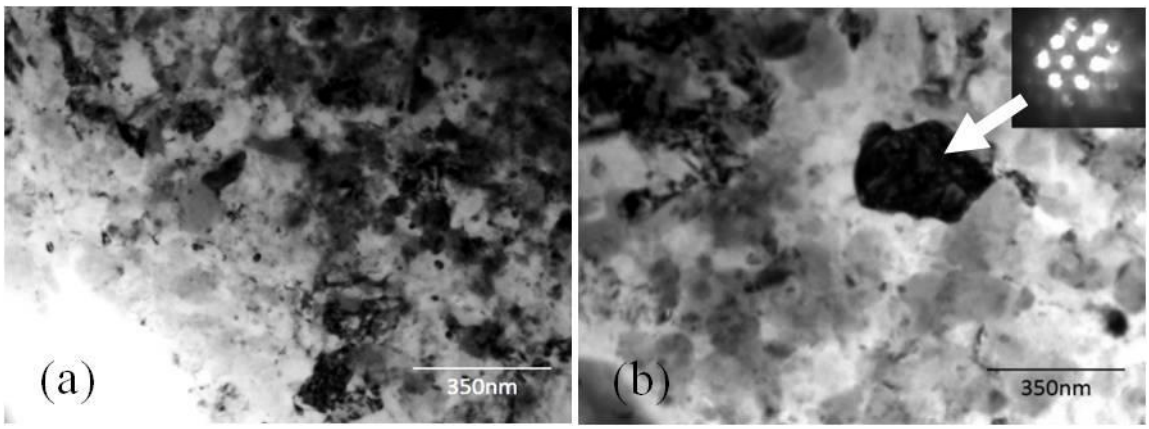

Figure 4.17: (a) Overall bar microstructure from the 1st powder batch in bar 0-1b, (b) 3-fold symmetry diffraction pattern form an ultra-fine grain in the Al matrix.

4.4 Summary

Two separate batches of $Al_{93}Fe_3Cr_2Ti_2$ alloy powders were successfully produced by industrial collaborator Alpoco with a chemical compositions $Al_{93.1}Fe_{2.9}Cr_{1.9}Ti_{1.9}$ (batch 1) and $Al_{93.0}Fe_{2.9}Cr_{1.9}Ti_{2.0}$ (batch 2). The fraction of the powders which was within the 0-25 µm diameter size was analysed and used. The morphology of the powder was elongated and nodular, with satellite particles welded to larger ones.

The regularity and scale of the internal microstructure of the cross sectioned powders was generally consistent within each single powder particle, but varied depending on the particle size. A coarser internal microstructure was found in larger particle sizes, while smaller particles were

found to have a very fine microstructure. Some occasional particles with a much coarser microstructure were also observed.

Intermetallic phases were identified within the FCC-Al matrix in the atomised powders, including icosahedral phase and a small amount of θ-$Al_{13}(Cr, Fe)_{2-4}$ phase. The FCC-Al matrix itself was found to contain amounts of Fe, Cr and Ti in solid solution higher than the equilibrium solid solubility of those elements.

Pure Al contamination was initially found in the 1st batch, which comes from the standard procedure of cleaning the atomiser with a pure Al run between runs of other alloys. However since cleanliness of the atomiser was improved before performing the second atomisation run, the 2nd batch was not found to contain contamination.

Two extruded bars were produced from the 1st powder batch and compared with the powder microstructure: the 0-1a and 0-1b bars. This comparative analysis revealed in both extruded bars a structure made of deformed well bonded powder particles with no evidence of residual porosity. Some of the pure Al contamination was detected in the 0-1a bar, and the Al powder particles had deformed into elongated fibres [Ped-10]. The amount of pure Al contamination was estimated at between 2-3 vol%. The absence of this contamination in the micrographs of the 0-1b bar can be explained as this contamination is randomly distributed throughout the 1st powder batch and evidently was more dominant in the powder used to produce the first bar. No extrusion of the 2nd powder batch was successful.

Both bars still retained the microstructure consisting mainly of FCC-Al and icosahedral phase after extrusion. Metastable θ-phase was no longer identifiable in either bar. Grain size distributions were measured in the FCC-Al matrix of the extruded bars. A bimodal distribution with peaks at d_1=0.32±0.25 μm and d_2=1.5±0.3 μm provided an improved fit for the experimental data from the 0-1a bar. ~70% of the area fraction of grains fit into the sub-micron peak. Some elongated bands of grains separated by low angle grain boundaries (less than 15 °) were visible, which could have been produced through the deformation of the individual powder particles. The 0-1b bar showed a

very different grain size and morphology. Experimental data was difficult to collect due to the grains observed by TEM being close to the resolution limit of the EBSD. The largest grains could be measured and their diameter was d=0.4±0.12 μm. All of grains measured fit into the sub-micron range. The grain size was significantly smaller than the measurements made on the 0-1a bar. There was also a distinct lack of low-angle grain boundaries in the EBSD. Comparing the bars 0-1a and 0-1b it became apparent that there is a change in texture shown qualitatively by XRD peak intensity comparison in the 0-1b bar as well as a smaller grain size and the lack of low angle grain boundaries detected by EBSD. Differences in texture can be created in several ways however it is likely that the changes occurred during the extended exposure to higher temperature and pressures due to the fact two extrusion attempts were made on this bar.

The measured chemical composition of the α-Al matrix of the 0-1a bar by TEM-EDX and of the powder from batch 1 was not altered by extrusion, within the experimental error. Both had a higher solute content than the equilibrium solid solubility of Fe, Cr and Ti in Al even after the extrusion at 400 °C [Mas-90], [Mon-43].

Both the as-atomized powder and the extruded bars contained icosahedral quasicrystalline particles embedded in an α-Al matrix. Particle size distributions were measured in the extruded 0-1a bar. A bimodal distribution with peaks at r_1=42.9±6.1 nm and r_2=128.6±6.1 nm gave an improved fit for the experimental data collected. The inter-particle spacing and volume fraction were calculated using the larger and smaller particle radii: using r_1 the partial volume fraction was f=0.15, $2R_s=1.8\times10^{-7}$ m and using r_2 the partial volume fraction was f=0.26 and $2R_s=4.12\times10^{-7}$ m. Assuming they can be added linearly the overall volume fraction of quasicrystalline and intermetallic particles was f=0.41. Which appears consistent with the literature as Audebert *et al.* found f=0.42 in melt-spun ribbons of the same composition [Aud-02], and Inoue *et al.* found a value of f=0.45 [Ino-99].

4.5 Conclusions

$Al_{93.1}Fe_{2.9}Cr_{1.9}Ti_{1.9}$ (batch 1) and $Al_{93.0}Fe_{2.9}Cr_{1.9}Ti_{2.0}$ (batch 2) alloy powders have been successfully produced very close to the target chemical composition of $Al_{93}Fe_3Cr_2Ti_2$. A small amount of pure Al contamination was found in batch 1.

The morphology of the powders was found to be elongated and nodular, with satellite particles welded to larger ones. The internal powder microstructure was found to consist of spherical icosahedral quasicrystalline phase in an FCC-Al matrix. Small amounts of other intermetallic phases were also detected.

After extrusion, both bars still retained the microstructure consisting mainly of FCC-Al and icosahedral particles. Particle size distributions were measured in the 0-1a bar. A bimodal distribution with peaks at r_1=42.9±6.1 nm and r_2=128.6±6.1 nm was found. The overall volume fraction of particles was f=0.41.

The 0-1a bar was found to have a bimodal grain size distribution with peaks at d_1=0.32±0.25 µm and d_2=1.5±0.3 µm. Elongated bands of grains separated by low angle grain boundaries (less than 15 °) were visible. The 0-1b bar showed only sub-micron grain size with a normal distribution peak d=0.4±0.12 µm.

The measured chemical composition of the α-Al matrix of the 0-1a bar by TEM-EDX and of the powder from batch 1 was not altered by the extrusion process. Both had a higher solute content than the equilibrium solid solubility of Fe, Cr and Ti in Al after the extrusion at 400 °C [Mas-90], [Mon-43], [Xu-06].

The most successful extrusion was the 0-1a bar, performed during a previous project on powder with ~2-3 vol% pure Al contamination, which allowed extrusion at 400 °C as opposed to 420 °C. An increase of 20 °C was sufficient to cause the sides of the extruded bar to peel and have a rough surface finish, as well as inducing changes in the microstructure.

References

[Aud-02] F. Audebert, F. Prima, M. Galano, M. Tomut, P. J. Warren, I. C. Stone, B. Cantor, Mat. Trans., 2002, A 43, 8, 2017

[Aud-99] F. Audebert, R. Colaco, R. Vilar, H. Sirkin, Scripta Mat., (1999), 40, 551.

[Ash-64] M. Ashby, Z. Metallk., (1964), 55, 5-17.

[Boh-86] J. W. Bohlen, R. J. Kar, G. R. Chanani, *Rapidly Solidified Powder Aluminum Alloys*, ASTM, STP, 890, 166, (1986).

[Bar-05] B. Bártová, D. Vojtech, J. Verner, A. Gemperle, V. Studnica, J. All. Comp., (2005), 387, 193.

[Cah-86] J. W. Cahn, D. Shechtman, D. Gratias, J. Mater. Res., (1986), 1-13.

[Cop-02] J. Copola, F. Audebert, S. Duhalde, J. Met. Nanocryst. Mater., (2002), 14, 14, 27.

[Gra-77] N. J. Grant, Proc. Int. Conf. Rapid Solid. Proc. (1977), 230.

[Gal-09a] M. Galano, F. Audebert, I. C. Stone, B. Cantor, Acta Mat., (2009), 57, 5107–5119.

[Gal-04] M. Galano, F. Audebert, B. Cantor, I. Stone, Mat. Sci. Eng., (2004), A, 375-377, 1206-1211.

[Gar-10] A. Garcia-Escorial, M. Echevarria, M. Lieblich, I. Stone, J. All. Comp., (2010), 504S, S519–S521.

[Gar-07] A. Garcia Escorial, V. F. Cremaschi, E. Natale, M. Lieblich, J. All. Comp., (2007), 434-435, 215-216.

[Gu-09] W-H Gu, Masters Degree Thesis, University of Oxford, (2009).

[Ino-02] H. Inoue, J. Jap. Inst. L. Met., (2002), 52, 11, 524-529.

[Ino-00] A. Inoue, H. Kimura, Mat. Sci. Eng., (2000), A286, 1-10.

[Ino-99] A. Inoue, H. Kimura, Nano Str., (1999), 11, 221-231.

[Ino-98] A. Inoue, Prog. Mat. Sci., (1998), 43, 365-520.

[Jia-14] X. Jiang, M. Galano, F. Audebert, Mat. Char., (2014), 88, 111-118.

[JCP-99] JCPDS-International Centre for Diffraction Data v2.02 Codes: 04-0787, 13-0146, 29-0014, 29-0042 (1999).

[Kim-00] H. Kimura, K. Sasamori, A. Inoue, Mat. Sci. Eng., (2000), 294-296, 168-172.

[Man-89] R. Manaila, V. Florescu, A. Jianu, O. Radulescu, Philos. Mag. B, (1989), 60,589.

[Mas-90] T. B. Massalski, H. Okamoto, P. R. Subramian, L. Kacrzak, editors. *Binary alloy phase diagrams*, Materials Park (OH): ASM International (1990).

[Mon-43] L. F. Mondolfo, *Metallography of Aluminum Alloys*, Wiley and Sons, (1943).

[Nic-68] N. Nichiporenko, O. S., Naida, Y. I. Poroshkovaya, Metallurgiya, (1968), 10, 70, 1.

[Özb-00] S. Özbilen, Powder Met., (2000), 43, 2,173.

[Özb-99] S. Özbilen, Powder Met., (1999), 42, 70.

[Por-92] D. A. Porter, K. E. Easterling, 2nd edition, Chapman and Hall, New York., (1992).

[Ped-10] S. Pedrazzini, Masters Degree Thesis, University of Oxford, (2010).

[Rou-12] N. J. Rounthwaite, DPhil Thesis, University of Oxford, (2012).

[Sin-06] D. Singh, S. Dangwal, J. Mat. Sci., (2006), 41, 3853.

[Smi-83] D. W. Smith, *Powder Metallurgy Applications, Advantages and Limitations*, ASM International 13, (1983).

[Tod-04] I. Todd, Z. Chlup, J.G. O'Dwyer, M. Lieblich, A. Garcia-Escorial, Mat. Sci. Eng., (2004), A 375–377, 1235–1238.

[Und-70] E. E. Underwood, *Quantitative Stereology*, p 80, Addison Wesley, (1970).

[Xu-06] L. Xu, Y.Y. Cui, Y.L. Hao, R. Yang, Mat. Sci. Eng., (2006), A 435–436, 638–647.

[Yam-07] M. Yamasaki, Y. Nagaishi and Y. Kawamura, Scripta Mat, (2007), 56, 785–788.

[Zhe-09] B. Zheng, Y. Lin, Y. Zhou, E. J. Lavernia, Metal. Mat. Trans. B, (2009), 40, 995.

[Zho-91] J. Zhou, B. Duszczyk, B. M. Korevaar, J. Mat. Sci., (1991), 26, 3292.

Chapter 5: Production and Characterisation of Al-Fe-Cr-Ti Composite Bars

This chapter describes the results of the production and consolidation process of the composite bars. Bulk nanoquasicrystalline $Al_{93}Fe_3Cr_2X$ bars (X=Ti or Nb) with added pure Al fibres have previously been produced by atomisation and warm extrusion [Gu-09], [Rou-12], [Ped-10]. Pedrazzini produced the first composites by adding pure Al powder to the nanoquasicrystalline $Al_{93}Fe_3Cr_2Ti_2$ alloy powder before extrusion [Ped-10]. It was found that extrusion could be performed at lower pressure and temperature and the resulting bars had improved ductility during mechanical testing. The following chapter investigates the microstructure of bars produced using the same method as the ones that showed such promising mechanical properties made by Pedrazzini [Ped-10] and compares them to those bars.

5.1 Pure Al Powder Characterisation

The two batches of $Al_{93}Fe_3Cr_2Ti_2$ powders analysed in Chapter 4 (1 and 2) were used to make composite bars with the addition of 10 and 20 vol% pure Al powder.

Prior to extrusion, the pure Al powder was analysed by ICP-OES analysis, then sieved into size fractions 0-25 µm, 25-50 µm and 50-75 µm. The 0-25 µm fraction, the same one used to produce the pure alloy bar, was used to produce the composites. The microstructure and phases present in the powder were analysed by XRD and SEM.

5.1.1 ICP-OES

The elemental composition of the pure Al powder batch was confirmed by an external contractor and the results of this analysis are shown in Table 5.1.

Element	*Pure Al powder*
*Al**	*99.9298*
Fe	*0.0358*
Cr	*0.0005*
Ti	*0.0034*
Zn	*0.0004*
Pb	*0.0001*
Co	*0*
Ni	*0.0023*
Si	*0.0231*
Mg	*0.0011*
Mn	*0.0005*
Cu	*0.0004*
Zr	*0.0003*
Ga	*0.0023*

*Table 5.1: chemical composition of all the powder batches measured by ICP-OES analysis. * pure Al amount calculated by subtraction.*

This confirmed that the actual composition of the powders is 99.9% pure Al. The prevalent impurities found in this powder appear to be 0.004 at% Fe and 0.02 at% Si. Oxygen is expected to be another prevalent impurity due to common industrial practice to deliberately oxidise the surface of the powders during atomisation to prevent explosion.

5.1.2 XRD

The phases present in the pure Al powder were confirmed by XRD. The results of the scans are shown in Figure 5.1. α-Al peaks were identified showing that the microstructure contains FCC-Al. No other phases were identified.

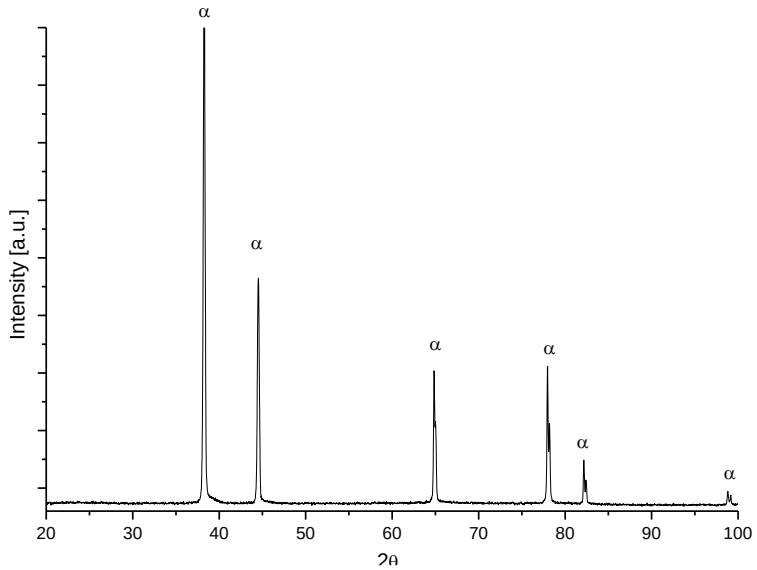

Figure 5.1: XRD scan showing the phases present in the <25 µm fraction of the atomized powder batches produced.

5.1.3 SEM Analysis of the Topography of the Powders

The morphology and topography of the pure Al powders was analysed. The secondary electron micrograph in Figure 5.2 show that the powder had irregular, elongated and nodular shapes. An observation which was consistent with both the $Al_{93}Fe_3Cr_2Ti_2$ powder batches analysed in Chapter 4. Non-spherical particles will have an increased surface area and therefore a larger amount of oxide around them [Smi-83].

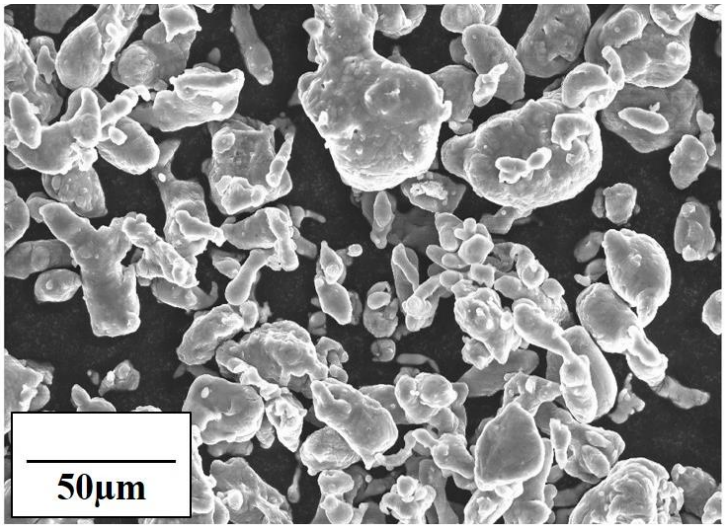

Figure 5.2: SEI micrograph of the as-atomised pure Al powder produced by Alpoco as one of their commercial products, <63 µm.

5.2 Powder Consolidation into Bulk Composite Specimens

Four bars were extruded, made of $Al_{93}Fe_3Cr_2Ti_2$ alloy powders. Two from batch 1 and two from batch 2 with 10 and 20 vol% pure Al addition. The extrusion temperature and pressure conditions are outlined in Table 5.2. The bars were then compared with other bars made during a previous project using the powder from batch 1 [Ped-10].

The bars were numbered following the same system used for the pure alloy bars described in Chapter 4: the first number refers to the vol% of pure Al added, the second number is the batch of powder used. The letter has just been added to differentiate between bars of the same composition, from the same powder batch produced separately.

						Temperature (°C)							
							Sample			*Pressure (MPa)*		*Force (kN)*	
#	*Batch*	*Powder Size*	*Al vol%*	*Powder weight (g)*	*Extrusion ratio*		*Max*	*Min*	*At Peak*	*Peak*	*Final*	*Peak*	*Final*
10-1a [Ped-10]	*1*	*<25 µm*	*10%*	*213*	*14:1*	*Aim: 375*	*388*	*333*	*347*	*1568*	*1299*	*2384*	*1975*
10-1b				*308*			*383*	*360*	*358*	*1641*	*1264*	*2495*	*1922*
10-2	*2*			*315*			*419*	*391*	*393*	*1667*	*1257*	*2535*	*1911*
20-1a [Ped-10]	*1*		*20%*	*211*			*389*	*344*	*359*	*1339*	*1099*	*2036*	*1671*
20-1b	*1*			*331*			*405*	*375*	*377*	*1460*	*1123*	*2220*	*1708*
20-2	*2*			*310*			*400*	*371*	*371*	*1460*	*1169*	*2220*	*1778*

Table 5.2: Table summarising the exact extrusion conditions for each bar. The bars 10-1a and 20-1a were provided from a previous project [Ped-10].

The microstructure of the alloy powders used for extrusion contains a large volume fraction of icosahedral phase detected by XRD and TEM in Chapter 4, which has been shown by other authors to decompose around 500-550 °C [Tod-04], [Gal-04], [Ino-98]. Therefore keeping the extrusion temperature below the phase transformation temperature was of vital importance in the production of the composites.

The combination of low extrusion temperatures and using the smallest powder size available to improve strength of the alloy pushed the extrusion press to its safety limits when the pure alloy powder was extruded (Chapter 4). Several attempts were made to extrude some of the pure alloy bars 0-1b and 0-2, and temperatures as high as 420 °C had to be used. However, the addition of pure Al powder before extrusion has been shown to decrease the breakthrough pressure required [Rou-12], [Gu-09]. All the composite bars extruded successfully on the first attempt.

The ram pressure and temperature of the billet during each extrusion were logged and Figure 5.3 shows plots of the extrusion data from the newly produced bars compared with the previously received bars 10-1a and 20-1a [Ped-10]. The different stages of extrusion can be identified in the plot. Initially the powder is compacted into the can to form a billet, producing a shallow, steadily increasing gradient in the curve. Then the breakthrough pressure was reached and the extrusion can containing loosely compacted powder starts coming out of the die [Zho-91]. Then the maximum pressure is reached when the fully consolidated powder starts being extruded. After this, a steady state pressure level is required in order to complete the extrusion process. The temperature was recorded with a thermocouple, which had to be removed from the die after the breakthrough pressure was reached as the bar started to emerge.

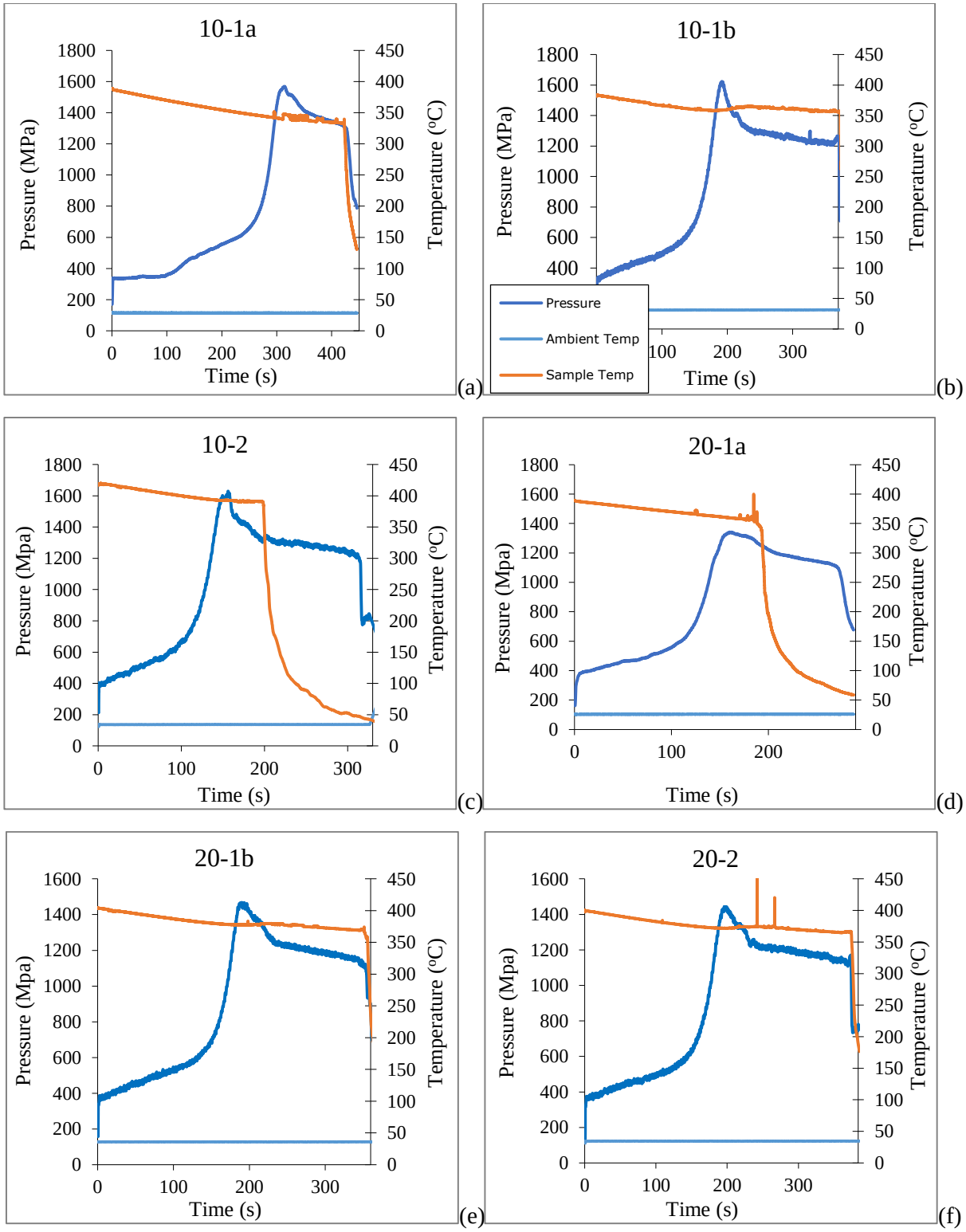

Figure 5.3: (a) Temperature and pressure conditions during extrusion of the bar 10-1a, (b) temperature and pressure conditions during the extrusion of bar 10-1b and (c) temperature and pressure conditions during the extrusion of the bar 10-2. (d) temperature and pressure conditions during extrusion of the bar 20-1a, (e) temperature and pressure conditions during the extrusion of bar 20-1b and (f) temperature and pressure conditions during the extrusion of the bar 20-2. The y axis on the left shows the extrusion pressure, while the one on the right shows the temperature.

5.3 Characterisation of the Extruded Composite Bars

This section describes the microstructural characterisation of the composite bars produced and relates these results to the batch of powder they were made from and their extrusion conditions. Two bars of each composition were extruded successfully, one from batch 1 and one from batch 2. The 10-1a and 20-1a bars were produced during a previous project [Ped-10] and specimens were received and further analysed during the current project.

5.3.1 Microstructural Characterisation of the Composites Containing 10 vol% Pure Al Fibres

5.3.1.1 XRD

The 10-1a bar was received from a previous project [Ped-10] and further analysis was performed. Its extrusion temperature was 388 °C, lower than the 400 °C necessary to extrude the pure alloy bar produced during the same project.

The previous projects microstructural characterisation of the 10-1a bar involved an XRD analysis of the cross section, the longitudinal section and the ground up filings made from the front of the bar. It showed that the microstructure and phases present did not change from the pure alloy to the extruded composite matrix. α-Al peaks were identified by indexing the reflections corresponding to the (111), (200), (220), (311), (222) and (400) planes in the 2θ = 20 °-100 ° range at 38.5 ° (100% intensity), 44.7 °, 65.2 °, 78.3 °, 82.5 ° and 99.2 ° [JCP-99] showing that a large proportion of the microstructure was made of a FCC-Al. Icosahedral phase could also be identified by broad peaks at 2θ ~ 22.9 °, 41.3 °, 43.5 °, 61.6 ° and 73.7 ° which were the 2θ values calculated following the icosahedral indexation scheme by other authors on an alloy of the same nominal chemical composition [Gal-09a], [Aud-02]. Additionally, the peaks found in the powders before extrusion at 2θ ~ 36.7 °and 75.5 ° were attributed to the metastable phase labelled by other authors as distorted monoclinic θ-$Al_{13}(Cr, Fe)_{2-4}$. θ-phase was no longer present after extrusion as an identifiable peak. The texture of the front of the bar was analysed in a qualitative way by comparing peak intensities concluding that anisotropy was likely to be found in this bar [Ped-10].

The analysis performed in the previous project did not include X-ray diffractograms of the back of the bar, which were performed to check for consistency and homogeneity within the extruded bar. They can be seen in Figure 5.4. The microstructure of the back of the bar consisted of an α-Al matrix and icosahedral phase. The θ-phase which was detected in the powder was no longer present in the front or the back of the bar after extrusion at 388 °C. If other intermetallic phases were present, a further investigation with other techniques is necessary to detect them.

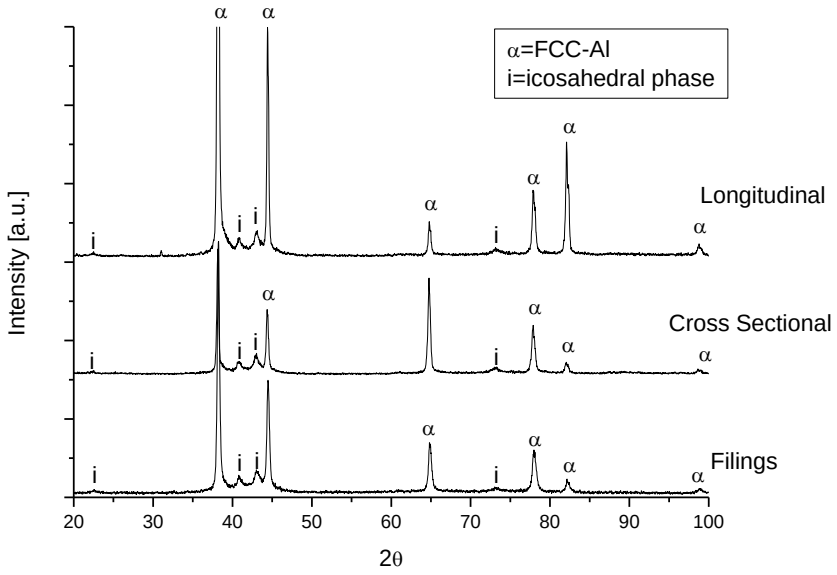

(a)

Figure 5.4: (a) XRD analysis of a longitudinal section, cross section and filings made from the back of the 10-1a bar to check for homogeneity with the front of the bar[Ped-10].

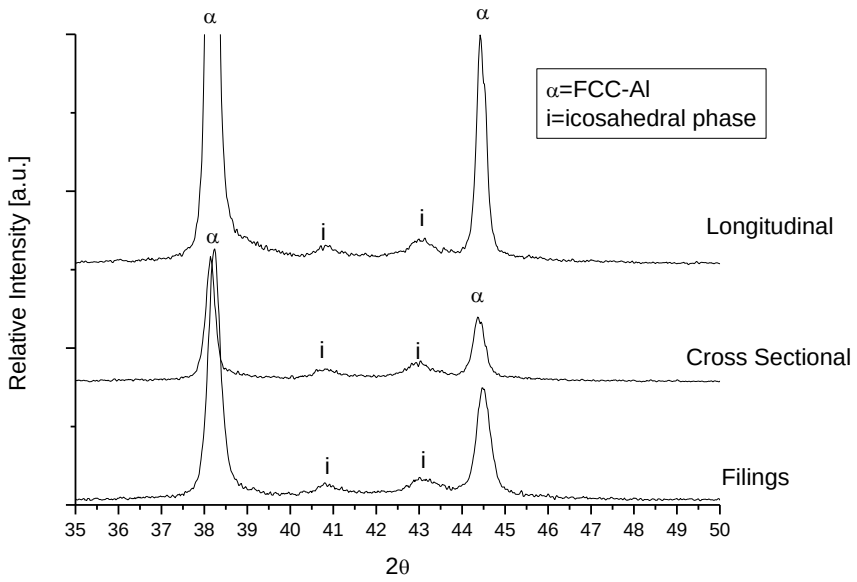

(b)

Figure 5.4: (b) an enlargement of the central section from 35-50 ° for a clearer peak identification.

Qualitative texture analysis performed by intensity comparison of the Al peaks is shown in Figure 5.5.

Both the front and the back of the bars were compared.

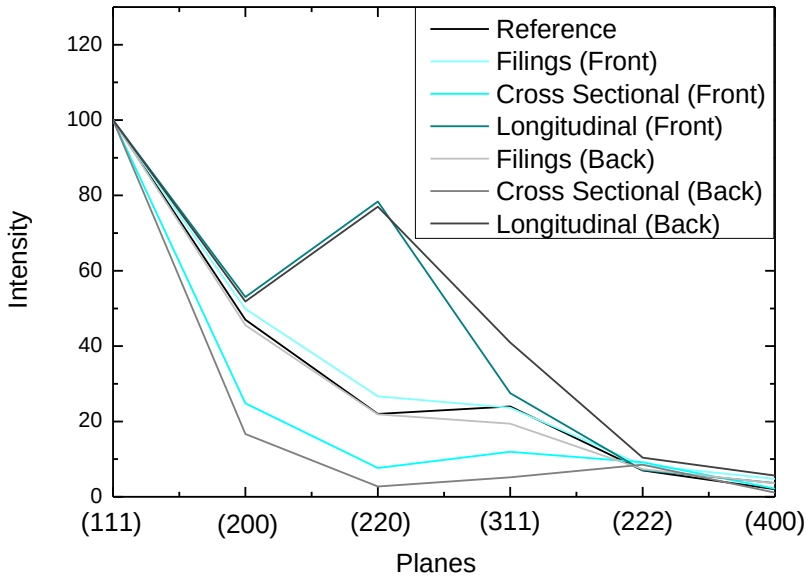

Figure 5.5: Texture analysis of the front and back of the 10-1a bar. The grey lines indicate the back of the bar while the blue ones the front. The analysis of peak intensity from the front of the bar was obtained from the XRD curves from a previous project [Ped-10].

According to Figure 5.5, the filings produced by grinding the front and back of the bar are untextured, their relative intensities matching the reference values. The cross section shows a texture reduction, particularly along the (200), (220) and (311) planes. In the longitudinal section, a large intensity (80% of the maximum intensity) was detected along (220) planes in both the front and the back of the bar.

The next bar analysed was the 10-1b bar, with the same composition as the 10-1a bar, which was pre-heated and extruded at a maximum temperature of 383 ℃.

The phases present in the 10-1b bar after extrusion were also analysed by XRD in the cross section, the longitudinal section and filings produced by grinding the bar. The X-ray diffractograms are shown in Figure 5.6. The phases detected were mainly FCC-Al and icosahedral phase. α-Al peaks were identified by indexing the reflections corresponding to the (111), (200), (220), (311), (222) and (400) planes at 38.5 ° (100% intensity), 44.7 °, 65.2 °, 78.3 °, 82.5 ° and 99.2 ° [JCP-99]. Icosahedral phase could also be identified by broad peaks at 2θ ~ 22.9 °, 41.3 °, 43.5 °, 61.6 ° and 73.7 ° [Gal-09a], [Aud-02]. The XRD scans were checked for metastable θ-phase and in this case the extrusion temperature of 383°C appears not have caused the complete decomposition of the θ-phase. The peaks attributed to the metastable phase labelled by other authors as distorted monoclinic θ-$Al_{13}(Cr, Fe)_{2-4}$ were found at 2θ ~ 36.7 °and 75.5 °. Other peaks from this phase were found to overlap with the large FCC-Al peaks.

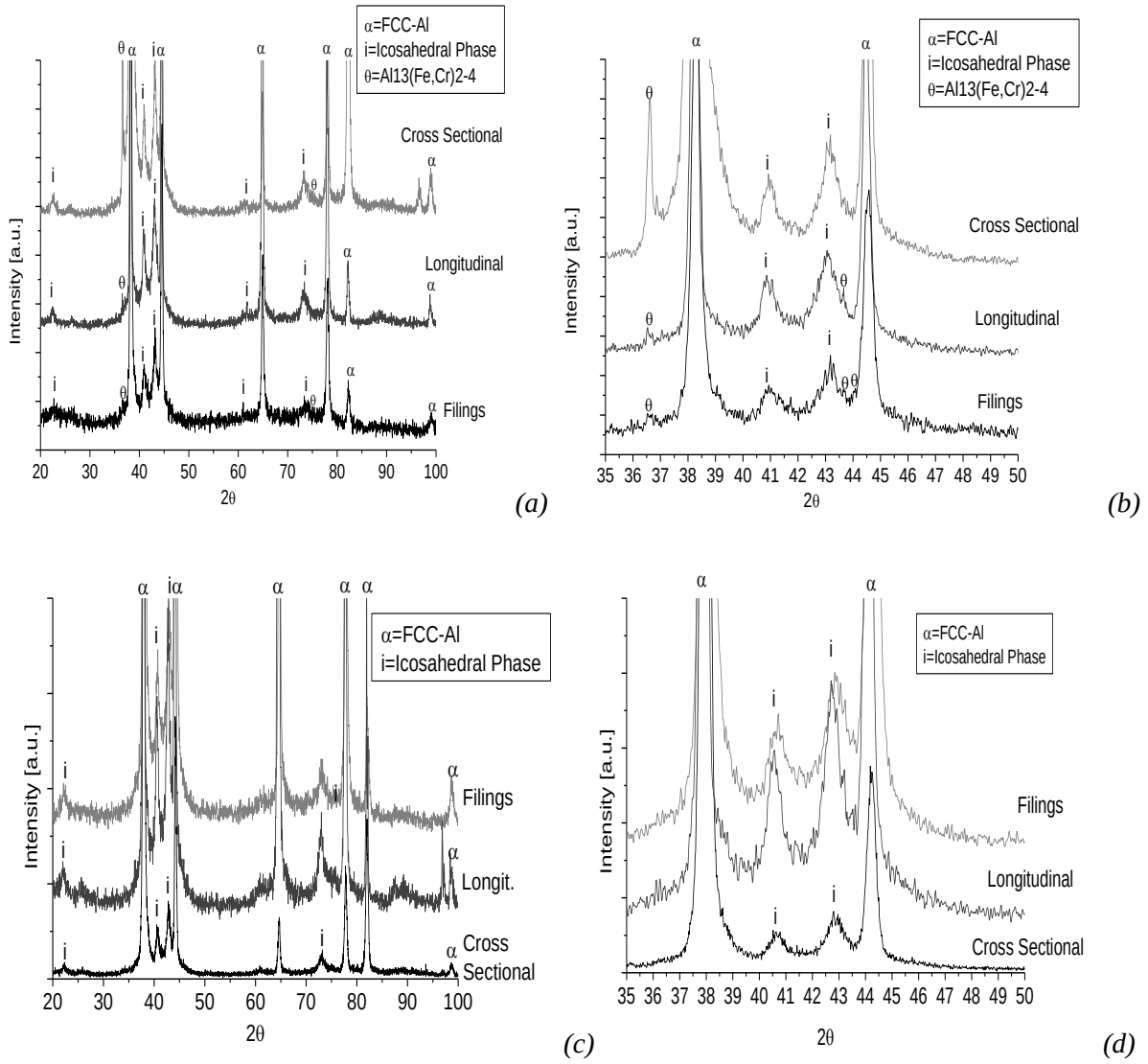

Figure 5.6: (a) x-ray diffractogram of the front of the 10-1b bar showing a cross section, a longitudinal section and powder made by grinding the bar and (b) an enlargement of the 35-50 ° section of the diffractogram to allow easier phase identification. (c) x-ray diffractogram of the back of the 10-1b bar showing a cross section, a longitudinal section and powder made by grinding the bar and (d) an enlargement of the 35-50 ° section of the diffractogram to allow easier phase identification.

Texture was introduced in the FCC α-Al matrix during extrusion. A qualitative analysis of the texture of the front and back of the bar 10-1b produced by comparison of relative intensities of the Al peaks can be seen in Figure 5.7.

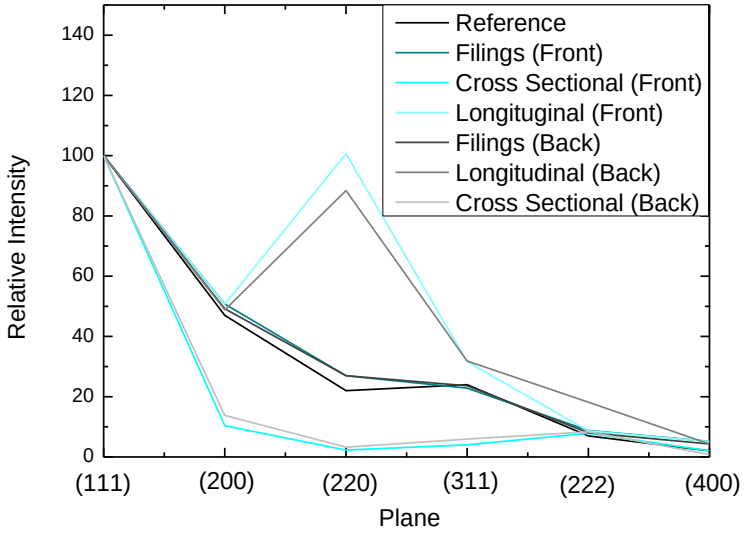

Figure 5.7: Texture analysis of the front and back of the 10-1b bar. The grey lines indicate the back of the bar while the blue ones the front.

The texture analysis of the 10-1b bar showed that the filings were untextured. Their relative intensities matched the reference values both in the front and the back of the bar. The cross section showed reduced texture along that plane and along the (200) and (311) planes. A higher intensity, between 90-100% of the maximum intensity of the (111) reference plane, was detected along the (220) plane in both the front and the back of the bar, in the longitudinal section.

The third bar produced with 10 vol% added Al was the 10-2 bar. It was pre-heated and extruded at a maximum temperature of 419 °C, which is 31-36 °C higher than the 10-1a and 10-1b bars.

The 10-2 bar required a higher breakthrough pressure compared to the other two composite bars. The pressure was 1667 MPa for the 10-2 bar and 1641 MPa and 1568 MPa for the 10-1b and 10-1a bars respectively. We therefore must conclude that this batch of powder requires higher threshold stress to initiate plastic flow. This is likely to be a combination of the composition being slightly depleted in Al (0.1 at% less than the previous batch) and enriched in Cr, Ti and Fe and also the lack of pure Al contamination in this powder batch, which in the 10-1a bar was estimated at 2-3 vol% and in the

10-1b bar could not be detected. A reduction as subtle as 0.8 at% in the Al content of an atomised $Al_{93}Fe_3Cr_2Nb_2$ alloy powder was shown to increase the breakthrough pressure by 300 MPa [Rou-12].

The phases present in the 10-2 bar after extrusion were analysed and the result of these scans are shown in Figure 5.8. The microstructure consists mainly of FCC Al and icosahedral phase. α-Al peaks were identified by indexing the reflections corresponding to the (111), (200), (220), (311), (222) and (400) planes at 38.5 ° (100% intensity), 44.7 °, 65.2 °, 78.3 °, 82.5 ° and 99.2 ° [JCP-99]. Icosahedral phase could also be identified by broad peaks at 2θ ~ 22.9 °, 41.3 °, 43.5 °, 61.6 ° and 73.7 ° [Gal-09a], [Aud-02]. The XRD scans were checked for metastable θ-phase and in this case it was also still present. The peaks attributed to θ-Al_{13}(Cr, Fe)$_{2-4}$ were found at 2θ ~ 36.7 °and 75.5 °. Other peaks from this phase were found to overlap with the large FCC-Al peaks. Small volume fractions of Al_3Ti intermetallic phase can also be identified through the peaks at 39.3 °, 45.6 °, 66.5 °, 80.1 ° and 84.4 ° corresponding to the (111), (200), (220), (311) and (222) planes [JCP-99].

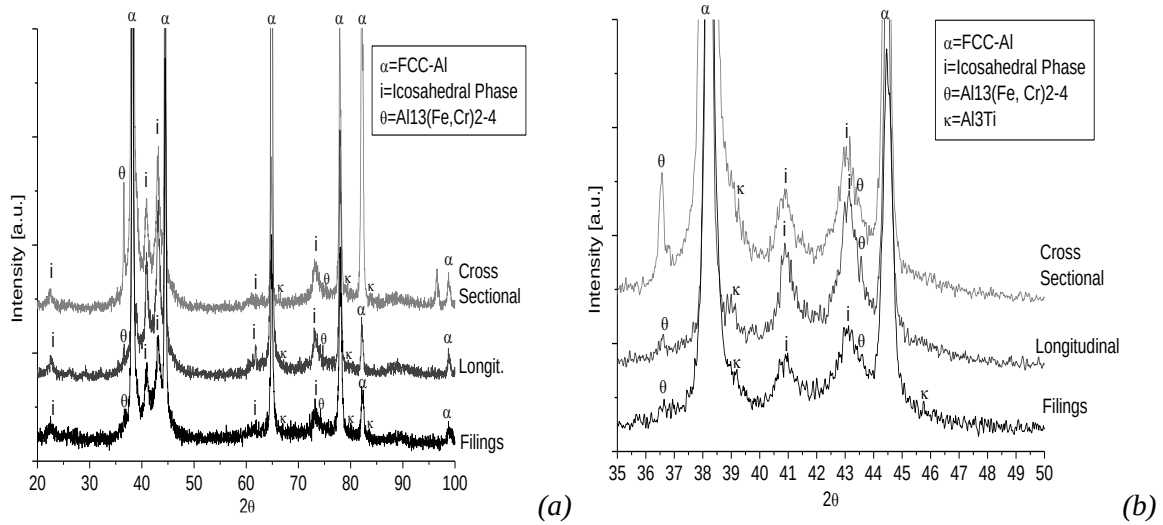

Figure 5.8: (a) x-ray diffractogram of the front of the 10-2 bar showing a cross section, a longitudinal section and filings made by grinding the bar. (b) an enlargement of the 35-50 ° section of the diffractogram to allow easier phase identification.

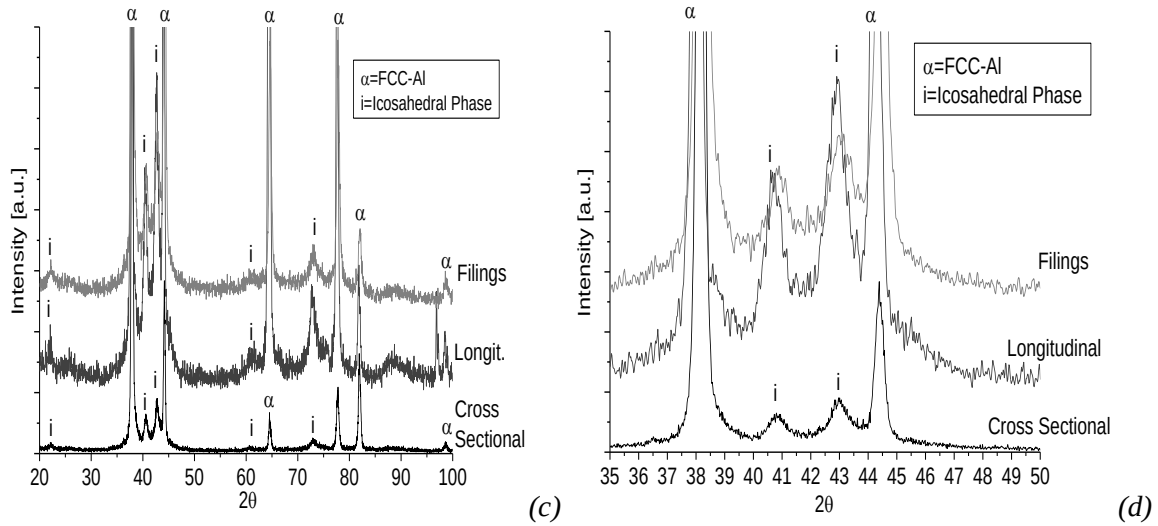

Figure 5.8: (cont.): (c) x-ray diffractogram of the back of the 10-2 bar showing a cross section, a longitudinal section and powder made by grinding the bar. (d) an enlargement of the 35-50 ° section of the diffractogram to allow easier phase identification.

Texture and a preferred orientation were also qualitatively analysed in this bar, and the comparison of the Al peak intensities can be seen in Figure 5.9.

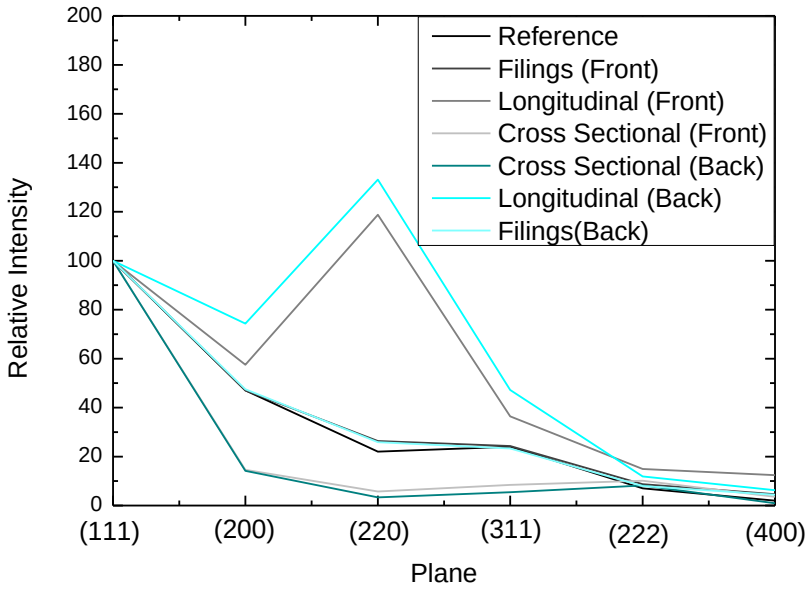

Figure 5.9: Texture analysis of the front and back of the 10-2 bar. The grey lines indicate the back of the bar while the blue ones the front.

No difference in the texture of the back and front of the bars was detected beyond the reasonable experimental error. The (111) plane was taken as reference and assumed to be 100% intensity. In the 10-2 bar, the filings were untextured. The cross section showed reduced texture along the (200), (220) and (311), which is consistent with the analysis of the 10-1b and 10-1a bars. The (220) plane intensity detected exceeded that of the (111) being 130% and 120% in the longitudinal sections of the front and the back of the bar respectively.

5.3.1.2 SEM

The microstructural characterisation performed on the 10-1a bar during a previous project included SEM microscopy of the front of the bar. This analysis revealed a structure made of deformed well bonded powder particles with no evidence of residual porosity. The pure Al powders were visible, and the powder particles had deformed into elongated fibres [Ped-10].

SEM microscopy of the front of the 10-1b and 10-2 bars was performed. Some of the micrographs produced can be seen in Figure 5.10. Figure 5.10 (a) and (b) show backscattered electron micrographs of the overall microstructure produced, revealing a well compacted microstructure with no porosity or large defects. The pure Al particles deformed and bonded to the matrix forming fibres, highlighted in Figure 5.10 (b) and (d). Some smaller, undeformed satellite particles can also be seen, particularly within the pure Al fibres, highlighted in Figure 5.10 (a) and (c). Some of the larger intermetallic phases which could also be seen in the powders and the extruded pure alloy bars in Chapter 4 are also still present, as shown in Figure 5.10 (b).

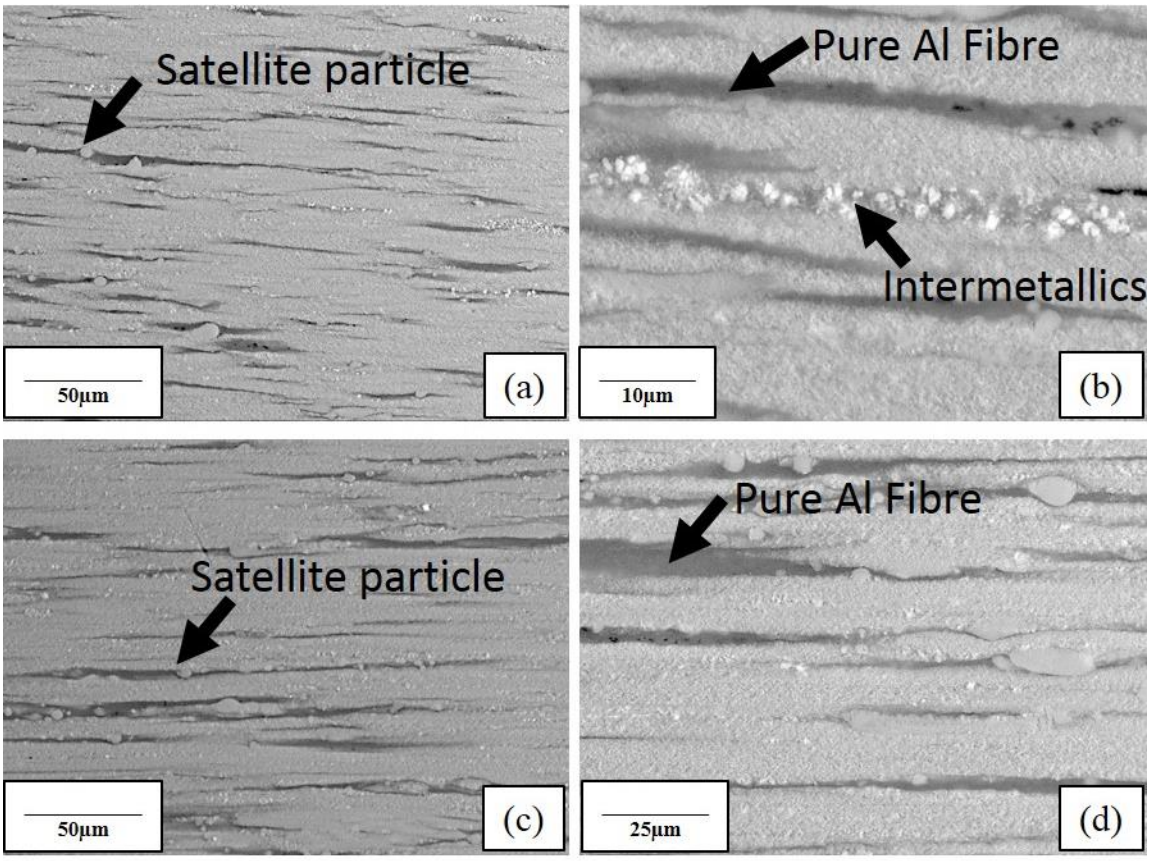

Figure 5.10: (a) SEM backscattered image showing the microstructure of the 10-1b bar and (b) a higher magnification overview with larger intermetallic particles, (c) SEM backscattered image showing the microstructure of the 10-2 bar and (d) a higher magnification overview with satellite particles in the pure Al fibres.

Some of the pure Al contamination could have been present in the 10-1b bar, but from the micrographs taken the pure Al content was estimated around ~10 vol%. This bar required a higher extrusion breakthrough pressure compared to the 10-1a bar. The pressure was 1641 MPa for the 10-1b bar and 1568 MPa for the 10-1a bar, despite both having nominal composition of 10 vol% pure Al. The 10-1a bar was shown to have ~12-13 vol% pure Al, of which 10vol% was a deliberate addition and the rest was contamination. Pure Al contamination was random within each batch of powder and non-consecutive extrusion runs were likely to vary. The composition of the 10-2 bar was estimated at 10 vol% pure Al.

5.3.1.3 TEM

Further microstructural analysis to confirm the phases present in the bars after extrusion and complement the XRD results was performed by TEM on all three of the extruded composite bars. The analysis performed on the 10-1a bar during a previous project did not include TEM [Ped-10]. Bright field TEM micrographs were taken with corresponding convergent beam diffraction patterns. These micrographs can be seen in Figure 5.11.

Lower magnification overviews of the microstructures of the 10-1a, 10-1b and 10-2 can be seen in Figure 5.11 (a), (c) and (e) respectively. They show a microstructure composed of spherical, evenly distributed dispersoids in an Al matrix. The dispersoids were confirmed to consist of icosahedral phase particles with their corresponding 5-fold symmetry diffraction patterns, which can be seen in Figure 5.11 (b), (d) and (f). This was consistent across the 10-1a, 10-1b and 10-2 bars.

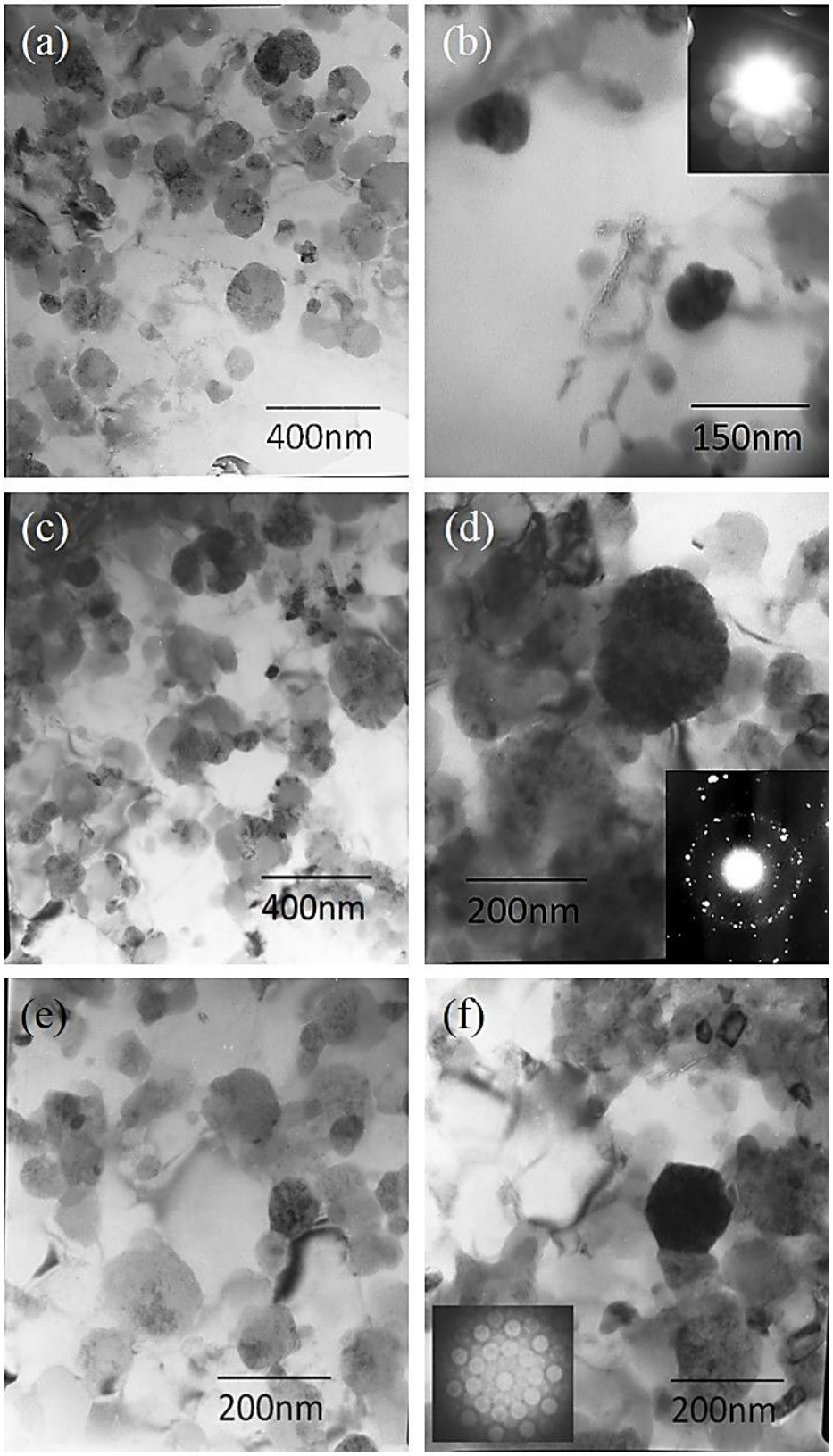

Figure 5.11: (a) Overall bar microstructure from the 10-1a bar, (b) 5x symmetry diffraction pattern from a particle of icosahedral phase in the bar 10-1a, (c) overall microstructure of the 10-1b bar, (d) 5-fold symmetry diffraction pattern associated with the icosahedral phase in the bar 10-1b, (e) overall microstructure of the 10-2 bar and (f) 5x symmetry diffraction pattern and micrograph of a particle of icosahedral phase in the bar 10-2.

TEM-EDX was used to confirm matrix compositions. Errors in the TEM-EDX measurements have been minimised by tilting the samples to establish whether the areas measured by EDX consisted solely of matrix with no underlying particles. Values for solutes in solid solution are found in Table 5.3.

	10-1a		*10-1b*		*10-2*	
Element	*Average*	*St Dev*	*Average*	*St Dev*	*Average*	*St Dev*
Al	*98.2*	*0.2*	*97.7*	*0.4*	*98.8*	*0.3*
Ti	*1.3*	*0.2*	*1.3*	*0.4*	*0.6*	*0.2*
Cr	*0.4*	*0.2*	*0.5*	*0.1*	*0.3*	*0.1*
Fe	*0.2*	*0.1*	*0.4*	*0.3*	*0.3*	*0.2*

Table 5.3: Matrix composition in the 10-1a, 10-1b and 10-2 composite bars, removing the C, and O impurities that come from processing and the top oxide layer.

The measured chemical composition by TEM-EDX of the bars after extrusion showed to be within the error bars of the powder matrix composition from their respective batches of origin, which can be found in Chapter 4, Table 4.2. In both cases the solute content in solid solution was higher than the equilibrium solid solubility of Fe (0.02 at%), Cr (0.18 at%) and Ti (0.032 at%) in Al even after the extrusion at 383 °C, 388 °C and 419 °C in the 10-1a, 10-1b and 10-2 bars respectively [Mas-90], [Mon-43], [Xu-06].

5.3.2 Microstructural Characterisation of the Composites Containing 20 vol% Pure Al Fibres

Two bars containing 20 vol% pure Al fibres were extruded, one from batch 1 and one from batch 2 and then compared to the 20-1a bar produced during a previous project [Ped-10]. The following sections compare their microstructures.

5.3.2.1 XRD

The 20-1a bar was extruded during a previous project [Ped-10]. Its extrusion temperature was 389 °C, and the ram pressure was 1339 MPa.

The previous projects microstructural characterisation involved an XRD analysis of the cross section, the longitudinal section and the ground up filings made from the front of the bar. It showed that the microstructure was made of mainly of FCC-Al and icosahedral phase. The metastable θ-phase was no longer present as an identifiable peak. Smaller amounts of other intermetallic phases could be present, but below the XRD detection limit. The texture of the front of the bar was analysed in a qualitative way and concluded that anisotropy was likely to be found in this bar [Ped-10].

The previous project did not include X-ray diffractograms of the back of the bar, which were performed to check for consistency and homogeneity within the extruded bar and can be seen in Figure 5.12. The microstructure of the back of the bar was also shown to consist of an α-Al matrix and icosahedral phase. The θ-phase which was detected in the powder is no longer visible in the bar after extrusion at 389 °C by XRD. α-Al peaks were identified by indexing the reflections corresponding to the (111), (200), (220), (311), (222) and (400) planes in the 2θ = 20 °-100 ° range at 38.5 ° (100% intensity), 44.7 °, 65.2 °, 78.3 °, 82.5 ° and 99.2 ° [JCP-99]. Icosahedral phase was shown by peaks at 2θ ~ 22.9 °, 41.3 °, 43.5 °, 61.6 ° and 73.7 ° [Cah-86], [Gal-09a], [Aud-02].

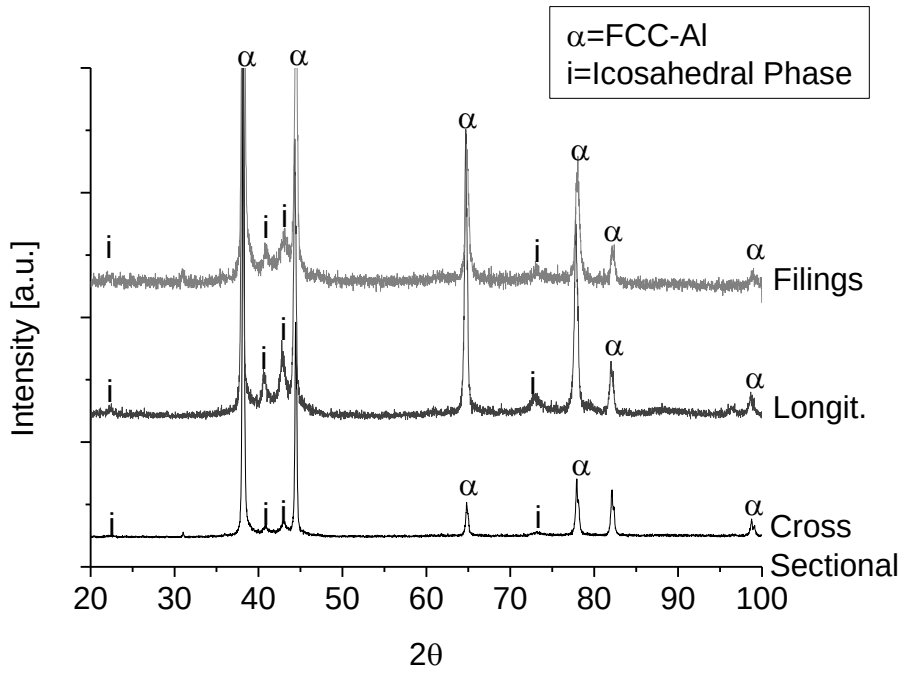

(a)

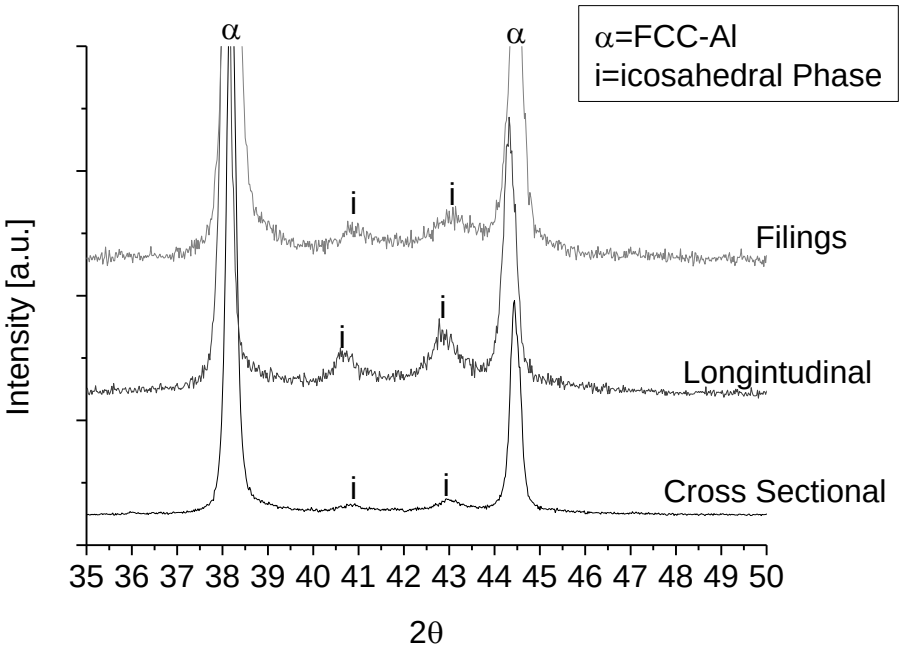

(b)

Figure 5.12: (a) XRD analysis of a longitudinal section, cross section and filings made from the back of the 20-1a bar to check for homogeneity with the front of the bar, (b) an enlargement of the central section from 35-50° for a clearer peak identification.

The intensity of the aluminium peaks in Figure 5.12 was compared to analyse qualitatively the presence and potential differences in texture between the front and the back of the bar. This is shown in Figure 5.13.

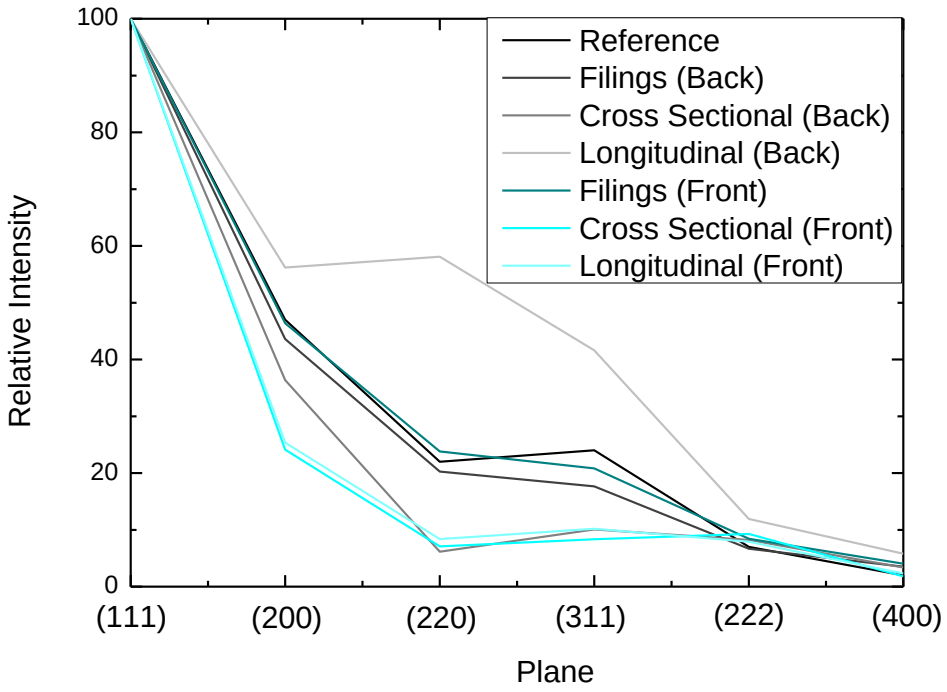

Figure 5.13: Texture analysis of the front and back of the 20-1a bar. The grey lines indicate the back of the bar while the blue ones the front.

The filings taken from the front and the back of the bar were untextured, matching the selected reference [JCP-99]. The cross section showed reduced texture along the (200), (220) and (311), which was consistent with the analysis of the 10-2, 10-1b and 10-1a bars. The peak intensity comparison revealed a difference in the texture between the back and front of the 20-1a bar in the longitudinal section. In this case the (220) plane intensity detected was 60% that of the reference (111) plane in the back of the bar. The longitudinal section of the front of the bar showed <10% intensity along the (220) direction, measured on the XRD plots taken from a previous projects analysis [Ped-10].

The 20-1b bar was also analysed by XRD. It was extruded at a maximum temperature of 405 °C.

This bar required an extrusion ram pressure of 1460 MPa, which is higher than the 1339 MPa needed to extrude the 20-1a bar at 389 °C. The phases present in the 20-1b bar after extrusion were analysed

and shown in Figure 5.14. Figure 5.14 (a) and (b) show the X-ray diffractograms of the samples taken from the front of the bar and (c) and (d) show the back of the bar.

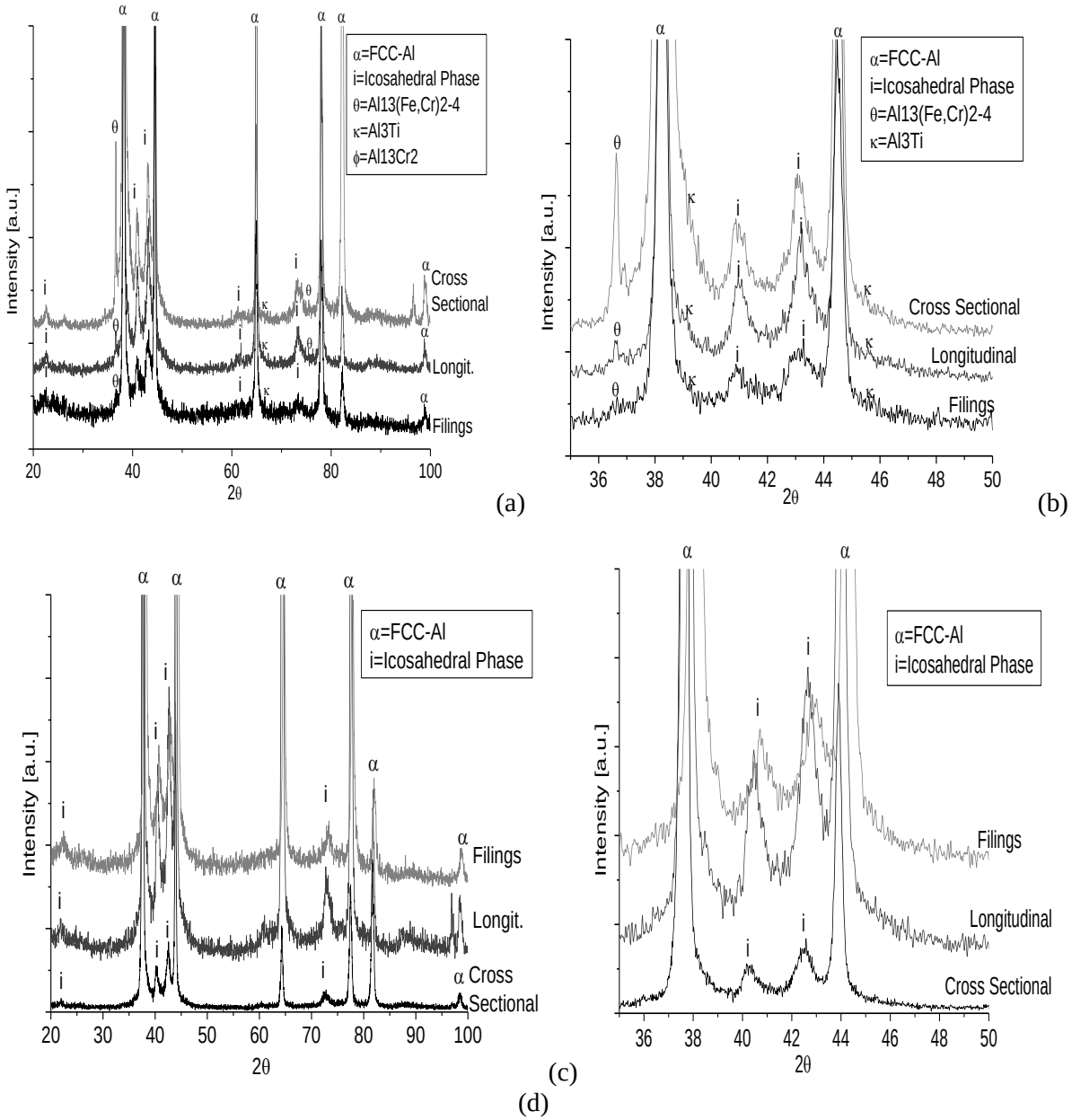

Figure 5.14: (a) X-ray diffractogram of the front of the 20-1b bar showing a cross section, a longitudinal section and powder made by grinding the bar. (b) an enlargement of the 35-50 ° section of the diffractogram, (c) X-ray diffractogram of the back of the 20-1b bar and (d) an enlargement of the 35-50 ° section of the diffractogram.

The phase analysis was consistent with all the previously produced bars consisting mainly of FCC-Al and icosahedral phase. α-Al peaks were identified by indexing the reflections corresponding to the (111), (200), (220), (311), (222) and (400) planes in the 2θ = 20°-100° range at 38.5 ° (100% intensity), 44.7 °, 65.2 °, 78.3 °, 82.5 ° and 99.2 ° [JCP-99]. Icosahedral phase was shown by peaks at 2θ ~ 22.9 °, 41.3 °, 43.5 °, 61.6 ° and 73.7 ° [Cah-86], [Gal-09a], [Aud-02]. The extrusion temperature of 405°C appears not have caused the complete decomposition of the θ-phase in the 20-1b bar, visible in the front of the bar in Figure 5.14 (a) and (b). Peaks at 2θ ~ 36.7 °and 75.5 ° were attributed to the θ-$Al_{13}(Cr,Fe)_{2\text{-}4}$ phase. It is also possible that it was not held at this temperature long enough to cause complete decomposition of the θ-phase. Al_3Ti intermetallic phase could also be identified through the peaks at 39.3 °, 45.6 ° and 66.5 corresponding to the (111), (200) and (220) planes [JCP-99].

The texture was analysed qualitatively by peak intensity comparison, in the front and the back of the bar 20-1b. It can be seen in Figure 5.15.

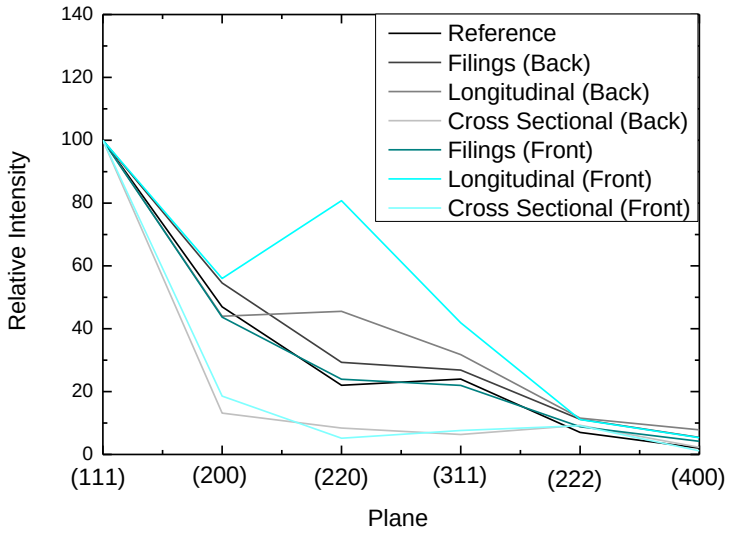

Figure 5.15: Texture analysis of the front and back of the 20-1b bar. The grey lines indicate the back of the bar while the blue ones the front.

The texture analysis of the 20-1b bar showed that the filings are untextured, their relative intensities matching the reference values. A higher intensity, 80% of the maximum intensity of the (111) reference plane, was detected along the (220) plane in the front of the bar in the longitudinal section and ~50% of the maximum intensity was detected along this plane in the back of the bar. The cross section shows reduced texture along that plane and along the (200) and (311).

The second bar produced with 20 vol% pure Al fibre additions was the 20-2 bar. This bar was pre-heated and extruded at a maximum temperature of 400 °C. This bar required the same ram pressure as the 20-1b to extrude. The pressure was 1460 MPa and the temperature at which the 20-1b was extruded was 405 °C while the 20-2 bar was extruded at 400 °C.

The results of the XRD phase analysis from the front and the back of the 20-2 bar are shown in Figure 5.16. The microstructure consists mainly of FCC Al and icosahedral phase. α-Al peaks were identified by indexing the reflections corresponding to the (111), (200), (220), (311), (222) and (400) planes in the 2θ = 20 °-100 ° range at 38.5 ° (100% intensity), 44.7 °, 65.2 °, 78.3 °, 82.5 ° and 99.2 ° [JCP-99]. Icosahedral phase was shown by peaks at 2θ ~ 22.9 °, 41.3 °, 43.5 °, 61.6 ° and 73.7 ° [Cah-86], [Gal-09a], [Aud-02]. θ-phase was detected with peaks at 2θ ~ 36.7 ° and 75.5 °. It was also still present in the 10-2 bar, the only other successful extrusion produced from the 2nd powder batch.

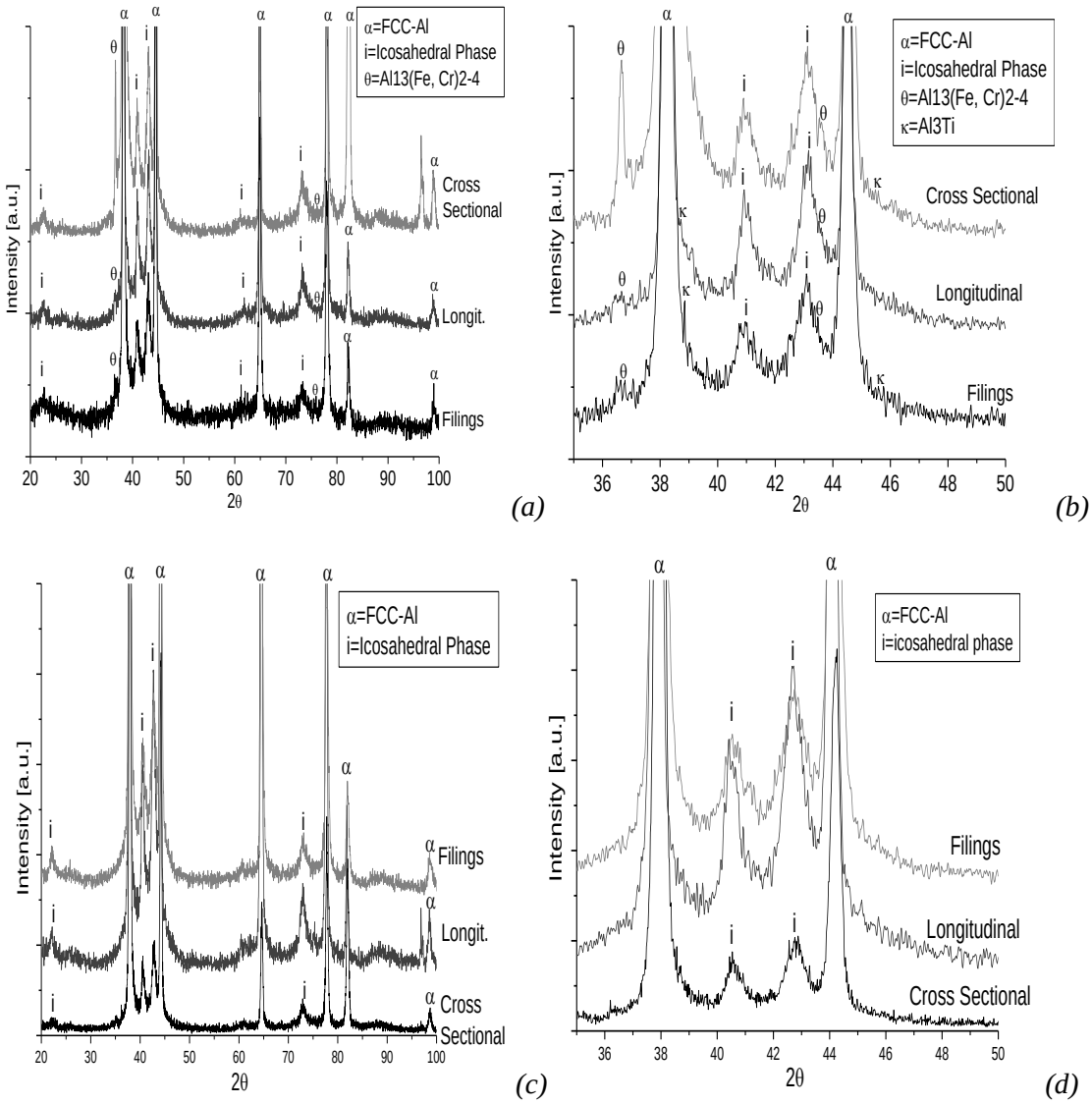

Figure 5.16: (a) x-ray diffractogram of the 20-2 bar showing a cross section, a longitudinal section and filings made by grinding the bar. (b) an enlargement of the 35-50 ° section of the diffractogram to allow easier phase identification, (c) x-ray diffractogram of the back of the 20-2 bar showing a cross section, a longitudinal section and powder made by grinding the bar. (d) an enlargement of the 35-50 ° section of the diffractogram to allow easier phase identification.

Qualitative texture analysis of the front and the back of the 20-2 bar was also performed and can be seen in Figure 5.17.

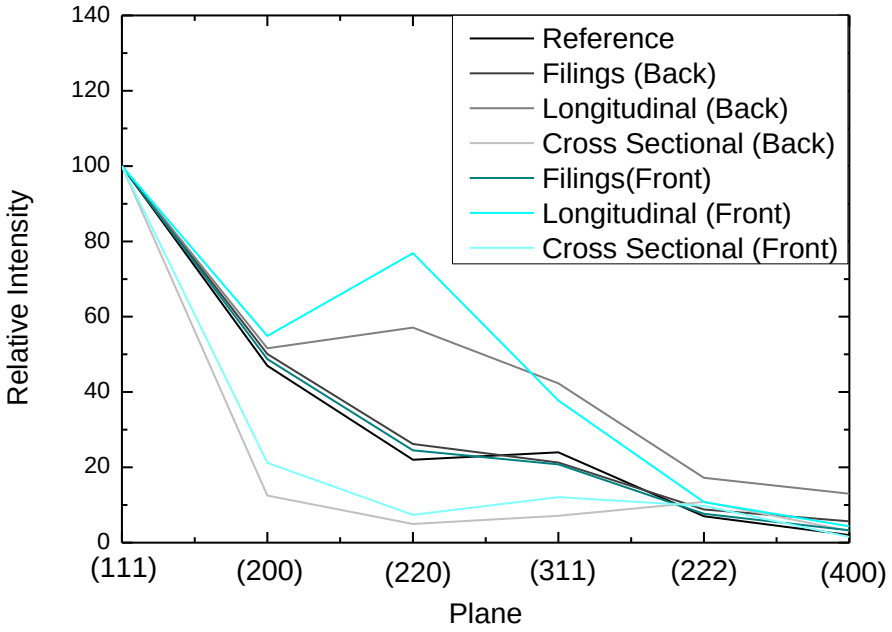

Figure 5.17: Texture analysis of the front and back of the 20-2 bar. The grey lines indicate the back of the bar while the blue ones the front.

The texture analysis of the 20-2 bar showed that the filings are untextured. A higher relative intensity, 75% of the maximum intensity of the (111) reference plane, was detected along the (220) plane in the front of the bar in the longitudinal section and ~60% of the maximum intensity was detected along this plane in the back of the bar. The cross section shows reduced texture along that plane and along the (200) and (311).

5.3.2.2 SEM

The microstructural characterisation performed on the 20-1a bar during a previous project also included SEM microscopy of the front of the bar. This analysis revealed a structure made of deformed well bonded powder particles with no evidence of residual porosity. The pure Al powders were visible, and the powder particles had deformed into elongated fibres [Ped-10].

SEM analysis of the 20-1b and 20-2 bars was performed in order to have an overview of the microstructure and the pure Al fibres. SEM micrographs of the bars can be seen in Figure 5.18. As with all the previous bars, no obvious defects or porosity were observed. The pure Al particles

deformed and bonded to the matrix forming fibres, which have been highlighted by arrows in Figure 5.18 (a) and (c). Some smaller, undeformed satellite particles could also be observed, particularly within the pure Al fibres. These can be seen in Figure 5.18 (b) and (d). Larger powder particles had a coarser microstructure made of larger intermetallic phases which have been highlighted in Figure 5.18 (b) and (d).

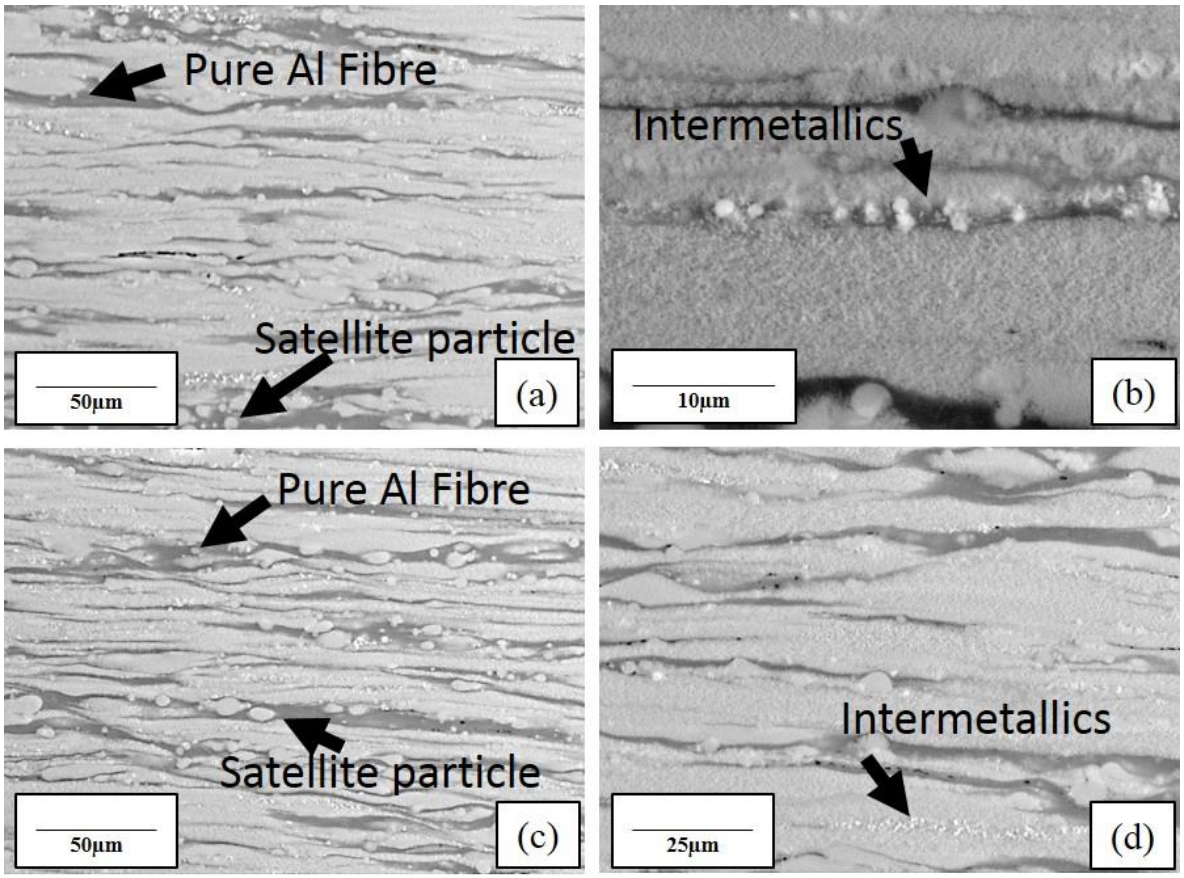

Figure 5.18: (a) SEM backscattered image showing the microstructure of the 20-1b bar, (b) a higher magnification overview of the larger intermetallic phases present, (c) SEM low magnification overview of the 20-2 extruded bar and (d) higher magnification detail showing some coarser intermetallic phases.

5.3.2.3 TEM

Further microstructural analysis to confirm the phases present in the bars after extrusion and complement the XRD results was performed by TEM. Bright field TEM micrographs were taken and convergent beam diffraction patterns. These micrographs can be seen in Figure 5.19.

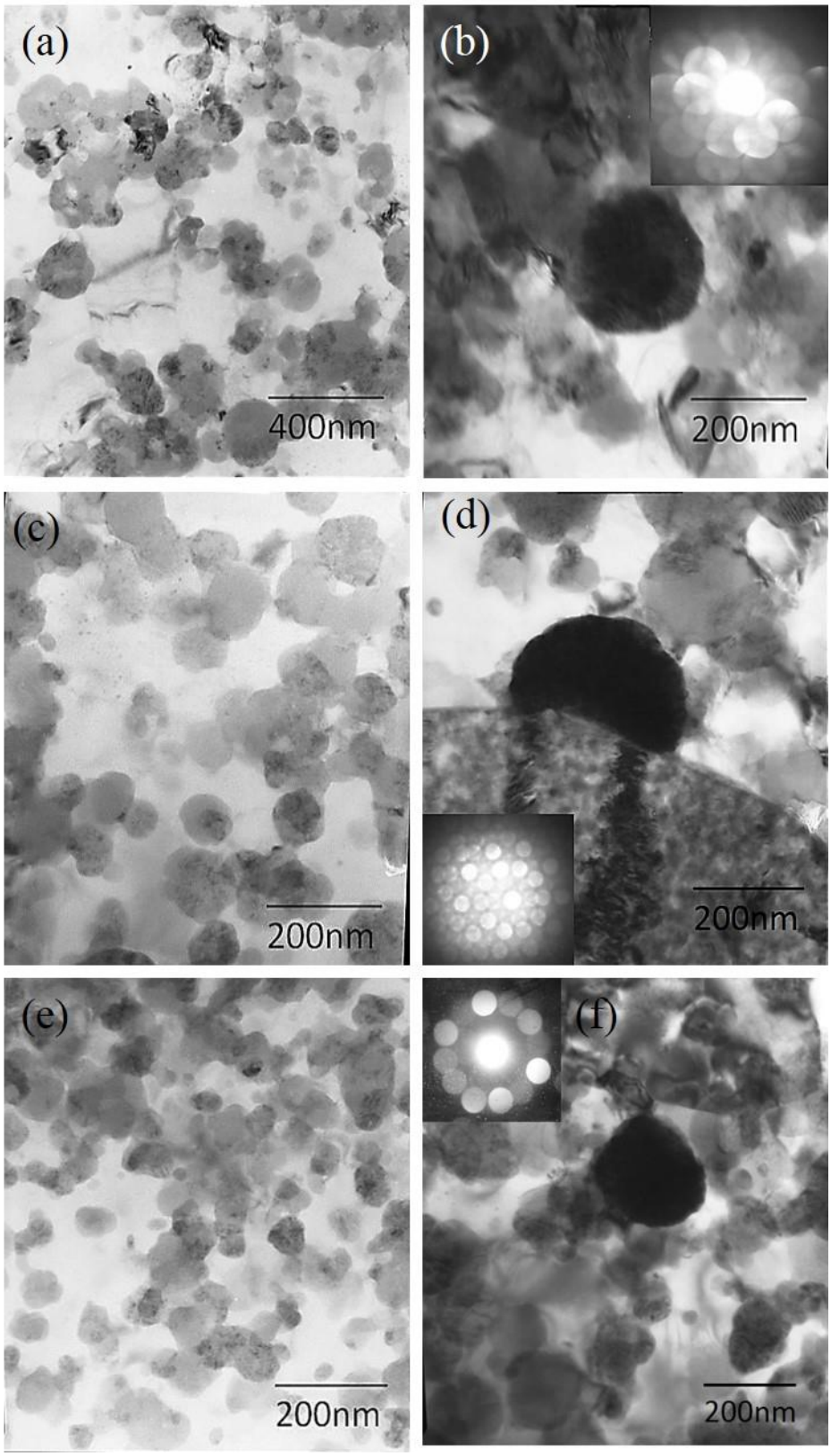

Figure 5.19: (a) Overall bar microstructure from the 20-1a bar, (b) 5x symmetry diffraction pattern characteristic of the icosahedral phase. (c) Overall bar microstructure from the 20-1b bar, (d) 5x symmetry diffraction pattern characteristic of the icosahedral phase. (e) Overall bar microstructure from the 2 batch, (f) 5x symmetry diffraction pattern from the quasicrystalline particle.

Microstructural analysis by TEM showed FCC-Al containing icosahedral phase in the form of small, spherical dispersoids. An overview of the microstructure of the 20-1a, 20-1b and 20-2 bars can be seen in Figure 5.19 (a), (c) and (e). The presence of the icosahedral quasicrystalline phase was confirmed by obtaining the characteristic 5x symmetry diffraction patterns in each bar, which can be seen in Figure 5.19 (b), (d) and (f).

TEM-EDX was used to confirm matrix compositions. Values for solutes in solid solution are found in Table 5.4.

	20-1a		*20-1b*		*20-2a*	
Element	*Average*	*St Dev*	*Average*	*St Dev*	*Average*	*St Dev*
Al	*98.1*	*0.2*	*98.5*	*0.9*	*98.6*	*0.7*
Ti	*1.3*	*0.4*	*1.0*	*0.8*	*0.8*	*0.4*
Cr	*0.4*	*0.2*	*0.2*	*0.1*	*0.3*	*0.2*
Fe	*0.2*	*0.1*	*0.3*	*0.2*	*0.3*	*0.2*

Table 5.4: (a) Matrix composition in the 20-1b bar, removing the C, and O impurities that come from processing and the top oxide layer. Averages and errors calculated over 10 measurements.

The measured chemical composition of the α-Al matrix by TEM-EDX before and after extrusion in all the bars showed to be the same as the composition of the powder batch they were made of, within experimental error. All the bars also have a higher solute content than the equilibrium solid solubility of Fe, Cr and Ti in Al even after the extrusion at 389 °C, 405 °C and 400°C [Mas-90], [Mon-43], [Xu-06]. The chemical composition of the 20-1a and 20-1b bars is also consistent with the previously extruded bars 10-1a, 10-1b. The 10-2 and the 20-2 bars are consistent with each other.

5.4 Summary

The two batches of $Al_{93}Fe_3Cr_2Ti_2$ alloy powders were used to produce composite bars with the addition of 10 and 20 vol% pure Al powder.

The extrusion pressures and temperatures required for the 10-1b and 20-1b bars were higher than the 10-1a and 20-1a extruded bars from the same batch of powder during a previous project [Ped-10]. Two bars were successfully produced from the 2nd powder batch, indicating that 10 and 20 vol% fibres were enough to lower the breakthrough pressure below the safety limit of the extrusion press and improve extrudability of the strongest batch of powders analysed.

SEM analysis of all the bars revealed a structure made of deformed well bonded powder particles with no evidence of large defects or residual porosity. All the extruded composite bars still retained a microstructure consisting mainly of FCC Al and icosahedral phase, confirmed by XRD and TEM analysis. Metastable θ-phase was only identifiable by XRD in three of the bars. The measured chemical composition of the α-Al matrix by TEM-EDX in the powder and extruded bars was shown to be unchanged, consistent within each powder batch and have a higher solute content than the equilibrium solid solubility of Fe, Cr and Ti in Al even after the extrusion at up to 419°C [Mas-90], [Mon-43], [Xu-06]. A summary of the phases, matrix compositions and particle sizes present in each bar and powder can be found in Table 5.5.

The addition of pure Al particles before extrusion did not affect the phases present in the alloy. It did however reduce the extrusion breakthrough pressures and therefore the temperatures required, improving extrudability and lowering the chances of phase transformations during processing.

The presence of texture (seen qualitatively by XRD analysis) and the elongation of the powder particles into "bands" visible in the SEM micrographs shows that the powder particles underwent a significant amount of plastic deformation during extrusion. Each "band" has a slightly different microstructure, which could be attributed to the individual microstructure of what used to be an individual powder particle [Zia-95]. The extensive plastic deformation between the bands and the fact that they are well bonded indicates that the oxide layer between them should have broken up during extrusion [Kaw-94].

	Maximum Extrusion Temp	***Phases Present***				***Matrix composition at%***			
Sample		***α-Al***	***i-phase***	***θ-phase***	***κ-Al3Ti***	***Al***	***Fe***	***Cr***	***Ti***
10-1a	*388*	*X*	*X*			*98.2*	*0.24*	*0.43*	*1.29*
10-1b	*383*	*X*	*X*	*X*	*X*	*97.7*	*0.4*	*0.5*	*1.3*
10-2a	*419*	*X*	*X*			*98.8*	*0.3*	*0.3*	*0.6*
20-1a	*389*	*X*	*X*			*98.1*	*0.2*	*0.4*	*1.0*
20-1b	*405*	*X*	*X*	*X*	*X*	*98.5*	*0.3*	*0.2*	*1*
20-2a	*400*	*X*	*X*	*X*	*X*	*98.6*	*0.3*	*0.3*	*0.8*

Table 5.5: summary of the phases, matrix compositions and particle sizes present in each bar and powder.

5.5 Conclusions

Composite bars have been successfully produced using $Al_{93}Fe_3Cr_2Ti_2$ alloy powders with the addition of 10 and 20 vol% pure Al fibres.

Pure Al additions decreased the ram pressure and temperature required for extrusion without impacting the phases or the microstructures present in the Al-Fe-Cr-Ti powder.

Successful extrusions even with the strongest powder batch (batch 2) were possible due to pure Al additions despite the fact the pure alloy bar made from the same batch did not extrude.

The pure Al powder particles deformed and bonded to the matrix forming fibres. The microstructure of the bars produced was fully consolidated with no evidence of defects or porosity.

The matrix of the extruded composite bars was found to consist of icosahedral phase within an FCC-Al matrix with small amounts of Al_3Ti intermetallics in some of the bars.

References

[Aud-02] F. Audebert, F. Prima, M. Galano, M. Tomut, P. J. Warren, I. C. Stone, B. Cantor, Mat. Trans., (2002), A 43, 8, 2017.

[Cah-86] J. W. Cahn. D. Shechtman, D. Gratias, J. Mater. Res., (1986), 1, 1, 13.

[Gal-09a] M. Galano, F. Audebert, I.C. Stone, B. Cantor, Acta Mat., (2009), 57 5107–5119.

[Gal-04] M. Galano, F. Audebert, B. Cantor, I. Stone, Mat. Sci. Eng., (2004), A, 375-377, 1206-1211.

[Gu-09] W-H Gu, Masters Degree Thesis, University of Oxford, (2009).

[Ino-98] A. Inoue, Prog. Mat. Sci., (1998), 43, 365-520.

[JCP-99] JCPDS-International Centre for Diffraction Data (1999).

[Kaw-94] Y. Kawamura, A. Inoue, K. Sasamori, T. Masumoto, Mat. Sci. Eng., (1994), A181-182, 1174.

[Mas-90] T. B. Massalski, H. Okamoto, P. R. Subramian, L. Kacrzak, editors. *Binary alloy phase diagrams*, Materials Park (OH): ASM International, (1990).

[Mon-43] L. F. Mondolfo, *Metallography of Aluminum Alloys*, John Wiley & Sons, (1943).

[Ped-10] S. Pedrazzini, Masters Degree Thesis, University of Oxford, (2010).

[Rou-12] N. J. Rounthwaite, DPhil Thesis, University of Oxford, (2012).

[Smi-83] D. W. Smith, *Powder Metallurgy Applications, Advantages and Limitations*, ASM International 13, (1983).

[Tod-04] I. Todd, Z. Chlup, J.G. O'Dwyer, M. Lieblich, A. Garcia-Escorial, Mat. Sci. Eng., (2004), A 375–377, 1235–1238.

[Xu-06] L. Xu, Y. Y. Cui, Y. L. Hao, R. Yang, Mat. Sci. Eng., (2006), A 435–436, 638–647.

[Zho-91] J. Zhou, J. Duszczyk, J. Mat. Shap.Tech., (1989), 6, 241.

[Zia-95] A. Ziani, G. Michot, A. Pianelli, A. Redjaïmia, C. Y. Zahra, A. M. Zahra, J. Mat. Sci., (1995), 30, 11, 2921.

Chapter 6: Thermal Stability and Phase Transformations

This chapter analyses the thermal evolution of the microstructure of the as-atomised nanoquasicrystalline $Al_{93}Fe_3Cr_2Ti_2$ alloy powder from batches 1 and 2 and the pure Al powder to investigate reactions which would potentially occur during warm extrusion at temperatures up to 420 °C.

This chapter also analyses the thermal evolution of the microstructure of the extruded bars to observe any phase transformations and reactions that are likely to occur as heat is applied in order to process these alloys into engineering components.

DSC was initially performed to select heat treatment temperatures. Then heat treatments were performed in a furnace and complemented with a characterisation of the samples by SEM, XRD, TEM and microhardness indentations. The pure alloy bar 0-1a was initially analysed, then compared with the composite bars produced using the same atomised powder batch 10-1a and 20-1a.

6.1 Thermal Analysis of the Atomised $Al_{93}Fe_3Cr_2Ti_2$ Alloy Powders

Thermal analysis of both powder batches was performed by DSC at a heating rate of 40 °C/min. This was done to highlight which reactions and phase changes would be taking place with increasing temperature, with a particular interest in any reactions which were likely to occur during the time the powder was held at temperatures between 375-420 °C during extrusion. These scans can be seen in Figure 6.1, whereby peaks show exothermic reactions and troughs show endothermic reactions.

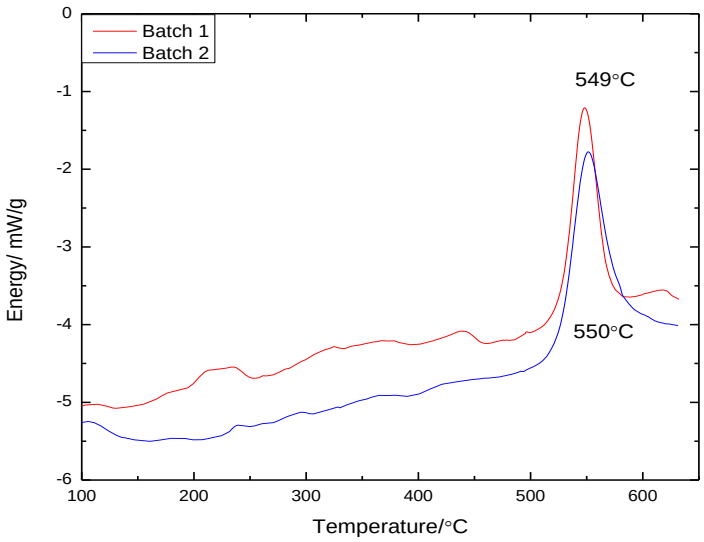

Figure 6.1: DSC scans of the powders at 40°C/minute up to 630 °C. Peaks show exothermic reactions, troughs show endothermic reactions.

In both powder batches the most evident reaction is a large, sharp exothermic peak at 550 °C. In the batch 2 powder the higher temperature shoulder of the peak is extended up to a more elevated temperature compared to the batch 1 powder. The onset of the peak and its maximum are however at the same temperature for both powder batches. The scans were processed by subtracting the empty pan, but some fluctuations in the baseline remain.

6.2 Thermal Analysis of the Atomised Pure Al Powder

In order to see if any reactions were likely to occur during the time the pure Al powder was held at temperatures between 383-420 °C for extrusion, DSC scans were performed. These scans can be seen in Figure 6.2. The major reaction observed begins at 630 °C and it shows the onset melting of the FCC-Al phase.

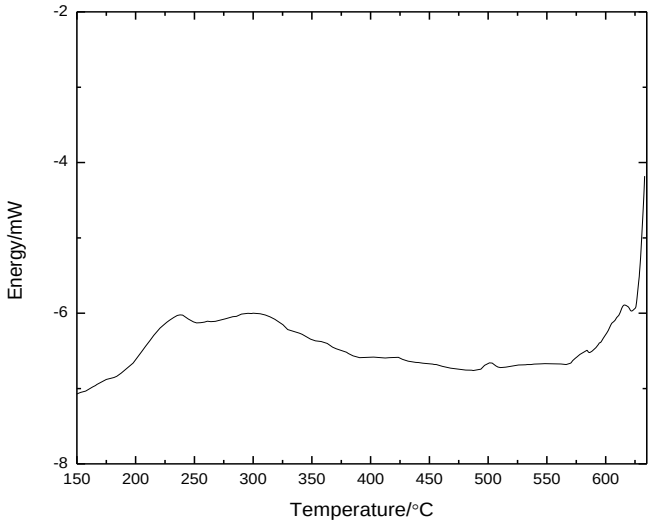

Figure 6.2: (a) DSC scans of the powders at 40 °C/minute up to 630 °C after subtracting the empty pan. Peaks show exothermic reactions, troughs show endothermic reactions.

6.3 Thermal Analysis of the Extruded $Al_{93}Fe_3Cr_2Ti_2$ Alloy Bar

6.3.1 DSC

DSC scans were performed on the pure alloy bar 0-1a at 40 °C/min up to 630 °C to study the stability and phase transformations that can take place in the extruded sample and establish what temperatures to use for heat treatments. The result of this scan can be seen in Figure 6.3. Peaks show exothermic reactions and troughs show endothermic reactions.

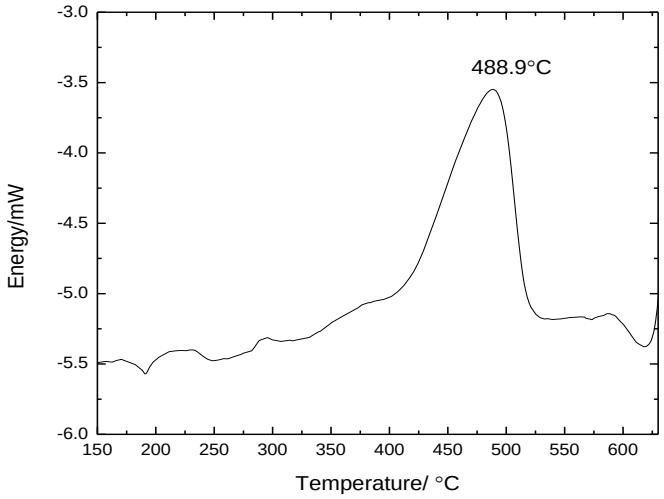

Figure 6.3: DSC scan of the 0-1a bar performed at 40 °C/min, showing the main exothermic event at 489 °C.

The main reaction detected by DSC in the 0-1a bar is a large, sharp exothermic peak at 489 °C. Despite the subtraction of the empty pan, fluctuations of the baseline at lower temperatures are still present.

6.3.2 Thermal Evolution: 1 Hour at 250 °C, 280 °C and 550 °C

Further thermal analysis of the extruded 0-1a bar was performed by heat treatments, followed by microhardness tests and microstructural characterisation. The temperatures for the heat treatments were selected based on the temperatures in which reactions were detected in the DSC scans, therefore 550 °C because it is just clear of the high temperature shoulder of the peak. Two more heat treatments were performed, both for one hour: one at 250 °C and one at 280 °C.

250 °C was selected as heat treatment temperature because mechanical tests of the 0-1a, 10-1a and 20-1a bars are available at 250 °C from a previous project and the bars retained 66% of their room temperature UTS at 250 °C [Ped-10], while conventional "high strength" 2020 T6 Al and 7178 T6 Al only retained 20% of their room temperature UTS at 250 °C [Ino-00]. 280 °C was selected as an intermediate temperature because Inoue *et al.* performed mechanical tests showing the UTS between 280-300 °C of $Al_{93}Fe_3Cr_2Ti_2$ alloy bars produced by warm extrusion from <26 μm atomised powder retained 60% of the room temperature strength, while conventional 2020 T6 Al alloy and 7178 T6 alloy only retained 10% of their original strength [Ino-00]. The mechanical properties and therefore the microstructural stability, of the $Al_{93}Fe_3Cr_2Ti_2$ are of particular industrial interest in this temperature range due to their superiority to currently used Al alloys for engineering applications.

Initially, 1 hour long heat treatments were performed at each of the selected temperatures. After heat treatment, XRD scans were performed and complemented with microhardness indents in order to have a preliminary analysis of whether the reactions detected in the DSC would affect the phases present and/or alter the microstructure in a way which could influence the mechanical properties.

XRD peaks were indexed as follows. α-Al peaks were identified by indexing the reflections corresponding to the (111), (200), (220), (311), (222) and (400) planes in the 2θ = 10 °-100 ° range

at 38.5 ° (100% intensity), 44.7 °, 65.2 °, 78.3 °, 82.5 ° and 99.2 ° [JCP-99]. The presence of the icosahedral phase was shown by broad peaks at 2θ ~ 22.9 °, 41.3 °, 43.5 °, 61.6 ° and 73.7 ° which were the peaks calculated by Galano *et al.* on melt spun ribbons of the same nominal chemical composition using Cahn's indexation scheme [Cah-86], [Gal-09a]. Other intermetallic phases were identified including Al_3Ti, $Al_{13}Fe_4$, $Al_{13}Cr_2$ which were indexed using data sheets [JCP-99]. The presence of Al_3Ti was shown by the peaks at 2θ~22.3 °, 31.9 °, 39.2 ° (100% intensity), 66.5 ° and 84.4 ° corresponding to the (100), (110), (111), (220), (311) reflections respectively. The $Al_{13}Fe_4$ was shown by peaks at 43.1 °, 44.2 ° and 44.4 ° corresponding to the 100% intensity $(\bar{6}23)$ reflection and the (025) and (423) respectively. The $Al_{13}Cr_2$ phase was shown by the peaks at 36.6 °, 41.2 °, 41.4 °, 41.5 °, 43.8 °, 43.9 ° (100% intensity), 44.0 °, corresponding to the $(\bar{1}31)$, $(\overline{11}13)$, (711), $(\bar{4}24)$, $(\overline{10}22)$, $(\bar{8}20)$ and $(\bar{3}33)$.

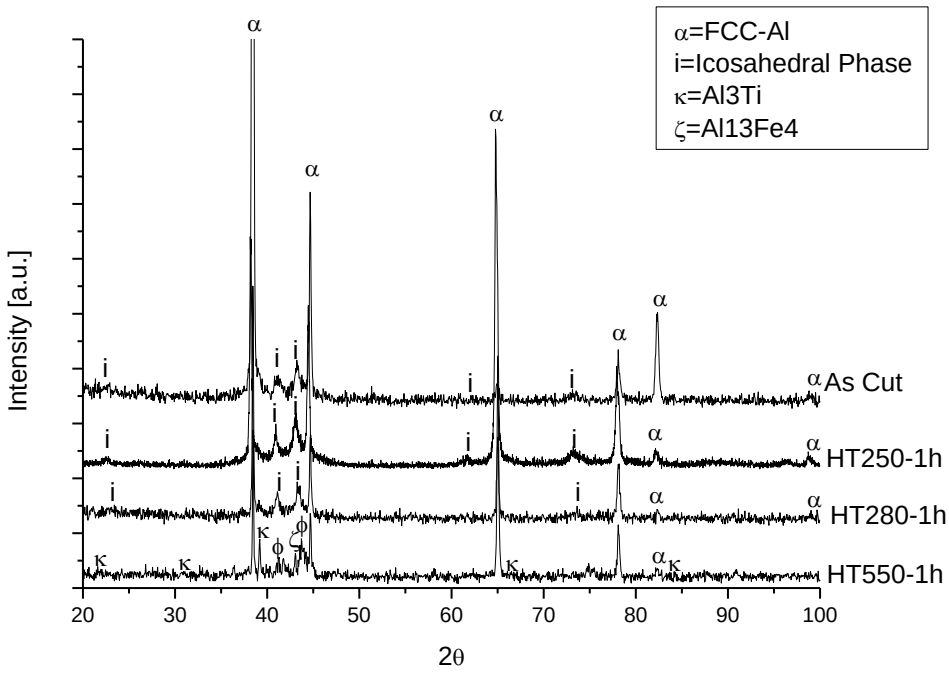

(a)

Figure 6.4: X-ray diffractograms of the 0-1a bar performed after 1 hour long heat treatments of the samples, followed by air cooling. (a) overall scan between 20-100 °.

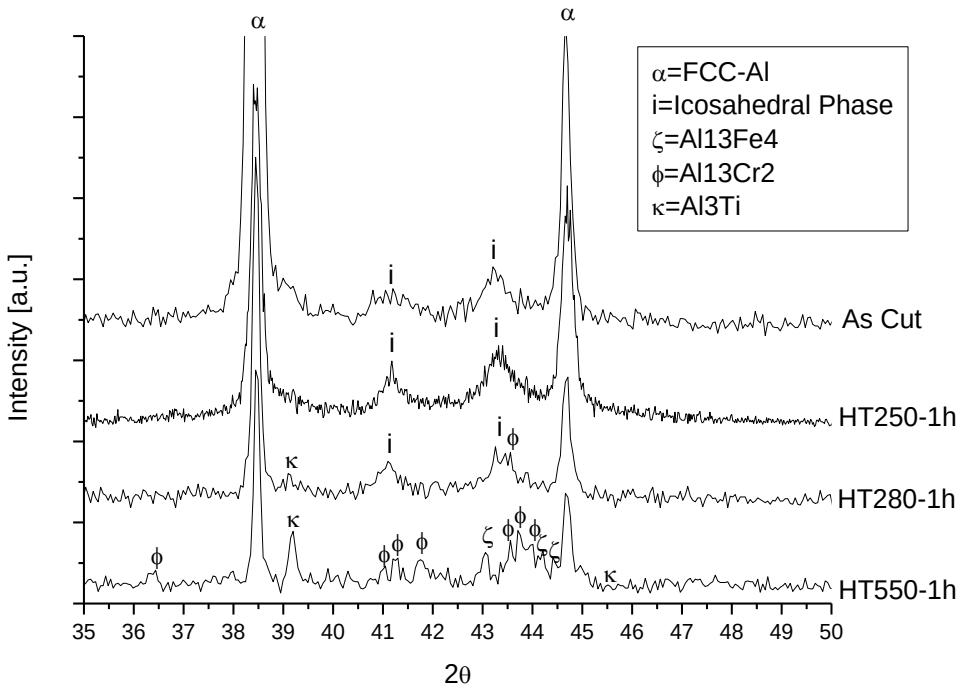

(b)

Figure 6.4 (cont.): X-ray diffractograms of the 0-1a bar performed after 1 hour long heat treatments of the samples, followed by air cooling. (b) enlargement of the central section for easier peak identification.

The results of the X-ray diffractograms of the 0-1a bar after one hour heat treatments at 250 °C, 280 °C and 550 °C can be seen in Figure 6.4, as well as a diffractogram of an as-cut sample before heat treatment. In the as-cut sample, the phases detected were only α-Al and icosahedral phase. No apparent difference was visible between the as cut sample and the sample heat treated at 250 °C. After one hour at 280 °C the icosahedral phase and α-Al are still present and some intermetallic precipitation starts to become visible in the form of κ-Al_3Ti and of ϕ-$Al_{13}Cr_2$. After heat treatment at 550 °C, the icosahedral phase can no longer be identified by XRD, but more stable intermetallic phases like κ-Al_3Ti, ϕ-$Al_{13}Cr_2$ and ζ-$Al_{13}Fe_4$ can be detected.

Microhardness indents were performed in an attempt to detect any change in the mechanical strength, and they can be seen in Figure 6.5.

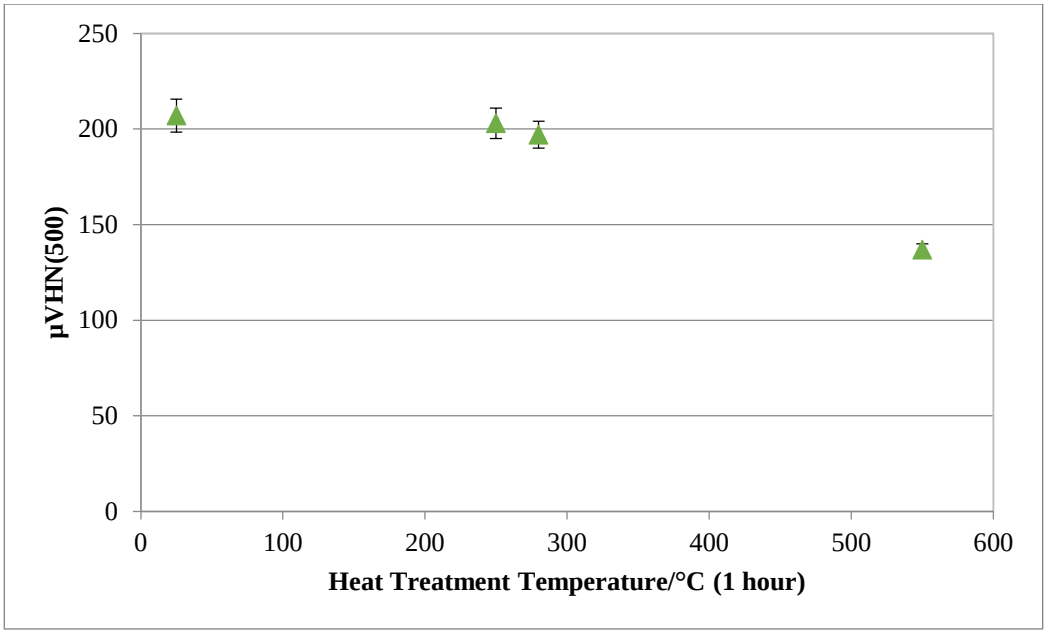

Figure 6.5: Microhardness indents performed on the 0-1a bar after 1 hour heat treatments at 250 °C, 280 °C and 550 °C. Each point is the average of 25 indents, the error bars are the standard deviation.

The indents performed on the as-cut bar, the bar heat treated at 250 °C and 280 °C are within each other's error bars, however a slight decreasing tendency can be observed. The main strength decrease occurs after heat treatment at 550 °C.

Further microstructural characterisation was performed of the samples after heat treatment at 550 °C for one hour using a combination of SEM, TEM and EDX to complement the XRD analysis. The XRD analysis in Figure 6.4 suggested that the DSC peak detected at 500 °C in corresponded to the decomposition of the icosahedral phase into more stable intermetallic phases.

In the SEM micrographs shown in Figure 6.6 we can see that after heat treatment at 550 °C the microstructure consists of intermetallic phases in an Al matrix in a series of different shapes, from spherical to lath-like. Figure 6.6 (a) gives an overview of the overall microstructure while Figure 6.6 (b) shows some of the shapes of the intermetallic phases.

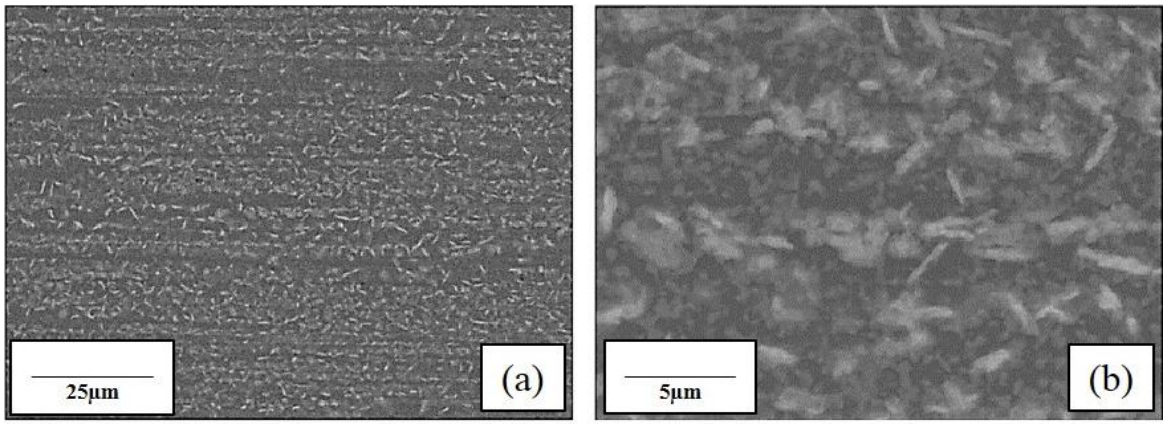

Figure 6.6: Backscattered SEM micrographs (a) at low magnification showing an overview of the microstructure and (b) a higher magnification detail showing the shape of some of the intermetallic phases.

The intermetallic phases produced by heat treatment at 550 °C, visible in the SEM micrographs in Figure 6.6 and identified in the X-ray diffractogram in Figure 6.4, have been analysed by TEM and EDX. The bright field TEM micrographs can be seen in Figure 6.7. Several phases with different shapes were visible, and an EDX analysis was performed to complement the XRD analysis and help with phase identification.

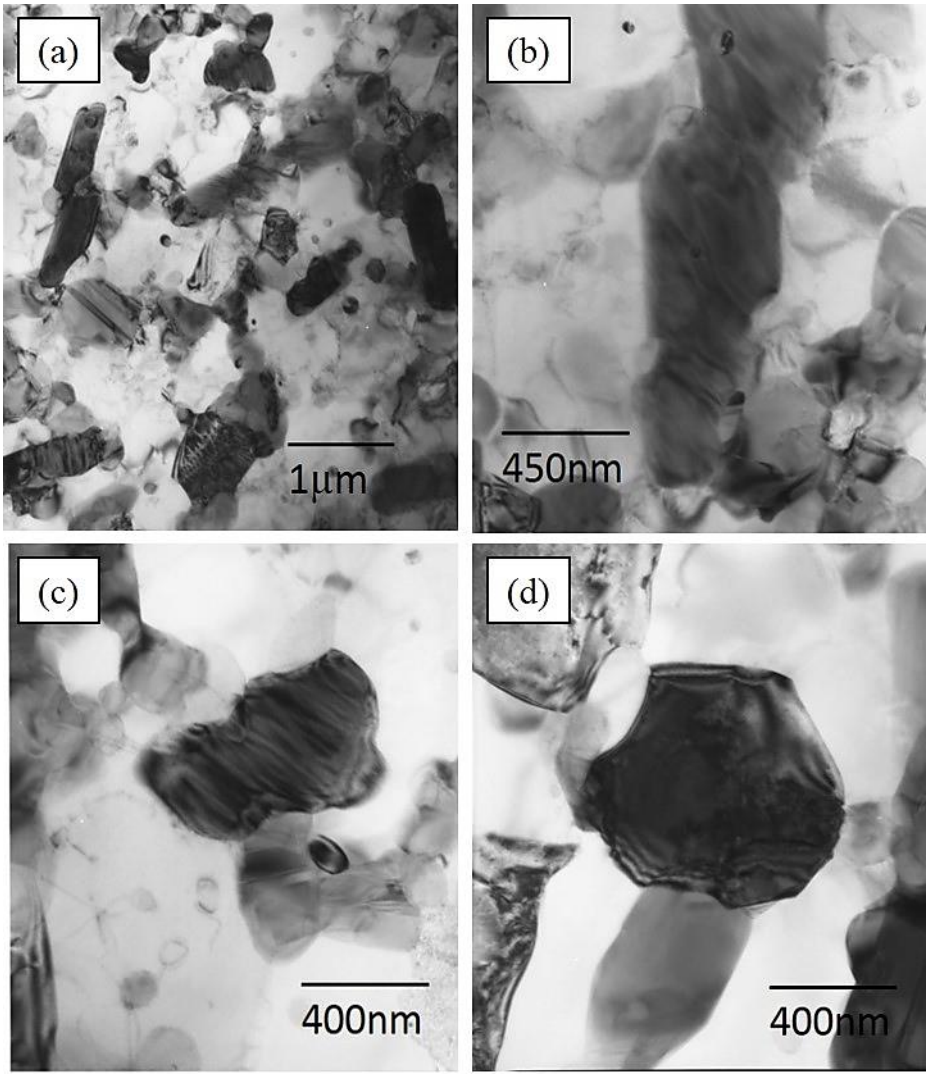

Figure 6.7: Bright field TEM micrographs of the heat treated 0-1a bar. (a) overview of the microstructure, (b) elongated, nodular Fe-based intermetallic phase, (c) smaller Fe-based intermetallic phase, (d) spherical intermetallic phase. The chemical composition of the Fe-enriched phases in (b) and (c) measured by EDX is in Table 6.1.

Elongated, nodular phases which can be seen in Figure 6.7 (a) and at higher magnification in Figure 6.7 (b) were shown by EDX to be Fe-enriched. Some more rounded particles, like the one seen in Figure 6.7 (c) were also shown to be Fe-enriched. The compositions of the particles in Figure 6.7 (b) and (c) can be seen in Table 6.1.

Other intermetallic phases, like the ones shown in Figure 6.7 (d), were more spherical in shape and smaller. Overlap with other phases was also seen, making the chemical composition difficult to measure individually.

Element	*Intermetallic phases in Figures 6.6 (b) and (c) at%*	*Error*
Al	*95.2*	*0.3*
Ti	*0.1*	*0.2*
Cr	*0.4*	*0.4*
Fe	*4.3*	*0.7*
Total	*100.0*	

Table 6.1: elemental composition of the elongated, nodular Fe-enriched intermetallic phases measured by TEM-EDX.

The composition of the matrix between the intermetallic phases was also measured. The Fe content was found to be higher than the equilibrium solid solubility of Fe at 550 °C, which is very limited at 0.025 at% [Mon-43]. The Cr content was 0.2 at% lower than the solid solubility limit of Cr at 550 °C [Mon-43]. The samples heat treated at 550 °C also had more Ti in solid solution (0.5 at %) than the equilibrium solid solubility of Ti in Al at 550 °C, which is 0.05 at% [Xu-06]. The EDX matrix compositions can be found in Table 6.2.

Element	*Average at%*	*Error*
Al	*99.2*	*0.5*
Ti	*0.5*	*0.3*
Cr	*0.1*	*0.1*
Fe	*0.1*	*0.1*

Table 6.2: elemental composition of the matrix after heat treatment at 550 °C for 1 hour measured by TEM-EDX. Averages were taken over 10 measurements.

So in summary, after heat treating for one hour at 250°C no reaction could be observed using the characterisation techniques used. At 280 °C some intermetallic precipitation was observed by XRD, but no noticeable difference was shown in the microhardness of the samples. After heat treatment at 550 °C the icosahedral phase could no longer be identified by XRD or TEM, but a number of intermetallic phases like Al_3Ti, $Al_{13}Fe_4$ and $Al_{13}Cr_2$ could be detected.

6.3.3 Thermal Stability: 1000 Hours at 250 °C

Longer heat treatments were performed at 250 °C to investigate microstructural stability over a longer period of time. Heat treatments were performed for 1 hour, 3, 10, 30, 100, 300 and 1000 hours. Each heat treatment was followed by XRD analysis and microindentation.

The X-ray diffractograms seen in Figure 6.8 and the microhardness indentation curve in Figure 6.9 do not show differences between the as-extruded samples and the samples heat treated for 300 hours at 250 °C. Both contain only FCC-Al and icosahedral phase in the XRD plot and have a microhardness within each other's experimental error. After 1000 hours at 250 °C no visible change in the microstructure is detected in the X-ray diffractogram but the microhardness indentations show a slight decreasing tendency from 206±2 to 199±3 μHV_{500}.

XRD peaks were indexed as follows. α-Al peaks were identified by indexing the reflections corresponding to the (111), (200), (220), (311) and (222) planes in the 2θ = 10 °-90 ° range at 38.5 ° (100% intensity), 44.7 °, 65.2 °, 78.3 ° and 82.5 ° [JCP-99]. The presence of the icosahedral phase was shown by broad peaks at $2\theta \sim$ 22.9 °, 41.3 °, 43.5 °, 61.6 ° and 73.7 ° [Aud-02], [Gal-09a].

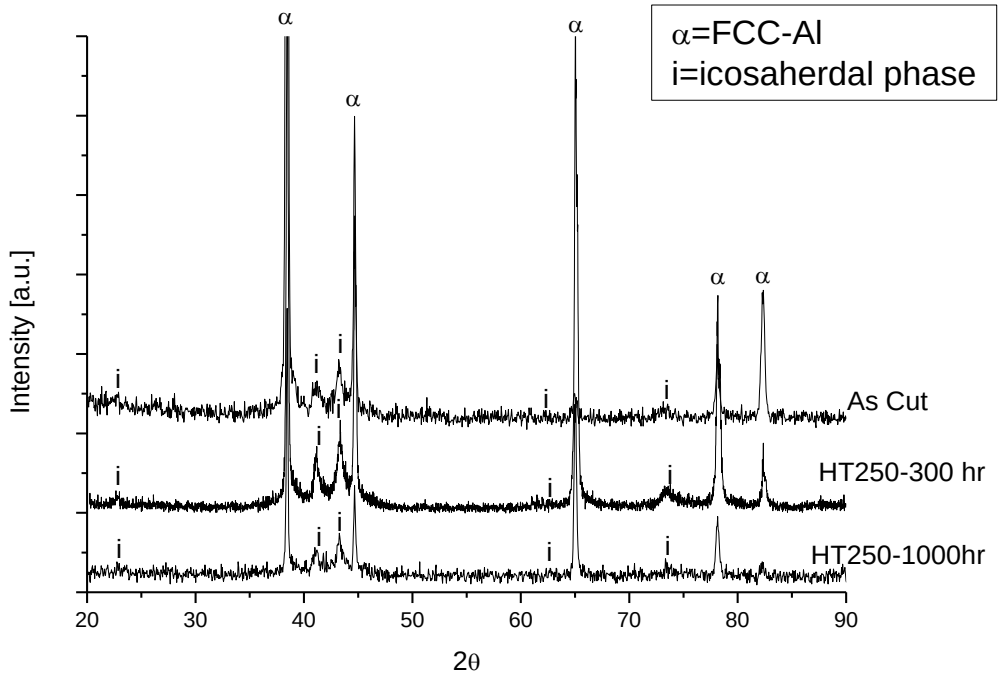

(a)

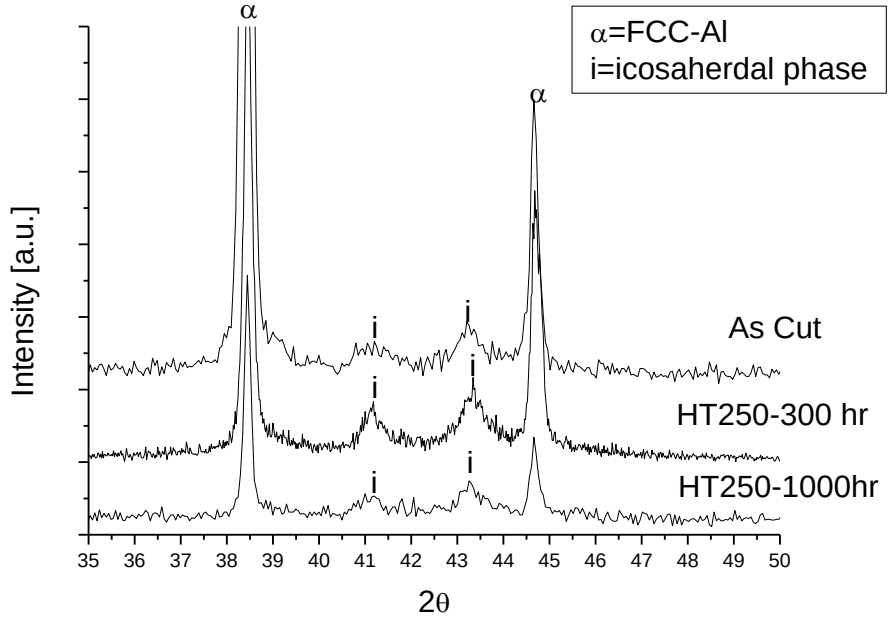

(b)

Figure 6.8: X-ray diffractogram showing the 0-1a sample after heat treatment for 300 hours and 1000 hours (a) overall scan between 20-90 °, (b) enlargement of the central section for easier peak identification.

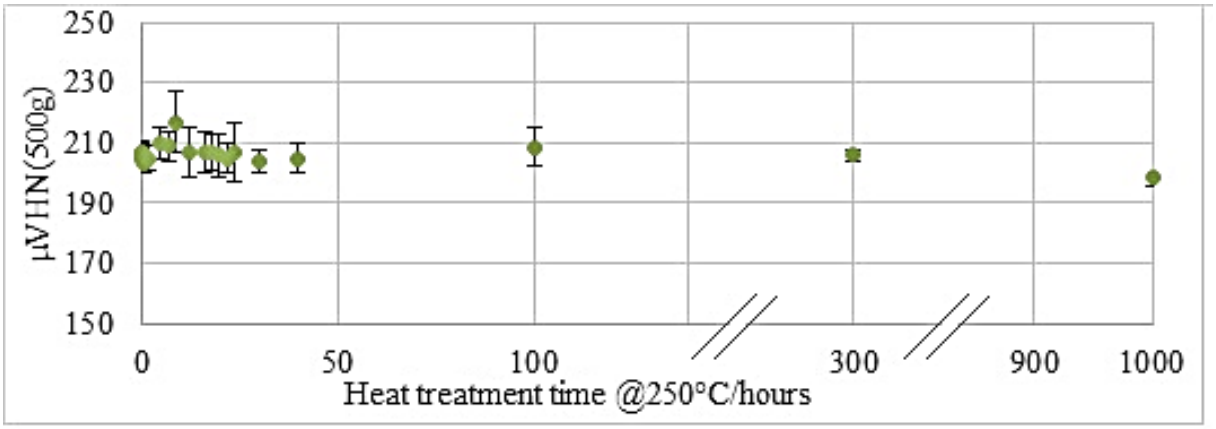

Figure 6.9: Microhardness indentation after heat treatments of different duration at 250 °C of the 0-1a bar.

SEM backscattered micrographs of the samples heat treated for 300 and 1000 hours at 250 °C can be seen in Figure 6.10. A microstructure consisting of elongated "bands" along the extrusion direction containing spherical intermetallic phases was visible after both heat treatments, and is shown in Figure 6.10 (a) and (b). Some of the bands contained groups of larger intermetallic phases, still present after heat treatment at 250 °C for 300 hours, which have been highlighted in Figure 6.10 (a). After 1000 hour of heat treatment, the microstructure shows elongated bands along the extrusion direction, some of them containing groups of large intermetallic phases but most of them containing small spherical shaped particles. This can be seen in Figure 6.10 (b). No change in the microstructure was detected after heat treatment at 250 °C for 1000 hours by SEM.

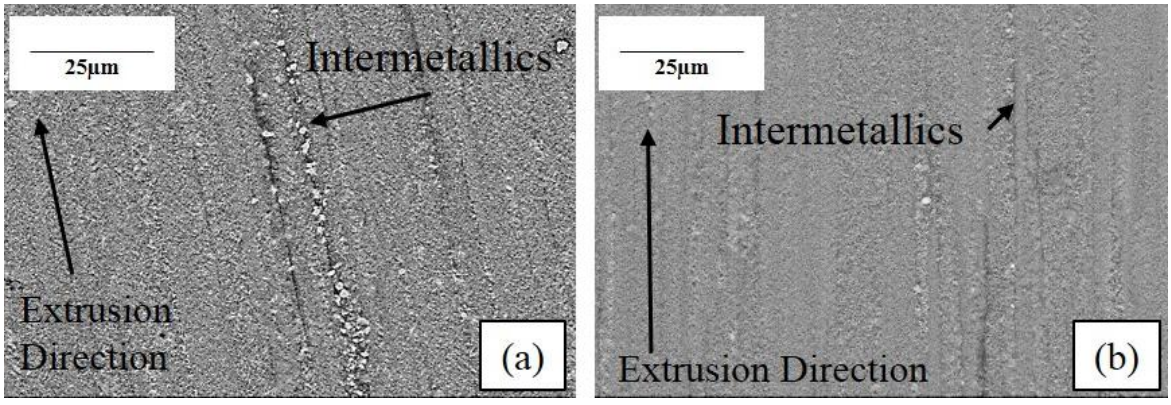

Figure 6.10: SEM BEI micrographs of (a) the 0-1a bar after heat treatment for 300 hours, (b) after heat treatment for 1000 hours.

TEM micrographs of the samples heat treated for 1000 hours at 250 °C showed a microstructure consisting of an even, widespread particle distribution of round shaped intermetallic phases. This can be seen in Figure 6.11 (a). Convergent beam diffraction of these phases produced 5-fold symmetry patterns characteristic of the icosahedral phase, which can be seen in Figure 6.11 (b). In Figure 6.11 (c) and (d) the particle highlighted by a circle in Figure 6.11 (a) was selected and tilted. This revealed the "particle" to be a cluster. In Figure (c) the difference in shade which can be observed in the outer edge particles is an indicator that they are diffracting the TEM beam along different planes. Figure (d) has been tilted to align the centre particle with its zone axis, however it proved to be too small to acquire a convergent beam diffraction pattern from.

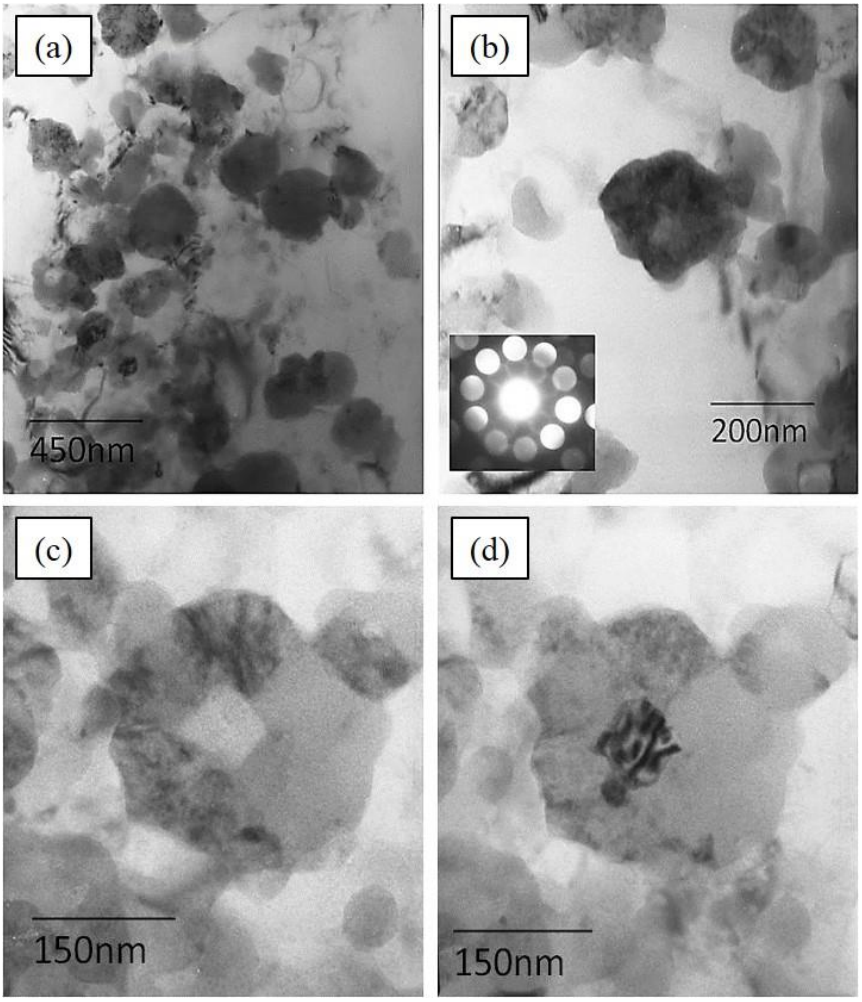

Figure 6.11: Bright field TEM micrographs of the 0-1a sample heat treated for 1000 hours at 250 °C showing (a) the overall microstructure with widespread, evenly distributed intermetallic phases in the matrix, (b) a close-up of one of the particles and it's convergent beam diffraction pattern showing 5x symmetry.(c) and (d) Bright field TEM micrographs showing a cluster of particles tilted at different angles.

EDX scans were performed of the centre, the outer "ring" and the surrounding matrix of a cluster similar to the one in Figure 6.11 (c) and (d) to determine the chemical composition of the different phases. The results are shown in Figure 6.12 and Table 6.3. The EDX scans of the matrix revealed it to be pure Al, the outer ring of particles revealed their composition to be similar to that of the icosahedral phase shown in Chapter 4 and the measurements on the same nominal chemical composition by Inoue and Galano *et al.* [Ino-00], [Gal-09a]. The internal phase was shown to be an Al-Ti intermetallic phase. The measured chemical composition of the central phase partially includes the surrounding particles, because the central intermetallic phase was too small to acquire a convergent beam diffraction pattern and it was also too small to converge the beam solely on the particle and acquire an EDX spectrum. The measured chemical composition can be found in Table 6.3.

	Centre	*Edge*	*Matrix*
Element	*Atomic%*	*Atomic%*	*Atomic%*
Al	*84.98*	*85.54*	*97.39*
Ti	*9.23*	*2.47*	*0.94*
Cr	*2.65*	*4.87*	*0.75*
Fe	*3.13*	*7.11*	*0.92*

Table 6.3: Chemical composition measured by EDX of the centre, edge and matrix surrounding the cluster of intermetallic particles in Figure 6.11.

The composition of the center of the cluster appears to be Ti-enriched in comparison with the composition of the outer "ring" of particles surrounding it and with the icosahedral phase composition presented in Chapter 4. The volume fraction of this intermetallic phase must be below the XRD detection limit (generally less than ~4 vol%) [Spe-10].

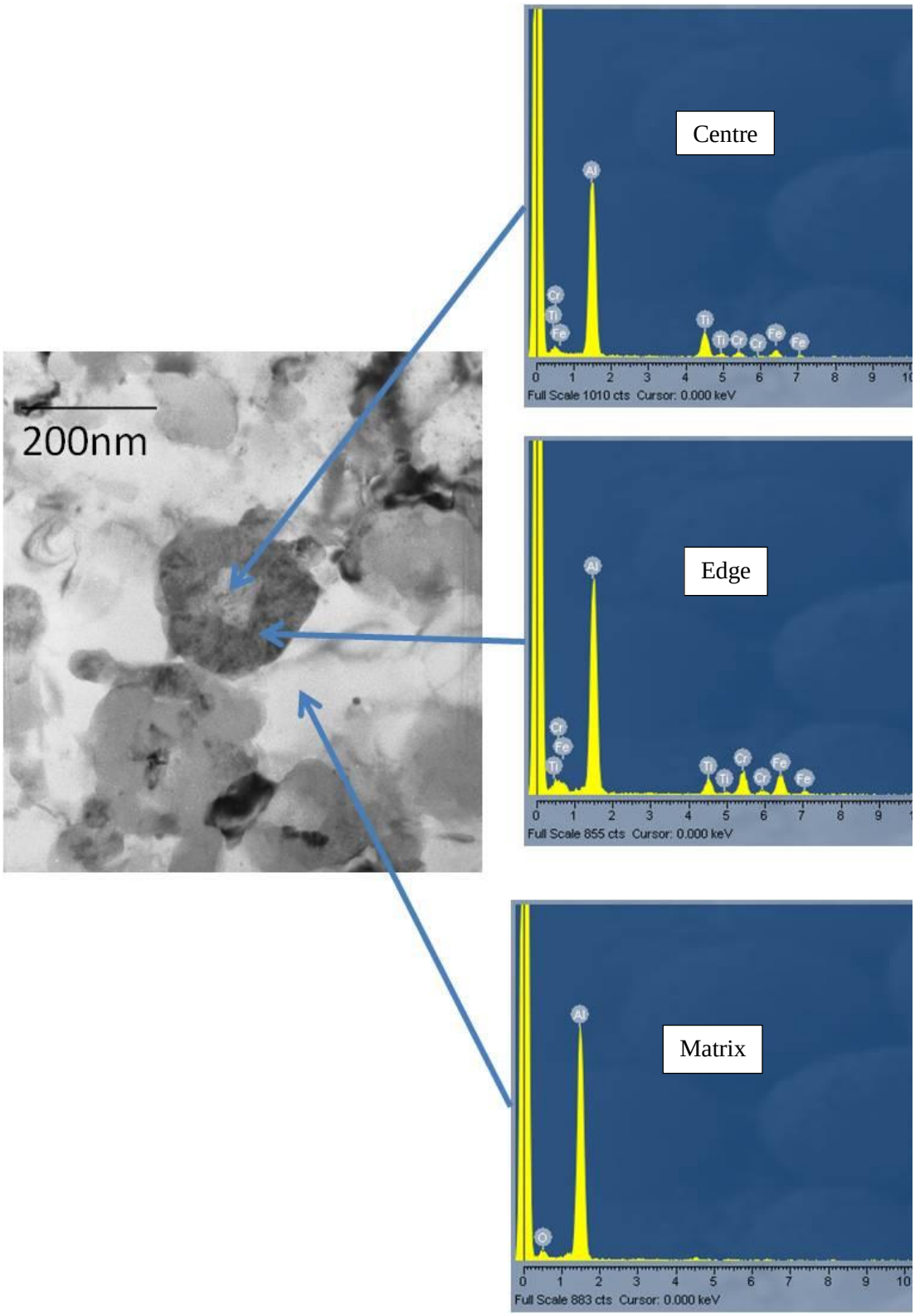

Figure 6.12: bright field TEM micrograph of the 0-1a bar heat treated for 1000 hours at 250 °C showing a cluster of intermetallic particles and 3 EDX spectra taken at the centre, on the outer ring and in the matrix surrounding the particle.

6.4 Thermal Analysis of the Extruded Composite Bars

6.4.1 DSC

The same analysis procedure used to investigate the thermal evolution of the pure alloy bar was applied to the composite bars in order to establish whether the fibres would alter the thermal evolution and if the lowered extrusion temperature of 388-389 °C (which was only possible due to the ductilising effect of the fibres) would cause any change in the thermal stability of the alloy and the fibres. DSC scans were performed on the composite bars 10-1a and 20-1a at 40 °C/min up to 630 °C to check for reactions occurring below the extrusion temperature and can be seen in Figure 6.13.

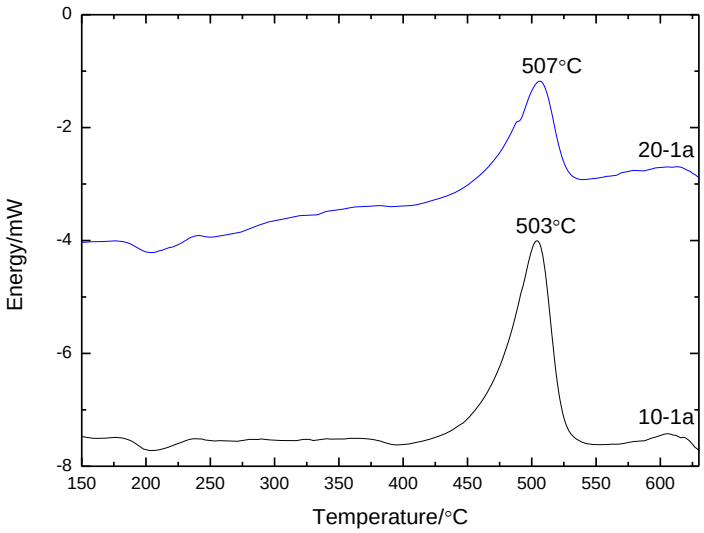

Figure 6.13: DSC scan of the 10-1a and 20-1a bars, performed between 150-630 °C at 40 °C/min.

The DSC analysis of the composites in Figure 6.13, shows the main exothermic peak at ~503-7 °C. In Figure 6.13 some minor fluctuations of the baseline are still present despite the subtraction of the empty pan.

6.4.2 Thermal Evolution: 1 Hour at 250°C, 280°C and 550°C

Further thermal analysis of the extruded 10-1a and 20-1a bars was performed by heat treatments, followed by microhardness tests and microstructural characterisation. The temperatures for the heat treatments selected are the same ones as the previous analysis on the 0-1a bar, therefore 250 °C, 280 °C and 550 °C. 1 hour long heat treatments were performed at each of the selected temperatures.

After heat treatment, XRD scans were performed and complemented with microhardness indents. The XRD peaks were indexed as follows: α-Al peaks were identified by indexing the reflections corresponding to the (111), (200), (220), (311), (222) and (400) planes in the 2θ = 10 °-100 ° range at 38.5 ° (100% intensity), 44.7 °, 65.2 °, 78.3 °, 82.5 ° and 99.2 ° [JCP-99]. The presence of the icosahedral phase was shown by broad peaks at 2θ ~ 22.9 °, 41.3 °, 43.5 °, 61.6 ° and 73.7 ° [Gal-09a]. Other intermetallic phases were identified including Al_3Ti, $Al_{13}Fe_4$, $Al_{13}Cr_2$ which were indexed using data sheets [JCP-99]. The presence of Al_3Ti was shown by the peaks at 2θ~39.2 ° (100% intensity) and 84.4 ° corresponding to the (111) and (311) reflections respectively. The presence of the $Al_{13}Fe_4$ monoclinic phase was shown by peaks at 22.4 °, 43.1 ° (100% intensity), 44.2 ° and 44.4 ° corresponding to the (003), ($\bar{6}23$), (025), (423) reflections respectively. The $Al_{13}Cr_2$ phase was shown by the peaks at 21.5 °, 36.6 °, 41.2 °, 41.4 °, 41.5 °, 43.8 °, 43.9 ° (100% intensity), 44.0 °, 75.3 ° and 75.7 ° corresponding to the ($\bar{5}11$), ($\bar{1}31$), ($\overline{11}13$), (711), ($\bar{4}24$), ($\overline{10}22$), ($\bar{8}20$) and ($\bar{3}33$), (15 3 $\bar{7}$) respectively.

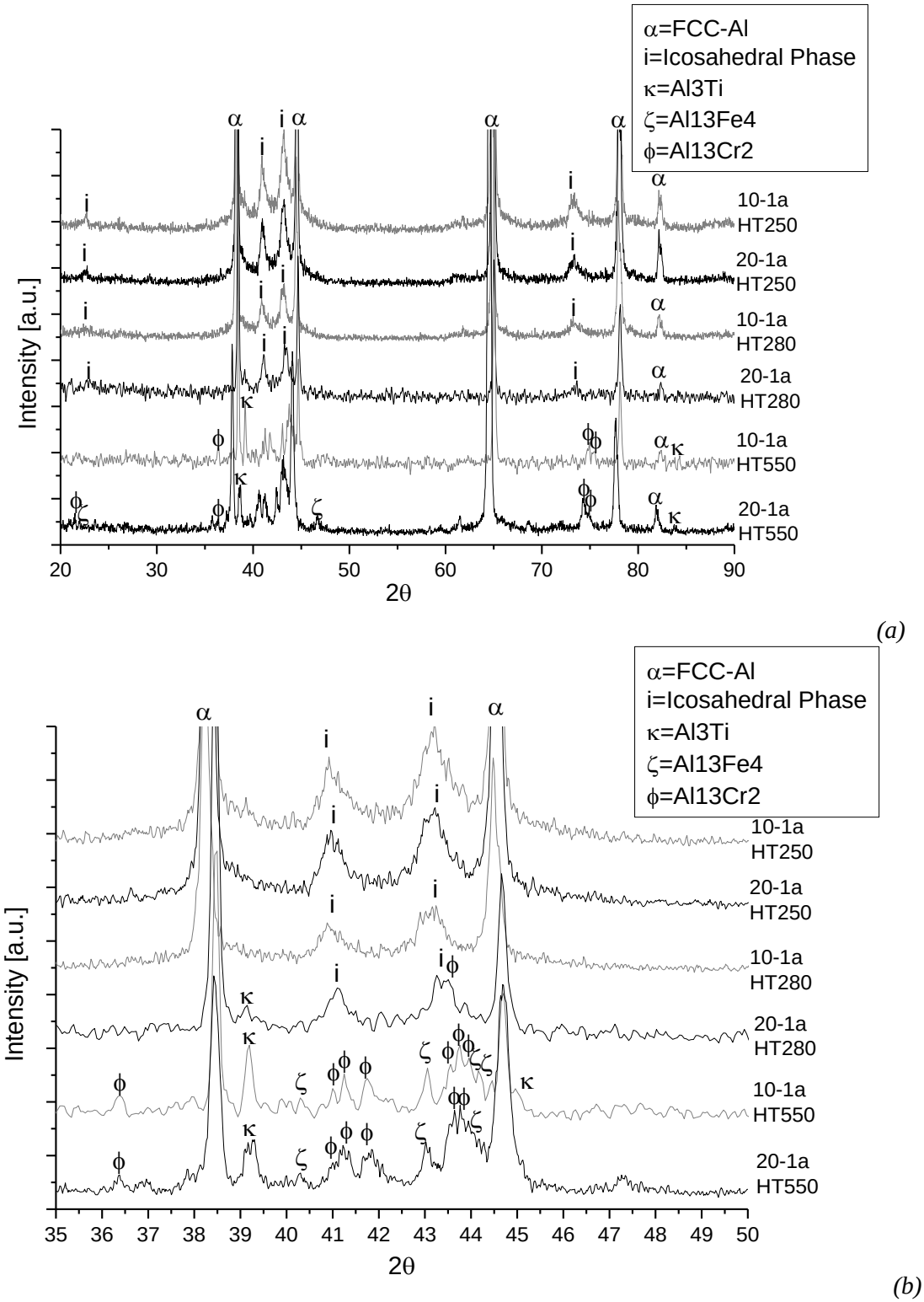

Figure 6.14: X-ray diffractograms of the 10-1a and 20-1a bars performed after 1 hour long heat treatments of the samples, followed by air cooling (a) overall scan between 20-90 ° and (b) enlargement of the 35-50 ° section.

The results of the X-ray diffractograms after one hour heat treatments can be seen in Figure 6.14.

The results were consistent with those measured for the 0-1a bar. After heat treatment at 250 °C the

icosahedral phase and α-Al are the only two phases detected. After one hour at 280 °C the icosahedral phase and α-Al are still present, however some intermetallic precipitation started to become visible in the form of κ-Al_3Ti. After heat treatment at 550 °C, the icosahedral phase could no longer be identified by XRD, but large amounts of more stable intermetallic phases were apparent, like κ-Al_3Ti, ϕ-$Al_{13}Cr_2$ and ζ-$Al_{13}Fe_4$.

Microhardness indents were performed in an attempt to detect changes in the mechanical strength and they can be seen in Figure 6.15.

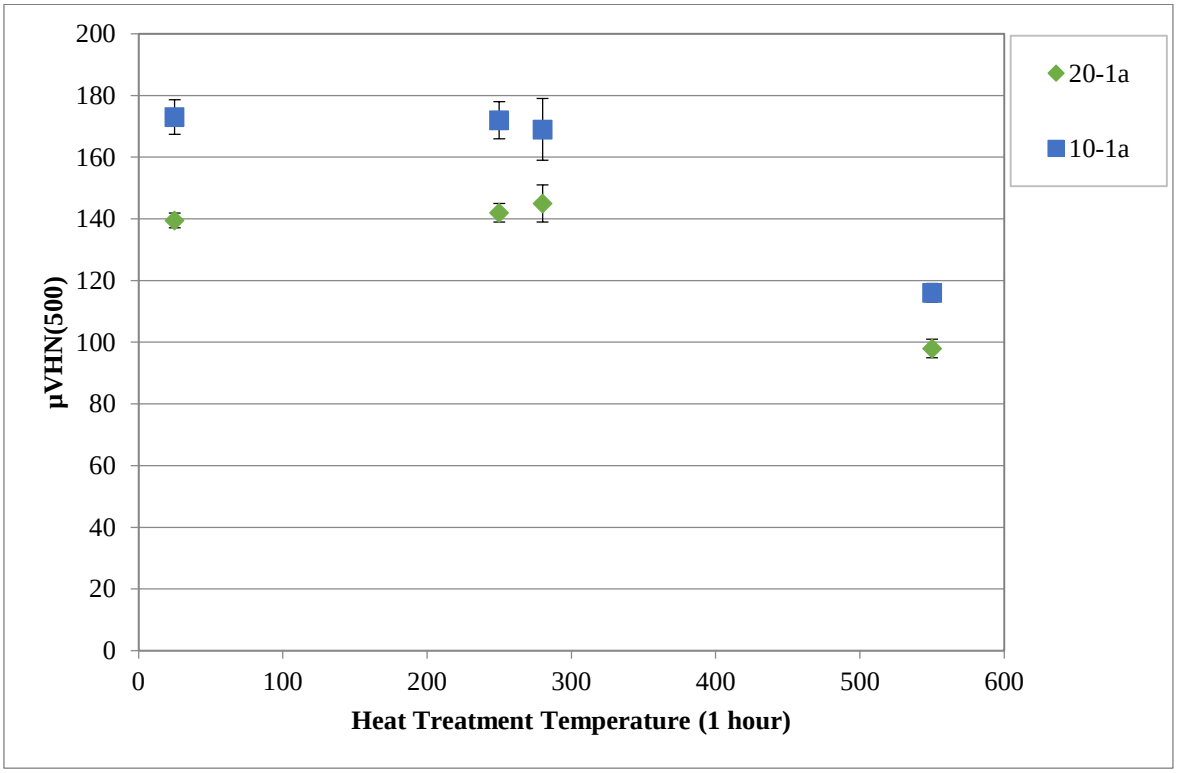

Figure 6.15: Microhardness indents performed on the 10-1a and 20-1a bars after 1 hour heat treatments at 250 °C, 280 °C and 550 °C. Each point is the average of 25 indents, the error bars are the standard deviation.

The main strength decrease occurs after heat treatment at 550 °C. The indents performed on the as-cut bar, the bar heat treated at 250 °C and 280 °C are within each other's error bars, however a slight decreasing tendency can be observed.

The major microstructural change detected by XRD and microhardness decrease occurred after heat treatment at 550 °C for one hour, therefore a more thorough microstructural characterisation was performed of those samples using a combination of SEM, TEM and EDX.

The SEM micrographs in Figure 6.16 show the pure Al fibres and intermetallic phases. Figure 6.16 (a) and (c) show a lower magnification overview of the microstructure of the 10-1a and 20-1a samples respectively. Figures 6.16 (c) and (d) show higher magnification details of the intermetallic phases and their elongated, nodular or lath like shapes.

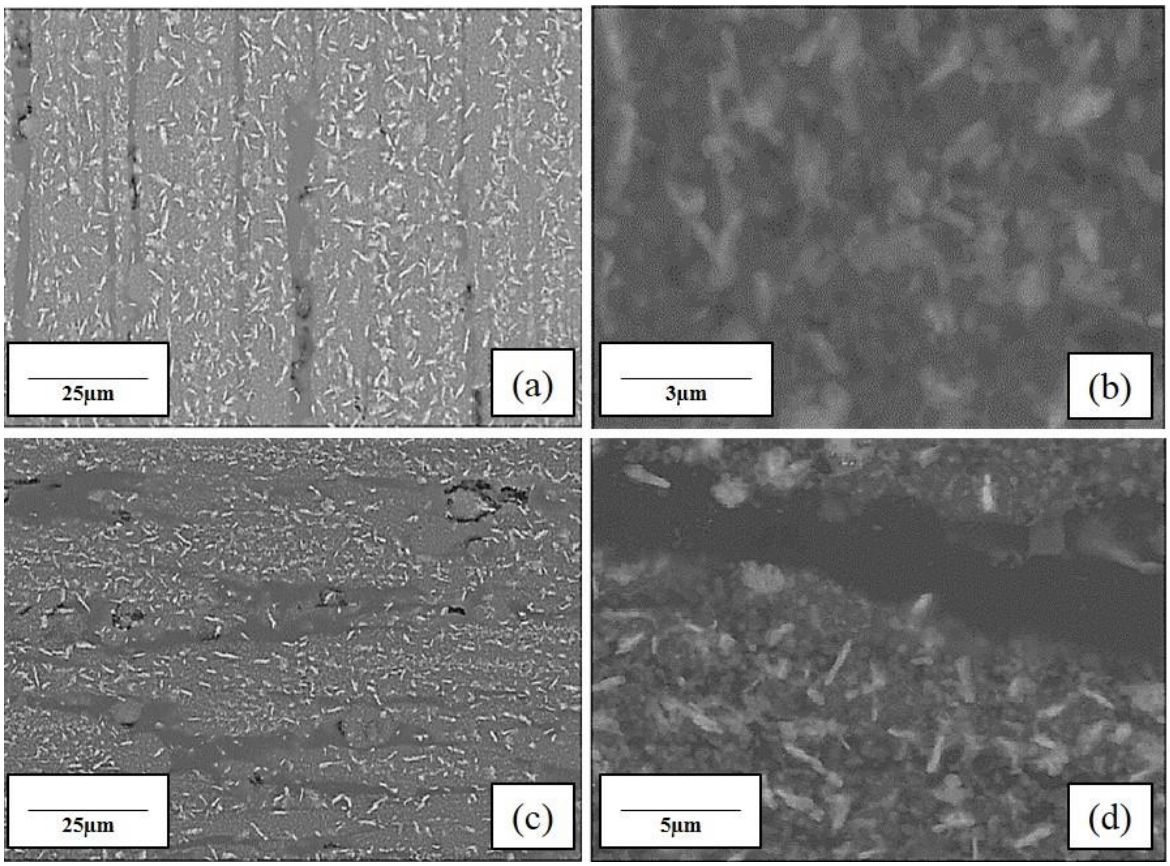

Figure 6.16: Backscattered SEM micrographs of (a) the 10-1a bar at low magnification showing an overview of the microstructure and (b) a higher magnification detail showing the shape of some of the intermetallic phases, (c) the 20-1a bar at low magnification showing the overall microstructure and the fibres and (d) a higher magnification detail showing some intermetallic phases.

The matrix was shown to behave in the same way as the pure alloy bar. However some of the more elongated intermetallic phases can be seen growing into the fibres, like in Figure 6.16 (d).

So in summary, the DSC scans of the composites showed the main reaction peak at ~500 °C. No difference was detected in the XRD scans and the SEM micrographs after heat treating for 1 hour at 250 °C. Some intermetallic precipitation was observed by XRD after heat treatment at 280 °C. After heat treatment at 550 °C the icosahedral phase could no longer be identified by XRD, but a number of intermetallic phases like Al_3Ti, $Al_{13}Fe_4$ and $Al_{13}Cr_2$ were observed.

6.4.3 Thermal Stability: 1000 Hours at 250°C

Longer heat treatments at 250 °C were used to investigate whether the addition of fibres caused changes in the microstructure which would occur over a longer period of time. Heat treatments were performed for 1 hour, 3, 10, 30, 100, 300 and 1000 hours. Each heat treatment was followed by XRD analysis and microindentation. The X-ray diffractogram in Figure 6.17 shows that the samples heat-treated at 250 °C only contain FCC-Al and icosahedral phase. α-Al peaks were identified by indexing the reflections corresponding to the (111), (200), (220), (311) and (222) planes at 38.5 ° (100% intensity), 44.7 °, 65.2 °, 78.3 ° and 82.5 ° [JCP-99]. The presence of the icosahedral phase was shown by broad peaks at 2θ ~ 22.9 °, 41.3 °, 43.5 °, 61.6 ° and 73.7 ° [Gal-09a].

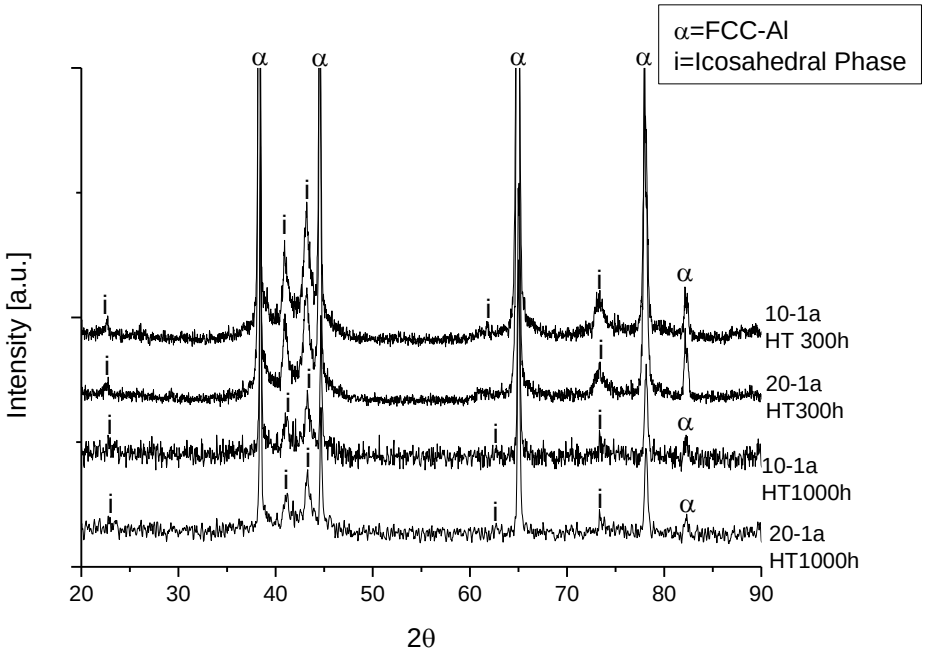

(a)

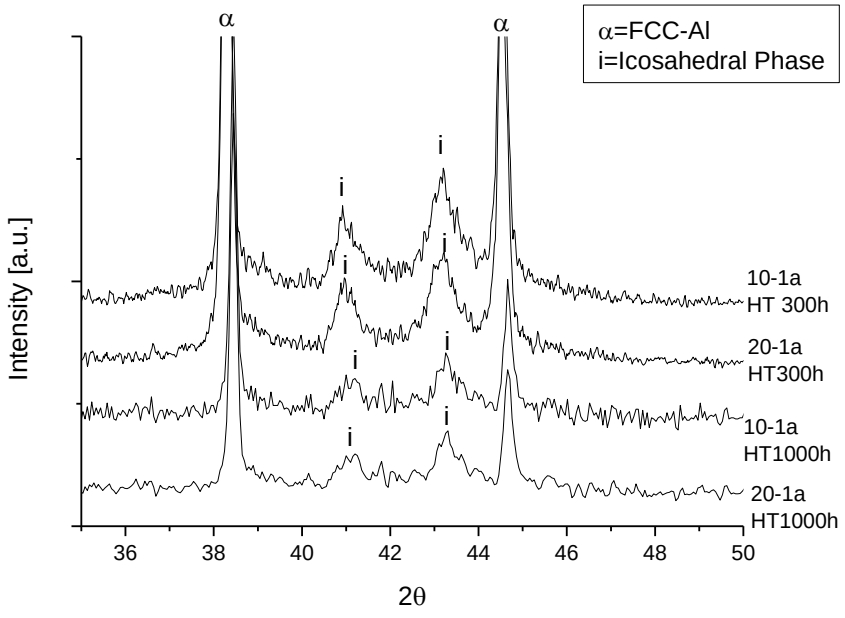

(b)

Figure 6.18: (a) X-ray diffractogram showing the 10-1a and 20-1a samples after heat treatment for 300 hours and 1000 hours at 250 °C, (b) enlargement of the central section of the X-ray diffractogram for easier phase identification.

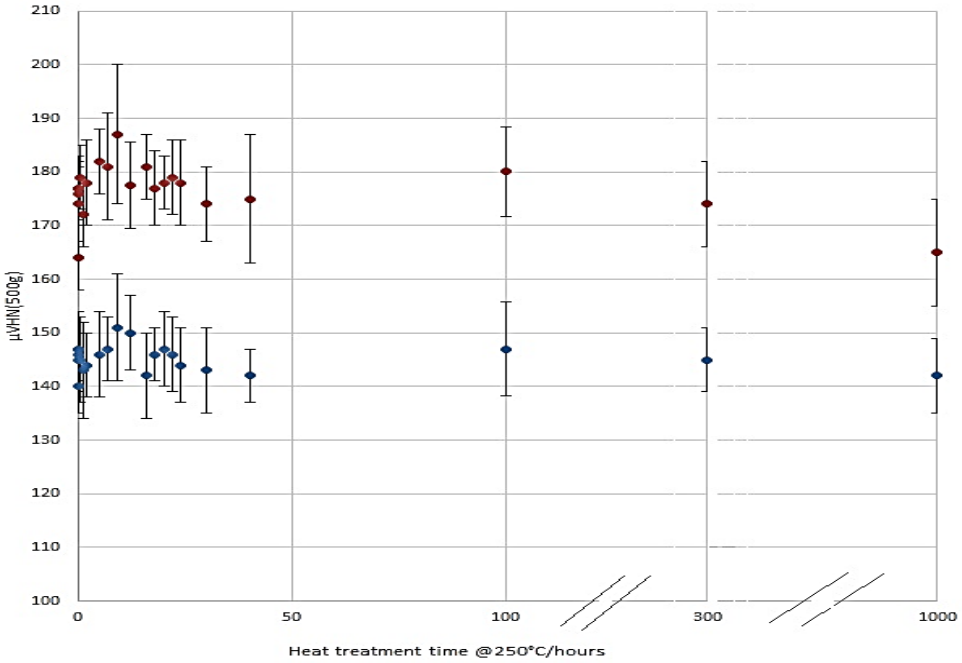

Figure 6.18: Microhardness indentation after heat treatments of different duration at 250 °C of the 10-1a and 20-1a bars.

The microhardness indentation curve in Figure 6.18 does not show differences between the as-extruded samples and the samples heat treated for 300 hours at 250 °C. After 1000 hours at 250 °C the microhardness indents in Figure 6.18 show decreasing tendency from 176±8 to 165±10 μHV_{500} for the 10-1a bar and from 145±6 to 142±7 μHV_{500} for the 20-1a bar. The pure alloy bar went down from 206±2 to 199±3 μHV_{500}, which is a decrease of 7 μHV_{500}, the 10-1a bar showed a decrease of 9 μHV_{500} and the 20-1a bar showed a decrease of 3 μHV_{500}.

SEM backscattered micrographs of the heat treated samples can be seen in Figure 6.19. A microstructure consisting of elongated "bands" along the extrusion direction containing spherical-shaped intermetallic phases was visible after all of the heat treatments, and is shown in Figure 6.19 (a), (b), (c) and (d). The observations made in Figure 6.8 on the pure alloy bar are valid for the matrix of the composite bars as well. No difference in the fibres could be observed by SEM in the composite bars after heat treating for 300 hours (Figure 6.19 (a) and (c)) and 1000 hours (Figure 6.19 (b) and (d)).

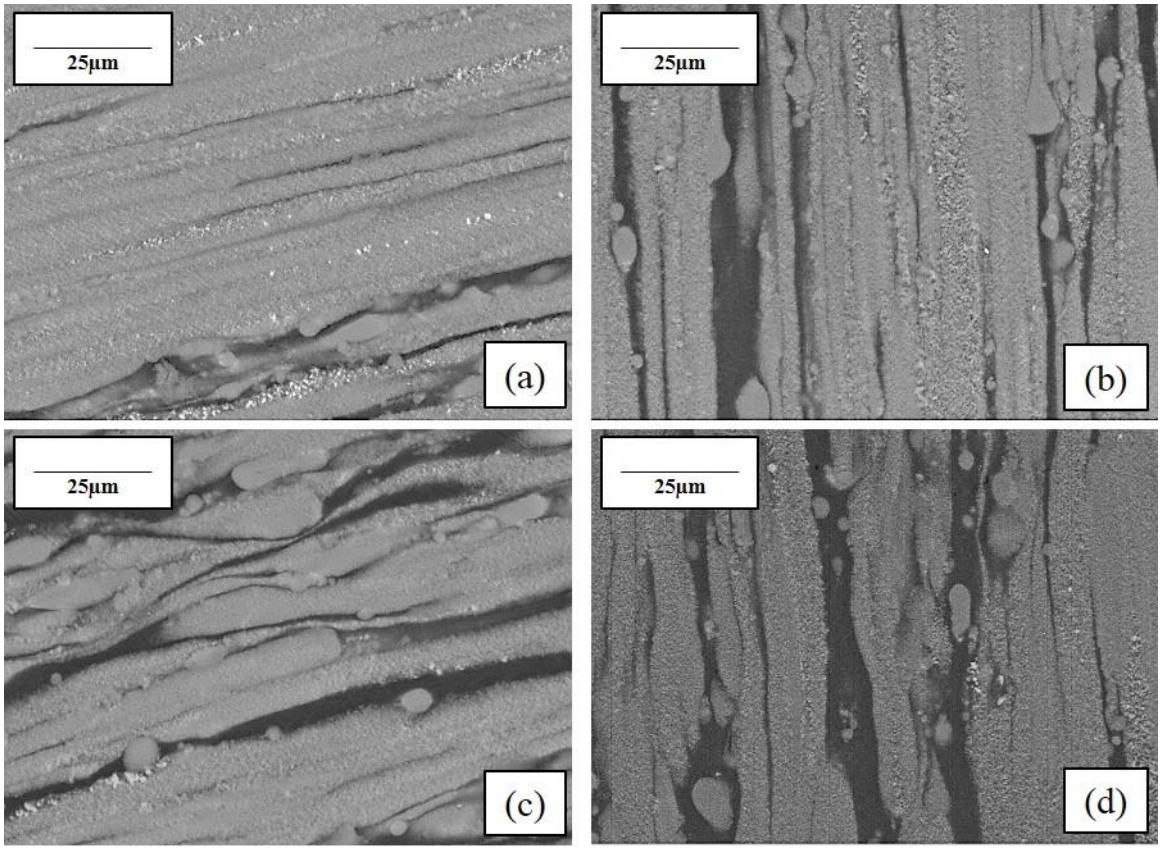

Figure 6.19: SEM BEI micrographs of (a) the 10-1a bar after heat treatment for 300 hours, (b) after heat treatment for 1000 hours, (c) the 20-1a bar after heat treatment for 300 hours and (d) after heat treatment for 1000 hours.

No noticeable difference in the microstructure could be detected by SEM analysis both after 300 hours and after 1000 hours at 250 °C. TEM micrographs were taken showing the matrix and the fibres after 1000 hours at 250 °C. In Figure 6.20 (a) and (c) icosahedral quasicrystalline phases can be seen with their characteristic 5-fold symmetry diffraction patterns in the 10-1a bar and 20-1a bar respectively. Figure 6.20 (c) also shows a cluster. TEM-EDX of the centre of the cluster in Table 6.4 showed it to be a Ti-enriched intermetallic phase just like the ones observed in the pure alloy bar. The fibres can be seen and grain boundaries within them in Figure 6.20 (b) and (c).

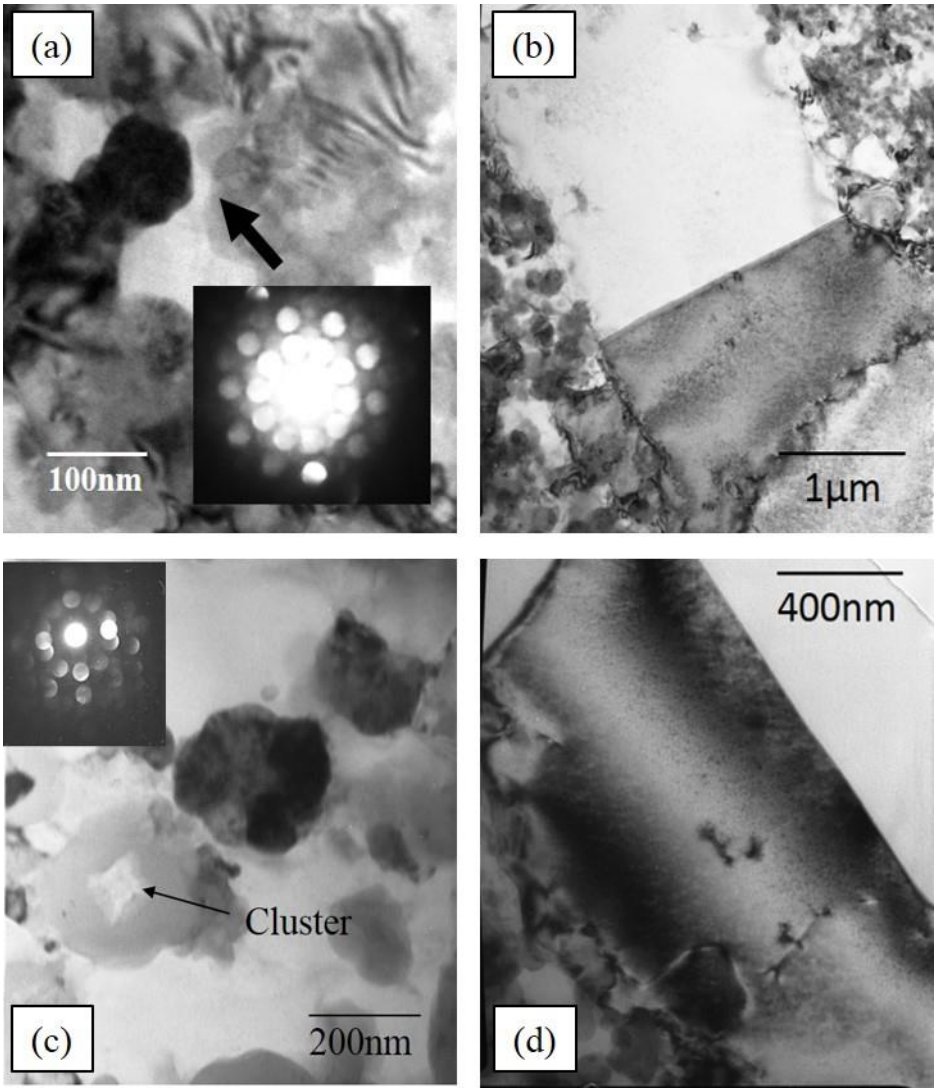

Figure 6.20: bright field TEM micrographs showing (a)icosahedral quasicrystal with 5x symmetry diffraction pattern in the 10-1a bar, (b) fibre in the 10-1a bar, (c) icosahedral phase in the 20-1a bar, and cluster of particles in the 20-1a bar and (d) fibre in the 20-1a bar.

EDX scans were performed of the centre, the outer "ring" and the surrounding matrix of the cluster in Figure 6.20 (c) to determine the chemical composition of the different phases. EDX scans of the matrix revealed it to be pure Al, the outer ring of particles revealed their composition to be similar to that of the icosahedral phase. The internal phase was shown to be a Ti-enriched intermetallic phase. The central phase proved to be too small to obtain an EDX spectrum, therefore some of the signal came from the outer ring-shaped intermetallics. The measured chemical composition can be found in Table 6.4. These clusters were also observed in the extruded pure alloy bar.

	Centre	*Edge*	*Matrix*
Element	*Atomic%*	*Atomic%*	*Atomic%*
Al	*88.3*	*84.1*	*98.0*
Ti	*8.1*	*3.9*	*0.8*
Cr	*1.4*	*6.3*	*0.5*
Fe	*2.2*	*5.7*	*0.7*

Table 6.4: Chemical composition measured by EDX of the centre, edge and matrix surrounding the cluster of intermetallic particles in Figure 6.20.

6.5 Discussion

Thermal analysis was performed on both powder batches to identify which reactions and phase changes would be taking place with increasing temperature, with a particular interest in any reactions which were likely to occur during the time the powder was held at temperatures between 400-420 °C during extrusion. In both powder batches the most evident reaction was a large exothermic peak at 550 °C. In the 2nd powder batch the higher temperature shoulder of the peak was extended up to a more elevated temperature compared to the 1st powder batch. The onset of the peak and its maximum are however at the same temperature for both powder batches.

Other DSC studies on rapidly solidified alloys of the same nominal chemical composition $Al_{93}Fe_3Cr_2Ti_2$ have been found in the literature. Two studies by Galano *et al.* [Gal-04] and Audebert *et al.* [Aud-02] have been found on melt spun ribbons and three studies by Kimura *et al.* [Kim-00], Todd *et al.* [Tod-04] and Rounthwaite [Rou-12] have been found on atomised powders. Audebert *et al.* [Aud-02] published a scan of a specimen heated at 40 °C/min form 100-600 °C. They identified two main peaks, located at ~430 °C and ~500 °C. Specimens heat treated past the first peak, which was very sluggish and broad in shape, were then analysed by XRD and the presence of Al_3Ti and metastable θ-phase was confirmed, as well as the icosahedral phase and FCC

Al matrix which were already present before. Small peaks occurring before the main sharp peak have been related to the possibility of precipitation from the supersaturated Al matrix [Gal-04]. Audebert *et al.* then analysed specimens heat treated past the second peak, which was very sharp and strong in shape, were then reported to have undergone a decomposition of the icosahedral phase into the stable Al_3Ti, $Al_{13}Fe_4$ and $Al_{13}Cr_2$ intermetallic phases. Galano *et al.* [Gal-04] published a scan also performed at 40°C/min from 150-650 °C. In their work only one peak was observed at ~500 °C but with a large shoulder on the lower temperature side of the peak. After XRD analysis, this peak was related to the precipitation of intermetallic phases as a result of the decomposition of the icosahedral phase and other metastable phases.

The study performed by Kimura *et al.*, also at 40 °C/min reported the main peak to be at ~520 °C and as no other peak in the plot was reported, it was associated with the decomposition of the icosahedral phase into Al_3Ti, $Al_{13}Fe_4$ and $Al_{13}Cr_2$ stable intermetallic phases [Kim-00]. Todd *et al.* performed their experiments at a heating rate of 20 °C/min and they also observed the main peak associated with the decomposition of the icosahedral phase at ~500 °C. They also observed two smaller peaks in the <25 µm powder which were located at ~330 °C and ~410°C and just like the ones found in the work by Audebert *et al.*, they were associated with precipitation from the supersaturated matrix [Tod-04]. The work performed by Rounthwaite [Rou-12] also at 40 °C/min on <25 µm powder showed the main exothermic peak at 550 °C associated with the decomposition of the icosahedral phase. The peak observed at ~400-500 °C was also seen as a shallow, sluggish peak only visible in larger powder size fractions. It was therefore suggested that this peak could be related to the chemical composition and the cooling rate [Rou-12].

Given the evidence from the literature it is reasonable to relate the peaks present at ~550 °C in both the 1st and 2nd powder batches in Figure 6.1 to the decomposition of the metastable icosahedral quasicrystalline phase into more stable intermetallic phases.

In the extruded bar the decomposition of the icosahedral phase occurred ~500 °C, as shown by DSC and proved by TEM and XRD. The work by Rounthwaite also showed DSC curves of extruded bars which were processed at ~400 °C and also found that the main exothermic event in

the curve occurred at ~500 °C [Rou-12]. He found that the peak in the bar was short, with extended shoulders on both sides, which was not the case in the present work. He also noted that there were several small exothermic peaks at lower temperatures which he associated with recrystallisation of the Al grains and precipitation involving more metastable phases such as δ-Al_6Fe [Rou-12]. δ-Al_6Fe was reported by Garcia Escorial *et al.* as well [Gar-10]. Inoue *et al.* reported that for the same alloy composition produced by warm extrusion at 400 °C the main exothermic event associated with the decomposition of the icosahedral phase in DSC scans occurred at ~470 °C when the heating rate was 0.67 °C/min [Ino-00].

Heat treatments and microstructural characterisation were also performed for 1 hour at 250°C, 280 °C and 550 °C. The results of the X-ray diffractograms showed no difference between the as cut samples and the samples heat treated at 250 °C. After one hour at 280 °C the icosahedral phase and α-Al were still present, however some intermetallic precipitation started to become visible in the form of κ-Al_3Ti and of ϕ-$Al_{13}Cr_2$. After heat treatment at 550 °C, the icosahedral phase could no longer be identified, but large amounts of more stable intermetallic phases became apparent, like κ-Al_3Ti, ϕ-$Al_{13}Cr_2$ and ζ-$Al_{13}Fe_4$. This result is consistent with the literature, which stated that at 500-550°C the decomposition of the icosahedral phase into more stable intermetallic phases occurs [Tod-04], [Gal-04], [Aud-02], [Gar-07]. Garcia Escorial *et al.* found that in extruded bars of the same nominal alloy composition some icosahedral phase could still be present after 1 hour heat treatment at 500 °C, but not after 1 hour at 550 °C [Gar-07].

Microhardness indents were performed on the as cut and heat treated bars and a strength decrease occurred after heat treatment at 550 °C. The indents performed on the as-cut bar, the bar heat treated at 250 and 280 °C were within each other's error bars, however a decreasing tendency could be observed. The addition of pure Al fibres caused a linear decrease in microhardness with vol% pure Al, which can be seen in Figure 6.21. The linearity shows that the microhardness of these fibre composites follows the rule of mixtures.

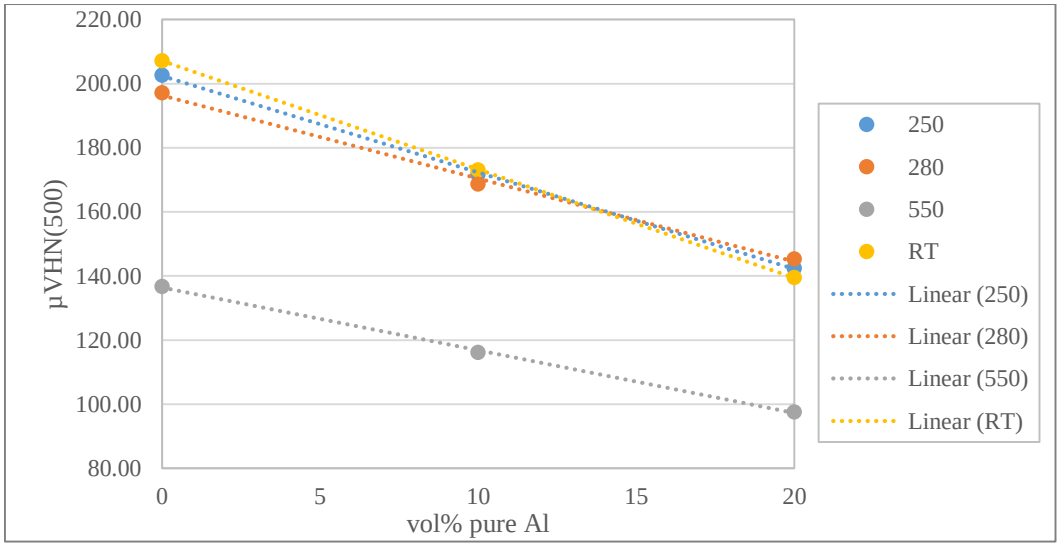

Figure 6.21: microhardness values plotted against pure Al content at room temperature (RT) and after heat treatments for 1 hour at 250 °C, 280 °C and 550 °C.

Longer heat treatments were performed at 250 °C for up to 1000 hours, followed by microstructural characterisation. No difference could be detected between the as-extruded samples and the samples heat treated for 1000 hours at 250 °C by XRD. However, the microhardness indents showed a slight decreasing tendency of 2-5% the original values both in the alloy and composite bars.

6.6 Conclusions

DSC analysis of the as-atomised $Al_{93}Fe_3Cr_2Ti_2$ powders from batch 1 and 2 did not highlight any reactions occurring up to the extrusion temperatures of 390-420 °C. The reaction detected occurred at 550°C and was associated with the decomposition of the icosahedral phase.

No reaction was detected in the Pure Al powder until the onset of melting at 630 °C.

After extrusion, the DSC, XRD and TEM analysis of the bars showed the decomposition of the icosahedral phase occurring at 500 °C, which is 50 °C below the reaction temperature measured in the powders before extrusion.

Heat treating the bars for 1 hour at 250 °C did not alter the microstructure or microhardness of the alloy and composite bars in a way which could be detected by SEM, TEM, XRD and microindentation. Heat treating for 1 hour at 280 °C caused some intermetallic precipitation in the form of κ-Al_3Ti and ϕ-$Al_{13}Cr_2$ detected by XRD, but the microhardness remained constant (within experimental error values). Heat treating the bars at 550 °C caused the complete decomposition of the icosahedral phase and the precipitation of κ-Al_3Ti, ϕ-$Al_{13}Cr_2$ and ζ-$Al_{13}Fe_4$ intermetallic phases and a ~33% reduction in microhardness of the 0-1a, 10-1a and 20-1a bars. The microhardness decreased linearly with increasing vol% pure Al fibre content following the rule of mixtures.

Analysing the microstructural stability at 250 °C for up to 1000 hours did not show any changes in the microstructure detected by SEM and XRD. After 1000 hours the microhardness of the 0-1a, 10-1a and 20-1a samples only went down by 2-5%.

References

[Aud-02] F. Audebert, F. Prima, M. Galano, M. Tomut, P. J. Warren, I. C. Stone, B. Cantor, Mat. Trans., (2002), A 43, 8, 2017.

[Gal-09a] M. Galano, F. Audebert, I.C. Stone, B. Cantor, Acta Mat., (2009), 57, 5107–5119.

[Gal-04] M. Galano, F. Audebert, B. Cantor, I. Stone, Mat. Sci. Eng., (2004), A, 375-377, 1206-1211.

[Gar-10] A. Garcia-Escorial, M. Echevarria, M. Lieblich, I. Stone, J. All. Comp., (2010), 504S, S519–S521.

[Gar-07] A. Garcia Escorial, V. F. Cremaschi, E. Natale, M. Lieblich, J. All. Comp., (2007), 434-435, 215-216.

[Ino-00] A. Inoue, H. Kimura, Mat. Sci. Eng., (2000), A286, 1-10.

[Ino-98] A. Inoue, Pro. Mat. Sci., (1998), 43, 365-520.

[JCP-99] JCPDS-International Centre for Diffraction Data v2.02 Codes: 04-0787, 13-0146, 29-0014, 29-0042 (1999).

[Kim-00] H. Kimura, K. Sasamori, A. Inoue, Mat. Sci. Eng., (2000), 294-296, 168-172

[Mon-43] L. F. Mondolfo, *Metallography of Aluminum Alloys*, John Wiley & Sons, (1943).

[Ped-10] S. Pedrazzini, Masters Degree Thesis, University of Oxford, (2010).

[Rou-12] N. J. Rounthwaite, DPhil Thesis, University of Oxford, (2012).

[Spe-10] S. Speller, XRD Lecture Notes, Oxford University, (2010).

[Tod-04] I. Todd, Z. Chlup, J.G. O'Dwyer, M. Lieblich, A. Garcia-Escorial, Mat. Sci. Eng., (2004), A 375–377, 1235–1238.

[Xu-06] L. Xu, Y.Y. Cui, Y.L. Hao, R.Yang, Mat. Sci. Eng., (2006), A 435–436, 638–647.

[Yam-07] M. Yamasaki, Y. Nagaishi and Y. Kawamura, Scripta Mat., (2007), 56, 785–788.

Chapter 7: Room Temperature Mechanical Testing

This chapter studies the mechanical behaviour at room temperature of the $Al_{93}Fe_3Cr_2Ti_2$ alloy and composite bars containing icosahedrical quasicrystalline and intermetallic nanoparticles dispersed in an α-Al matrix. The mechanical properties were assessed through Vickers microhardness tests, quasi-static tensile tests and dynamic tensile and compressive tests. The 0-1a, 10-1a and 20-1a bars were selected for room temperature mechanical testing to maintain consistency by using bars produced from the same powder batch.

7.1 Mechanical Testing

7.1.1 Microhardness

Vickers microhardness was measured during a previous project on the bars 0-1a, 10-1a and 20-1a along the extrusion direction obtaining the values summarised in Table 7.1 and Figure 7.1 [Ped-10].

Bar	VHN	St Dev	vol% pure Al fibres
0-1a	207	2	0
10-1a	173	6	10
20- 1a	140	9	20

Table 7.1: Vickers microhardness tests along the extrusion direction. Averages of at least 25 indents with a 500 g weight held 20 s with their respective standard deviation values [Ped-10].

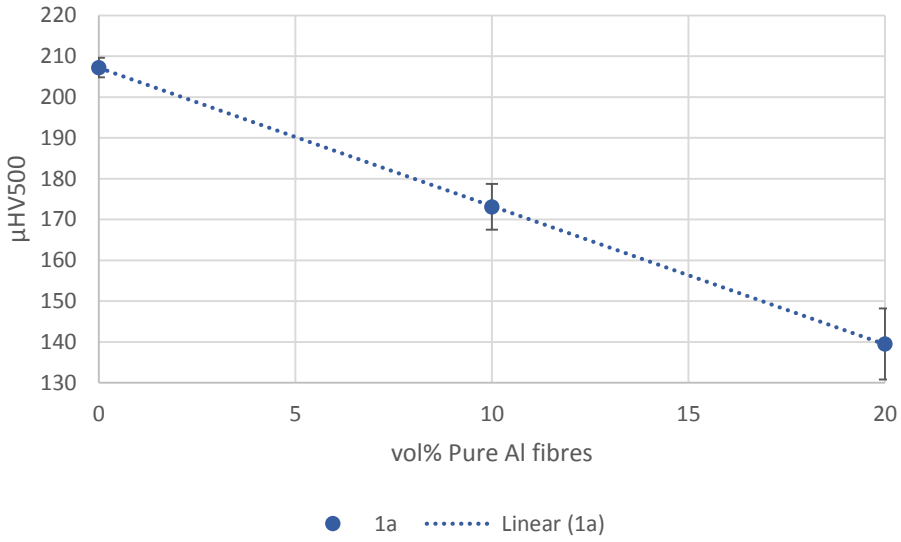

Figure 7.1: Plot of the variation of Vickers microhardness of each bars with the amount of pure Al fibres also showing the differences between powder batches [Ped-10].

Microhardness values were measured at 207±2 µVHN$_{500}$, 173±6 µVHN$_{500}$ and 140±9 µVHN$_{500}$ for the 0-1a, 10-1a and 20-1a bars respectively. A plot of the microhardness and vol% pure Al fibres showed a linear decrease in hardness with increasing fibre content.

7.1.2 Quasi-Static Tensile Strength

Figure 7.2 (a) shows the tensile engineering stress-strain curves measured on the 0-1a, 10-1a and 20-1a bars during a previous project at a strain rate 1x10^{-4} s^{-1} on dog-bone shaped threaded specimens [Ped-10]. The UTS values from this curve were plotted against vol% pure Al in Figure 7.2 (b) and summarised in Table 7.2.

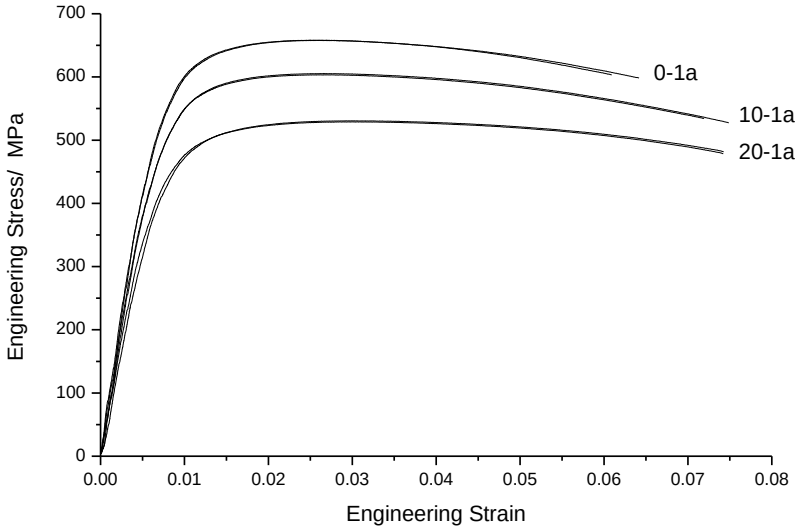

(a)

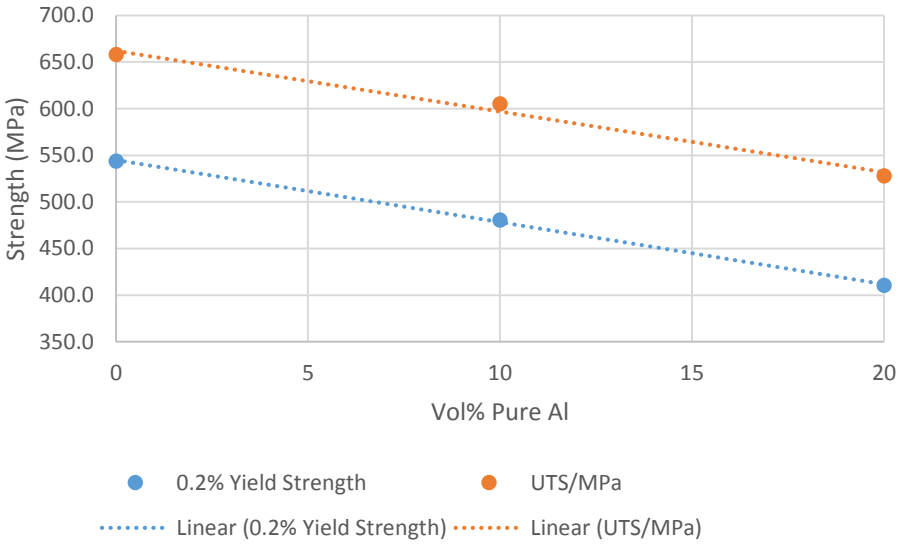

(b)

Figure 7.2: (a) Tensile stress-true strain curves of the 0-1a, 10-1a and 20-1a bars performed at strain rate of $1x10^{-4}$ s^{-1}, (b) plot of UTS and vol % pure aluminium showing a linear decrease in strength [Ped-10].

Sample	Vol% Al	UTS(MPa)	0.2% Yield Strength (MPa)	Strain-to-Failure
0-1a	0	658	543.6	6.50%
10-1a	10	605	480.6	7.50%
20-1a	20	528	410.6	7.50%

Table 7.2: Tensile stress- strain data performed at strain rate of $1x10^{-4}$ s^{-1} [Ped-10].

The tensile tests showed a 0.2% proof stress of 543.6 MPa and 6.5-7.5% strain to failure for the pure $Al_{93}Fe_3Cr_2Ti_2$ alloy bar 0-1a and a linear decrease in strength with the addition of pure Al fibres for the bars 10-1a and 20-1a following the rule of mixtures [Ped-10], [Cly-95].

7.1.3 Dynamic Tensile Strength

Dynamic tensile tests were performed at 2200 s^{-1} strain rate. Figure 7.3 shows the engineering stress-strain curves for the dynamic tensile tests.

The dynamic flow stress of the pure alloy bar and the composites containing 10 and 20 vol% pure Al fibre samples were 970 MPa, 875 MPa and 770 MPa respectively. The pure alloy and composites showed an increase of 350-400 MPa in the UTS from the quasi-static tests performed at $1x10^{-4}$ s^{-1} strain rate to the dynamic tests at 2200 s^{-1}, and a strain-to-failure decrease from 6.5-7.5% to 3-4.5%.

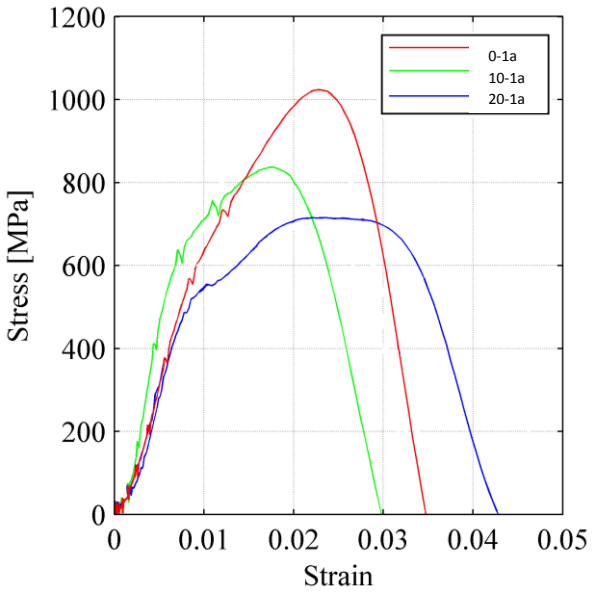

Figure 7.3: the engineering stress-strain curves for the dynamic tensile tests performed at strain rate 2200 s^{-1} of the pure alloy and composites.

During a previous project, some preliminary tests of the 0-1a, 10-1a and 20-1a bars with only one sample from each bar at 2200 s^{-1} strain rate were performed [Ped-10]. However accuracy issues

arose from the previous data due to the lack of repeat tests and the fact that the 0-1a sample failed on a large defect and the strain gauge fell off the 10-1a sample during testing [Ped-10]. The tests performed in the present work on the 0-1a, 10-1a and 20-1a bars have been performed with 2-4 tests per condition to confirm and improve the accuracy of the previous results.

7.1.4 Dynamic Compressive Strength

Dynamic compressive tests were performed at 3000 s^{-1} strain rate. Figure 7.4 shows the nominal stress-strain curves for the tests. During a previous project, preliminary tests of the 0-1a, 10-1a and 20-1a bars with only one sample from each bar at 3000 s^{-1} strain rate were performed. However accuracy issues arose from the previous data due to the lack of repeat tests [Ped-10]. These tests have been performed on the 0-1a, 10-1a and 20-1a bars, with 4 tests per condition to confirm and improve the accuracy of the previous results.

The pure alloy and composites showed a significant increase in the UTS with increasing strain rate compared to the quasi static compressive tests performed at $1x10^{-4}$ s^{-1} strain rate by Pedrazzini [Ped-10], and still retained about 20-30% strain to failure in compression. The UTS of the samples was 1020 MPa for the pure alloy bar, 1000 MPa for the composite with 10 vol% pure Al and 790 MPa for the one with 20 vol% Al respectively. All the bars had good strain-to-failure in the high strain rate tests, but it can be seen that the composites showed more ductility than the pure alloy sample (25% instead of 40%).

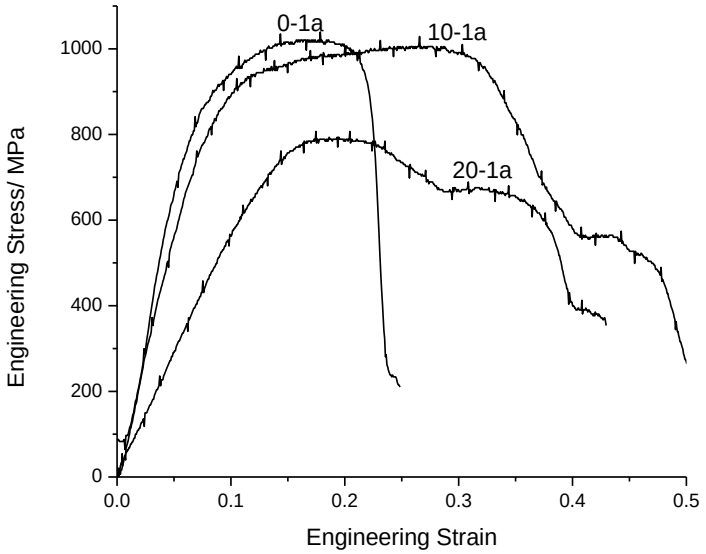

Figure 7.4: dynamic stress strain curve for the compression tests at 3000 s^{-1} strain rate.

The area under the curves was also calculated as an indicator of the total mechanical energy per unit volume necessary to deform the specimen at high strain rate, which can be related to toughness. Toughness is defined as the amount of energy per unit volume the material can absorb before fracture. The energy values obtained from integrating the curves in Figure 7.4 were 193 J/kg, 381 J/kg and 248 J/kg for the 0-1a, 10-1a and 20-1a bars respectively.

7.2 Discussion

7.2.1 Microhardness

Microhardness values obtained for the 0-1a, 10-1a and 20-1a bars were compared with the literature. Todd *et al.* found for an alloy of nominal chemical composition $Al_{93}Fe_3Cr_2Ti_2$ and measured chemical composition $Al_{92.5}Fe_{3.2}Cr_{2.3}Ti_{2.0}$ extruded from the same powder size, same extrusion temperature but extrusion ratio of 10:1 instead of 14:1 to have a microhardness of μVHN_{25}=172±8.9 [Tod-04]. Galano *et al.* found for melt-spun ribbons of the same nominal composition and actual composition $Al_{92.94}Fe_{3.02}Cr_{2.02}Ti_{2.02}$ to have an outstanding microhardness of

μVHN_{100}=351 [Gal-09b]. Despite all those values being measured using different test loads, all those values appear to be higher than the corresponding hardness of commercial high strength Al-based alloys such as 7075 T6 ~172 VHN, 7079 T5 ~128 VHN, 2024 T86 ~155 VHN [Smi-83].

Microhardness values measured on the 0-1a, 10-1a and 20-1a bars were found to be lower than those measured by Galano *et al.* on melt spun ribbons [Gal-09b] but higher than the values obtained by Todd *et al.* on extruded bars (with a different extrusion ratio and small differences in chemical composition) [Tod-04]. The microhardness of each bar was shown to decrease linearly with increasing volume % of pure Al fibres, which would suggest that the short fibre contents effect on the microhardness of the composites can be predicted using the rule of mixtures [Cly-95].

7.2.2 Quasi-Static Tensile Strength

Quasi-static tensile tests performed on commercially used high strength Al-based alloys exhibit a lower room temperature yield strength than the values for the 0-1a, 10-1a and 20-1a bars shown in Figure 7.2. Examples of this are 7075-T6 with σ_y= 505 MPa and 2014-T6 with σ_y= 415 MPa [Smi-83]. Ti6Al4V is commonly used in the aerospace industry in applications where lightweight, high strength alloys are required and it has a room temperature yield strength of σ_y= 940 MPa, which exceeds that of nanoquasicrystalline $Al_{93}Fe_3Cr_2Ti_2$. However when the specific yield strengths of the alloys are compared (dividing by the density[2]) then Ti6Al4V has a yield point of σ_y= 212.7 MPa/gcm^{-3} and the pure $Al_{93}Fe_3Cr_2Ti_2$ 0-1a bar has the outstanding specific yield strength of σ_y= 192.7 MPa/gcm^{-3}.

Previous studies on rapidly solidified Al-Fe-Cr-Ti(-Si) alloys showed that the main strengthening mechanisms involved are the small grain size [Gal-09b], [Aud-02], [Voj-07], the presence of hard, incoherent nanoparticles [Gal-09b], [Aud-02], [Voj-07], [Ino-99], [Ino-00] and solutes in solid solution [Gal-09b], [Aud-02]. Inoue *et al.* have produced the same alloy with a microstructure

[2] The density of Ti6Al4V was taken from Smithell's Metals Handbook [Smi-83], while that of the $Al_{93}Fe_3Cr_2Ti_2$ alloy was calculated stochiometrically based on the densities of the pure elements to be 2.88 kg/m^3. Taking into account 3 vol% pure Al contamination the density would be 2.87 kg/m^3.

made of icosahedral phase in a single grain FCC-Al matrix and therefore attribute the high ductility of their alloy to the lack of grain boundaries [Ino-00], [Ino-99].

A comparative study of the mechanical properties of a series of nanostructured Al-based melt-spun ribbons was carried out by Audebert *et al.* at room temperature and Galano *et al.* at high temperatures with the conclusion that the outstanding mechanical properties of the alloy are the result of a combination of solid solution strengthening, particle dispersion and grain refinement strengthening [Gal-09b], [Aud-02]. No attempt to quantify the various contributions of each strengthening mechanism was made.

An estimation of the various contributions of different strengthening mechanisms to the overall strength of an $Al_{92.4}Fe_{1.2}Cr_{3.3}Ti_{2.4}Si_{0.7}$ at% alloy produced by powder metallurgy was carried out by Vojtech *et al.*, who concluded that Hall-Petch strengthening was the dominant mechanism, followed by Orowan strengthening; the solid solution mechanisms can be neglected due to the hot processing methods which reduce the solute content in solid solution retained after the rapid solidification process [Voj-07].

7.2.3 Dynamic Tensile Strength

The average dynamic flow stress measured for the pure alloy bar was 970 MPa, while the composites showed 875 MPa (10 vol% Al) and 770 MPa (20 vol% Al). When divided by the density, their specific strength was measured to be 346 MPa, 313 MPa and 287 MPa respectively. Values for commercially available Al alloys tested at similar strain rates were obtained from the literature and used as comparison. Tests were found on 6000 and 7000 series Al alloys performed by Chen *et al.* [Che-09] at 1000 s^{-1} strain rate. They found that 6060-T6 alloy had a specific dynamic flow stress of 100 MPa, for 6082-T6 it was found to be 133 MPa, 7003 T6 was 167 MPa and 7108-T6 was 185 MPa. Reyes *et al.* performed tests at 1300 s^{-1} strain rate and found that 7003-T79 had a dynamic flow stress/density of 185 MPa and 7108-T6 was 143 MPa [Rey-06]. The most comparable value found of high strain rate tests of Ti6Al4V was performed at 3500 s^{-1} and it

had a specific flow stress of 356 MPa [ElM-06]. Therefore in terms of specific properties, the $Al_{93}Fe_3Cr_2Ti_2$ alloy and composites show a strength which is much higher than commercially available Al alloy, and which is comparable to Ti6Al4V.

7.2.4 Dynamic Compressive Strength

Values for commercially available Al alloys tested at similar strain rates were obtained from the literature and used as comparison. Tests were found on 7000 series Al alloys performed by Oosterkamp *et al.* [Oos-00] at 3000 s^{-1} strain rate. They found that 6082-T6 alloy had a specific dynamic flow stress of 137 MPa, for 7108-T79 it was found to be 166 MPa. El-Magd *et al.* performed tests at 2500, 3500 and 5000 s^{-1} strain rate and found that 7075 had a dynamic flow stress/density of 240 MPa, 248 MPa and 259 MPa respectively [ElM-06]. The most comparable value found of high strain rate tests of Ti6Al4V was performed at 2300, 3100 and 3900 s^{-1} and it had a specific flow stress of 377, 388 and 400 MPa for each strain rate [ElM-06]. In terms of specific properties, the $Al_{93}Fe_3Cr_2Ti_2$ alloy and composites show a strength which is higher than commercially available Al alloy, and which is comparable to Ti6Al4V.

7.3 Conclusions

Microhardness tests have been performed on the pure alloy and composites and the measured value was 20% higher than the commercial “high strength” 7075 T6 and up to 40% higher than the other 2000 and 7000 series alloys it was compared to. It was also 40% lower than the value measured on melt spun ribbons of the same nominal composition [Gal-09b]. The microhardness of the composites decreased linearly with increasing vol% pure Al following the rule of mixtures [Cly-95].

Quasi static tensile tests have been performed at $1x10^{-4}$ s^{-1} strain rate. The quasi-static UTS measured, when divided by the density, was only 10% lower than that of Ti6Al4V and at least 25%

higher than any of the commercial high strength Al alloys used as comparison. The UTS of the composites decreased linearly with increasing vol% pure Al following the rule of mixtures [Cly-95].

Dynamic tensile tests have been performed at 2200 s^{-1} strain rate. The specific UTS and was 45-67% higher than the 2000 and 7000 series alloys used for comparison and only 3% lower than Ti6Al4V.

Dynamic compression tests have been performed at 3000 s^{-1} strain rate. The specific UTS was found to be 30% higher than 7075 Al alloy and only 10% lower than Ti6Al4V. The total strain to failure was also increased by ~25% in the composites than in the pure $Al_{93}Fe_3Cr_2Ti_2$ alloy, showing an improvement in ductility with fibre addition.

The energy absorbed during dynamic compressive tests was calculated as the total area under the composites curves. It was 50% larger in the 10-1a curve and 33% larger in the 20-1a curve than the 0-1a curve. This area is indicative of the total work to fracture, showing that the composites are significantly tougher than the base alloy under high strain rate conditions.

References

[Aud-02] F. Audebert, F. Prima, M. Galano, M. Tomut, P. J. Warren, I. C. Stone, B. Cantor, Mat. Trans. A, (2002), 43, 8, 2017.

[Che-09] Y. Chen, A. H. Clausen, O. S. Hopperstad, M. Langseth, Int. J. Sol. and Struc., (2009), 46, 3825–3835.

[Cly-95] T. W. Clyne, P. J. Withers, *An introduction to metal matrix composites*, Cambridge University Press, (1995).

[ElM-06] E. El-Magd, M. Abouridouane, Int. J. Impact Eng., (2006), 32, 741–758.

[Gal-09b] M. Galano, F. Audebert, I. C. Stone, B. Cantor, Acta Mat., (2009), 57, 5120–5130.

[Gal-04] M. Galano, F. Audebert, B. Cantor, I. C. Stone, Mat. Sci. Eng. (2004), A 375-377, 1206-1211.

[Ino-00] A. Inoue, H. Kimura; Mat. Sci. Eng., (2000), A286, 1-10.

[Ino-99] A. Inoue, H. Kimura, Nano. Structured Mat., (1999), 11, 2, 221–231.

[Oos-99] L. Djapic Oosterkamp, A. Ivankovic, G. Venizelos, Mat. Sci. Eng., (2000), A278, 225–235.

[Ped-10] S. Pedrazzini, Masters thesis, Department of Materials, University of Oxford, (2010).

[Rey-06] A. Reyes, O. S. Hopperstad, O. G. Lademo, M. Langseth, Comput. Mat. Sci., (2006), 37, 246–268.

[Smi-83] E. A. Brandes, G. B. Brooks editors, *Smithells Metals Reference Book*, Butterworth-Heinemann, (1983).

[Tod-04] I. Todd, Z. Chlup, J.G. O'Dwyer, M. Lieblich, A. Garcia-Escorial, Mat. Sci. Eng., (2004), A 375–377, 1235–1238.

[Voj-07] D. Vojtěch, J. Verner, J. Šerák, F. Simancik, M. Balog, J. Nagy, Mat. Sci. Eng., (2007), A 458, 1-2, 15, 371.

Chapter 8: Mechanical Properties at Elevated Temperature

This chapter studies the high temperature compressive strength of the $Al_{93}Fe_3Cr_2Ti_2$ alloy and composite bars. The compressive strength of pure alloy samples and composite samples was measured at strain rates 0.1 s^{-1}, 1 s^{-1}, 10 s^{-1} and 50 s^{-1} at 350 °C, 400 °C, 450 °C and 500° C. The results were used to investigate the forging conditions required to make this alloy and composites into engineering components. These tests were carried out on the bars 0-1b, 10-1b and 20-1b in order to maintain consistency by using bars made from the same powder batch.

8.1 Compressive Testing the Pure Alloy Bar

Figure 8.1 shows true stress-true strain curves from the compressive tests of the pure $Al_{93}Fe_3Cr_2Ti_2$ bar (0-1b) plotted at constant strain rate and varying temperature between 350-500 °C.

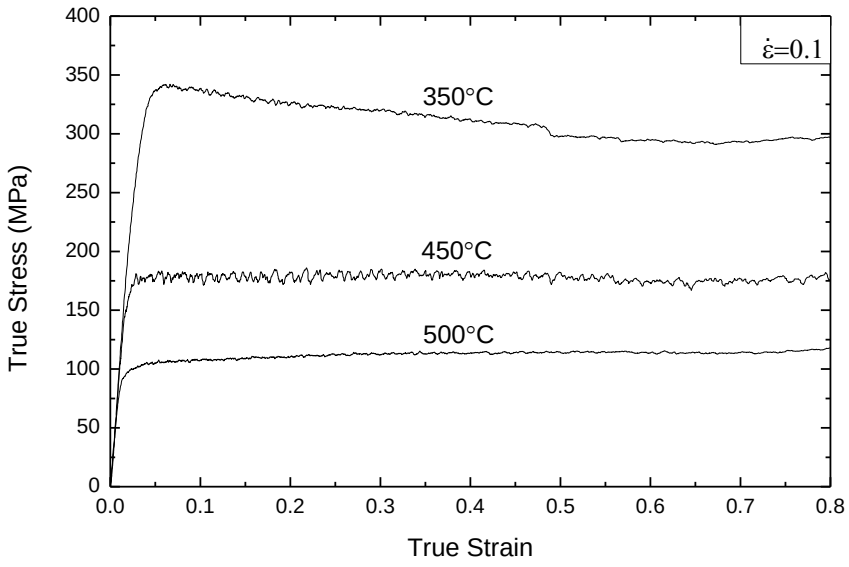

(a)

Figure 8.1: compressive tests of the 0-1b bar at constant strain rate and varying temperature. (a) samples tested at strain rate 0.1 s^{-1} at temperatures 350 °C, 450 °C and 50 °C.

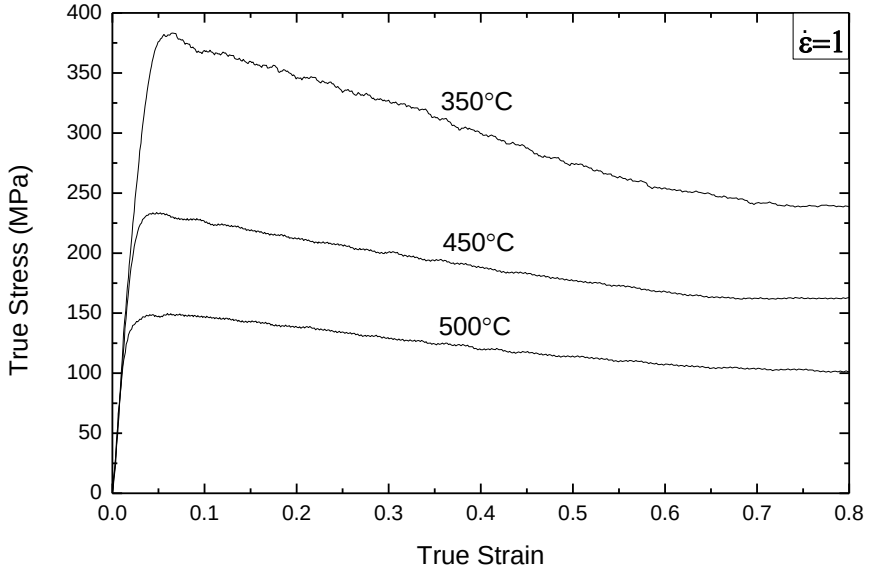

(b)

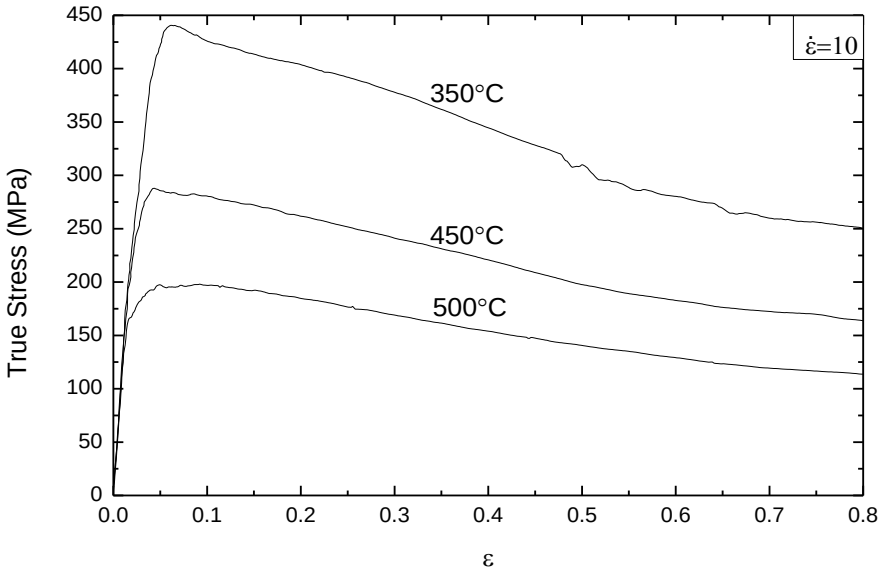

(c)

Figure 8.1 (cont.): compressive tests of the 0-1b bar at constant strain rate and varying temperature. (b) tests performed at strain rate 1 s^{-1} and temperatures 350 °C, 450 °C and 500 °C, (c) samples tested at strain rate 10 s^{-1} and temperatures 350 °C, 450 °C and 500 °C.

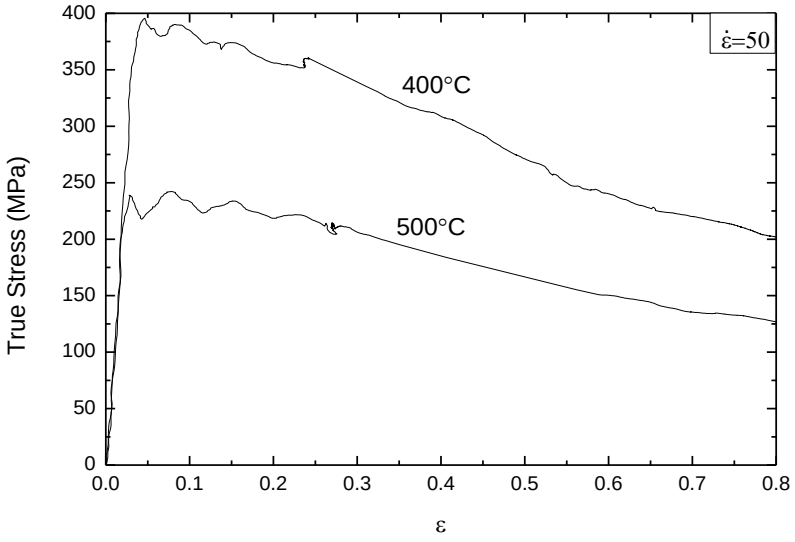

(d)

Figure 8.1 (cont.): compressive tests of the 0-1b bar at constant strain rate and varying temperature. (d) samples tested at strain rate 50 s^{-1}. Due to a shortage of material these could only be performed at 400 °C and 500 °C.

The curves displayed in Figure 8.1 (a), (b), (c) and (d) show that at constant strain rate the yield strength decreases with increasing temperature. Also, the gradient of the plastic zones of all the curves at constant strain rate varies with changing temperature. A negative gradient of the plastic zone of the compressive true stress-true strain curve indicates that the material is softening under the applied stress, a positive gradient indicates that the material is hardening. If the gradient is zero, that indicates a steady state. Figure 8.1 (a) shows three curves, all taken at strain rate 0.1 s^{-1}. The curve at T= 500 °C is hardening, the curve at T=450 °C is at a steady state and the one at T=350 °C was softening. Serrated flow can be observed at 350 °C and 450 °C at strain rates 0.1 s^{-1} and at 350 °C at strain rate 1 s^{-1} in the curves in Figure 8.1 (a) and (b). All the three curves measured at strain rate 1 s^{-1} and shown in Figure 8.1 (b) show a softening behaviour, more evident with a steeper gradient at 350 °C, in the early stage of plastic deformation however they flatten into a steady state between true strain 0.6-0.8. In Figure 8.1 (c) the three curves at strain rate 10 s^{-1} are shown. All three curves also show a softening behaviour in the plastic zone, with the lowest temperature curve showing the steepest decreasing slope. All three curves also have a shallower gradient between true strains 0.6-0.8. Figure 8.1 (d) shows the two curves taken at the highest

strain rate: 50 s^{-1}. Multiple large serrations can be observed at the onset of plastic deformation in both curves obtained at strain rate 50 s^{-1} with more of a softening effect in the lower temperature curve at 400 °C.

X-ray diffraction studies have been performed on the samples and are shown in Figure 8.2. They show the thermal evolution of the samples after compression testing at different temperatures between 350-500 °C. The icosahedral phase was labelled "i", the FCC-Al matrix was labelled α, then φ was $Al_{13}Cr_2$, ζ was $Al_{13}Fe_4$ and κ was Al_3Ti.

XRD peaks were indexed as follows. α-Al peaks were identified by indexing the reflections corresponding to the (111), (200), (220), (311), (222) and (400) planes in the 2θ = 10 °-100 ° range at 38.5 ° (100% intensity), 44.7 °, 65.2 °, 78.3 °, 82.5 ° and 99.2 ° [JCP-99]. The presence of the icosahedral phase was shown by broad peaks at 2θ ~ 22.9 °, 41.3 °, 43.5 °, 61.6 ° and 73.7 ° [Gal-09a]. Other intermetallic phases were identified including Al_3Ti, $Al_{13}Fe_4$, $Al_{13}Cr_2$ which were indexed using data sheets [JCP-99]. The presence of Al_3Ti was shown by the peaks at 2θ~22.3 °, 31.9 °, 39.2 ° (100% intensity), 66.5 ° and 84.4 ° corresponding to the (100), (110), (111), (220), (311) reflections respectively. The $Al_{13}Fe_4$ was shown by peaks at 43.1 °, 44.2 ° and 44.4 ° corresponding to the 100% intensity $(\bar{6}23)$ reflection and the (025) and (423) respectively. The $Al_{13}Cr_2$ phase was shown by the peaks at 36.6 °, 41.2 °, 41.4 °, 41.5 °, 43.8 °, 43.9 ° (100% intensity), 44.0 °, 75.3 °, 75.7 ° corresponding to the $(\bar{1}31)$, $(\overline{11}13)$, (711), $(\bar{4}24)$, $(\overline{10}22)$, $(\bar{8}20)$, $(\bar{3}33)$, $(15\ 3\ \bar{7})$ and (335).

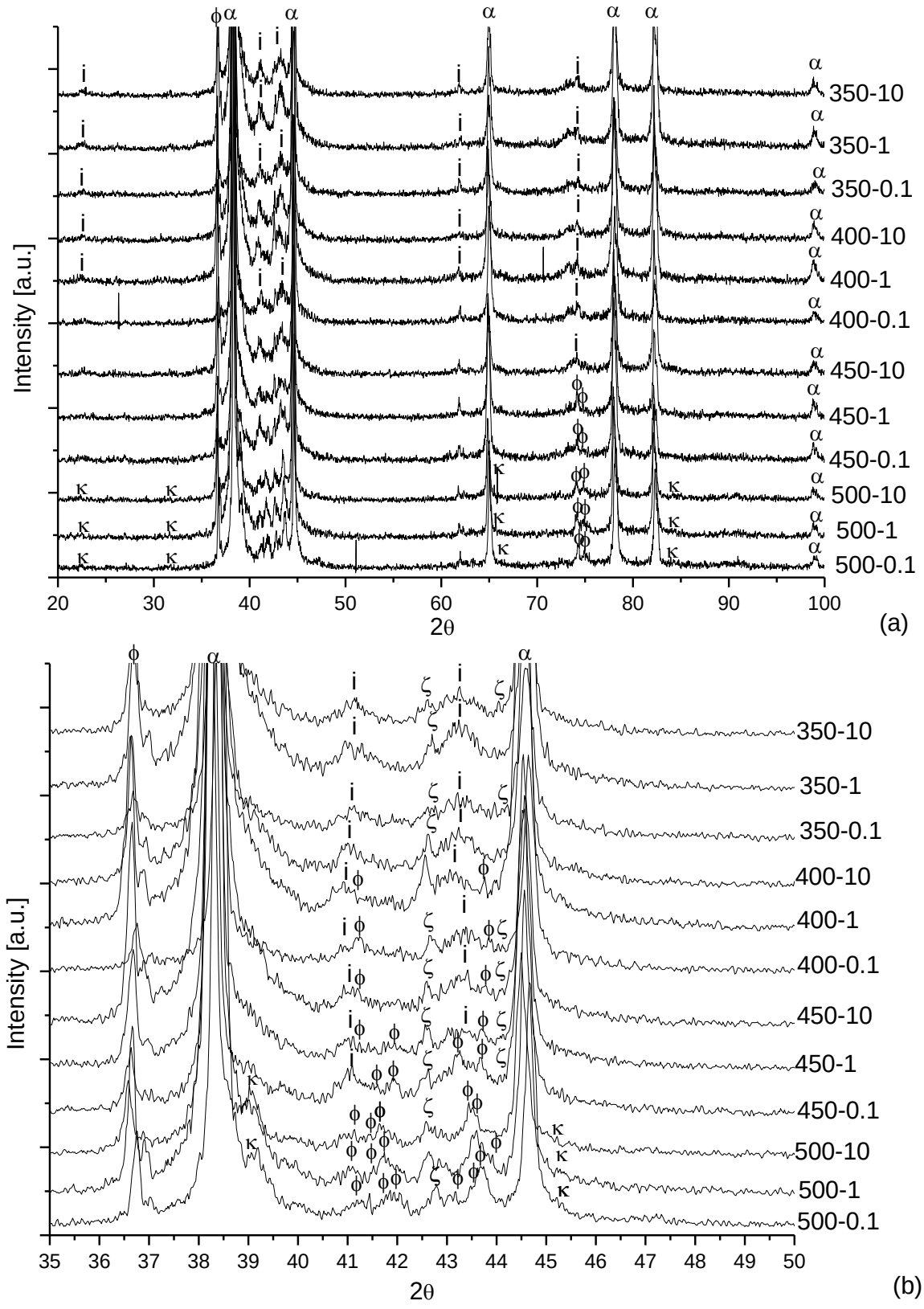

Figure 8.2: X-ray diffractograms of the samples after compression testing at different temperatures and strain rates. (a) full scan from 20-100 °, (b) enlargement of the 35-50 ° section.

After testing at 350 °C FCC-Al, icosahedral quasicrystals, $Al_{13}Fe_4$ and $Al_{13}Cr_2$ intermetallic phases could be identified by XRD. At 400 °C the same phases were present, however the peaks size is increasing when compared to the XRD of the samples after testing at 350 °C. At 450 °C a combination of both icosahedral phase and the more stable intermetallic phases like $Al_{13}Fe_4$, $Al_{13}Cr_2$ could be detected, but the icosahedral peaks became less evident and the peaks associated to the other intermetallic phases became more defined. At 500 °C, the icosahedral phase could not be indexed by XRD. Al_3Ti was also detected by XRD at 500 °C, as well as $Al_{13}Fe_4$ and $Al_{13}Cr_2$.

According to the results of the DSC and heat treatments described in Chapter 6 and the literature, ~500 °C the decomposition of the icosahedral phase into more stable intermetallic phases occurs [Rou-12], [Tod-04].

8.2 Compressive Tests of the Composite Bars

Figure 8.3 shows the effect of changing temperature while keeping the strain rate constant during testing of the 10-1b bar. One extra test was performed at strain rate 0.01 s^{-1} which was not done with the other bars because an extra sample was available from this extruded bar.

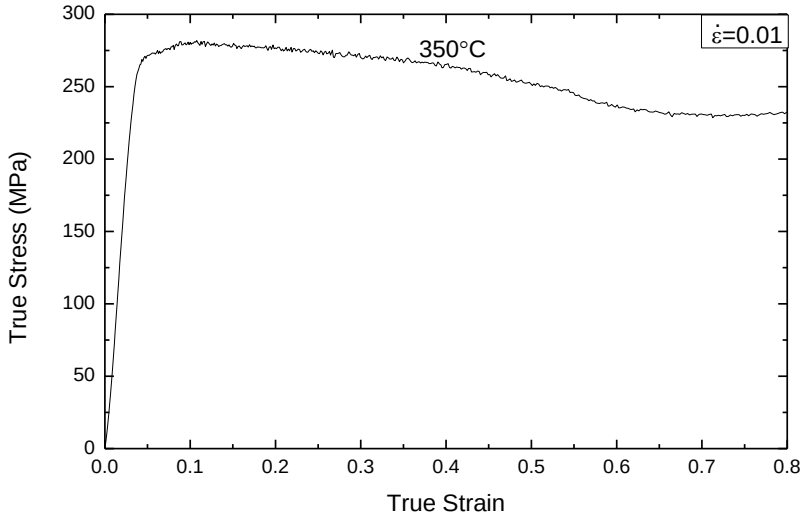

(a)

Figure 8.3: compression tests of the 10-1b bar at constant strain rate and varying temperature. (a) test performed at strain rate 0.01 s^{-1} and T=350 °C.

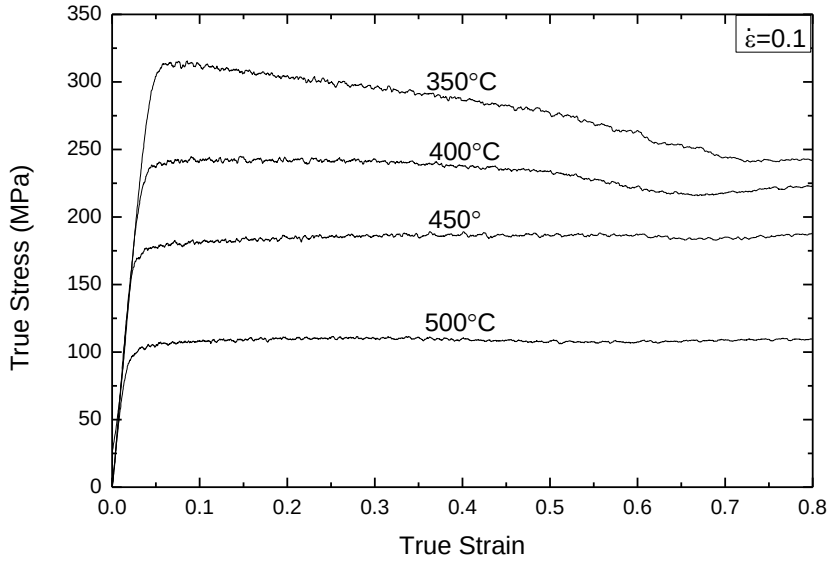

(b)

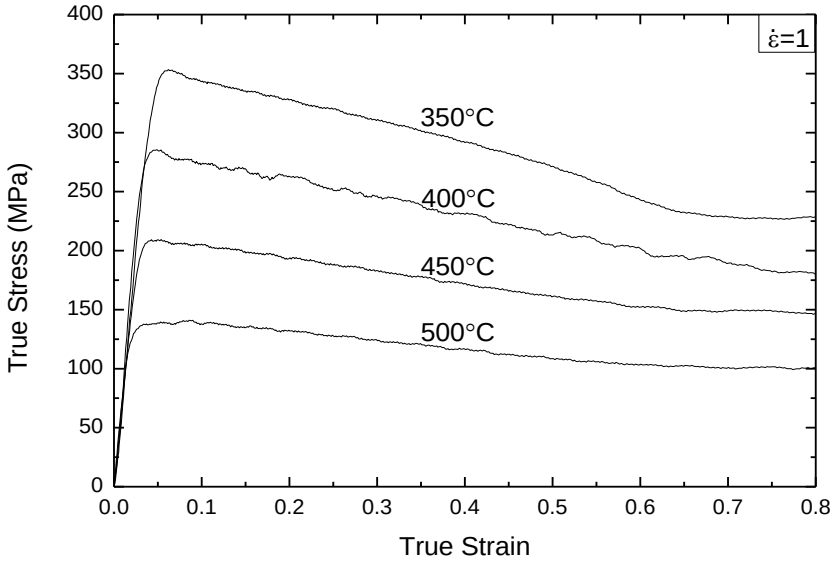

(c)

Figure 8.3: compression tests of the 10-1b bar at constant strain rate and varying temperature. (b) tests performed at 0.1 s^{-1} and a varying temperature between 350-500 °C, (c) tests performed at strain rate 1 s^{-1} and temperature between 350-500 °C.

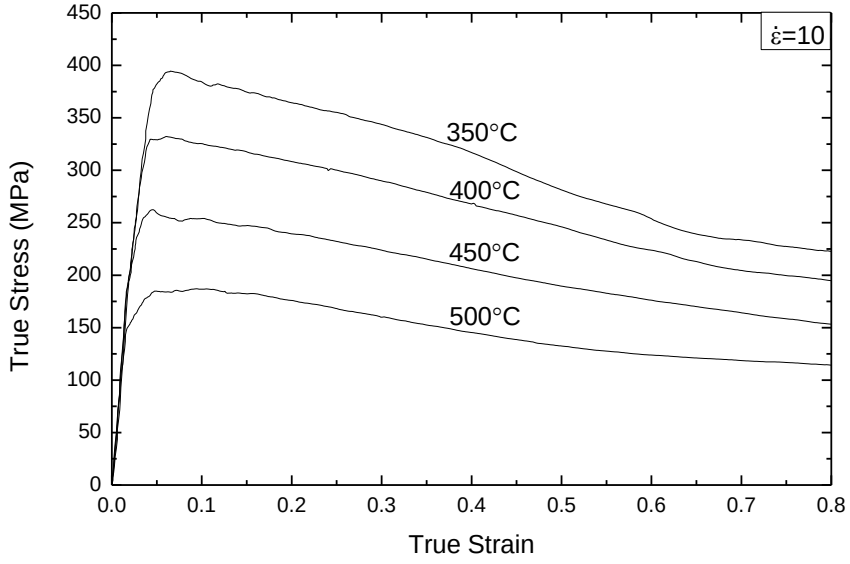

(d)

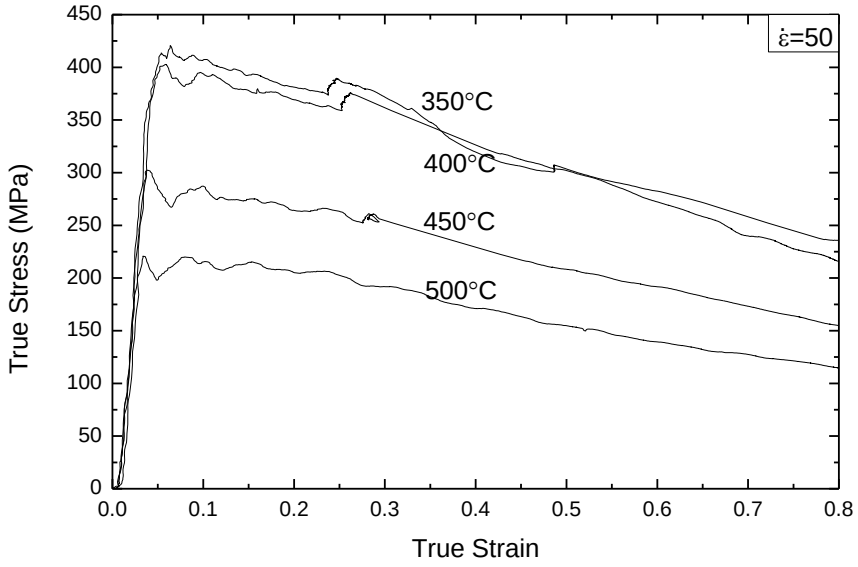

(e)

Figure 8.3: (cont): compression tests of the 10-1b bar at constant strain rate and varying temperature. (d) tests performed at strain rate 10 s^{-1} and temperature between 350-500 °C, (e) tests performed at strain rate 50 s^{-1} and temperature between 350-500 °C.

The plots in Figure 8.3 analyse the temperature effect on the compressive yield strength and the slope of the plastic zone at constant strain rate. From the curves presented in Figure 8.3 (b), (c), (d) and (e) we can see that an increase in temperature causes a decrease in the yield strength of the composite samples. It is also noticeable that the gradient of the plastic zones of all the curves at

constant strain rate varies with changing temperature. Figure 8.3 (b) shows the curves taken at strain rate 0.1 s^{-1}. The curves at T= 500 °C and T=450 °C are both hardening, the curve at T=400 °C is at a steady state and the one at T=350 °C is softening. All four curves taken at strain rate 1 s^{-1} at T=350 °C, 400 °C, 450 °C and 500 °C and shown in Figure 8.3 (c) show a softening behaviour in the plastic zone, more evident with a steeper gradient at 350 °C. They show softening in the early stage of plastic deformation however they reach a steady state between true strain 0.6-0.8. In Figure 8.3 (d) the four curves at strain rate 10 s^{-1} are shown. All of the curves show a softening behaviour in the plastic zone, with the lowest temperature curve showing the steepest decreasing slope. They also have a flatter gradient between true strains 0.6-0.8. Figure 8.3 (e) shows the four curves taken at 50 s^{-1} strain rate. Multiple large serrations can be observed at the onset of plastic deformation in the curves obtained at strain rate 50 s^{-1}.

The effect of the fibres addition has been studied by also plotting the tests performed on the 20-1b bar at constant strain rate and varying temperatures in Figure 8.4 and using them for comparison.

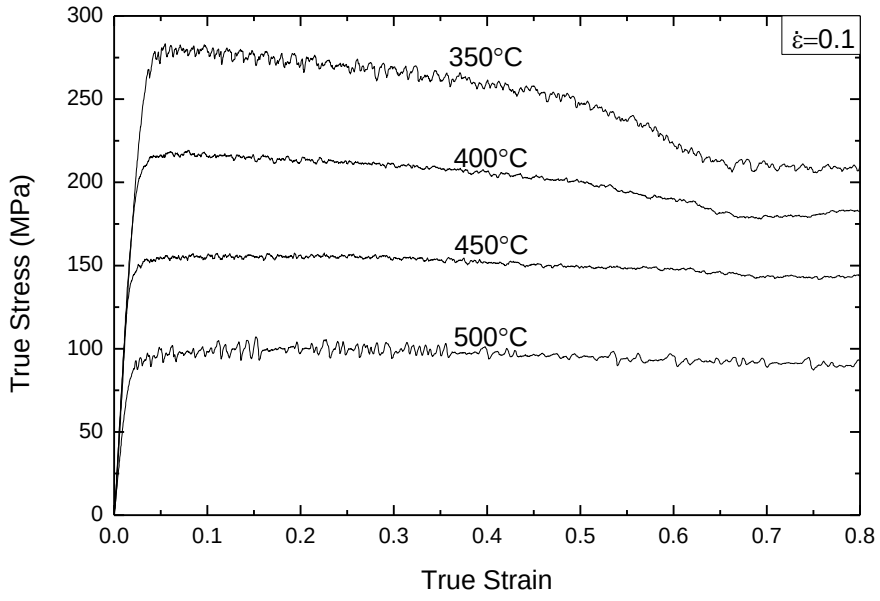

(a)

Figure 8.4: compression curves obtained by testing the 20-1b bar at constant strain rate and varying temperatures. (a) Tests at strain rate 0.1 s^{-1} and temperatures between 350-500 °C.

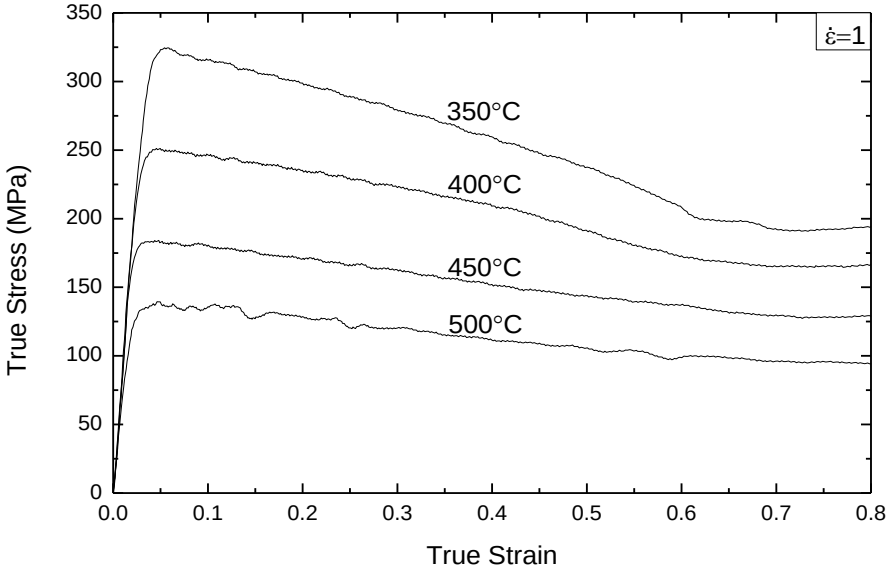

(b)

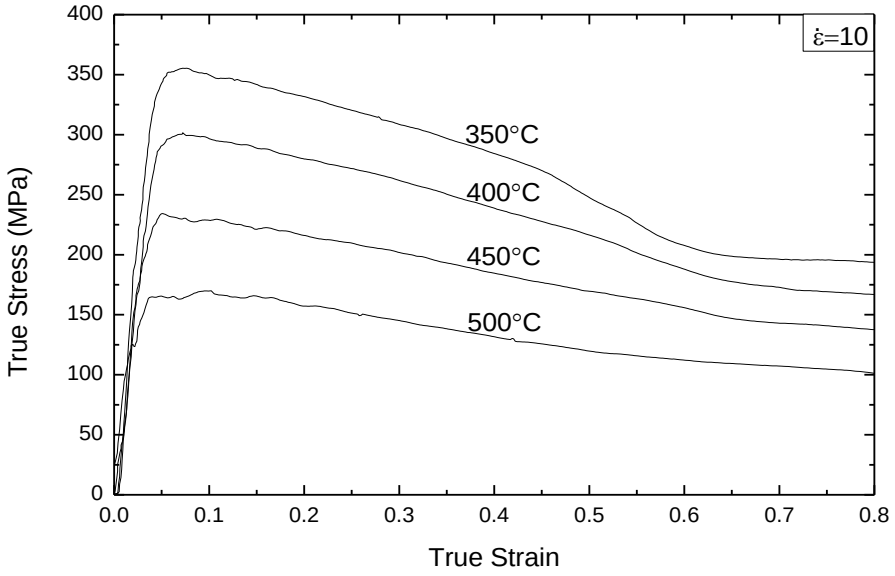

(c)

Figure 8.4 (cont.): compression curves obtained by testing the 20-1b bar at constant strain rate and varying temperatures. (b) tests performed at strain rate 1 s^{-1} and temperatures 350-500 °C, (c) Tests performed at strain rate 10 s^{-1} and temperatures 350-500 °C.

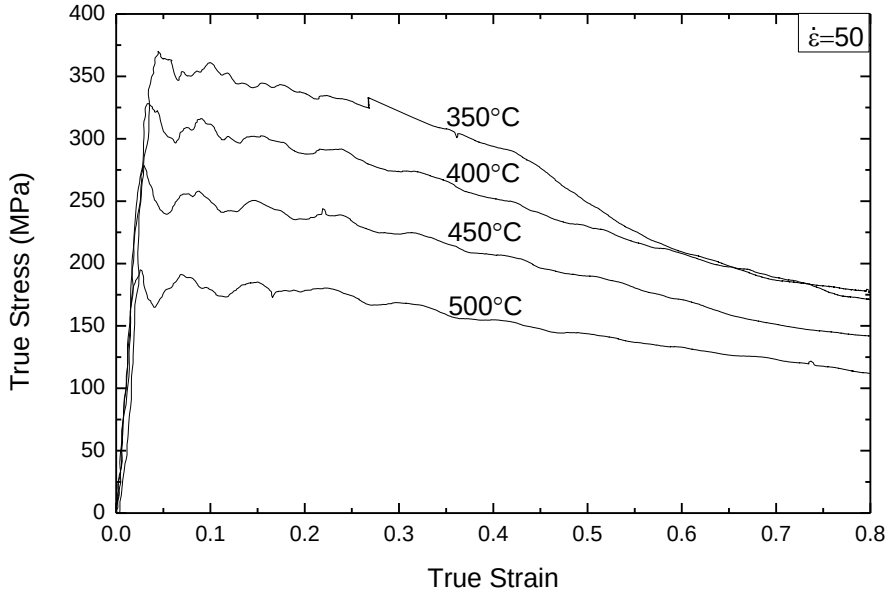

(d)

Figure 8.4: (cont.): compression curves obtained by testing the 20-1b bar at constant strain rate and varying temperatures. (d) tests performed at strain rate 50 s^{-1} and temperatures between 350-500 °C.

A temperature increase causes a decrease in yield strength of the samples made from the 20-1b bar. From the curves presented in Figure 8.4 (a), (b), (c) and (d) it can also be seen that the gradient of the plastic zones of all the curves at constant strain rate varies with changing temperature. Figure 8.4 (a) shows the curves taken at strain rate 0.1 s^{-1}. The curve at T= 500 °C is hardening, the curve at T=450 °C is at a steady state and the ones at T=400 °C and T=350 °C are softening. All four curves taken at strain rate 1 s^{-1} at T=350 °C, 400 °C, 450 °C and 500 °C and shown in Figure 8.4 (b) show a softening behaviour in the plastic zone, more evident with a steeper gradient at 350 °C. They show softening in the early stage of plastic deformation however they flatten into a steady state between true strain 0.6-0.8. In Figure 8.4 (c) the four curves at strain rate 10 s^{-1} are shown. All of the curves show a softening behaviour in the plastic zone, with the lowest temperature curve showing the steepest decreasing slope. They also have a shallower gradient between true strains 0.6-0.8. Figure 8.4 (d) shows the four curves taken at 50s^{-1} strain rate. Multiple large serrations can be observed at the onset of plastic deformation in the curves obtained at strain rate 50s^{-1}.

8.3 Discussion

8.3.1 Strain Rate Effect

The yield strength of all the samples tested is lower at lower strain rates and it increases with increasing strain rates. The measured value of yield strength of the 0-1b sample at 0.1 s^{-1} strain rate was 340 MPa at 350 °C and 100 MPa at 500 °C. A value of yield strength was found in the literature for 7075 T6 Al under the same testing conditions, with the same sample size and equipment and it was 110 MPa at 350 °C, just under 1/3 of the strength of the $Al_{93}Fe_3Cr_2Ti_2$ alloy, decreasing to 75 MPa at 500 °C [Lin-12].

Increasing the strain rate causes a softening effect which is evident form the slope of the curves in the plastic regime becoming steeper at higher strain rates. In the literature, several models have been proposed to describe the hot compressive behaviour of Al alloys. The traditional method considers the flow stress to have a power law dependence on the imposed strain rate [Nar-03], [Su-04], [Sri-08]:

$$\sigma = C\dot{\varepsilon}^m \tag{8.1}$$

where C is a parameter which depends on many factors including the structure of the material and testing temperature and m is the strain rate sensitivity parameter. Equation 8.1 is therefore only valid at constant temperature. The strain rate sensitivity parameter quantifies the effect of strain rate on the flow stress and can be derived based on Equation 8.1 by finding the gradient of the plot of $\ln(\sigma)$ and $\ln(\dot{\varepsilon})$ at steady state and constant temperature [Sas-01], [Hos-11]. This plot can be seen in Figure 8.15 (a) for the 0-1b bar, (b) for the 10-1b bar and (c) for the 20-1b bar.

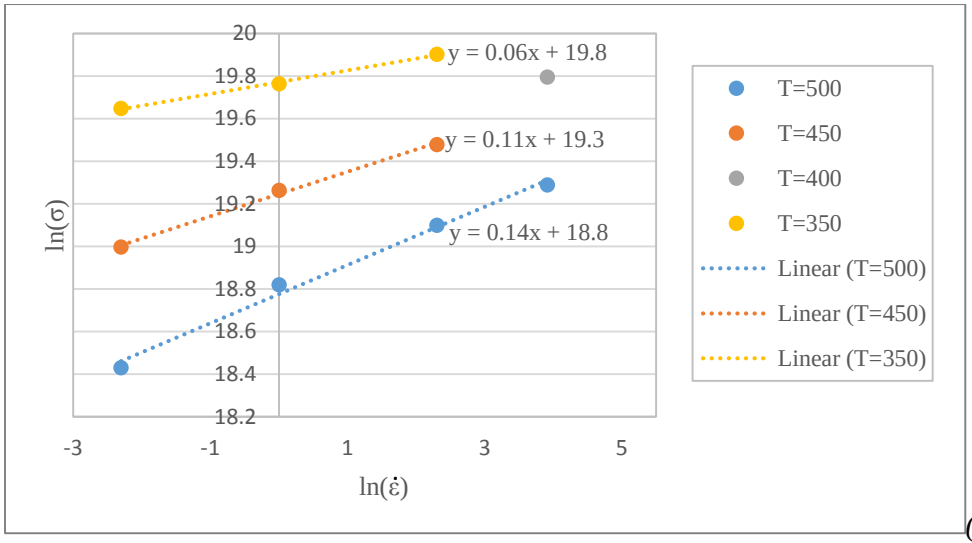

(a)

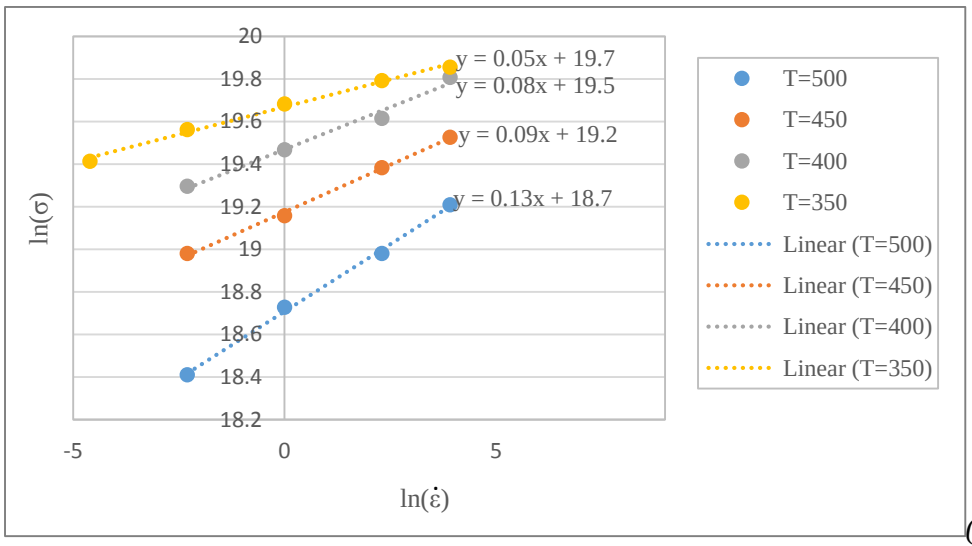

(b)

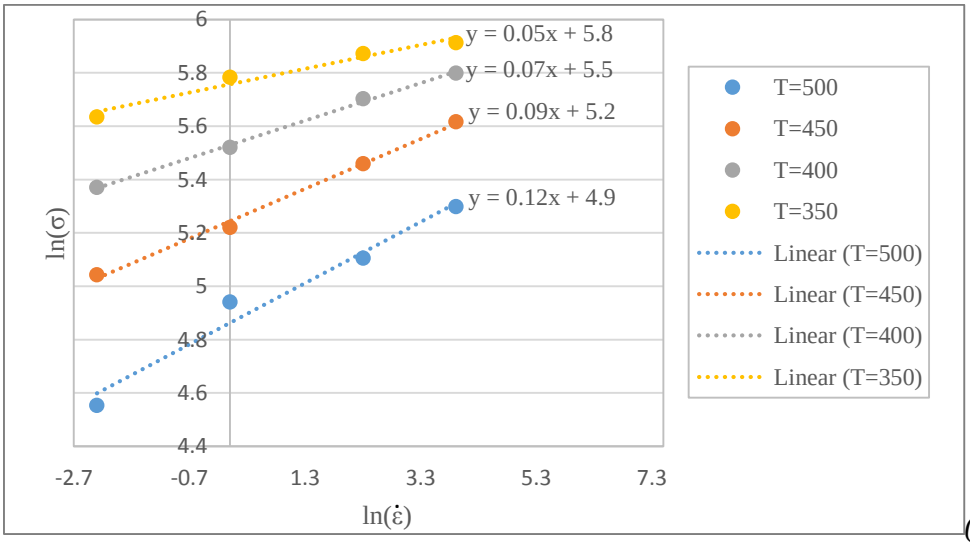

(c)

Figure 8.5: the variation of ln(steady state stress) with ln(strain rate) at constant temperature of the bars (a) 0-1b, (b) 10-1b and (c) 20-1b used to determine the strain rate sensitivity parameter m.

The relationship between stress and strain rate indicates that the material hardens with increasing strain rate. The strain rate sensitivity parameter can be estimated from the gradient of the curve in Figure 8.5 [Sas-01]. The values of m obtained in the present study were in the range of 0.05-0.14. The values of m measured in 2024 alloy at 0.6-0.8 of the homologous temperature were also found to be in the range of 0.05-0.15 [Hos-11], [Fie-59]. The homologous temperature is calculated by dividing the testing temperature by the melting temperature of the alloy in Kelvin. The variation of strain rate sensitivity parameter with temperature compared to the values of 2024 Al alloy [Hos-11] can be seen in Figure 8.6.

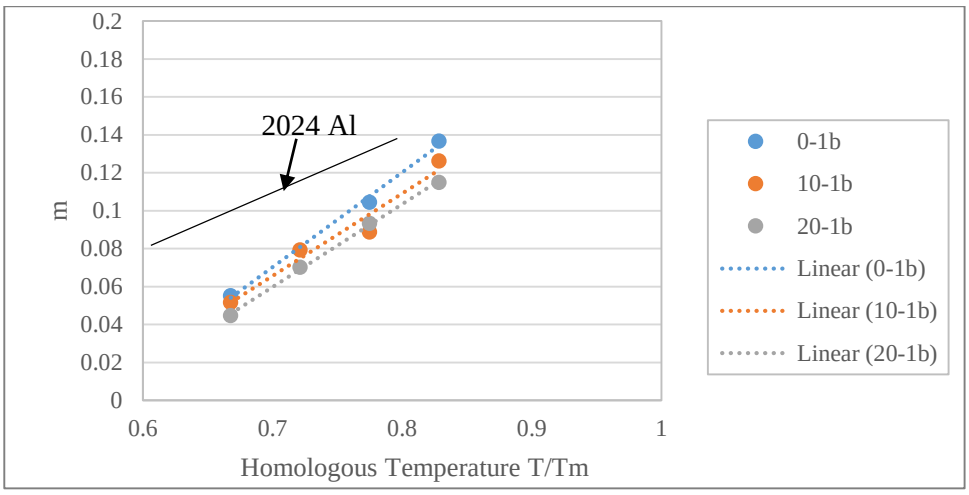

Figure 8.6: variation of strain rate sensitivity with temperature for the 0-1b, 10-1b and 20-1b bars between 350-500°C compared to the values for 2024 Al alloy [Hos-11].

8.3.2 Temperature Effect

The effect of working temperature on the flow stress behaviour of the alloy and composites can be described by the Arrhenius-type equation [Cav-06], [Gan-04], [Sri-08]:

$$\dot{\varepsilon} = A\sigma^n e^{\frac{-Q}{RT}} \tag{8.2}$$

where A is a constant, n is the stress exponent (=1/m), R is the gas constant and Q the activation energy. At a given strain rate therefore the slope of ln(σ) and 1/T will give the value of the activation energy Q divided by m and the gas constant R (only valid in the steady state condition). This plot can be found in Figure 8.7.

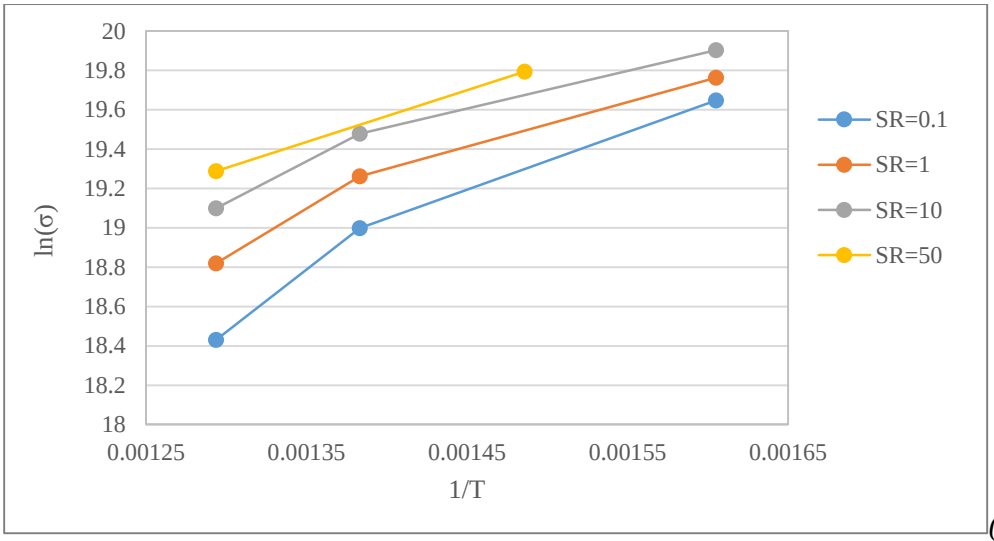

(a)

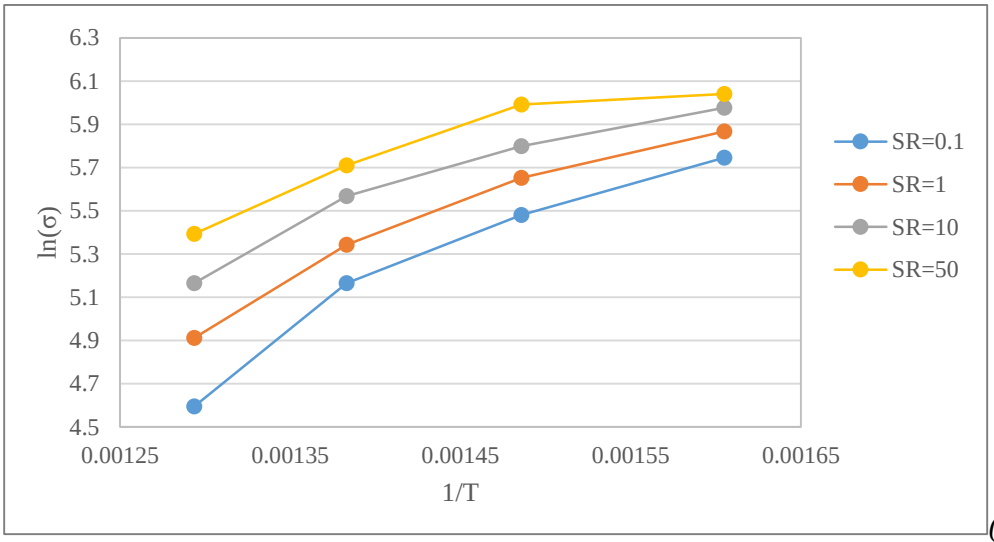

(b)

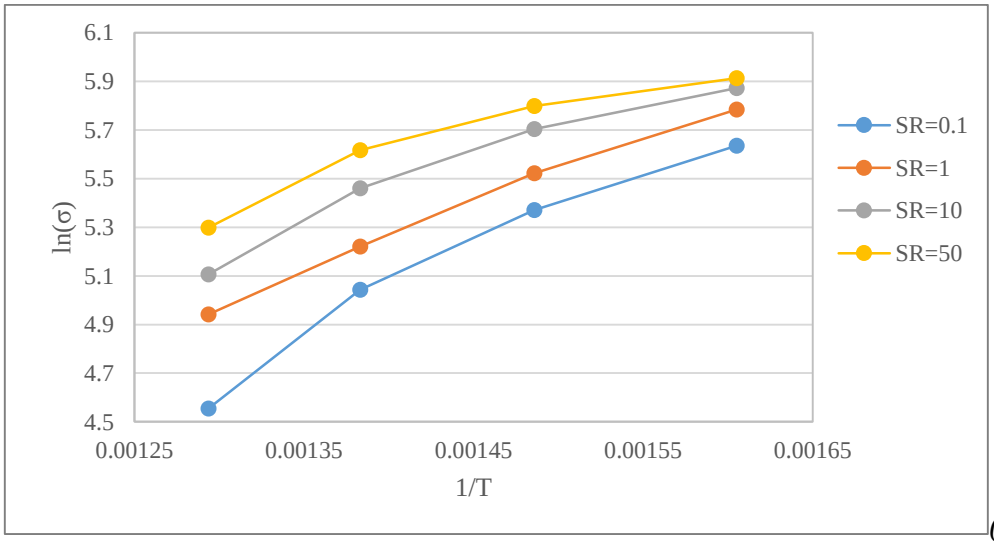

(c)

Figure 8.7: plot of ln(σ) and 1/T used at steady state to determine the apparent activation energy required of the microstructural mechanisms which govern the plastic flow behaviour of the material.

From Figure 8.7 (a), (b) and (c) it is clear that the plot of ln(steady state stress) and 1/T is not perfectly linear, and that the linearity is lost particularly at the higher temperature end of the plot. This can be explained as the material undergoes a phase transformation in that temperature range. The transformation involves the decomposition of the icosahedral phase into more stable intermetallic phases. At 350 °C the microstructure was shown by XRD in Figure 8.2 to consist of icosahedral phase, $Al_{13}Fe_4$, $Al_{13}Cr_2$ and FCC-Al. Between 400-450 °C there is a transition which involves the icosahedral peaks becoming less defined and the peaks of other intermetallic phases becoming sharper. The icosahedral phase could not be indexed by XRD after testing at 500 °C. The apparent activation energy can be derived from the Arrhenius plot in Figure 8.7 only if the correlation is linear, which is not the case.

8.3.3 Fibre Effect

Comparing the three bar compositions tested shows that the addition of pure Al fibres causes a linear decrease in yield strength at constant temperature in the range of 350-500 °C (as shown in Figure 8.8) following the rule of mixtures [Cly-95].

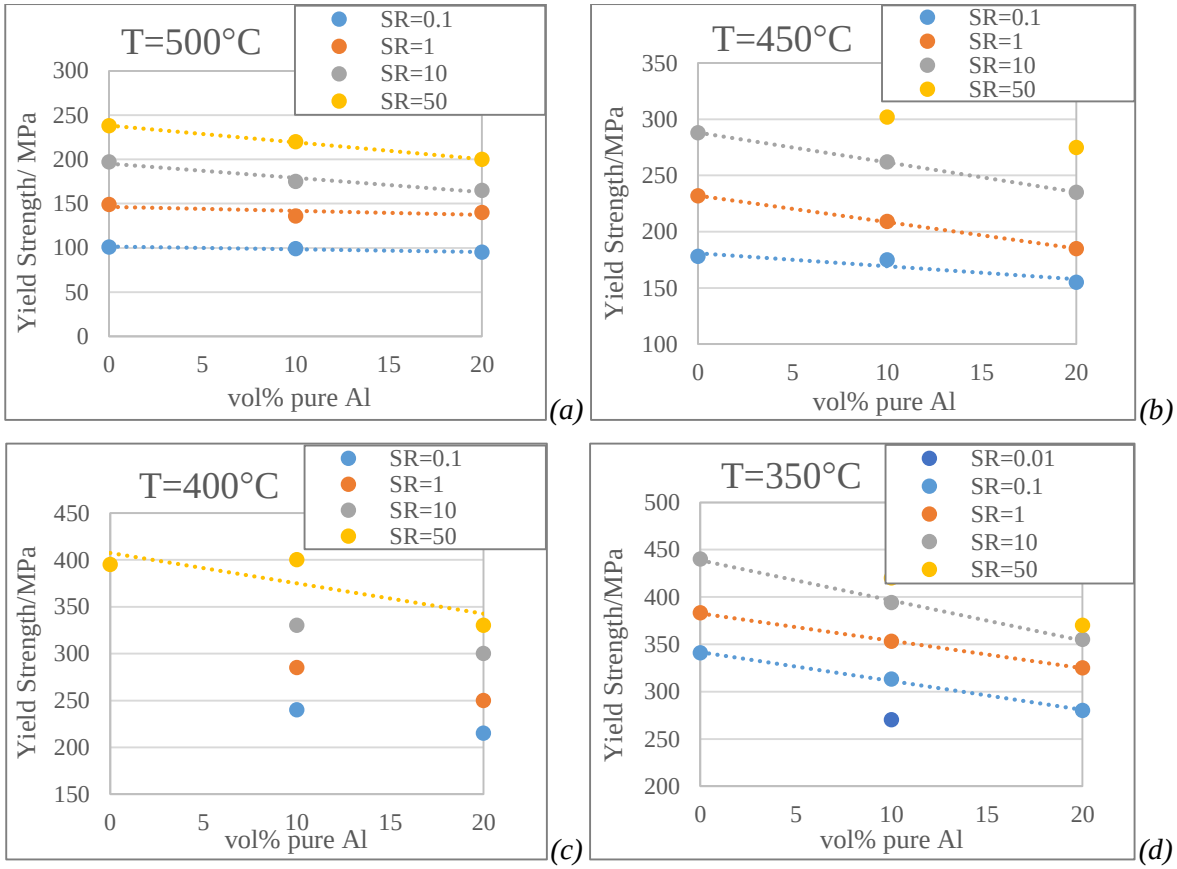

Figure 8.8: plot of strength with varying composition at constant temperature and different strain rates (a) T=500 °C, (b) T=450 °C, (c) T=400 °C, (d) T=350 °C.

8.3 Conclusions

The compressive yield strength of the pure alloy bar was measured to be 340 MPa at 350 °C, decreasing with increasing temperature up to 500 °C. It was also found to increase with increasing strain rate between 0.1 and 50 s^{-1}.

The gradient of the plastic zone of the compression tests was used as an indicator of whether the pure alloy samples were hardening or softening during tests. It was found to decrease with increasing temperature, showing that the material was softening at lower temperature and higher strain rates. Only the curve at the highest temperature and lowest strain rate (at 500 °C and 0.1 s^{-1}) showed hardening.

The yield strength of the composites was also shown to decrease with increasing temperature and increase with strain rate within the range tested. The effect of 10 vol% and 20 vol% fibre addition changed the yield strength following the rule of mixtures.

The strain rate sensitivity parameter was calculated to be in the range of 0.05-0.14 for the pure alloy and composites, decreasing linearly over the temperatures tested.

Within the range of temperatures tested major microstructural changes are occurring within the samples. The microstructure was shown by XRD to undergo a phase transformation which result in the decomposition of the icosahedral phase at 500 °C into more stable intermetallic phases.

References

[Cav-06] P. Cavaliere, E. Evangelista, Compos. Sci. Tech. 66 (2006) 357–362.

[Cly-95] T. W. Clyne, P. J. Withers, *An Introduction to Metal Matrix Composites*, Cambridge University Press, (1995).

[Gan-04] G. Ganesan, K. Raghukandan, R. Kartikeyan, B.C. Pai, Mater. Sci. Eng., (2004), A 369, 230–235.

[Gal-09a] M. Galano, F. Audebert, I.C. Stone, B. Cantor, Acta Mat., (2009), 57, 5107–5119.

[Fie-59] D. S. Fields, W. A. Backofen, Trans. ASM, (1959), 51.

[Hos-11] W. F. Hosford, R. M. Caddell, *Metal Forming: Mechanics and Metallurgy*, Cambridge University Press, (2011).

[JCP-99] JCPDS-International Centre for Diffraction Data v2.02 Codes: 04-0787, 13-0146, 29-0014, 29-0042 (1999).

[Lin-12] Y. C. Lin, L. T. Li, Y. X. Fu, Y. Q. Jiang, J. Mater. Sci., (2012), 47, 1306–1318.

[Nar-03] S. V. S. Narayana Murty, B. Nageswara Rao, B. P. Kashyap, Compos. Sci.Tech. 63 (2003) 119–135.

[Rou-12] N. J. Rounthwaite, DPhil Thesis, University of Oxford, (2012).

[Sas-01] D. H. Sastry, Y. V. R. K. Prasad, S. C. Deevi, Mat. Sci. Eng., (2001), A 299, 157-163.

[Sri-08] V. C. Srivastava, V. Jindal, V. Uhlenwinkel, K. Bauckhage, Mat. Sci. Eng., (2008), A 477, 86–95.

[Su-04] Y. H. Frank Su, Y. C. Chen, C. Y. A. Tsao, Mat. Sci. Eng., (2004), A 364, 296–304.

[Tod-04] I. Todd, Z. Chlup, J. G. O'Dwyer, M. Lieblich, A. Garcia-Escorial, Mat. Sci. Eng., (2004), A 375–377, 1235–1238.

Chapter 9: General Discussion

This section will discuss matters which overlap the scope of several chapters and correlate them to each other, drawing conclusions both from the partial conclusions of each chapter and from this correlative discussion.

9.1 Microstructural Comparison

This section will compare the microstructure of the pure alloy bars with the composites and discuss the changes brought by the addition of pure Al fibres using results presented in Chapters 4 and 5.

9.1.1 Phase Analysis

All powders and bars produced, whether made of the pure alloy of fibre composites, contained FCC-Al and icosahedral quasicrystalline phases detected by XRD and TEM. Some of the bars and the powders also contained small quantities of other intermetallic phases detected by XRD, a summary of which can be found in Table 9.1.

	Maximum Extrusion Temp	***Phases Present***			
Sample		***α-Al***	***i-phase***	***θ-phase***	***κ-Al_3Ti***
Batch 1 Powder	*n/a*	*X*	*X*	*X*	*X*
Batch 2 Powder	*n/a*	*X*	*X*	*X*	*X*
0-1a	*400*	*X*	*X*		
0-1b	*420*	*X*	*X*		*X*
10-1a	*388*	*X*	*X*		
10-1b	*383*	*X*	*X*	*X*	*X*
10-2	*419*	*X*	*X*		
20-1a	*389*	*X*	*X*		
20-1b	*405*	*X*	*X*	*X*	*X*
20-2	*400*	*X*	*X*	*X*	*X*

Table 9.1: Summary of the extrusion temperatures and phases present before and after extrusion in each bar.

In alloy systems of the same nominal chemical composition $Al_{93}Fe_3Cr_2Ti_2$ other authors have also found a microstructure consisting mostly of FCC-Al and a variety of intermetallic phases. In melt spun ribbons produced using a wheel speed of 40 m/s, Galano *et al.* found icosahedral quasicrystals and small amounts of $Al_{13}(Fe, Cr)_{2-4}$ [Gal-09a]. Prima *et al.* only found icosahedral phase in melt spun ribbons produced using wheel speeds of 40 m/s and 20 m/s. At wheel speeds of 10m/s they found icosahedral phase, but also $Al_{13}Cr_2$ and $Al_{23}Ti_9$ intermetallic phases [Pri-04]. Sahoo *et al.* only found icosahedral quasicrystalline phases in their melt spun ribbons produced using a wheel speed of 40 m/s [Sah-05]. Several publications were also found describing the phase composition of gas-atomised powders. Inoue *et al.* analysed powder size fractions from 26-125 µm in diameter and found icosahedral phase and $Al_{23}Ti_9$ intermetallic phases [Ino-99], [Kim-00]. Todd *et al.* analysed powders <100 µm in diameter and found icosahedral phase and $Al_{23}Ti_9$ both before and after extrusion at 400 °C with a ratio of 10:1 [Tod-04]. Using the same extrusion conditions, Garcia Escorial *et al.* found a phase structure consisting of icosahedral phase and Al_3Ti intermetallics instead of the $Al_{23}Ti_9$ found by Todd *et al.* (also monoclinic, but of a slightly different chemical composition) [Gar-07], [Tod-04]. Yamasaki *et al.* studied a powder <38 µm in diameter extruded at 500 °C with a ratio of 5:1 and found Al_3Ti and icosahedral phase intermetallics [Yam-07]. The present work consistently found FCC-Al and icosahedral phase in all the powders and the bars. In the powders $Al_{13}(Fe, Cr)_{2-4}$ was detected by XRD, however it was no longer present five of the bars after extrusion. It could still be detected in the 10-1b bar, 20-1b bar and 20-2 bar. Small quantities of Al_3Ti intermetallics were also detected, only in the 0-1b, 10-1b bar, 20-1b bar and 20-2 bars. The difference of up to 30 °C in extrusion temperature did not have an identifiable correlation with the phases present in the bars.

9.1.2 Texture Analysis

The analysis of the texture introduced in the FCC-Al matrix during extrusion showed similar trends across all bars, whether made of the pure alloy or composites, with the exception of the 0-1b bar. In the qualitative texture analysis performed by XRD, the filings were always seen to be untextured

when compared to the reference values. The cross sections showed reduced texture and the longitudinal section showed increased texture compared to the reference values, particularly along the (220) plane. This was consistent across all extruded bars, including the 0-1b.

The intensity of the (220) plane was 60-100% of the maximum intensity in the 0-1a bar, reduced to 40-60% of the maximum intensity in the 0-1b bar. Also, the 0-1b bar showed a 10% increase in relative intensity along the (311) plane. Differences in texture were then detected by EBSD analysis, the 0-1b bar did not show a defined texture trend and had a grain size distribution which was on average less than half of the size of the 0-1a bar. Grain sized were measured by TEM and EBSD confirming this. The 10-2 bar was extruded at 419 °C and its texture trend matched that of the other bars, therefore it is unlikely that the differences in texture detected in the 0-1b bar would be only a result of the extrusion performed at 420 °C. The differences in texture detected are most likely an effect of the extended exposure to elevated temperature and pressures during the two extrusion attempts. The 0-1a bar was extruded at 400 °C. The 0-1b bar was initially taken to 400 °C in the first, failed extrusion attempt. The second attempt was performed at 420 °C.

The composites with 10 vol% pure Al showed an increase in the intensity of the (220) plane from 80% in the 10-1a to 90-100% in the 10-1b and 100-120% in the 10-2 bar, likely to be related to the amount of plastic deformation that each bar underwent under different extrusion ram pressures. The ram pressures were 1568 MPa for the 10-1a bar and 1641 MPa and 1667 MPa for the 10-1b and 10-2 bars respectively. The composites with 20 vol% pure Al also showed an increase in intensity along the (220) plane from 60% for the 20-1a, 80% for the 20-1b and 75% for the 20-2 bar respectively. Unlike the composites with 10 vol% Al, the longitudinal section taken from the front of the 20-1a, 20-1b and 20-2 bars showed ~20-30% higher intensity along this plane than the longitudinal section taken from the back of the bar. The cross section showed reduced texture along that plane and along the (200) and (311) both in the front and the back of the bars. The filings were always untextured.

The texture analysis trends observed in the composite bars matched the trends observed for the 0-1a bar and were consistent with a comparison with the literature [Rou-12], [Ped-10], [Gu-09], [Jia-14].

9.1.3 Matrix Compositions

This section analyses whether the changes in extrusion temperature of up to 30 °C affected the amounts of solutes in solid solution.

The Al matrix composition was measured in all the bars and powders from either batch by TEM-EDX and are summarised in Table 9.2. The composition of the bars are the consistent with the powder batch they were made of.

	Maximum Extrusion Temp	***Matrix composition at%***			
Sample		***Al***	***Fe***	***Cr***	***Ti***
Equilibruim Solid Solubility in Al at 400°C	*At 400 °C*	*-*	*0.02*	*0.18*	*0.032*
Batch 1 Powder	*n/a*	*98.2*	*0.2*	*0.3*	*1.4*
Batch 2 Powder	*n/a*	*97.9*	*0.6*	*0.5*	*1.0*
0-1a	*400*	*98.2*	*0.2*	*0.4*	*1.3*
10-1a	*388*	*98.2*	*0.4*	*0.2*	*1.3*
10-1b	*383*	*97.7*	*0.4*	*0.5*	*1.3*
10-2	*419*	*98.8*	*0.3*	*0.3*	*0.6*
20-1a	*389*	*98.1*	*0.2*	*0.4*	*1.3*
20-1b	*405*	*98.5*	*0.3*	*0.2*	*1*
20-2	*400*	*98.6*	*0.3*	*0.3*	*0.8*

Table 9.2: solid solubility of Fe, Cr and Ti in Al at 400°C taken from the literature [Mas-90], [Mon-43], [Xu-06] compared to the composition of the bars and the powders.

All of powder matrix compositions measured exceed the expected solid solubility limit of Fe, Cr and Ti in Al at room temperature [Mas-90], [Mon-43], [Xu-06]. After extrusion the measured

composition of all the bars also exceeded the maximum solid solubility of Fe, Cr and Ti at 400 °C. The equilibrium solid solubility for Cr in Al at 400 °C is ~0.18 at% [Mon-43], the solid solubility of Fe at 400 °C is ~0.02 at% [Mon-43] and the maximum solid solubility of Ti in Al at 400 °C is ~0.032 at% [Xu-06]. The heat treatment during extrusion was not sufficient to alter the chemical composition of the matrix.

9.2 Extrudability

In this section, the effect of fibre additions on extrudability will be discussed, using results presented in Chapters 4 and 5. The effect of pure Al contamination will also be discussed.

Contamination in the form of pure Al was detected in the $Al_{93}Fe_3Cr_2Ti_2$ alloy powder from batch 1, and also in the extruded bars 0-1a, 10-1a and 20-1a, in a previous project [Ped-10]. By analysing their SEM micrographs, the contamination was estimated at 2-3 vol%.

The 10-1b and 20-1b bars produced from the 1st batch of powder, with the same vol% pure Al additions as the 10-1a and 20-1a would have been expected to extrude both equally at the same temperature and require the same ram pressures. However the 10-1b and 20-1b bars extruded at a higher temperature and pressure than the 10-1a and 20-1a bars. A plot of the breakthrough pressures and the vol% pure Al added, excluding contamination, can be seen in Figure 9.1.

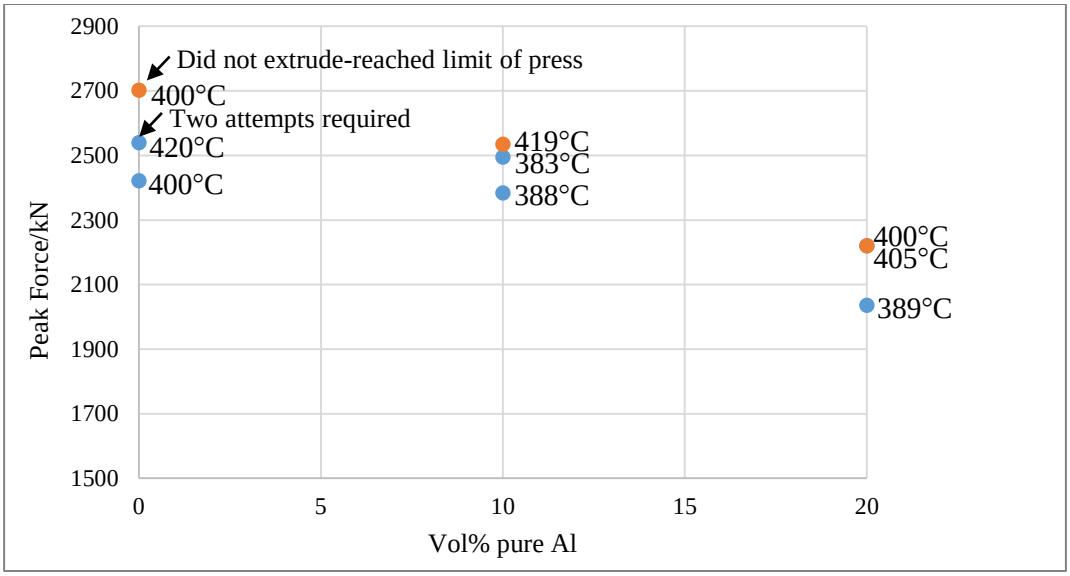

Figure 9.1: Summary of the extrusion breakthrough pressures with content of pure Al and temperature. Red indicates powders from the 2nd batch while blue indicates powders from the 1st batch. No correction was made to account for contamination. The temperature of each extrusion is documented next to each pressure value.

An increase in extrusion temperature is documented to cause a decrease in breakthrough pressure in bars made with the same powder batch and size fraction [Rou-12]. A likely reason for the differences in breakthrough pressure and temperature would be the pure Al powder contamination which was present in the bar 0-1a, 10-1a and 20-1a bars but was not detected in the 0-1b bar, 10-1b and 20-1b bars [Ped-10], [Rou-12].

No pure Al contamination was observed in the powder batch 2. This partly explains the increased extrusion ram pressure required to consolidate the bars which can be seen in Figure 9.1. Batch 2 also had 0.1 at% less Al in the base $Al_{93}Fe_3Cr_2Ti_2$ alloy powder than batch 1. A reduction of 0.8 at% in the Al content of the alloy powder has been shown to increase the breakthrough pressure by 300 MPa and have a negative effect on extrudability [Rou-12]. The 0-2 bar did not extrude as it reached the maximum pressure safety limit of the extrusion press.

Adjusting the compositions to account for the pure Al contamination to the plot in Figure 9.1 produces a decrease in pressure with vol% pure Al and can be seen in Figure 9.2.

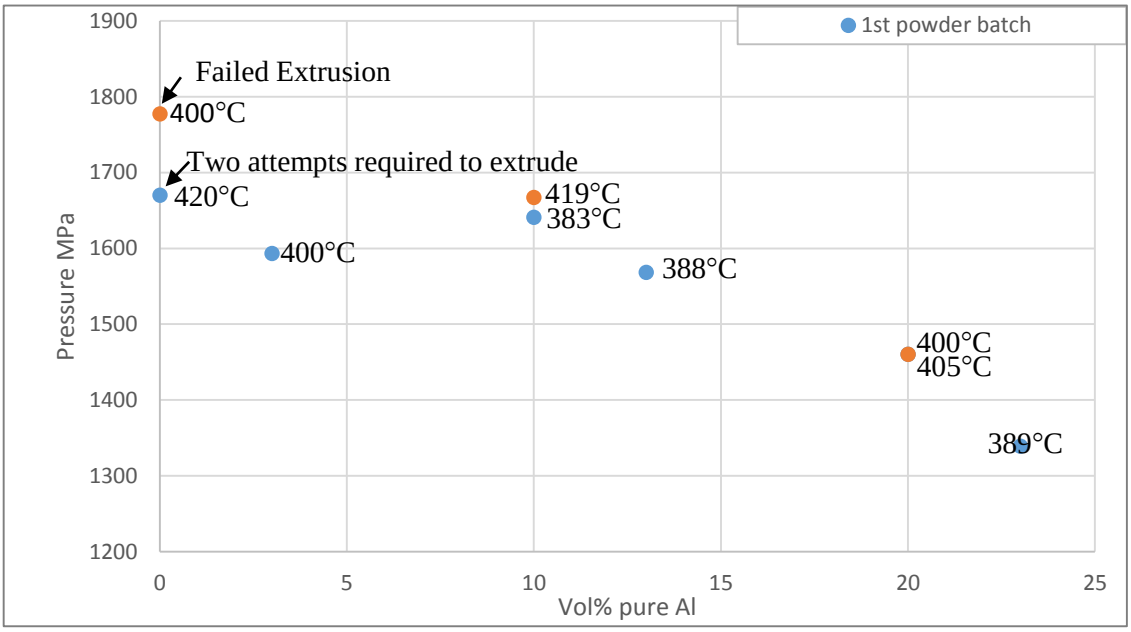

Figure 9.2: Summary of the extrusion breakthrough pressures with content of pure Al and temperature corrected for pure Al contamination.

The 0-1b and 0-2 points need to be discarded in this analysis because the 0-2 bar did not extrude, therefore the value in the graph is not a value of the breakthrough pressure but of maximum pressure reached and the 0-1b was already pre-deformed at high temperature and pressures before the second (and successful) extrusion attempt was made. Previous work analysing nanoquasicrystalline $Al_{93}Fe_3Cr_2Nb_2$ composites with pure Al additions showed a linearly decreasing tendency of the breakthrough pressure with vol% pure Al [Rou-12].

9.3 Mechanical Strength at Room Temperature

This section uses the quasi-static tensile strength measurements at room temperature presented in Chapter 7 to study the different contributions to the strengthening processes and correlate them with microstructural features observed and described in Chapters 4 and 5. The results of this study were used to fit theoretical models that describe the various contributions of each mechanism to the overall yield strength of the material. The analytical modelling work was carried out on the bars

0-1a, 10-1a and 20-1a in order to maintain consistency by using bars made from the same powder batch.

The yield strength measurement used, 544 MPa for the pure alloy bar 0-1a, is the 0.2% proof stress taken from the quasi-static tensile tests at room temperature and strain rate $1x10^{-4}$ s^{-1}. This measurement is in itself an approximation due to the fact that the present work studies a polycrystalline material with a bimodal grain size distribution. In a polycrystalline material the most favourably oriented grains will have undergone plastic deformation prior to the least favourably oriented grains therefore creating a yield "range" rather than a specific yield point [Hon-77]. Also, a bimodal grain size distribution has been shown to lead to a significant back-stress effect (small grains remaining elastic while large grains deform plastically at an earlier stage) [Hon-77]. This material would therefore exhibit a longer elastoplastic transition and defining the yield point as the 0.2% proof stress is an approximation.

Previous studies on nanoquasicrystalline Al-Fe-Cr-Ti(-Si) alloys showed that the main strengthening mechanisms involved are the small grain size [Gal-09b], [Aud-02], [Voj-07] the presence of hard, incoherent nanoparticles [Gal-09b], [Aud-02], [Voj-07] and the solutes in solid solution [Gal-09b], [Aud-02]. Inoue *et al.* have produced the same alloy with a microstructure made of icosahedral phase in a single grain FCC Al matrix and therefore attribute the high ductility of their alloy to the lack of grain boundaries [Ino-00], [Ino-99]. In this case a combination of classic strengthening mechanisms including the Orowan effect, the Hall-Petch effect, work hardening and solid solution strengthening were used.

The Orowan effect calculations had to be performed taking into account that the particle size distribution measured from the TEM micrographs was bimodal. Bimodal particle size distributions have been observed in rapidly solidified Al-Cu alloys produced through powder metallurgy routes by adding powders of slightly different compositions and coarsening phases by heat treatment in order to produce a bimodal distribution of particle sizes [Con-00]. It has also been reported in hyper-eutectic Al-Be alloy systems produced by melt-spinning [Van-85]. Moreover, it was observed by other authors in melt-spun nanoquasicrystalline alloys the presence of small fractions

of quasicrystalline particles with very large size in comparison with the average size quasicrystalline particles in the alloy [Gal-09a], [Hum-01].

The bimodal particle size distribution observed in the current work has been used to fit the model of Orowan strengthening. Other studies on similar alloy systems have found the Orowan equation $\sigma_{Or}=3Gb/L$ where 3 is the Taylor factor, G is the shear modulus of the matrix (for Al G=26 GPa [Voj-07]), b is the Burgers vector (for Al b= 0.286 nm [Voj-07]) and L is the inter-particle distance to describe accurately the strength measured experimentally [Ehl-94], [Voj-07]. The bimodal particle size distribution measured in Chapter 4 was fitted with peaks at: $r_1=42.9\pm6.1$ nm (with f=0.15 and $2R_s=1.8x10^{-7}$ m) and $r_2=128.6\pm6.1$ nm (with f=0.26 and $2R_s=4.12x10^{-7}$ m). Using the Orowan equation and adding the two contributions linearly according to their relative fractions we get an overall Orowan strengthening contribution of $\Delta\sigma_{Or}\sim180$ MPa. Linear addition simplifies calculations but relies on the assumption that the two different particle sizes have completely separate effects on dislocation motion which do not influence each other. Other assumptions made in order to perform these calculations include an even spacing between the particles which act as impenetrable obstacles to dislocations and a spherical shape. Further refinements to Orowans model have been performed by Foreman and Makin [For-67] and Kocks [Koc-67] to account for the effect of non-regular distributions of obstacles using the concept of effective obstacle spacing. Later, Hirsch and Humphreys [Hir-69] and Bacon [Bac-73] proposed models on elastic field screening, which imposes a logarithmic dependency of dislocation line energy and the effect of precipitate finite size. Then many Dislocation Dynamics (DD) simulations have been performed by computational investigation to account for increasingly realistic microstructures [Moh-01], [Moh-04], [Sih-05]. Despite all these efforts quantitative prediction of particle strengthening remains difficult in some materials. The model used in the present work relies on the assumption of a more idealized microstructure.

Other studies calculate the relative contributions of the Orowan strengthening effect and the Hall-Petch model and compare them to each other in order to determine which strengthening mechanism is dominant.

Ehlstrom *et al.* found that the Hall-Petch effect appears to be the main strengthening mechanism responsible for the strength of their rapidly solidified Al-Fe-X alloys [Ehl-94], and Vojtech *et al.* had a similar observation for an atomised, extruded Al-Fe-Cr-Ti-Si alloy [Voj-07]. Wang *et al.* studied rapidly solidified Al-Ti-B and actually found the Orowan effect to be negligible compared to the Hall-Petch effect [Wan-04]. Therefore on rapidly solidified alloy systems the strengthening mechanisms appear to be varying strongly with very small alterations in the processing methods and their resulting microstructures. The current calculations appear to show that strength predictions on this alloy system, (which experimentally shows a quasi-static tensile yield strength of 544 MPa) would be incomplete if the only strengthening mechanism taken into account was due to the hard incoherent particles, therefore several analytical models of calculating the grain size contribution to the overall strength were reviewed. While grain size can influence the whole stress-strain curve, the effect on the elastic limit (yield point) is particularly marked.

The nanoquasicrystalline Al-Fe-Cr-Ti alloy studied in the present work has been shown to have a bimodal grain size distribution, measured by EBSD in Chapter 4.

The strengthening contribution of the Hall-Petch effect [Hal-51] has been calculated using the empirically derived equation: $\sigma=\sigma_O+kd^{-1/2}$, where k is the Hall-Petch coefficient and d is the grain size. The methods for calculating k values vary strongly depending on the model used [Esh-51], [Con-63], [Li-63], therefore in this case it was deemed appropriate to use empirical values measured on similar alloy systems [Voj-07], [Bra-97] for atomised and extruded Al-Fe-Cr-Ti-Si, $k=171\ MPa\mu m^{-1/2}$. The bimodal grain size distribution measured by EBSD was fitted with peaks at: $d_1=0.32\pm0.25$ µm (with an area fraction of 0.7) and $d_2=1.5\pm0.3$ µm (with an area fraction of 0.3). Stereology structure factors were calculated using the method developed by Ashby *et al.* [Ash-64], which says that assuming all particles are spherical and working from measurements from planar surfaces: using r_s as mean radius of interaction with a planar surface ($=d_s/2$) and r_v as 3D particle radius, then $r_v=r_s/\sqrt{\frac{2}{3}}$. This gives 3D grain radii as defined by the peaks of the bimodal distribution are $d_1=0.4\pm0.3$ µm and $d_2=1.8\pm0.36$ µm.

The mechanical response of metals with a bimodal grain size distribution has been modelled extensively throughout the literature using the Mori-Tanaka mean field approach [Mor-73] as an alternative to Finite Element Analysis. A modified version was proposed by Joshi *et al.* to model the constitutive response of bimodal metals [Jos-06] by analyzing a material constituted solely of the ultra-fine grained phase and a simulation of the coarse grained material. Joshi *et al.* proves that the stress-strain response of the bimodal material is a linear addition of the two separate stress strain responses of each phase adjusted by the volume fraction [Jos-06]. Joshi presents a Voce-type equation which describes the stress strain response of each phase individually, but relies on the measurements of the initial yield stress, the saturation stress, the plastic strain and the characteristic strain of each phase of different grain sizes separately, and then adds up the contributions following the rule of mixtures. However, as the material used in this study was produced with a bimodal grain size distribution, these measurements performed on the individual phases are not available, particularly the saturation stress measurements as Bauschinger tests were not performed due to availability issues of material and equipment. Using the same approximation, but calculating the strength using the Hall-Petch equation and adding the two contributions of the two individual size fractions linearly we get an overall strengthening contribution of $\Delta\sigma_{HP}$~167 MPa for the pure nanoquasicrystalline $Al_{93}Fe_3Cr_2Ti_2$ alloy studied in the present work.

If it is assumed that the grain size effect and the particle strengthening influence dislocation motion in completely separate ways then they can be added linearly to each other and get an estimation of the yield strength to be σ_y~347 MPa. This approximation has been used extensively in literature as the simplest method to obtain an estimate of the overall strengthening effects [Voj-07] [Ehl-94], [Wan-04]. This value is significantly lower than the experimentally measured 544 MPa, likely due to both errors, approximations and other mechanisms like solid solution strengthening or work hardening playing a role in the overall strengthening of the $Al_{93}Fe_3Cr_2Ti_2$ alloy.

A combination of factors are likely to cause errors in the Hall-Petch calculations. Some studies have shown that in the sub-micron range (which represents the biggest size fraction of the grains, 0.7 vol%) there is no guarantee that the Hall-Petch slope would remain constant. For instance the

work of Yu *et al.* [Yu-05] divided the grain sizes and the predominant deformation mechanisms into 3 main groups: (a) the "traditional" group ($d>\sim10^{-6}$) which mostly deforms by dislocation intersections [Con-03], [Che-03], (b) the "ultra-fine grained" group ($\sim10^{-8}<d<\sim10^{-6}$) which would deform by dislocation emission by grain boundary sources [Con-03], [Hay-04] or grain boundary shear due to dislocation pile ups [Che-03], and (c) the nanocrystalline group ($d<\sim10^{-8}$) which deforms by grain boundary processes only [Con-03], [Che-03]. The bimodal grain size distribution found in the quasicrystalline Al-Fe-Cr-Ti analysed in the current work has two main peaks which lie one in group (a) and one in group (b).

The transition from the traditional regime to the ultra-fine grained regime in Al was studied by Yu *et al.* [Yu-05]. A model was proposed to explain the deformation behaviour, and it was found to be temperature and strain rate dependent. As grain size decreased below a critical value the grain boundaries became the main obstacle reducing the mean free path of dislocations. Above the critical value the mean free path was dictated by the dislocation substructure within the grain. This effect was found to enhance dynamic recovery rate and reduce the hardening rate in ultra-fine grained Al causing a yielding peak and Lüders band to appear and tensile elongation to be reduced [Yu-05]. Also, so far in this section the assumption has been made that high angle grain boundaries contribute by acting as barriers to dislocation motion, while low angle boundaries (5-15 °) do not. Due to the extensive presence of texture produced by warm extrusion a number of low-angle grain boundaries have been observed in the EBSD maps in Chapter 4. In the sample analysed, 0.3% of the grain boundaries were between 5-15 ° and 0.7% were 15-180 °, and the low angle grain boundaries will also interact with dislocations.

Also, recently Dunstan and Bushby developed an alternative equation to the well-established Hall-Petch relation and fitted it to data-sets used from Conrad [Con-63], Eshelby [Esh-51] and Li [Li-63] as well as many other data-sets providing a fit, which was shown to be more accurate through Bayesian statistical analysis [Dun-14]. According to their theory, the relationship between the yield strength and the grain size should be an inverse linear relationship instead of an inverse square root: $\sigma_Y \propto kD^{-1}$ [Dun-14]. Using their equation instead of the Hall-Petch and adding the

contributions of the two grain sizes linearly, the overall strength prediction is σ_y~170 MPa. The value is very similar to the σ_y~167 MPa prediction made using the Hall-Petch relation.

The work hardening contribution to the yield strength due to the plastic deformation induced during extrusion must also be playing an important role in the strength of the $Al_{93}Fe_3Cr_2Ti_2$ alloy. Work hardening as a result of interactions of dislocations with other dislocations and with other barriers to their motion within the lattice can be estimated using the basic equation relating flow stress to structure [Die-88]:

$$\Delta\sigma_y \approx \alpha G b \rho^{1/2} \text{ [Die-88]} \quad (9.1)$$

Where $\Delta\sigma_y$ is the yield strength increase, α is a constant which is 1 for most cases, but can be 0.5-1, G is the shear modulus of the matrix (=26 GPa for Al [Voj-07]), b is the magnitude of the Burgers vector (0.286 nm in Al [Voj-07]) and ρ is the density of dislocations. By fitting this model to achieve a work hardening contribution of 200 MPa to the yield strength, the required dislocation density would be ~$7x10^{14}$ m^{-2}. According to the literature, a reasonable value of dislocation density of aluminium samples after a few per cent deformation through cold working it should be 10^{12}-10^{13} m^{-2} and in an extremely cold worked sample it should be ~10^{15}-10^{16} m^{-2} [Yos-85], [Sma-99]. In this case, the extrusion ratio was 14:1, therefore the dislocation density is expected to be in the highest range, however the extrusion temperature of 400 °C could have decreased the value. No values of dislocation density of Al-based samples after warm extrusion at 400 °C were found in the open scientific literature.

Solid solution strengthening could also be an active strengthening mechanism contributing to the overall strength of this alloy. Other authors found that Hall-Petch is the dominant strengthening mechanism in rapid solidified Al alloys, moreover some of them found the solid solution mechanism is negligible due to the hot processing methods employed to consolidate the rapidly solidified alloys [Ehl-94], [Voj-07], [Wan-04]. In the present work for the $Al_{93}Fe_3Cr_2Ti_2$ alloy extruded from <25 μm atomized powder the Orowan mechanism has a more important

contribution ($\Delta\sigma_O$~180 MPa) than the Hall-Petch mechanism ($\Delta\sigma_{HP}$~170 MPa) to the yield strength. Moreover, it is observed that another important contribution is required to reach the measured yield stress of 544 MPa, which is reasonable to relate predominantly to work hardening.

However the solid solution mechanism could also be active as the relative amounts of solutes in solid solution in the Al matrix are higher than the stable solubility of each element in Al. The EDX measurements performed on TEM samples detected a matrix composition of 0.22±0.1 at% Fe, 0.25±0.2 at% Cr and 1.26±0.4 at% Ti. The stable solid solubility of each element in Al solid solution at the extrusion temperature of 400 °C is 0.02 at% Fe, 0.18 at% Cr and 0.03 at% Ti [Mas-90], [Mon-43], [Xu-06].

Strength in solid solution hardening depends on the strain fields around each solute atom which depends on the misfit radii. However quantitative measurements of atomic radii are generally difficult due to the radius not being a well-defined physical entity but a probability distribution without a sharp cut-off point which is also affected by electronegativity interactions with the surrounding atoms [Sla-64]. A quantitative value of the atomic radii data of atoms in the elemental state can be found in Table 9.3.

Atomic radius	*[Smi-83]*
Al	*143*
Fe	*128*
Cr	*128*
Ti	*147*

Table 9.3: Value of atomic radius of Al, Fe, Cr and Ti[3].

Friedel's equation [Fri-67] for the prediction of the yield strength based on the lattice misfit says that

$$\Delta\sigma_y = \alpha f G \Omega_M \frac{\delta}{b} \text{ [Fri-67]} \quad (9.2)$$

[3] Atomic radius data from Smithells' Metals Reference Book, 8th edition, Table 4.21 (p. 4-25).

Where $\Delta\sigma_y$ is the yield strength increase, α is a constant which is 1 for most cases, but can be 0.5-1, f is the fraction, G is the shear modulus of the matrix (=26 GPa for Al [Voj-07]), Ω_M=1.9x10^{-10} for Al 5000 series alloys [Rob-09], δ is the lattice misfit and b is the burgers vector (=0.286 nm for Al [Voj-07]).

Using these values, the total contribution to the yield strength from each element of Cr, Ti and Fe in solid solution can be estimated as low as ~10 MPa. The solid solution mechanism was also found negligible by other authors on rapidly solidified Al-TM alloy systems prepared both by extrusion of atomised powders and extrusion of melt spun, ground ribbons [Ehl-94], [Voj-07], [Wan-04].

The effect of the fibres can be modelled using the rule of mixtures [Cly-95]. Yield strength was shown to decrease linearly with increasing vol% pure Al fibres in Section 7.1.2.

In summary, efforts to correlate the microstructure to the mechanical strength measured in quasi-static conditions at room temperature concluded that many strengthening mechanisms are active. Contributions from the hard, incoherent particles and grain sizes have been estimated relying on assumptions of a more idealized microstructure with perfectly spherical, equally spaced particles and spherical, equiaxed grains separated by high angle grain boundaries and they underestimate the strength of the material. Other mechanisms must therefore be active including work hardening. Errors could also come from the fact these models don't account for the effect of low-angle grain boundaries and that the Hall-Petch slope will not necessarily stay linear for sub-micron sized grains.

9.6 Thermal Evolution

This section discusses the results of the heat treatments performed in Chapter 6 and the final microstructures compared to the as extruded bars presented in Chapters 4 and 5.

At 550 °C the microstructure underwent a major microstructural change as the icosahedral phase, which was measured to be 0.41 vol% of the as-extruded bars, underwent a transformation decomposing into more stable intermetallic phases such as κ-Al_3Ti, ϕ$Al_{13}Cr_2$ and ζ-$Al_{13}Fe_4$. This transformation was detected through TEM and XRD analysis in Chapter 6. The FCC-Al matrix composition between the intermetallic phases was also measured before and after heat treatment at 550 °C for 1 hour by TEM-EDX, and can be seen in Table 9.4. The Fe and Cr content of all of them was similar, the main difference was found in the Ti content. The samples heat treated at 550 °C appear to have less Ti in solid solution (0.5 at%) than the as-extruded bars, but more than the equilibrium solid solubility of Ti in Al at 550 °C (0.05 at%). This would suggest that at 550 °C some of the Ti could have diffused and formed intermetallic phases which were seen by XRD, as was suggested by the work of other authors in this alloy system [Gar-10].

	Temperature	***Matrix composition at%***			
Sample		***Al***	***Fe***	***Cr***	***Ti***
Equilibruim Solid Solubility in Al	*550*	*-*	*0.025*	*0.3*	*0.05*
0-1a	*550*	*99.2*	*0.1*	*0.1*	*0.5*

Table 9.4: Matrix composition between intermetallic phases measured by TEM-EDX after heat treatment for 1 hour at 550 °C and compared to the equilibrium solid solubility of Fe, Cr and Ti in Al [Xu-06], [Mon-43].

Longer heat treatments were performed at 250 °C to test long-term microstructural stability. The X-ray diffractograms and the microhardness indentation curve do not show differences between the as-extruded samples and the samples heat treated for 300 hours at 250 °C. After 1000 hours at

250 °C some intermetallic precipitation starts to become visible in the form of $Al_{13}Fe_4$ and $Al_{13}Cr_2$ phases and the microhardness indent shows a drop from 206 to 198 μHV_{500}. Inoue *et al.* saw no difference in microstructure or microhardness after heat treating a single crystal alloy of the same nominal chemical composition at 300 °C for 1000 hours [Ino-99], [Ino-00].

After 1000 hours at 250 °C, the matrix composition, compared to the matrix composition in the as-atomised powder also appears depleted in Ti, Fe and Cr. A comparison of the chemical composition of the as-atomised powder, the bar after extrusion at 400 °C (held at temperature for 30 minutes) and the bar after heat treatment at 250 °C for 1000 hours can be found in Table 9.5.

	Atomised powder		*Extruded*		*HT250-1000 hours*	
Element	*At%*	*Error*	*At%*	*Error*	*At%*	*Error*
Al	*98.1*	*0.2*	*98.2*	*0.2*	*98.9*	*0.2*
Ti	*1.4*	*0.3*	*1.3*	*0.2*	*0.7*	*0.1*
Cr	*0.3*	*0.1*	*0.4*	*0.2*	*0.2*	*0.1*
Fe	*0.2*	*0.1*	*0.2*	*0.1*	*0.1*	*0.1*

Table 9.5: Comparison of the chemical composition measured by EDX of the as-atomised powder matrix, the extruded bar matrix and the heat treated bar matrix after 1000 hours at 250°C. Errors were calculated over 10 measurements by doing an average of the maximum and minimum value.

This would show a decreasing trend in the amount of solutes in solid solution in the Al matrix after heating, it is therefore reasonable to assume that diffusion is taking place at a sufficient speed to enable solutes to either join pre-existing precipitates or create new ones. The most noticeable difference is in the amount of Ti in solid solution, and the appearance of Ti-based intermetallic phases which could be observed in the centre of clusters in the TEM micrographs in Chapter 6. The measured chemical composition of the α-Al matrix by TEM-EDX before and after extrusion was similar and have a higher solute content than the equilibrium solid solubility of Fe, Cr and Ti in Al at 400 °C [Mas-90]. The equilibrium solid solubility for Cr in Al at 400 °C is ~0.18 at% [Mon-43], the solid solubility of Fe at 400 °C is ~0.02 at% [Mon-43] and the maximum solid solubility of Ti

in Al at 400 °C is ~0.032 at% [Xu-06]. After 1000 hours at 250 °C the amount of solutes in solid solution is decreasing and getting closer but still exceeding the equilibrium values.

9.7 High Temperature Serrated Flow in Compression

Serrated flow is evident in the high temperature compression tests at strain rate 0.1 s^{-1} at all the temperatures tested, between 350-500 °C, presented in Chapter 8. It is greatly reduced at strain rate 1 s^{-1} and no longer present at strain rates above that. Serrated flow caused by dynamic strain ageing in stress strain curves is extremely common in a very broad range of commercial and non-commercial Al based alloys and substitutional or interstitial solutes have been considered responsible [Rob-94a]. It is generally not possible to derive reliable values for the activation energies associated with DSA experimentally. In this case, it is also impossible to measure the hardening contribution to the flow stress due to DSA as the behaviour of the material without DSA is unknown.

What follows is a semi-quantitative analysis which attempts to identify the species in solid solution responsible for dynamic strain ageing. The model used relies on the assumptions that a single solute species migrates without forming complexes and that the microstructure does not evolve with temperature at 350 °C.

Due to the composition of this alloy, it is likely that any one or any combination of Fe, Cr or Ti found in excess of the solid solubility due to the rapid solidification production technique is responsible for dynamic strain ageing. Previous work by Skinner *et al.* [Ski-89] used an Al-Si-Fe and Al-Si-Ti alloy and proved that at room temperature DSA behaviour was caused by the migration of the Si atoms interfering with dislocation motion, but over ~167 °C the titanium atoms also started contributing to this effect and over 227 °C the Fe atoms started contributing too. All their alloys in this study showed ductility reductions at temperature ranges that varied depending on which solute atom is in solid solution and depending on the strain rate of the tests. Bouchaud *et al.* worked on a rapidly solidified Al-Fe-V-Si alloy and concluded similarly that at room

temperature Si atoms were responsible for this effect, but between 127-227 °C Fe atoms became primarily responsible for dynamic strain ageing [Bou-91]. Serrated flow and a reduction in ductility were also found in tensile tests performed at 250 °C on the bars 0-1a, 10-1a and 20-1a by a previous project [Ped-10].

Both the papers by Skinner *et al.* [Ski-89], [Ski-88] and Bouchaud *et al.* [Bou-91] perform semi-quantitative analyses which rely on calculations of diffusion coefficients of substitutional atoms at different temperatures and match their speed to the speed of dislocations moving at the applied strain rate to determine which of the alloying elements is responsible for dynamic strain ageing at which temperature range. This relies on extensive testing at a variety of temperatures and strain rates to find out the minimum in ductility and the range in which it happens. In the current study tests were performed at strain rates 0.1-50 s^{-1} and temperatures between 350-500 °C. Previous compression tests performed on the same alloy composition both at room temperature and 250 °C and a strain rate $1x10^{-4}$ s^{-1} did not show serrated flow [Ped-10], so the range in which serrated flow is visible can be narrowed down to between 250-400 °C and $1x10^{-4}$ and 1 s^{-1} strain rates. Based on the current set of data, the starting point cannot be established more precisely, therefore temperature values from the literature will be used to perform a semi-quantitative analysis which estimates the diffusion coefficients in an attempt to tentatively identify which species is likely to cause DSA at the selected testing temperature of 350 °C (625 K).

Diffusion coefficients can be calculated at the strain rate and temperature which correspond to the strain rate sensitivity minimum using the formula used by Bouchaud *et al.* taken from Friedel's *Dislocations*:

$$D = \left(\frac{k_B T}{3|W|}\right)\left(\frac{b^2}{\tau}\right)\left(\frac{c_1}{\pi c_0}\right)^{3/2} \text{ [Bou-91], [Fri-67]} \quad (9.3)$$

Where k_B is the Boltzmann constant $1.38x10^{-23}$, T is the temperature at which SRS effect is minimum, W is the absolute value of the interaction energy between dislocations and diffusing species, b is the Burgers vector (for pure Al=0.286 nm [Bou-91]), c_1 is the concentration of solute atoms at dislocation line at saturation (typically 0.5), c_0 is the total concentration of diffusing

species (total number of diffusing atoms/total number of atoms) and τ is the relaxation time [Bou-91]. As shown in Table 9.5, the solutes in solid solution would decrease when the rapidly solidified alloy is kept at 250 °C for 1000 hours, but as the compression tests were induction heated for less than 5 minutes to reach the required temperature these calculations have been performed using the values of solutes in solid solution before heat treatment.

When ductility and strain rate sensitivity are minimum Orowan's law says that:

$$\tau = t_w = (b\rho_m\rho_f^{-\frac{1}{2}})/\dot{\varepsilon} \text{ [Bou-91]} \quad (9.4)$$

Where ρ_m is the density of mobile dislocations (in rapidly solidified extruded Al-Fe-V-Si ~10^{11} m^{-2} [Bou-91]), ρ_f is the density of forest obstacles (~10^{12} m^{-2} [Bou-91]), $\rho_f^{-1/2}$ is the mean spacing between forest obstacles, b is the burgers vector, $\dot{\varepsilon}$ is the strain rate, in this case 0.1 s^{-1}.

Matching the diffusion coefficient equation with the dislocation speed at the ductility minimum, the equation to calculate diffusion coefficients becomes [Bou-91]

$$D = \left(\frac{kT}{3|W|}\right)\left(\frac{b\dot{\varepsilon}}{\rho_m\rho_f^{-\frac{1}{2}}}\right)\left(\frac{c_1}{\pi c_0}\right)^{3/2} \text{ [Bou-91]} \quad (9.5)$$

The interaction energy between dislocations and diffusing species $|W|$can be calculated as follows: the interaction energy varies from 0 to W_{min} when the impurity atom reaches a dislocation. A measure of the limiting values of concentration (c_0) and temperature (T) at which dynamic strain ageing can occur is given by $c_0 \geq c_1 \exp\left(\frac{W}{kT}\right)$ [Fri-67], [Cot-53]. W is at a minimum when impurity atom reaches a dislocation so

$$c_0 = c_1 \exp\left(\frac{W_{min}}{kT}\right) \text{ [Fri-67], [Cot-53]} \quad (9.6)$$

When the force between the dislocation and the impurity atom is attractive, c_1~0.5 [Fri-67] so

$$W_{min} = kT \ln\left(\frac{c_0}{0.5}\right) \text{ [Fri-67]} \quad (9.7)$$

Applying this formula to the current experimental values and using temperatures taken from the literature for the point of minimum ductility caused by Ti and Fe atoms in solid solution, the diffusion coefficients obtained are of the order of ~10^{-16} for Fe, 10^{-16} for Cr and ~10^{-18} for Ti, as seen in Table 9.6.

Diffusing element	*Fe*	*Cr*	*Ti*
T_{min} for each element/ K	*~440 [Ski-89]*	*~413 [Bou-91]*	*~500-525 [Ski-89]*
C_0 in solid solution (at%)	*0.2±0.1*	*0.4±0.2*	*1.3±0.2*
W_{min} (using T_{min} from lit.)/ J/atom	*$-5.6x10^{-21}$*	*$-1.3x10^{-21}$*	*$6.6x10^{-21}$ (at 500K)*
			$6.9x10^{-21}$ (at 525K)
D using T_{min} from lit./ m^2/s	*$7.3x10^{-17}$*	*$1.1x10^{-16}$*	*$4.3x10^{-18}$*
D at the testing temperature of 625K/m^2/s	*$1.0x10^{-16}$*	*$1.6x10^{-16}$*	*$5.2x10^{-18}$*

Table 9.6: calculations of interaction energies and diffusion coefficients at the selected experimental setup.

As a comparison, values taken from the literature of tracer impurity diffusion coefficients of Ti in Al at 625 K are in the order of magnitude of 10^{-17} m^2/s, for Fe in Al 10^{-18} m^2/s [Smi-12]. The diffusion coefficient is however influenced also by both the mechanical deformation at the applied strain rate and the concentrations, which values from the literature do not account for. Therefore the diffusion coefficients calculated in Table 9.6 are more accurate than the literature values given for comparison.

It is generally accepted in literature that DSA occurs when the diffusion coefficient is of the order of D~10^{-18} m^2/s [Bou-91], [Fri-67]. The semi-quantitative analysis whose results are available in Table 9.6 would tentatively suggest that Ti could be a likely solute to cause DSA at the selected temperature at which the compression tests were made of 625 K. These calculations are estimates performed using values from the literature, further extensive mechanical testing at different strain rates would be needed to obtain accurate values for this alloy. Robinson and Shaw say evidence suggests that the T_{min} occurs at T~$0.3T_m$ where T_m is the homologous melting temperature.

Assuming T_m is ~660 °C, then T_{min}~198 °C, which is also close to the values taken from Bouchaud and Skinners papers [Rob-94b], [Bou-91], [Ski-89].

References

[Aud-02] F. Audebert, F. Prima, M. Galano, M. Tomut, P. J. Warren, I. C. Stone, B. Cantor, Mat. Trans., (2002), A 43, 8, 2017.

[Ash-64] M. Ashby, Z. Metallk., (1964), 55, 5-17.

[Bac-73] D. J. Bacon, U. F. Kocks, R. O. Scattergood, Philos Mag, (1973), 28, 1241.

[Bou-91] E. Bouchaud, L. Kubin and H. Octor: Metall. Trans., (1991), 22A, 1021.

[Bra-97] A. Brahmi, T. Gerique, M. Torralba, M. Lieblich, Scripta Mat., (1997), 37, 11, 1623-1629.

[But-93] M. Z. Butt and P. Feltham, J. Mat. Sci., (1993), 28, 2553-2576.

[Che-03] S. Cheng, J. A. Spencer, W. W. Milligan, Acta Mater., (2003), 5, 4505.

[Cly-95] T. W. Clyne, P. J. Withers, *An Introduction to Metal Matrix Composites*, Cambridge University Press, (1995).

[Con-00] K. T. Conlon, E. Maire, D. S. Wilkinson, H. Henein, Met. Trans. A, (2000), 31A, 249.

[Con-63] H. Conrad, Acta Metall., (1963), 11, 75.

[Con-03] H. Conrad, Mat. Sci. Eng., (2003), A341, 216.

[Cot-53] A. Cottrell, *Dislocations and plastic flow in metals*, Oxford University Press, (1953).

[Die-88] G. E. Dieter, *Mechanical Metallurgy*, McGraw-Hill, 2nd Edition, (1988).

[Dun-14] D.J. Dunstan and A. J. Bushby, Int. J. Plast., (2014), 53, 56-65.

[Ehl-94] J. C. Ehlstrom, A. Pineau, Mat. Sci. Eng., (1994), A 186, 55-64.

[Esh-51] J. D. Eshelby, F. C. Frank, F. R. N. Nabarro, Phil. Mag. (1951), 42, 351.

[Fle-63] R. L. Fleischer, Acta Met., (1963), 11, 203-209.

[Fri-64] J. Friedel, *Dislocations*, p 379, Pergamon Press, Oxford, (1964).

[Fri-67] J. Friedel, *Dislocations in Crystals*, Pergamon Press, (1967).

[For-67] A. J. E. Foreman, M. J. Makin, Can. J. Phys., (1967), 45, 511.

[Gal-09a] M. Galano, F. Audebert, I.C. Stone, B. Cantor, Acta Mat., (2009), 57, 5107–5119.

[Gal-09b] M. Galano, F. Audebert, I. C. Stone, B. Cantor, Acta Mat., (2009), 57, 5120–5130.

[Gal-04] M. Galano, F. Audebert, B. Cantor, I. Stone, Mat. Sci. Eng., (2004), A, 375-377, 1206-1211.

[Gar-10] A. Garcia-Escorial, M. Echevarria, M. Lieblich, I. Stone, J. All. Comp., (2010), 504S, S519–S521.

[Gar-07] A. Garcia Escorial, V. F. Cremaschi, E. Natale, M. Lieblich, J. All. Comp., (2007), 434-435, 215-216.

[Gu-09] W-H. Gu, Masters Thesis, University of Oxford, (2009).

[Han-75] K. Hanson and J. W. Morris Jr., J. Appl. Phys., (1975), 46, 3, 983-990.

[Hay-04] R. W. Hayes, D. Witkin, F. Zhou, E. J. Lavernia, Acta Mat., (2004), 52, 4259.

[Hir-69] P. B. Hirsch, F. J. Humphreys. In: Argon AS, editor. *The physics of strength and plasticity*. Cambridge (MA): MIT Press; (1969).

[Hum-01] E. S. Humphreys, P. J. Warren, J. M. Titchmarsh, A. Cerezo, Mat. Sci. Eng, (2001), A304–306, 844–848.

[Hal-51] E. O. Hall, Proc. Phys. Soc., London, (1951), B, 64, 747.

[Hon-77] R. W. K. Honeycombe, *The Plastic Deformation of Metals*, Edward Arnold Publishers, (1977).

[Ino-00] A. Inoue, H. Kimura; Mat. Sci. Eng., (2000), A286, 1-10.

[Ino-99] A. Inoue, H. Kimura, Nano. Structured Mat., (1999), 11, 2, 221–231.

[Jia-14] X. Jiang, M. Galano, F. Audebert, Mat. Char., (2014), 88, 111-118.

[Jos-06] S. P. Joshi, K. T. Ramesh, B. Q. Han, E. J. Lavernia, Met. Trans A, (2006), 37A, 2397-2404.

[Kim-00] H. Kimura, K. Sasamori, A. Inoue, Mat. Sci. Eng., (2000), 294-296, 168-172.

[Koc-67] U. F. Kocks, Can. J. Phys., (1967), 45, 737.

[Lab-70] R. Labusch, Phys. Status Solidi, (1970), 41, 650.

[Li-63] J. C. M. Li, Trans. AIME, (1963), 227, 239.

[Mas-90] T. B. Massalski, H. Okamoto, P. R. Subramian, L Kacrzak, editors. *Binary alloy phase diagrams*, Materials Park (OH): ASM International, (1990).

[Mot-48] N. F. Mott and F. R. N. Nabarro, Phys. Soc., (1948), p1.

[Mey-82] M. A. Meyers, E. Ashworth, Phil. Mag. A, (1982), 46, 737.

[Moh-01] V. Mohles, Mat. Sci. Eng., (2001), A309–310, 265.

[Moh-04] V. Mohles, Mat. Sci. Eng., (2004), A365, 144.

[Mon-43] L. F. Mondolfo, *Metallography of Aluminum Alloys*, John Wiley & Sons, (1943).

[Mor-73] T. Mori, K. Tanaka, Acta. Met., (1973), 21, 571-574.

[Nab-77] F. R. N. Nabarro, Phil. Mag., (1977), 35, 613.

[Oro-40] E. Orowan, Proc. Phys. Soc., (1940), 52, 8.

[Ped-10] S. Pedrazzini, Masters Degree Thesis, University of Oxford, (2010).

[Pri-04] F. Prima, M. Tomut, I.C. Stone, B. Cantor, D. Janickovic, G. Vlasak, and P. Svec. Mat. Sci. Eng. A, (2004), 375-377, 772-775.

[Rob-94a] J. M. Robinson, Int. Mat. Rev., (1994), 39, 6, 217.

[Rob-94b] J. M. Robinson and M. P. Shaw, Int. Mat. Rev., (1994), 39, 3, 113.

[Rob-09] S. Roberts, Microplasticity Course Lecture Notes, University of Oxford, (2009).

[Rou-12] N. J. Rounthwaite, DPhil Thesis, University of Oxford, (2012).

[Sah-05] K.L. Sahoo and I.C. Stone, Phil. Mag. Lett., (2005), 85, 231–245.

[Ski-88] D. J. Skinner, V. R. V. Ramanan, M. S. Zedalis, H. J. Kim, Mat. Sci. Eng., (1988), A99, 407-411.

[Ski-89] D. J. Skinner, M. S. Zedalis, P. Gilman, Mat. Sci. Eng., (1989), A119, 81-86.

[Sih-05] C. S. Shin, M. C. Fivel, M. Verdier, C. Robertson, Mat. Sci. Eng., (2005), A400–401, 166.

[Sla-64] J. C. Slater, J. Chem. Phys., (1964), 41, 3199.

[Sma-99] R. E. Smallman, and R. J. Bishop. *Modern physical metallurgy and materials engineering*. Butterworth-Heinemann, (1999).

[Smi-83] E. A. Brandes, G. B. Brooks editors, *Smithells Metals Reference Book*, Butterworth-Heinemann, (1983).

[Sut-96] A. P. Sutton, R. W. Balluffi, *Interfaces in Crystalline Materials*, Oxford

University Press; (1996).

[Tay-34] G. I. Taylor, Proc. Roy. Soc. A, (1934), 145, 362.

[Und-70] E. E. Underwood, *Quantitative Stereology*, p 80, Addison Wesley, (1970).

[Van-85] D. Van Aken and H. Fraser, Acta Metall., (1985), 33, 6, 963-974.

[Voj-07] D. Vojtěch, J. Verner, J. Šerák, F. Simancik, M. Balog, J. Nagy, Mat. Sci. Eng., (2007), A 458, 1-2, 15, 371.

[Wan-04] Y. Wang, Z. Zhang, W. Wang, X. Bian, Mat. Sci. Eng., (2004), A366, 17–24.

[Wen-90] G. C. Weng, J. Mech. Phys. Solids, (1990), 38, 3, 419-441.

[Xu-06] L. Xu, Y.Y. Cui, Y. L. Hao, R. Yang, Mat. Sci. Eng., (2006), A 435–436, 638–647.

[Yam-07] M. Yamasaki, Y. Nagaishi, Y. Kawamura, Scripta Mat., (2007), 56, 785-788.

[Yos-85] H. Yoshinaga, S. Matsuo, H. Kurishita, Trans. Japan Inst. Met., (1985), 26, 6, 423-432.

[Yu-05] C.Y. Yu, P. W. Kao, C. P. Chang, Acta Mat., (2005), 53, 4019–4028.

Chapter 10: Conclusions

10.1 Aims and Achievements

This rapidly solidified alloy system has been produced before, however this kind of in-depth study has never been performed on this alloy and composites. This work correlates the production of the alloy and composites using viable, industrial scale production methods, with the resulting microstructures. It tests and develops an analytical method for the prediction of the yield strength at room temperature (which is essential for use as engineering components as they would always only be used in the elastic range) and analyses the alterations to the strength and microstructure brought by the industrially used processing methods which involve plastic deformation at temperature. A study like this had never been performed on this alloy and composites before and this knowledge is a step forwards towards its safe use in engineering applications.

10.2 Powder Production and Characterisation

Two separate batches of $Al_{93}Fe_3Cr_2Ti_2$ alloy powders were successfully produced by means of atomisation runs performed at 1200 °C in a N_2 atmosphere with 3% added O_2. The morphology of the powders was elongated and nodular. The microstructure of the 0-25 μm size fraction from both batches consisted mainly of FCC-Al containing a distribution of sub-micron icosahedral quasicrystalline phases and small amounts of metastable monoclinic θ-phase intermetallics. Some of the icosahedral phase particles were found to produce ring-shaped clusters surrounding some FCC-Al matrix. 2-3 vol% pure Al contamination was found in the 1st batch but no contamination was identified in the 2nd batch.

DSC analysis of the as-atomised $Al_{93}Fe_3Cr_2Ti_2$ powders from batch 1 and 2 did not highlight any reactions occurring up to the extrusion temperatures of 390-420 °C. The only reaction detected occurred at 550 °C and was associated with the decomposition of the icosahedral phase. No reaction was detected in the Pure Al powder until the onset of melting at 630 °C.

10.3 Extrusion and Characterisation of the $Al_{93}Fe_3Cr_2Ti_2$ Alloy and Composites

One bar of pure $Al_{93}Fe_3Cr_2Ti_2$ alloy was extruded at 420 °C using an extrusion ratio of 14:1 and a ram speed 0.3 mm/s and compared to a bar extruded during a previous project at 400 °C [Ped-10]. Four more bars of composites containing 10 vol% and 20 vol% pure Al fibres were successfully extruded, two from either powder batch, and compared to two composite bars produced during a previous project [Ped-10].

Warm extrusion caused the powder particles to become well bonded and elongated in the extrusion direction introducing a preferred orientation in the FCC-Al grains. A bimodal distribution of grains was observed after extrusion. Several low angle (5-15 °) grain boundaries were also identified by EBSD along the extrusion direction. The selected temperatures caused the decomposition of the θ-phase in most bars and the precipitation of small amounts of other intermetallic phases detected after extrusion. No obvious change in size or shape was observed in the icosahedral phase (a bimodal distribution of hard, incoherent precipitates was observed after extrusion), or any change in the amount of solutes in solid solution in the Al matrix. The fibre addition did not cause visible changes to the microstructure of the matrix.

10.4 Mechanical Testing at Room Temperature

Room temperature microhardness, quasi-static tensile tests and dynamic tensile and compression tests showed at least a 10% improvement when using the pure $Al_{93}Fe_3Cr_2Ti_2$ alloy compared to current commercial high strength 7075 T6 Al alloy tested under the same conditions. In terms of specific strength, this alloy gave values only ~10% lower than Ti6Al4V under the conditions tested (only 5% lower than Ti6Al4V in the case of dynamic tensile tests) [ElM-06]. The specific values of 0.2% proof stress in tension are shown in Figure 10.1. The outstanding strength observed (and more specifically the yield strength, as engineering components would only be used in the elastic range) were fitted to analytical models based on microstructural observations. A combination of the classic strengthening mechanisms Orowan, Hall-Petch and work hardening [Voj-07], [Oro-40],

[Hal-51], [Die-88] was used, corrected to accommodate different microstructural observations such as a bimodal distribution of hard, incoherent particles and a polycrystalline material with a bimodal grain size distribution [Ash-64], [Und-70]. It was found that the strength of the $Al_{93}Fe_3Cr_2Ti_2$ alloy came primarily from a combination of the effect of the hard, incoherent nanoparticles, the small grain size and work hardening. The fibre addition to this alloy caused a linear decrease in mechanical strength with increasing vol% pure Al.

This work represents the first quantitative estimate of which strengthening mechanisms are active and how much they influence the mechanical strength of gas atomised, extruded $Al_{93}Fe_3Cr_2Ti_2$ alloy and composites.

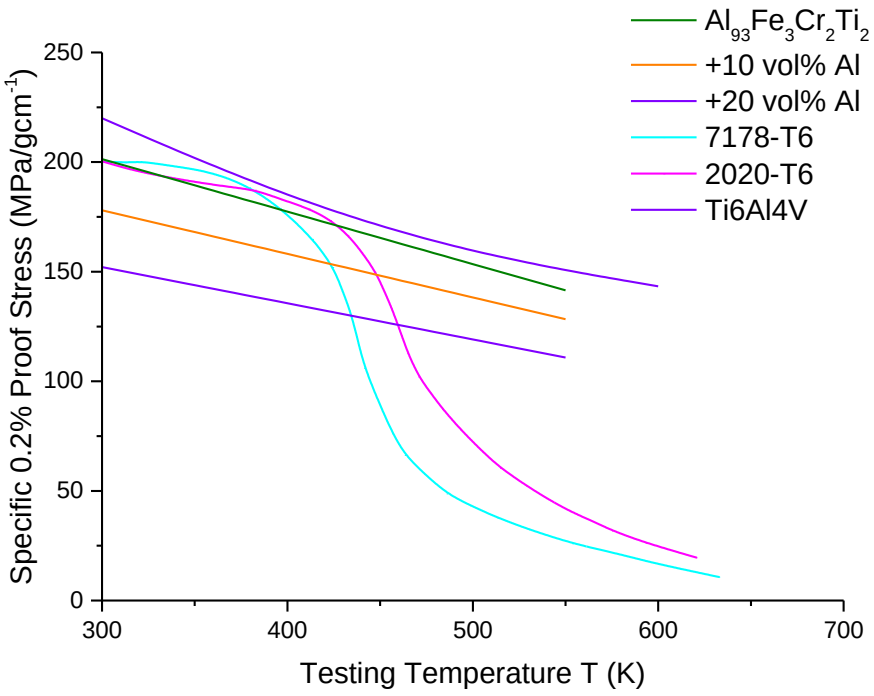

Figure 10.1: Specific yield strength of the $Al_{93}Fe_3Cr_2Ti_2$ alloy and composites compared to commercially available Al-based alloys [Ino-00] and Ti6Al4V [Smi-92] and their variation with temperature.

10.5 Thermal Analysis

Plastic deformation at temperature is used as a processing method to produce engineering components from Al-based alloys. The thermal evolution of the extruded bars was analysed before hot mechanical testing.

After extrusion, the DSC, XRD and TEM analysis of the bars showed the decomposition of the icosahedral phase occurring at 500 °C, which is 50 °C below the reaction temperature measured in the powders before extrusion.

Heat treating the bars for 1 hour at 250 °C did not alter the microstructure or microhardness of the alloy and composite bars in a way which could be detected by SEM, TEM, XRD and microindentation. Heat treating for 1 hour at 280 °C caused some intermetallic precipitation in the form of κ-Al_3Ti and ϕ-$Al_{13}Cr_2$ detected by XRD, but the microhardness remained constant (within experimental error values). Heat treating the bars at 550 °C caused the complete decomposition of the icosahedral phase and the precipitation of κ-Al_3Ti, ϕ-$Al_{13}Cr_2$ and ζ-$Al_{13}Fe_4$ intermetallic phases and a ~33% reduction in microhardness of the 0-1a, 10-1a and 20-1a bars. The microhardness decreased linearly with increasing vol% pure Al fibre content following the rule of mixtures [Cly-95].

Analysing the microstructural stability at 250 °C for up to 1000 hours did not show any changes in the microstructure detected by SEM and XRD. After 1000 hours the microhardness of the 0-1a, 10-1a and 20-1a samples only went down by 2-5%. Conventional "high strength" 2020 T6 Al and 7178 T6 Al only retain 20% of their room temperature UTS after heat treatment for 100 hours at 250 °C [Ino-00].

10.6 High Temperature Mechanical Testing

Compression testing at a variety of temperatures and strain rates between 350-500 °C and 0.1-50 s^{-1} was performed for the first time on this type of alloy system to investigate the possibility

of using processes which involve plastic deformation at elevated temperatures to produce engineering components.

The tests revealed a compressive yield strength of the pure alloy bar to be 340 MPa at 350 °C, decreasing with increasing temperature. The yield strength of 7075 T6 Al under the same testing conditions, was 110 MPa at 350 °C, just under 1/3 of the strength of the $Al_{93}Fe_3Cr_2Ti_2$ alloy [Lin-12].

The yield strength of the $Al_{93}Fe_3Cr_2Ti_2$ alloy was also found to increase with increasing strain rate between 0.1 and 50 s^{-1}. The gradient of the plastic zone was found to decrease with increasing temperature, showing that the material was softening at lower temperature and higher strain rates. Only the curve the highest temperature and lowest strain rate (at 500 °C and 0.1 s^{-1}) showed hardening. The yield strength of the composites was also shown to decrease with increasing temperature and increase with strain rate within the range tested. The effect of 10 vol% and 20 vol% fibre addition decreased the yield strength following the rule of mixtures.

The strain rate sensitivity parameter was calculated to be in the range of 0.05-0.14 for the pure alloy and composites, decreasing linearly over the temperatures tested.

However, major microstructural changes occurred within the samples in the range of temperatures tested. The microstructure was shown by XRD to undergo a phase transformation which resulted in the decomposition of the icosahedral phase at 500 °C into more stable intermetallic phases.

The high temperature compressive data was also used for the first time in a semi-quantitative analysis to determine which species in solid solution (Fe, Cr or Ti) was likely to cause serrated flow. Using a dynamic strain ageing model which calculates the diffusion coefficients at the minimum in ductility and strain rate sensitivity suggested the Ti in solid solution in the matrix could be the most likely candidate.

10.7 Future Developments

There are a number of areas in which further work would complement and advance the present investigation.

- A mechanical strength model was suggested in the present work based on analytical equations which rely on the assumption of a more idealised microstructure. Further simulations which account for more realistic microstructural features, such as grain shapes and particle distributions would be extremely interesting. Particularly when complemented with 3D measurements of the grain structure below the surface performed using techniques such as serial-section EBSD. Dislocation dynamics simulations which predict the extent of work hardening would also improve the accuracy of the strength prediction.
- It was previously mentioned that due to the fact that a polycrystalline material was analysed with a bimodal grain size distribution the 0.2% proof stress measured would only be an approximation of the yield strength of the material, which certainly undergoes a longer elastoplastic transition. Bauschinger tests (traction with unloading followed by compression) would provide an interesting supplement to the present set of data allowing observations of how the yield strength varies depending on the loading path and direction.
- Further studies which widen the range of strain rates at which room temperature mechanical tests are performed by adding intermediate values would allow an investigation of the strain rate sensitivity.
- Further elevated temperature compression and tensile tests with the objective of narrowing down the range in which serrated flow occurs would complement and improve the accuracy of the predictions performed during the present work. Particularly if supplemented with an analysis technique which would allow the observation and the chemical identification of solutes responsible for pinning the dislocation lines on the atomic scale such as Atom Probe Tomography or Electron Energy Loss Spectroscopy.
- Tests which assess the fatigue strength of this powder processed alloy and composites would be essential before its use in engineering applications.

- Measurements which test the mechanical strength in a different direction (which is not parallel to the extrusion direction), would allow an understanding of the extent of the anisotropy of the mechanical properties.
- And finally, an extremely interesting future development of this work would involve changing the material the fibres are made of, for example pure Ti could lead to improved mechanical strength despite a slight increase in the weight of the alloy. Changing the fibres could allow the strength to weight ratio of these composites to be tailored specifically to the requirements of individual components for engineering applications.

References

[Ash-64] M. Ashby, Z. Metallk., (1964), 55, 5-17.

[Cly-95] T. W. Clyne, P. J. Withers, *An Introduction to Metal Matrix Composites*, Cambridge University Press, (1995).

[Die-88]G. E. Dieter, *Mechanical Metallurgy*, McGraw-Hill, (1988).

[ElM-06] E. El-Magd, M. Abouridouane, Int. J. Imp. Eng., (2006), 32, 741–758.

[Hal-51] E. O. Hall, Proc. Phys. Soc., London Sect B, (1951), 64, 747.

[Ino-00] A. Inoue, H. Kimura; Mat. Sci. Eng., (2000), A286, 1-10.

[Lin-12] Y. C. Lin, L. T. Li, Y. X. Fu, Y. Q. Jiang, J. Mater. Sci., (2012), 47, 1306–1318.

[Oro-40] E. Orowan, Proc. Phys. Soc., (1940), 52, 8.

[Ped-10] S. Pedrazzini, Masters Degree Thesis, University of Oxford, (2010).

[Smi-92] Edited by E. A. Brandes, G. B. Brook, *Smithells Metals Reference Book*, 7th Ed, Butterworth-Heinemann, (1992).

[Und-70] E. E. Underwood, *Quantitative Stereology*, p 80, Addison Wesley, (1970).

[Voj-07] D. Vojtěch, J. Verner, J. Šerák, F. Simancik, M. Balog, J. Nagy, Mat. Sci. Eng., (2007), A 458 1-2 15 371.

Appendix 1: EBSD Resolution

An Electron Backscatter Pattern is formed when the incident electron beam hits the sample tilted at 70 ° from the perpendicular axis (conversely tilted up to 20 ° from the incident beam). Electrons enter the sample and have an interaction depth which depends on the voltage, the spot size and the type of material. Scattering events which occur within the sample can be elastic, which involve a significant change in electron direction and the interaction of which will involve atomic nuclei, or inelastic, which will have a change in energy but no significant change in direction and the interaction of which will involve electrons.

Due to the highly tilted angle of the sample with respect to the incident beam, some of these electrons are scattered and continue on a path which exits the sample. Elastic scattering events within the sample will encourage electron emission, while inelastic scattering events will discourage it. When the electrons are scattered, the incoming planar wave will be scattered into a spherical wave (Huygens Wave), which has amplitude f_{HW} that depends on the scattering angle (θ) and the wavelength (λ) through $s=\sin(\theta)/\lambda$. F(s) is called the atomic scattering factor, or form factor. As the backscattered electrons leave the sample, they can interact with the periodic lattice of the crystal and many of them will interfere and therefore diffract according to Bragg's law (several theories for diffraction have been developed [Win-08], [Win-09], [Win-07].

Diffraction patterns occur due to the constructive interference of waves scattered from atomic nuclei. Constructive interference only occurs at the Bragg angle, destructive interference is also possible but it would not result in a visible pattern. Multiple scattering of the incident beam leads to a situation in which electrons are impinging on diffraction planes in essentially every direction. Solving the Bragg equation therefore corresponds to a cone about the normal to a given diffraction plane. A second cone on the other side of the plane exists as well, they are called Kossel cones, separated by the angle 2θ.

Bragg angles are extremely small (generally 1-4 °), therefore the diffraction cones are flattened. Intersecting the cones with a planar phosphor screen produces two nearly straight parallel lines (Kikuchi lines). The angle between the Kikuchi lines is $2\theta_B$. The band width is proportional to the interplanar spacing.

By imaging the Kikuchi lines it is possible to gain information of the crystallography of the volume with which the incoming beam interacted. The resultant diffraction pattern is called an Electron Backscatter Pattern (EBSP). An individual crystal will typically have multiple planes which can each diffract to produce a set of bands on the phosphor, with positions dependent on the orientation of the crystal with respect to the electron beam and the phosphor. An intersection of two or more bands will correspond to individual zone axes, which are also spaced according to the atomic arrangement within the crystal and the crystal orientation. Thus, correct identification of either the zone axes or the bands allows for identification of the crystal orientation, provided one knows pattern centre [Kri-99], [Kri-93]. Furthermore, any elastic strain present within the crystal will both appear as a relative shift of these features, compared with their positions in the unstrained state, and also a change in band width (due to a change in lattice spacing). Plastic strain present within the material will be visible as band blurring and also by local variations in the crystal orientation due to the presence of lattice curvature caused by the storage of dislocations.

Identification of band positions and orientations is performed using automated software which uses Hough (Radon) transforms [Hou-62]. This transforms a series of lines in real space to localised points in the Hough accumulator array. The bands are bright at the centre and dark at the edges and not perfectly parallel (due to the fact they come from the interaction of cones with a plane), therefore typically a band will transform into a set of three points, two dark ones on the outside and a bright one in the centre. This series of points can be detected automatically more easily than the bands in the original EBSP using a convolution mask.

Once the pattern orientation is determined and the centre is known, then the crystal orientation can be uniquely determined by calculating the orthogonal reference frame within the pattern from 3 intersecting bands and this frame can be compared against a similar orthogonal reference frame constructed as a reference orientation. The rotation of one frame against the other describes the crystal orientation present [Wri-00]. TSL have patented a "voting scheme" developed by Wright [Wri-92] and a fitting scheme [Kri-94]. In the voting scheme, one vote for a particular crystal orientation is made up by each tri-band point. As more and more points are considered the number of votes for the most likely solution increases. In this solution, the number of votes for the most likely solution V_1 will be considered against the number of votes for the next most likely solution V_2 (or potentially more than one) as a fraction of the total number of potential votes made V_t. This allows a calculation of a confidence index CI: $CI=(V_1-V_2)/V_t$.

It has been empirically found that a pattern will be indexed correctly 95% of the times with a confidence index >0.1 for FCC-Al [Wri-92].

In the fitting scheme, a kinematic simulation of a diffraction pattern is compared to the interplanar angles measured and the "fit" between the simulation and the measurements is compared. As more and more angles are measured the best solution can be determined.

Orientation maps are created by successive sampling of the electron beam over the surface of the sample to generate a map of data points. Binning the maps can increase the speed at which the map is acquired (a 1000x1000 pixel map if binned 2x2 will go down to a 500x500 pixel map), but it will reduce the spatial resolution. Increasing the probe current or the voltage will also speed up the pattern acquisition, but it will also increase the interaction size and reduce the spatial resolution [Dea-05].

The accuracy of the measurement can be defined in terms of angular resolution and spatial resolution. Angular resolution involves the accuracy of the measurement of the incoming beam angle which therefore also affects the measurement of the diffracted angle. There are two main sources of error which control the angular resolution, the errors in absolute orientation when indexing a single crystal [Nol-07] and the comparative error when measuring the misorientaiton between two crystals [Hum-01]. These depend on errors in the tilt axes, microscope alignment, pattern quality (ie deformation in the crystal) and the detector [Nol-07], [Hum-01].

The spatial resolution however will depend on the volume of material with which the electrons can diffract and escape from, which depends on the microscope employed, the probe current, emission tip, sample tilt, material atomic number and voltage. It will also depend heavily on the surface quality as the diffraction originates from a small, near surface volume. As the sample is highly tilted, the resolution of the sample in the Y direction is worse than the X direction.

There have been many studies and simulations which can quantify the size of the interaction volume of the incoming electrons in a Scanning Electron Microscope, however backscattered electrons will only come from elastic scattering events in the higher energy area of the interaction volume, which is smaller and more surface-specific.

Looking at the literature, there seems to be a lot of different data for the maximum resolution (in terms of step size) achievable in Aluminium ranging from 50-500 nm [Che-11], 200-500 nm [Hum-98], [Pett-98], 50-150 nm [Far-98], [Hum-99], 40 nm [Wil-12] and 200 nm [Hum-01], ~35 nm for Al at 30 kV [Wil-10], ~20 nm for Al at 10 kV [Wil-10], ~20 nm [Bri-13]. There could be several reasons for these differences.

The effective spatial resolution achievable by EBSD is a combination of physical parameters (where the BE come from) and detection/distinction (indexing). Physical parameters are governed by probe size (tungsten is 100+ nm, FEG <20 nm, also depending on the voltage), deformation state (blurring) and Z number. Detection/distinction is controlled by indexing performance, as well as brightness/brilliance of the source.

The size of the probe also means that the minimum achievable step size in perfect conditions (with the height exactly 15 mm, in a completely undeformed matrix at the exact angle, etc…) using the smallest probe size achievable by W filament SEM at and the lowest possible voltage which still produces an indexable pattern and the highest camera resolution (low binning, long exposure time) is ~100 nm, because that is the minimum probe size in the X direction. In the Y direction the resolution is typically 3x worse [Fie-05]. Therefore (if at least 10 points per grain need to be measured[4]) the minimum grain diameter measurable in a W-filament SEM will be ~300 nm and a FEG-SEM is ~60 nm.

However real experimental conditions cannot be considered to be perfect, which explains why there is so much variation in the maximum achievable resolution by EBSD in Al in the literature.

The pattern indexability doesn't only depend on the perfect microscope setup, plastic deformation in the sample causes blurring of the patterns [Wil-91a], [Wil-91b] which reduces resolution.

References:

[Bri-13] T. B. Britton, Lecture notes, Department of Materials, Imperial College, (2013).

[Che-11] D. Chen, J-C. Kuo, W-T. Wu, Ultramicroscopy, (2011), 111, 1488-1494.

[Dea-05] A. Deal, X. D. Tao, A. Eades, Surf. Interf. Analysis, (2005), 37, 11, 1017-1020.

[Far-98] T. Farstad, K. Johannessen, J. Hjelen, in: proceedings of the 14th International Congress on Electron Microscopy (ICEM-14), Cancun, Mexico, (1998), pp. 753–754.

[Fie-05] D. P. Field, Microsc. Microanalysis, (2005), 11, 52-53.

[Hou-62] P. Hough, USP Office, Editor., (1962), USA.

[Hum-01] F. J. Humphreys, J. Mat. Sci., (2001), 36, 16, 3883-3854.

[Hum-99] F.J. Humphreys, Y. Huang, I. Brough, C. Harris, J. Micros., (1999), 195, 212–216.

[4] An assessment of how representative a data set might be must be made if for example the grain size distribution is known to be unimodal then the general agreement throughout the literature is that a minimum of 200 grains should be sampled with at least 10 points across a grain therefore the spot size should be set as a 10th of the first guess of the grain size [Hum-01], [Wil-12], [Ran-09]

[Hum-98] F. J. Humphreys, J. Micros., (1999), 195, 3,170-185.

[Kri-99] N. C. Krieger Lassen, J. Micros., (1999), 195, 204-211.

[Kri-93] N. C. Krieger-Lassen and J. B. Bildesorensen, J. Micros., (1999), 170, 125-129.

[Nol-07] G. Nolze, Ultramicroscopy, (2007), 107,2-3, 172-183.

[Pet-98] T. Pettersen, G. Heiberg, J. Hjelen, in: proceedings of the 14th International Congress on Electron Microscopy (ICEM-14), Cancun, Mexico, (1998), 775-776.

[Ran-09] V. Randle, Mat. Charact., (2009), 60, 913-922.

[Wil-12] A. J. Wilkinson, T. B. Britton, Mat. Today, (2012), 15, 9, 366-376.

[Wil-10] A. J. Wilkinson, Lecture notes, Department of Materials, University of Oxford, (2010).

[Wil-91a] A. J. Wilkinson, Mat. Sci. Eng., (1991), A 135, 189-193.

[Wil-91b] A. J. Wilkinson, Acta Metall. Mater, (1991), 39, 12, 3047-3055.

[Win-09] A. Winkelmann, A. J. Schwarz *et al.* editors, Kluwer Academic/ Plenum publishers, (2009).

[Win-08] A. Winkelmann, Ultramicroscopy, (2008), 108, 12, p1546-1550.

[Win-07] A. Winkelmann, C. Trager-Cowan, F. Sweeney,A. P. Day, P. Parbrook, Ultramicroscopy, (2007), 107, 4-5, 414-421.

[Wri-00] S. I. Wright, Editors AJ Schwarz, M. Kumar and B. L. Adams, Kluwer Academic/Plenum publications, New York, 51-65, (2000).

[Wri-92] S. I. Wright, (1992), Yale University, p.125

[Wri-92] S. I. Wright and B. L. Adams, Met Trans A, (1992), 23, 3, 759-767.